ISSN 0022-0248

JOURNAL OF CRYSTAL GROWTH

VOLUME 181, Nos. 1/2
OCTOBER II (1997)

EDITORS:

M. SCHIEBER (Principal Editor),
Hebrew University

R.S. FEIGELSON, Stanford University

D.T.J. HURLE, University of Bristol

R. KERN, Université Aix–Marseille

T. NISHINAGA, University of Tokyo

G.B. STRINGFELLOW, University of Utah

CO-FOUNDERS: N. CABRERA, B. CHALMERS, F.C. FRANK
ADVISOR: R.A. LAUDISE

North-Holland

http://www.elsevier.nl

JCRGAE 181 (1/2) 1–170 (1997)

Journal of Crystal Growth

EDITORIAL BOARD

M. SCHIEBER (Principal Editor)
The Fredy and Nadine Herrmann
Graduate School of Appl. Sci.
Hebrew University, Jerusalem 91904, Israel
Telefax: +972-2-566 3878

R. KERN
CRMC², CNRS, Campus Luminy, Case 913
F-13288 Marseille Cedex 9, France
Telefax: +33-91-4-418 916

R.S. FEIGELSON
Ctr. Materials Res., 105 McCullough Bldg.
Stanford Univ., Stanford, CA 94305-4045, USA
Telefax: +1-415-723 3044

T. NISHINAGA
Dept. Electron. Eng., Univ. of Tokyo
7-3-1, Hongo, Bunkyo-ku, Tokyo 113, Japan
Telefax: +81-3-5684-3974

D.T.J. HURLE
H.H. Wills Phys. Lab., Univ. Bristol
Tyndall Avenue
Bristol BS8 1TL, UK

G.B. STRINGFELLOW
Dept. Mater. Sci., 304 EMRO, Univ. of Utah
Salt Lake City, UT 84112, USA
Telefax: +1-801-581 4816

ASSOCIATE EDITORS

A. BARONNET (*Industrial, Biological, Molecular Crystals*)
CRMC², CNRS, Campus Luminy, Case 913
F-13288 Marseille Cedex 9, France
Telefax: +33-91-4-418 916

K.W. BENZ (*Microgravity, Electronic Materials*)
Kristallographisches Inst., Universität
Hebelstr. 25, D-79104 Freiburg, Germany
Telefax: +49-761-203 4369

A.A. CHERNOV (*Kinetics of Crystallization, Protein Crystallization*)
Inst. Crystallography, Acad. of Sciences
Leninskii Prosp., Moscow 117333, Russian Fed.
Telefax: +7-095-135 011

A.Y. CHO (*Molecular Beam Epitaxy*)
Room IC-323, AT&T Bell Laboratories
Murray Hill, NJ 07974-2070, USA
Telefax: +1-908-582 2043

B. COCKAYNE (*IOCG News*)
School of Metallurgy and Mater.
Univ. Birmingham, P.O. Box 363,
Edgbaston, Birmingham, B15 2TT, UK
Telefax: +44-121-471 2207

S.R. CORIELL (*Theory*)
A153 Mater, Natl. Inst. of Standards & Technol.
Gaithersburgh, MD 20899-0001, USA
Telefax: +1-301-975-4553

J.J. DERBY (*Computational models*)
Dept. Chem. Eng. & Mater. Sci., Univ. Minnesota
151 Amundson Hall, 421 Washington Ave. S.E.
Minneapolis, MN 55455-0132, USA
Telefax: + 1-612-626 7246

M.E. GLICKSMAN (*Solidification*)
School of Eng., Mater. Eng. Dept.,
Rensselaer Polytechnic Inst.
Troy, NY 12180-3590, USA
Telefax: +1-518-276 8554

M.A.G. HALLIWELL (*X-ray Diffraction*)
Philips Analytical X-ray, Lelyweg 1
7602 EA Almelo, The Netherlands

T. HIBIYA (*Oxides, Melt Thermophysical Properties, Microgravity*)
Fundamental Res. Labs., NEC CORPORATION
34, Miyukigaoka, Tsukuba 305, Japan
Telefax: +81-298-566 136

H. KOMATSU (*Proteins Molecular Crystallization, Growth from Solutions*)
Inst. Mater. Res., Tohoku Univ.
Katahira 2-1-1, Sendai 980, Japan
Telefax: +81-22-215 2011

T.F. KUECH (*Thin Films and Electronic and Optical Devices*)
Dept. Chem. Eng., Univ. Wisconsin-Madison
Madison, WI 53706, USA
Telefax: +1-608-265 3782

A. McPHERSON (*Protein Growth*)
Dept. Biochemistry, Univ. of California
Riverside, CA 92521, USA
Telefax: +1-909-787 3790

P.A. MORRIS HOTSENPILLER (*Electrooptical Crystals, Book Reviews, Oxide Thin Films*)
E.I. du Pont de Nemours & Co., Exp. Station
Wilmington, DE 19888-0358, USA
Telefax: +1-302-695 1664

J.B. MULLIN (*Semiconductors*)
EMC, "The Hoo", Brockhill Road
West Malvem, Worcs., WR14 4DL, UK
Telefax: +44-1684-575 591

K. NAKAJIMA (*Liquid and Vapor Phase Epitaxy*)
Integrated Mater. Lab., Fujitsu Labs. Ltd.
Morinosato-Wakamiya 10-1, Atsugi 243-01, Japan
Telefax: +81-462-48 3473

H. OHNO (*Epitaxy*)
Research Inst. of Electrical Commun.
Tohoku Univ., Sendai 980 77, Japan
Telefax: +81-22-217 5553

K. PLOOG (*Molecular Beam Epitaxy*)
Paul-Drude-Inst. für Festkörperelektronik
Hausvogteiplatz 5–7, D-10117 Berlin, Germany
Telefax: +49-30-203 77201

R.W. ROUSSEAU (*Solution Growth, Industrial Crystallization*)
School of Chem. Eng., Georgia Inst. of Technol.
Atlanta, GA 30332-0100, USA
Telefax: +1-404-894 2866

K. SATO (*Biocrystallization and Organic Crystals*)
Fac. Appl. Biol. Sci., Hiroshima Univ.
Higashi-Hiroshima 724, Japan
Telefax: +81-824-227 062

L.F. SCHNEEMEYER (*Superconductivity, Oxides, Novel Materials*)
Room 1A-363, AT&T Bell Labs.
Murray Hill, NJ 07974-2070, USA
Telefax: +1-908-582 2521

D.W. SHAW (*Semiconductors, Epitaxy, Devices*)
Texas Instruments Inc., P.O. Box 655936, MS 147
Dallas, TX 75265, USA
Telefax: +1-214-995 7785

I. SUNAGAWA (*Minerals*)
3-54-2 Kashiwa-cho, Tachikawa-shi
Tokyo 190, Japan
Telefax: +81-425-35 3637

G. VAN TENDELOO (*Electron Microscopy, Fullerenes, Superconductivity*)
University of Antwerp, RUCA
Groenenborgerlaan 171, B-2020 Antwerp-Belgium
Telefax: +32-3-2180 217

A.F. WITT (*Semiconductor Crystals*)
Dept. of Metall. & Mater. Sci., Massachusetts
Inst. of Technol., Cambridge, MA 02139, USA
Telefax: +1-617-253 5827

A. ZANGWILL (*Theory (Epitaxy)*)
School of Physics, Georgia Inst. of Technol.
Atlanta, GA 30332, USA
Telefax: +1-404-894 9958

Scope of the Journal
Experimental and theoretical contributions are invited in the following fields: Theory of nucleation and growth, molecular kinetics and transport phenomena, crystallization in viscous media such as polymers and glasses. Crystal growth of metals, minerals, semiconductors, magnetics, inorganic, organic and biological substances in bulk or as thin films. Apparatus instrumentation and techniques for crystal growth, and purification methods. Characterization of single crystals by physical and chemical methods.

Abstracted/Indexed in:
Aluminium Industry Abstracts; Chemical Abstracts; Current Contents; Physical, Chemical and Earth Sciences; EI Compendex Plus; Engineered Materials Abstracts; Engineering Index; INSPEC; Metals Abstracts.

Subscription Information 1997
Volumes 170–181 of Journal of Crystal Growth (ISSN 0022-0248) are scheduled for publication. (Frequency: semimonthly.) Prices are available from the publishers upon request. Subscriptions are accepted on a prepaid basis only. Issues are sent by SAL (Surface Air Lifted) mail wherever this service is available. Airmail rates are available upon request. Please address all enquiries regarding orders and subscriptions to:

Elsevier Science, B.V., Order Fulfilment Department
P.O. Box 211, 1000 AE Amsterdam, The Netherlands
Tel: +31 20 485 3642; Fax: +31 20 485 3598

Claims for issues not received should be made within six months of our publication (mailing) date.

US mailing notice–*Journal of Crystal Growth* (ISSN 0022-0248) is published semimonthly by Elsevier Science B.V., Molenwerf 1, P.O. Box 211, 1000 AE Amsterdam, The Netherlands. Annual subscription price in the USA is US $7081 (valid in North, Central and South America only), including air speed delivery. Periodicals postage paid at Jamaica NY 11431.
US postmasters: Send address changes to Journal of Crystal Growth, Publications Expediting, Inc., 200 Meacham Avenue, Elmont NY 11003. Airfreight and mailing in the USA by Publications Expediting.

The paper used in this publication meets the requirements of ANSI/NISO Z39.48-1992 (Permanence of Paper)

PRINTED IN THE NETHERLANDS

North-Holland, an imprint of Elsevier Science

JOURNAL OF CRYSTAL GROWTH

EDITORIAL BOARD

M. SCHIEBER (Principal Editor)
The Fredy and Nadine Herrmann
Graduate School of Appl. Sci.
Hebrew University, Jerusalem 91904, Israel
Telefax: +972-2-566 3878

R. KERN
CRMC², CNRS, Campus Luminy, Case 913
F-13288 Marseille Cedex 9, France
Telefax: +33-91-4-418 916

R.S. FEIGELSON
Ctr. Materials Res., 105 McCullough Bldg.
Stanford Univ., Stanford, CA 94305-4045, USA
Telefax: +1-415-723 3044

T. NISHINAGA
Dept. Electron. Eng., Univ. of Tokyo
7-3-1, Hongo, Bunkyo-ku, Tokyo 113, Japan
Telefax: +81-3-5684-3974

D.T.J. HURLE
H.H. Wills Phys. Lab., Univ. Bristol
Tyndall Avenue
Bristol BS8 1TL, UK

G.B. STRINGFELLOW
Dept. Mater. Sci., 304 EMRO, Univ. of Utah
Salt Lake City, UT 84112, USA
Telefax: +1-801-581 4816

ASSOCIATE EDITORS

A. BARONNET (*Industrial, Biological, Molecular Crystals*)
CRMC², CNRS, Campus Luminy, Case 913
F-13288 Marseille Cedex 9, France
Telefax: +33-91-4-418 916

K.W. BENZ (*Microgravity, Electronic Materials*)
Kristallographisches Inst., Universität
Hebelstr. 25, D-79104 Freiburg, Germany
Telefax: +49-761-203 4369

A.A. CHERNOV (*Kinetics of Crystallization, Protein Crystallization*)
Inst. Crystallography, Acad. of Sciences
Leninskii Prosp., Moscow 117333, Russian Fed.
Telefax: +7-095-135 011

A.Y. CHO (*Molecular Beam Epitaxy*)
Room IC-323, AT&T Bell Laboratories
Murray Hill, NJ 07974-2070, USA
Telefax: +1-908-582 2043

B. COCKAYNE (*IOCG News*)
School of Metallurgy and Mater.
Univ. Birmingham, P.O. Box 363,
Edgbaston, Birmingham, B15 2TT, UK
Telefax: +44-121-471 2207

S.R. CORIELL (*Theory*)
A153 Mater, Natl. Inst. of Standards & Technol.
Gaithersburgh, MD 20899-0001, USA
Telefax: +1-301-975-4553

J.J. DERBY (*Computational models*)
Dept. Chem. Eng. & Mater. Sci., Univ. Minnesota
151 Amundson Hall, 421 Washington Ave. S.E.
Minneapolis, MN 55455-0132, USA
Telefax: +1-612-626 7246

M.E. GLICKSMAN (*Solidification*)
School of Eng., Mater. Eng. Dept.,
Rensselaer Polytechnic Inst.
Troy, NY 12180-3590, USA
Telefax: +1-518-276 8554

M.A.G. HALLIWELL (*X-ray Diffraction*)
Philips Analytical X-ray, Lelyweg 1
7602 EA Almelo, The Netherlands

T. HIBIYA (*Oxides, Melt Thermophysical Properties, Microgravity*)
Fundamental Res. Labs., NEC CORPORATION
34, Miyukigaoka, Tsukuba 305, Japan
Telefax: +81-298-566 136

H. KOMATSU (*Proteins Molecular Crystallization, Growth from Solutions*)
Inst. Mater. Res., Tohoku Univ.
Katahira 2-1-1, Sendai 980, Japan
Telefax: +81-22-215 2011

T.F. KUECH (*Thin Films and Electronic and Optical Devices*)
Dept. Chem. Eng., Univ. Wisconsin-Madison
Madison, WI 53706, USA
Telefax: +1-608-265 3782

A. McPHERSON (*Protein Growth*)
Dept. Biochemistry, Univ. of California
Riverside, CA 92521, USA
Telefax: +1-909-787 3790

P.A. MORRIS HOTSENPILLER (*Electrooptical Crystals, Book Reviews, Oxide Thin Films*)
E.I. du Pont de Nemours & Co., Exp. Station
Wilmington, DE 19888-0358, USA
Telefax: +1-302-695 1664

J.B. MULLIN (*Semiconductors*)
EMC, "The Hoo", Brockhill Road
West Malvem, Worcs., WR14 4DL, UK
Telefax: +44-1684-575 591

K. NAKAJIMA (*Liquid and Vapor Phase Epitaxy*)
Integrated Mater. Lab., Fujitsu Labs. Ltd.
Morinosato-Wakamiya 10-1, Atsugi 243-01, Japan
Telefax: +81-462-48 3473

H. OHNO (*Epitaxy*)
Research Inst. of Electrical Commun.
Tohoku Univ., Sendai 980 77, Japan
Telefax: +81-22-217 5553

K. PLOOG (*Molecular Beam Epitaxy*)
Paul-Drude-Inst. für Festkörperelektronik
Hausvogteiplatz 5–7, D-10117 Berlin, Germany
Telefax: +49-30-203 77201

R.W. ROUSSEAU (*Solution Growth, Industrial Crystallization*)
School of Chem. Eng., Georgia Inst. of Technol.
Atlanta, GA 30332-0100, USA
Telefax: +1-404-894 2866

K. SATO (*Biocrystallization and Organic Crystals*)
Fac. Appl. Biol. Sci., Hiroshima Univ.
Higashi-Hiroshima 724, Japan
Telefax: +81-824-227 062

L.F. SCHNEEMEYER (*Superconductivity, Oxides, Novel Materials*)
Room 1A-363, AT&T Bell Labs.
Murray Hill, NJ 07974-2070, USA
Telefax: +1-908-582 2521

D.W. SHAW (*Semiconductors, Epitaxy, Devices*)
Texas Instruments Inc., P.O. Box 655936, MS 147
Dallas, TX 75265, USA
Telefax: +1-214-995 7785

I. SUNAGAWA (*Minerals*)
3-54-2 Kashiwa-cho, Tachikawa-shi
Tokyo 190, Japan
Telefax: +81-425-35 3637

G. VAN TENDELOO (*Electron Microscopy, Fullerenes, Superconductivity*)
University of Antwerp, RUCA
Groenenborgerlaan 171, B-2020 Antwerp-Belgium
Telefax: +32-3-2180 217

A.F. WITT (*Semiconductor Crystals*)
Dept. of Metall. & Mater. Sci., Massachusetts
Inst. of Technol., Cambridge, MA 02139, USA
Telefax: +1-617-253 5827

A. ZANGWILL (*Theory (Epitaxy)*)
School of Physics, Georgia Inst. of Technol.
Atlanta, GA 30332, USA
Telefax: +1-404-894 9958

JOURNAL OF

CRYSTAL GROWTH

EDITORS

M. SCHIEBER
Principal Editor

R.S. FEIGELSON

D.T.J. HURLE

R. KERN

T. NISHINAGA

G.B. STRINGFELLOW

VOLUME 181 (1997)

ELSEVIER

Amsterdam – Lausanne – New York – Oxford – Shannon – Tokyo

Copyright © 1997 Elsevier Science B.V. All rights reserved

This journal and the individual contributions contained in it are protected by the copyright of Elsevier Science B.V., and the following terms and conditions apply to their use:
Photocopying
Single photocopies of single articles may be made for personal use as allowed by national copyright laws. Permission of the Publisher and payment of a fee is required for all other photocopying, including multiple or systematic copying, copying for advertising or promotional purposes, resale, and all forms of document delivery. Special rates are available for educational institutions that wish to make photocopies for non-profit educational classroom use.
In the USA, users may clear permissions and make payment through the Copyright Clearance Center Inc., 222 Rosewood Drive, Danvers, MA 01923, USA. In the UK, users may clear permissions and make payment through the Copyright Licensing Agency Rapid Clearance Service (CLARCS), 90 Tottenham Court Road, London W1P 0LP, UK. In other countries where a local copyright clearance centre exists, please contact it for information on required permissions and payments.
Derivative works
Subscribers may reproduce tables of contents or prepare lists of articles including abstracts for internal circulation within their institutions.
Permission of the Publisher is required for resale or distribution outside the institution.
Permission of the Publisher is required for all other derivative works, including compilations and translations.
Electronic storage
Permission of the Publisher is required to store electronically any material contained in this journal, including any article or part of an article.
Contact the Publisher at the address indicated.
Except as outlined above, no part of this publication may be reproduced, stored in a retrieval system or transmitted in any form or by any means, electronic, mechanical, photocopying, recording or otherwise, without prior written permission of the Publisher.

No responsibility is assumed by the Publisher for any injury and/or damage to persons or property as a matter of products liability, negligence or otherwise, or from any use or operation of any methods, products, instructions or ideas contained in the material herein. Although all advertising material is expected to conform to ethical (medical) standards, inclusion in this publication does not constitute a guarantee or endorsement of the quality or value of such product or of the claims made of it by its manufacturer.

♾ The paper used in this publication meets the requirements of ANSI/NISO Z39.48-1992 (Permanence of Paper)

PRINTED IN THE NETHERLANDS

ELSEVIER

Journal of Crystal Growth 181 (1997) 1–8

JOURNAL OF CRYSTAL GROWTH

Influence of substrate misorientation on quality of active region and performance of GaAs/AlGaAs triple-quantum-well lasers grown by molecular beam epitaxy

D.H. Zhang[a,*], C.Y. Li[b], S.F. Yoon[a]

[a] *School of Electrical and Electronic Engineering, Block S2, Nanyang Technological University, Singapore 639798, Singapore*
[b] *Chartered Semiconductor Manufacturing Ltd., 60 Woodlands Industrial Park D, Street 2, Singapore 738406, Singapore*

Received 5 March 1996; accepted 10 April 1997

Abstract

The influence of substrate misorientation on the quality of the active region with low AlAs portion barrier layers and the performance of the GaAs/AlGaAs grade index separate-confinement triple-quantum-well lasers grown under at a higher CO pressure are investigated. It is found that the threshold current could be reduced from 32.5 to 15.7 mA by tilting the substrate 6° and the high-quality lasers show a characteristic temperature as high as 260°C, indicating a high output stability. The luminescence results reveal that carbon impurity, like oxygen, could also be incorporated and trapped at and near AlGaAs/GaAs interfaces during growth and cause roughness, resulting in excessive scattering and loss and thus a high threshold current. Substrate misorientation for 6° toward ⟨1 1 1⟩A could reduce the incorporation of carbon impurity to an unobservable level.

PACS: 42.55.Px; 78.55.Cr; 71.55.Eq

Keywords: Quantum well laser; Photoluminescence; Molecular beam epitaxy

1. Introduction

Since the effects of substrate misorientation on the properties of AlGaAs grown by molecular beam epitaxy (MBE) were first reported by Tsui et al. in 1985 [1], a considerable effort has been made in investigating the influence of the misorientation on GaAs/AlGaAs heterostructures [2, 3] and quantum wells (QW) [4, 5] as they play an important role in single- and multiple-QW laser devices. Recently, the direct correlation between the misoriented substrate and the performance of the QW lasers of several material systems, including GaAs/AlGaAs [6–8], InGaAs/GaAs [9, 10], InGaAs/InGaAsP/InGaP [11], and GaInP/AlInP [12], have been studied extensively. It is reported that the InGaAs-strained QWs grown on GaAs (1 1 1)B by MBE have high quality at misorientation

* Corresponding author. Fax: + 65 7920415; e-mail: edhzhang@ntuvax.ntu.ac.sg.

0022-0248/97/$17.00 © 1997 Elsevier Science B.V. All rights reserved
PII S0022-0248(97)00248-0

angles between 1 and 1.5°, and the strained-QW lasers have a threshold current density of as low as 250 A/cm^2 [9]. The lasing performance of the GaInP/AlInP lasers grown on the misoriented substrate by gas source MBE is found strongly dependent on misorientation angle [12] and such QWs with high quality are usually grown on highly misoriented substrate [13, 14]. The InGaAs/InGaAsP/InGaP aluminum free, strained-layer double quantum well (DQW) lasers with continuous wave output power of 3 W, grown on exact (1 0 0)GaAs substrate, have been successfully fabricated recently. These devices are reported to show a week temperature dependence for both the threshold current and the external differential quantum efficiency which become worse when grown on misoriented substrate [11].

For the GaAs/AlGaAs grade index confinement (GRINSC) QW lasers, the threshold current could be significantly reduced by tilting the GaAs substrate several degrees off (1 0 0) toward ⟨1 1 1⟩A [6, 7], in good agreement with the theory which ascribes the reduction in the threshold current to the enhanced light-hole behavior. It is reported that by misorienting the substrate several degree off (1 0 0) toward ⟨1 1 1⟩A, the structural, electrical and optical properties of the AlGaAs layers and the GaAs/AlGaAs interface smoothness could be substantially improved due to the decrease of the accumulated impurities, especially oxygen which functions as nonradiative center and degrades the laser performance. Mihashi et al. [15] quantitatively studied the effect of oxygen incorporation into the epitaxial layers on the threshold current density of the AlGaAs multiple QW lasers grown by metal organic chemical vapor deposition (MOCVD) and reported that an oxygen less than 10^{17} cm^{-3} in the cladding layer is necessary to obtain low-threshold current lasers. More recently, the DQW GaAs/AlGaAs ridge-waveguide lasers with integrated passive sections, showing a threshold current as low as 18 mA from a 2×460 μm active section, is reported.

In this paper we present the direct correlation between substrate misorientation, threshold current of the GRINSC triple-QW lasers grown at a slightly high CO background and the photoluminescence of their corresponding active region with $Al_{0.2}Ga_{0.8}As$ barriers. It is found that by misorienting GaAs substrate 6° off (1 0 0) toward ⟨1 1 1⟩A, the threshold current of the lasers with a cavity of 300 μm could be reduced from 32.5 to 15.7 mA with a characteristic temperature T_0 as high as 260°C. Photoluminescence (PL) results suggest that like oxygen, carbon impurity could also be incorporated and trapped at and near the AlGaAs/GaAs interfaces of the active region and causes roughness and degradation in the laser performance.

2. Experimental procedure

The GaAs/AlGaAs GRINSC triple-QW laser structures studied were grown in a VG Semicon V80 MBE system on n-type GaAs substrates being tilted 0 and 6° off (1 0 0) towards ⟨1 1 1⟩A, respectively. The residual background impurities are monitored by a mass spectrometer during growth and show a CO intensity of 6.0×10^{-9}. The schematic drawing of the epitaxial structure is shown in Fig. 1. As shown in this figure, the structure consists of a 1 μm thick Si-doped GaAs buffer layer, a n-type $Al_{0.48}Ga_{0.52}As$ cladding layer, an active region sandwiched by two undoped GRINs, a p-type $Al_{0.48}Ga_{0.52}As$ cladding layer and a p^+ GaAs contact layer. The n- and p-type cladding layers are 1.5 μm thick and doped with Si of 2×10^{18} cm^{-3} and Be of 7×10^{18} cm^{-3}, respectively. The active regions contain three undoped GaAs wells with a nominal thickness of 80 Å each, separated by two undoped 200 Å thick $Al_{0.2}Ga_{0.8}As$ barriers, while the GRIN layers vary Al content from 0.2 to 0.48. The employment of low Al content in the barriers and GRINSC layers aims to reduce the incorporation of the oxygen-related impurities which, functioning as nonradiative centers, have been reported to degrade the performance of laser devices. The growth temperature is 590°C for the Si-doped buffer and p^+ contact layers, 620°C for the n- and p-type cladding layers and varies between 590 and 620°C for the GRIN layers. The growth rate is 0.68 μm/h for GaAs and 0.43 μm/for AlGaAs, respectively. The substrate was rotated at 20 rpm during growth to assure the uniformity of the grown layers.

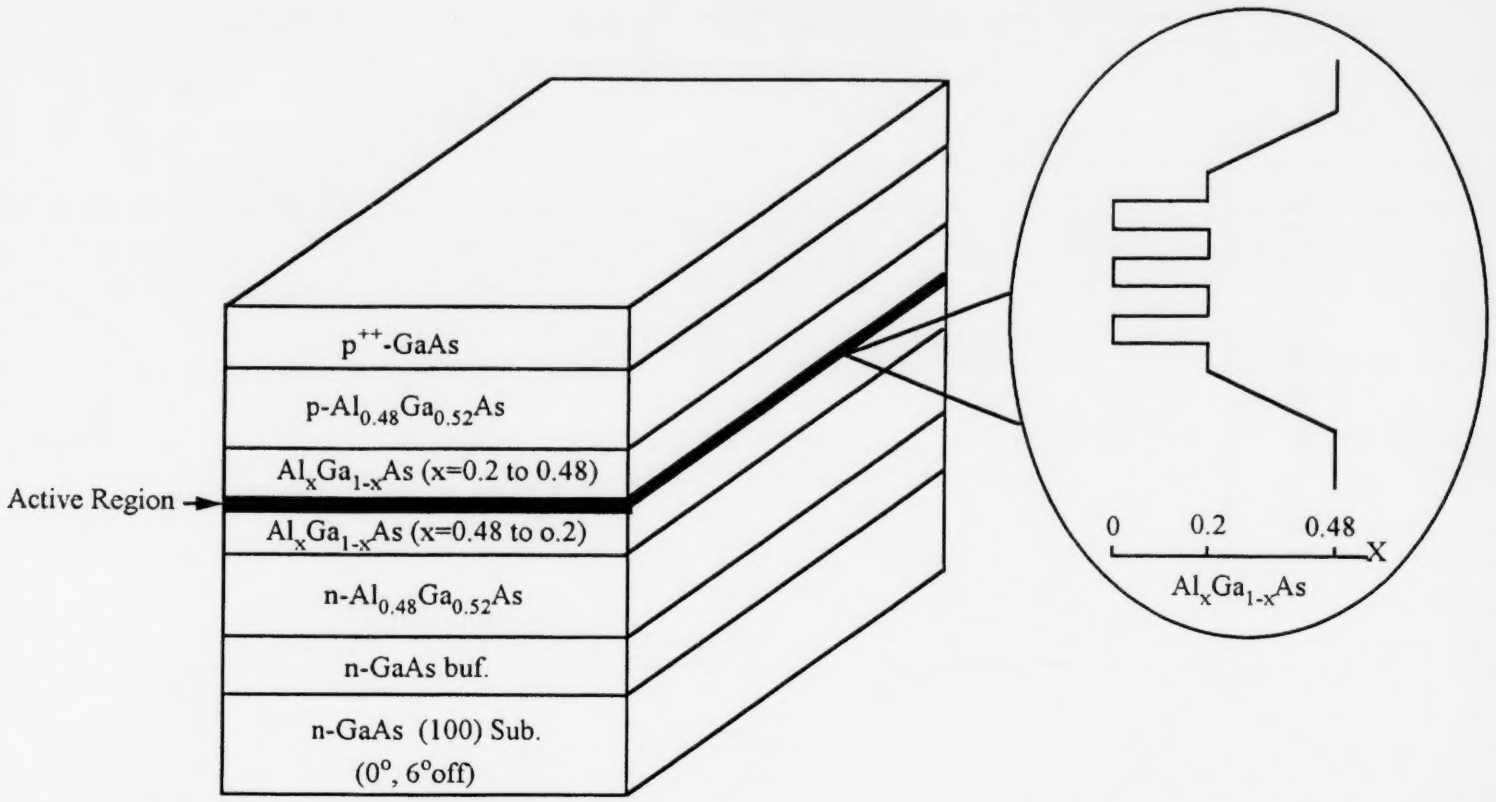

Fig. 1. Schematic diagram of the epitaxial structure of the GaAs/AlGaAs grade-index separate-confinement (GRINSC) triple-quantum-well (TQW) lasers grown by MBE.

The optical output power versus injection current of our GRINSC triple-QW lasers studied was measured at a temperature range of 5–70°C on 18×300 μm strips using an Advantest lasertest system. In order to investigate the correlation of laser performance and the quality of the active regions of the laser structures, low-temperature photoluminescence measurements were carried out from the samples, cut from the same wafer as the laser devices with the top p^+ GaAs and the upper part of the p-type cladding layer being etched off, in a system consisting of a 514.5 nm laser excitation, a conventional 0.75 m grating spectrometer and a Peltier-effect-cooled GaAs photomultiplier detector.

3. Laser performance

Fig. 2 shows the optical output power of GRINSC triple-QW lasers versus injection current (P–I) as a function of substrate misorientation angle. As shown in this figure, the threshold current I_{th} is 32.5 A for the laser deposited on an exact (1 0 0) substrate and 15.7 A for the laser deposited on the substrate 6° off (1 0 0) toward ⟨1 1 1⟩A. In addition, the slope of the linear part which is proportional to the differential quantum efficiency, becomes obviously greater as the substrate is tilted.

The temperature dependence of the P–I curve of the lasers grown on a 6°-tilted substrate in a range of 8–70°C is illustrated in Fig. 3a. It is clearly shown that the threshold current increases monotonically with the environment temperature while the slope of the linear region or differential quantum efficiency decreases as the temperature is increased. By plotting logarithm of the threshold current versus measurement temperature, (Fig. 3b), an exponential relationship, as reported by Tsang et al. who have done pioneering work for double-heterostructure (DH) lasers [8], could be extracted.

$$I_{th} \sim \exp[T/T_0], \tag{1}$$

where T is temperature in °C and T_0 is a characteristic temperature with a value of 260°C, much greater than that reported for DH lasers. The high

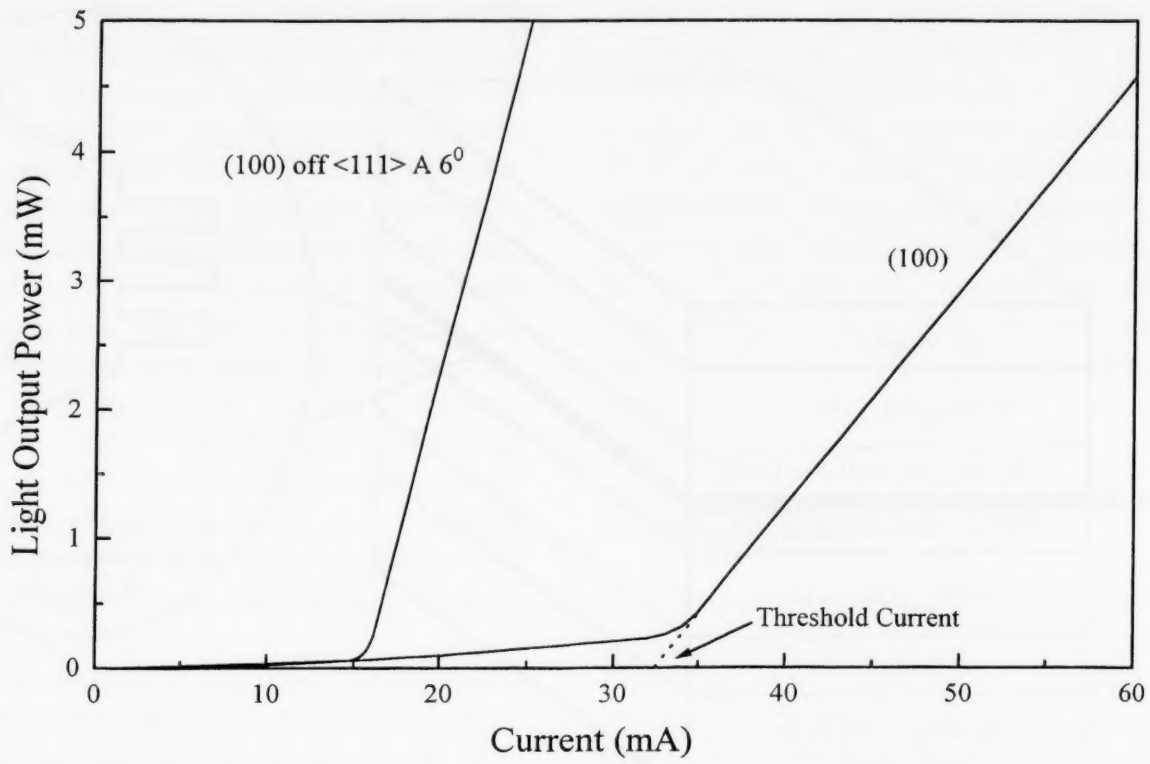

Fig. 2. Light output power of the GRINSC TQW lasers grown on substrate misoriented 0 and 6° off (1 0 0) toward ⟨1 1 1⟩A as a function of injection current. The devices tested are stripes with a width of 18 μm and a cavity of 300 μm.

T_0, indicating a much less sensitivity to temperature, may enhance the output stability of the lasers.

4. Photoluminescence results

After etching off the top p^+-GaAs and the upper part of the p-type cladding layer, the PL spectra of the active region of the lasers were measured at 10 K, and the results are shown in Fig. 4. Following features could be observed: Firstly, the spectrum of 0° tilted samples shows two emission peaks, labeled 1.558 and 1.548 eV in Fig. 4a, while that of 6° tilted samples shows only a high-energy peak at about 1.560 eV. Secondly, the full-width at half-maximum (FWHM) of the spectrum is as wide as 26 meV for the untilted samples and is as narrow as 6.4 meV for the tilted ones. The high-energy peak appeared at the spectra of the two type of samples may be ascribed to the radiative recombination of the $n = 1$ confined electrons with heavy holes (e–hh), while the low-energy peak at 1.547 eV appeared only in the untilted samples is probably corresponding to the carbon acceptor related transition. The details will be discussed later.

5. Discussion

By comparing the threshold current of our lasers (grown at a CO intensity of 6×10^{-9}) shown in Fig. 2 and the PL spectra of their active regions in Fig. 4, it is seen that the high threshold current and low differential quantum efficiency lasers grown on (1 0 0) substrate correspond to a wide PL spectrum with two peaks, while the low threshold current and high differential quantum efficiency lasers grown on a 6°-tilted substrate toward ⟨1 1 1⟩A correspond to a narrow and sharp PL spectrum. It is obvious that performance of the lasers is at least at some extent related to the quality of their active region consisting of 3QWs.

It is well known that oxygen, as a common containment, forms nonradiative centers in GaAs, AlGaAs and GaAs/AlGaAs heterostructures and the level is typically below the detecting limit of the secondary ion mass spectrometry (SIMS) in GaAs.

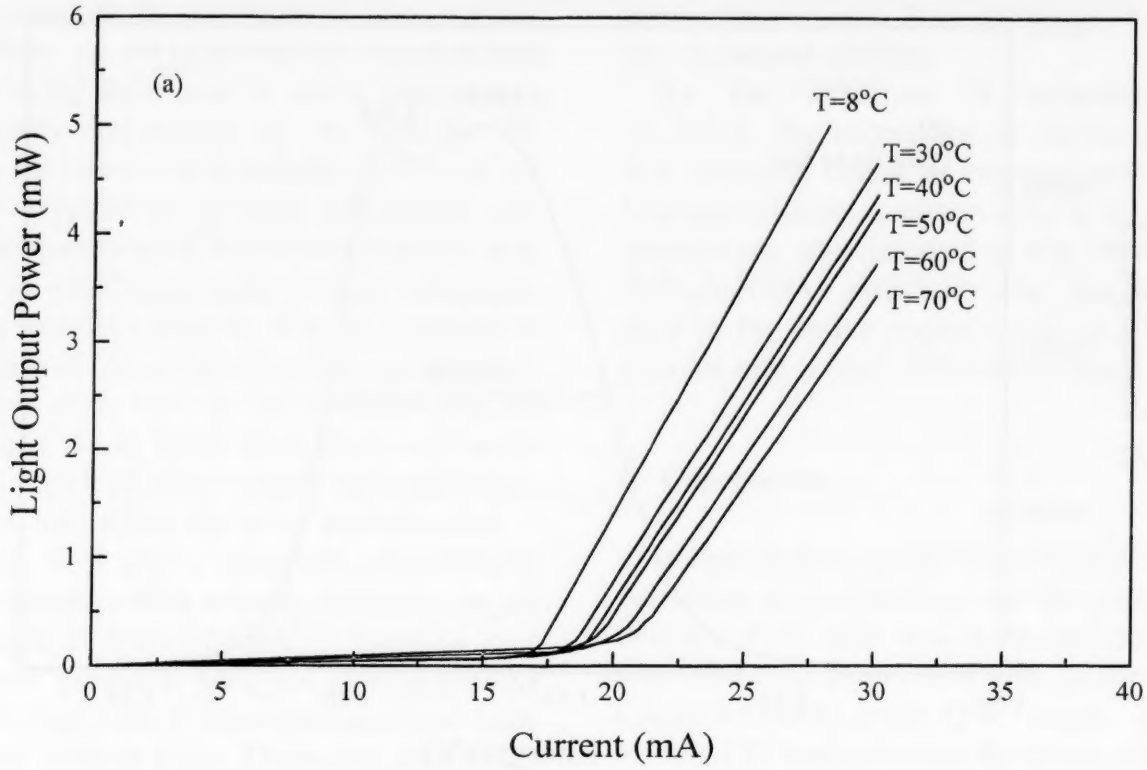

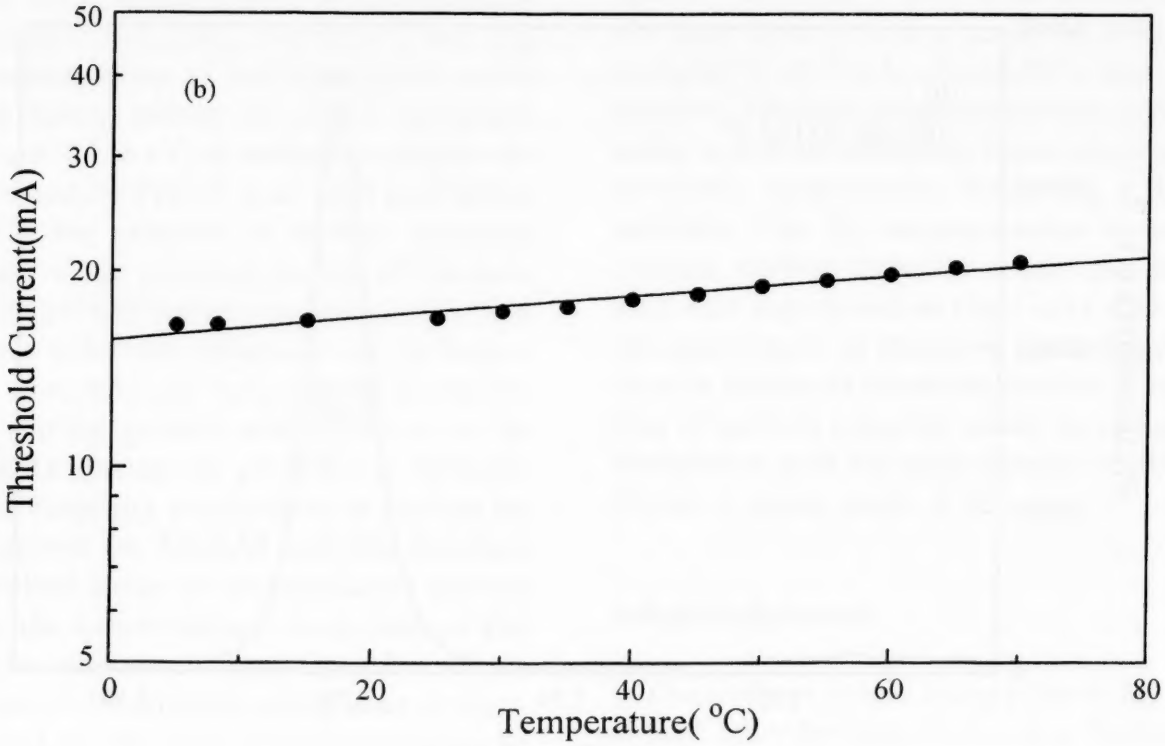

Fig. 3. (a) Light output power of the 6°-tilted GRINSC TQW laser versus injection current measured at different temperatures. (b) Plot of threshold current of the 6° tilted GRINSC TQW laser as a function of temperature at which the laser device was measured.

Due to the high reactivity of Al (with oxygen), oxygen can be easily incorporated in AlGaAs with a typical density of $\geqslant 10^{17}\,\mathrm{cm}^{-3}$ at a AlAs composition of 30% and increases with increasing composition of AlAs [4, 5, 17]. Oxygen atoms are found mobile enough during growth to segregate on the surface and remain trapped at GaAs/AlGaAs inverted interfaces [5, 17, 18], resulting in roughness

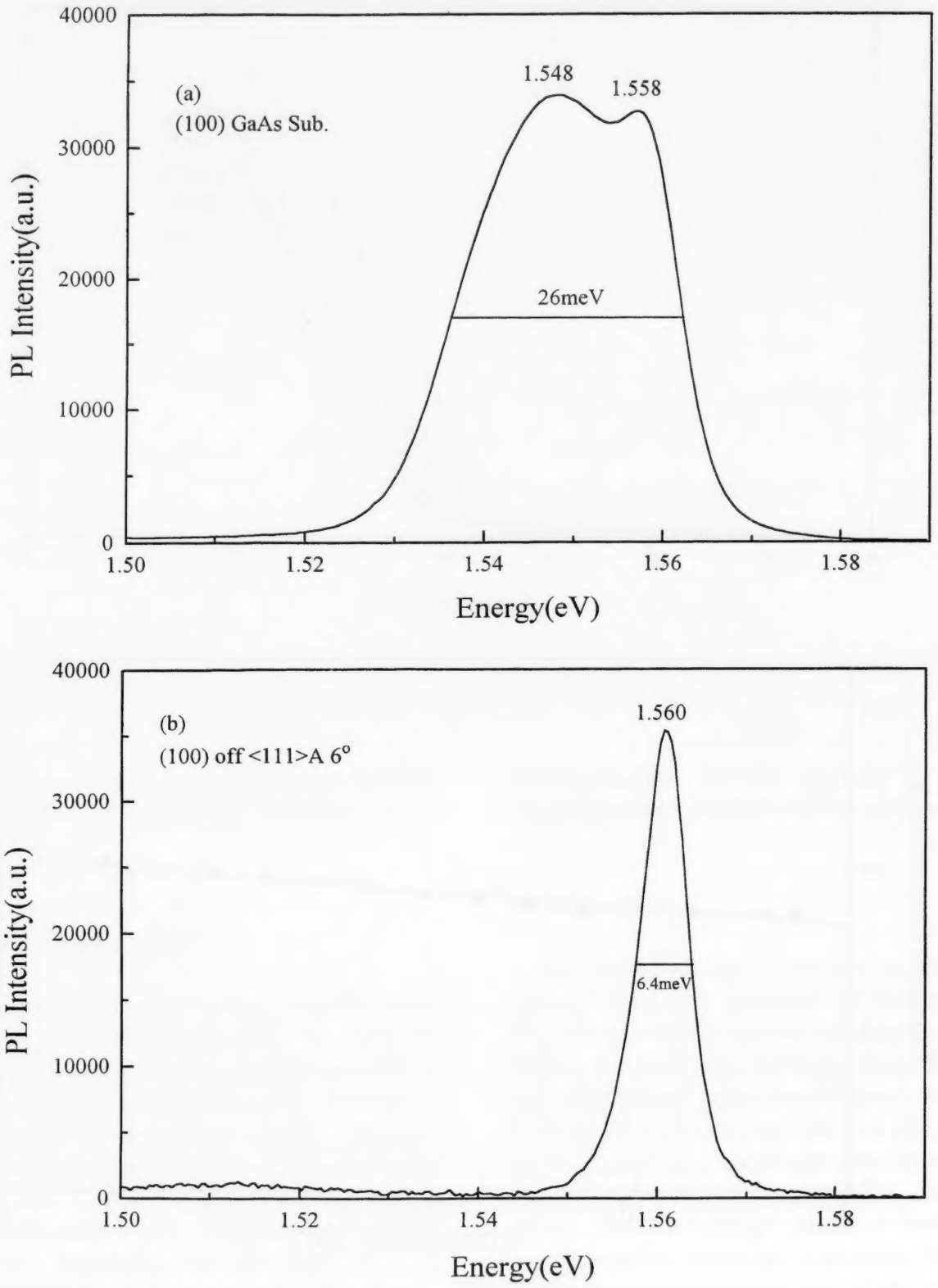

Fig. 4. (a) PL spectrum (measured at 10 K) of the GRINSC TQW lasers grown on exact (1 0 0) GaAs substrates. The high-energy peak at about 1.558 eV may be ascribed to the recombination of $n = 1$ electron to heavy hole (e–hh) while the low-energy peak at about 1.548 eV is probably C related. (b) 10 K PL of the lasers grown on substrates misoriented 6° off (1 0 0) toward ⟨1 1 1⟩A. Only the high-energy peak at about 1.560 eV is observed.

and a reduction in radiative efficiency [18–20]. Tsang et al. [16] previously reported that the non-radiative centers in the AlGaAs cladding layer could increase the threshold current in the GaAs/AlGaAs DH lasers due to tunneling of the confined carriers in the active region to the

nonradiative centers. In our laser devices studied, the segregation of oxygen-related nonradiative centers at inverted interfaces of active region may be only partially responsible for the broader PL FWHM and the increased threshold current of the untilted laser structure as we have deliberately employed low composition of AlAs in the barrier and cladding layers, which may reduce oxygen incorporation during structure growth. The PL intensity of the active region of the untilted laser is, indeed, only slightly weaker than that of the 6°-tilted one, as shown in Fig. 4. It is likely that there are some other sources which at some extent have contribution to the PL and affect the laser performance.

Like oxygen, C is also a common contaminant for MBE materials, which usually functions as an acceptor dopant. It is worthwhile to mention that the GaAs layers grown at such a CO background indeed show a high rate C incorporation and high density of oval defects [21]. There are also evidences showing incorporation of C in AlGaAs materials, for example Ref. [18]. We believe that the low-energy luminescence of the triple-QW active region of the lasers grown on (1 0 0) substrate, peaked at about 1.548 eV, is probably carbon related. It is reported by Petroff et al. [18] and Miller et al. [22] that the presence of carbon degrades the smoothness of the growing surface of AlGaAs layers due to its growth inhibiting nature. It is then suggested that a solubility difference for the impurity in GaAs and AlGaAs makes it float on the AlGaAs film during growth and causes it to be trapped at GaAs during its growth on AlGaAs. This presumed trapping mechanism of carbon by a GaAs-well grown on AlGaAs and the interface roughness resulted from the accumulated carbon could explain the luminescence properties of the triple-QW active region and thus the influence on the performance of the corresponding laser devices. On the one hand, as the total concentration of the carbon impurity in the GaAs wells, which may exist as a point defect or combined with others to form a complex, is increased by normal incorporation and trapping, the carbon impurity-related luminescence is greatly enhanced. On the other hand, the roughness resulted from the accumulation of carbon-related defects at the AlGaAs/GaAs interfaces in the active region of the lasers could cause excessive scattering and loss, resulting in an increase in the threshold current.

As the substrate is misoriented towards ⟨1 1 1⟩A, the incorporated concentration of carbon impurity could be tremendously reduced and becomes almost unobservable by PL for a 6° misorientation, as evidenced in Fig. 4b. The smoother AlGaAs/GaAs interfaces and less impurity trapping in the active region result in a low threshold current and a high differential quantum efficiency.

6. Conclusions

In conclusion, we have investigated the effects of substrate misorientation on the properties of the active region with low AlAs composition barrier and cladding layers and the performance of the GaAs/AlGaAS triple-QW lasers grown under a high CO background. By tilting the (1 0 0) substrate 6° towards ⟨1 1 1⟩A, the threshold current of the laser devices with a cavity of 300 μm could be reduced to 15.7 mA, about 50% less than that of untilted. The low threshold current and high differential quantum efficiency lasers show a high characteristic temperature, indicating a high output stability. The PL measurements reveal that, like oxygen, carbon impurity could also be incorporated and segregated at the GaAs/AlGaAs interfaces, resulting in an excessive scattering and loss and thus an increased threshold current. The incorporation of carbon impurity could be reduced by misorientation and becomes almost unobservable by PL for a tilting angle of 6°.

Acknowledgements

The authors would like to thank Mr. A. Raman at the Center for Optoelectronics, National University of Singapore for growing isolating films, Ms. D.X. Qi and Mr. C.P. Luo for their assistance in PL measurements.

References

[1] R.K. Tsui, J.A. Curless, G.D. Kramer, M.S. Peffley, D.L. Rode, J. Appl. Phys. 58 (1985) 2570.

[2] D.C. Radulescu, G.W. Wicks, W.J. Schaff, A.R. Calawa, L.F. Eastman, J. Appl. Phys. 63 (1988) 5115.
[3] N. Chand, A.S. Jordan, S.N.G. Chu, Appl. Phys. Lett. 59 (1991) 2874.
[4] N. Chand, A.S. Jordan, S.N.G. Chu, M. Geva, Appl. Phys. Lett. 59 (1991) 3270.
[5] T. Achtnich, G. Burri, M.A. Py, M. Ilegems, Appl. Phys. Lett. 50 (1987) 1730.
[6] H.Z. Chen, A. Ghaffari, H. Morkoc, A. Yariv, Appl. Phys. Lett. 51 (1987) 2094.
[7] A. Ghiti, W. Batty, E.P. O'Reily, Superlattices and Microstructures 7 (1990) 353.
[8] H.H. Yee, S. Ayling, R.M. De La Rue, B. Vogele, Y.P. Song, IEE Proc. Optoelectron. 143 (1996) 94.
[9] T. Takeuchi, K. Muraki, Y. Hanamaki, S. Fukatsu, N. Yamada, N. Ogasawara, N. Mikoshiba, Y. Shiraki, J. Crystal Growth 150 (1995) 1338.
[10] Hayakawa Toshiro, Nagal Masaharu, Horie Hideyoshi, Niwata Yoshihisa, J. Crystal Growth 127 (1993) 532.
[11] L.J. Mawst, A. Bhattacharya, M. Nesnidal, J. Lopez, D. Botez, J.A. Morris, P. Zory, Appl. Phys. Lett. 67 (1995) 2901.
[12] K. Akihiko, K. Katsumi, J. Crystal Growth 127 (1993) 9.
[13] D. Bour, R.S. Geels, D.W. Treat, T.L. Paoli, F. ponce, R.L. Thornton, B.S. Krusor, R.D. Bringans, D.F. Welch, IEEE J. Quantum Electron. QE-30 (1994) 133.
[14] M. Jou, J. Lin, C. Chang, C. Lin, M. Wu, B. Lee, Jpn. J. Appl. Phys. 32 (1993) 4460.
[15] Y. Mihashi, M. Miyashita, N. Kaneno, M. Tsugami, N. Fujii, S. Takamiya, S. Mitsui, J. Crystal Growth 141 (1994) 22.
[16] W.T. Tsang, R.A. Logan, J.P. Van der Ziel, Appl. Phys. Lett. 34 (1979) 644.
[17] M.T. Asom, S.N.G. Chu, M. Geva, R.E. Leibenguth, Appl. Phys. Lett. 59 (1991) 976.
[18] P.M. Petroff, R.C. Miller, A.C. Gossard, W. Wiegmann, Appl. Phys. Lett. 44 (1984) 217.
[19] K. Akimoto, M. Kamada, K. Taira, M. Arai, N. Watanabe, J. Appl. Phys. 59 (1986) 2833.
[20] C.T. Foxon, J.B. Clegg, K. Woodbridge, D. Hilton, P. Dawson, P. Blood, J. Vac. Sci. Technol. B 3 (1985) 703.
[21] C.Y. Li, D.H. Zhang, J. Crystal Growth 165 (1996) 15.
[22] R.C. Miller, W.T. Tsang, O. Munteanu, Appl. Phys. Lett. 41 (1982) 376.

ELSEVIER

Journal of Crystal Growth 181 (1997) 9–16

JOURNAL OF CRYSTAL GROWTH

Study of Zn diffusion into GaSb from the vapour and liquid phase

A.W. Bett, S. Keser, O.V. Sulima*

Fraunhofer-Institut für Solare Energiesysteme (ISE), Oltmannsstraße 5, D-79100 Freiburg, Germany

Received 24 January 1997; accepted 24 February 1997

Abstract

In order to develop a simple and reproducible method to fabricate p–n structures on GaSb for optoelectronic devices, the Zn-diffusion into n-doped GaSb substrates was studied. Two methods of Zn-diffusion were experimentally investigated: (a) diffusion from the vapour phase in a pseudo-closed box system and (b) diffusion from the liquid phase from a Ga–Sb–Zn melt. The process parameters, which provide good control over Zn surface concentration and p–n junction depth, were determined.

PACS: 66.30. – h; 61.72.Vv; 84.60.Jt

Keywords: Diffusion; GaSb; Zn; Photovoltaic cells

1. Introduction

GaSb and related compounds are of large interest for many optoelectronic devices, e.g.

(i) bottom (infrared) cells in high-efficiency mechanically stacked tandem solar cells with AlGaAs/GaAs top cells [1, 2]

(ii) photovoltaic (PV) cells in radioisotope thermovoltaic generators at relatively low temperatures (e.g. $< 1250°C$) [3] or in the newly developed thermophotovoltaic electric generators with a hydrocarbon burner [4]

(iii) lasers, LEDs and photodiodes [5, 6].

To meet the demands of a large-scale production one should develop a GaSb-cell technology which will exhibit high reproducibility, simplicity and be harmless to the environment.

Nowadays, most of the III–V structures for optoelectronic application are produced by different epitaxial methods: metalorganic chemical vapour deposition (MOCVD), molecular beam epitaxy (MBE) or liquid-phase epitaxy (LPE). In order to avoid problems arising from a high surface recombination, a heterostructure multilayer design is commonly used. However, GaSb has a low surface recombination (~ 100 cm/s [7]). Therefore, a more simple, pure diffusion process can be successfully used to fabricate different optoelectronic device structures (solar cells, PV cells, photodetectors). In

* Corresponding author. Fax: + 49 761 4588250; e-mail: sulima@ise.fhg.de.

0022-0248/97/$17.00 © 1997 Elsevier Science B.V. All rights reserved
PII S0022-0248(97)00186-3

this work the pseudo-closed box (PCB) method was used to perform the diffusion. This method avoids the inconvenience of sealed ampoules and proved to be quite simple and reproducible.

The main objective of this work is the study of the PCB method as a simple and productive technology for GaSb-based optoelectronic devices, for example, PV cells. The modelling of PV cells has shown a strong dependence of the efficiency on the diffused emitter thickness and the Zn surface concentration [8]. Therefore, the reproducible regulation of these parameters of the diffused layer should be determined.

As an alternative method, the Zn diffusion into n-GaSb substrate from a Ga–Sb–Zn melt was studied. Our experience in the field of the Zn diffusion into GaAs from a Ga–As–Al–Zn melt shows that such type of diffusion is not only reproducible but also improves the n-GaAs substrate parameters, for example, the diffusion length [9, 10]. The improvement can be explained by a "getter effect" during the heat treatment under a Ga-based melt. It was expected that the same effect takes place in the GaSb (substrate)/Ga–Sb–Zn (melt) system.

2. Experimental procedure

Two methods of Zn-diffusion were experimentally investigated: (a) diffusion from the vapour phase in a pseudo-closed-box system, and (b) diffusion from the liquid phase from a Ga–Sb–Zn melt. The p-GaSb diffused layers were studied by secondary ion mass spectroscopy (SIMS), Raman scattering spectroscopy and electrochemical capacity–voltage (C–V) profiling. Anodic oxidation and selective etching were used for a precise thinning of diffused GaSb layers.

2.1. Zn-diffusion from the vapour phase

Zn-diffusion from the vapour phase was performed into $2.5 \times 2.5\ \mathrm{cm}^2$ n-GaSb : Te ($n \approx 3 \times 10^{17}\ \mathrm{cm}^{-3}$) (1 0 0) substrates. The diffusion process was performed in a H_2 atmosphere, purified by a Pd cell, in a specially designed multi-wafer graphite boat shown in Fig. 1. The multi-wafer boat allows

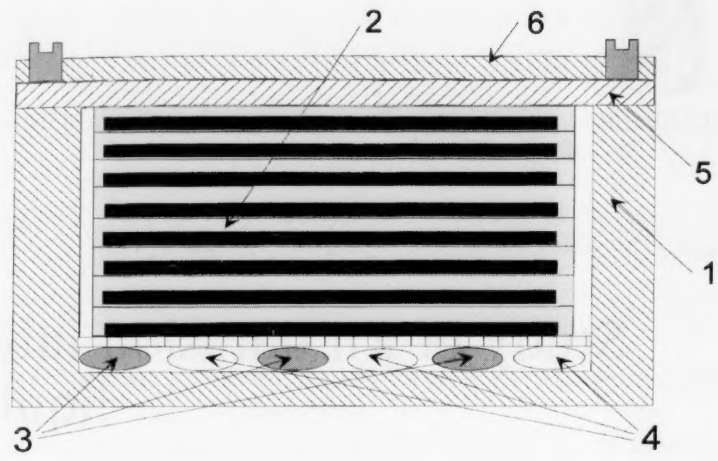

Fig. 1. Scheme of the graphite diffusion boat for the wafer in horizontal position; 1 – body of the boat, 2 – GaSb wafers in a holder, 3 – Zn or Zn + Ga as sources of Zn vapour, 4 – Sb as a source of Sb vapour, 5 – cover, 6 – plate with screws.

(i) to place $4 \times 4\ \mathrm{cm}^2$ or smaller wafers vertically or horizontally by simple changing of the substrate holder, (ii) to vary the distance between the wafers with a minimum distance of 0.5 mm, (iii) to use several Zn vapour sources (pure Zn or Zn and Ga melt) and Sb vapour sources. This design of the graphite boat ensures the uniformity of the Zn vapour pressure across the wafer surface, and thus, the uniformity of the p-GaSb layer depth. If not mentioned specially, zinc and antimony were always used in more than sufficient quantities to provide saturation vapour pressures.

2.2. Zn-diffusion from the liquid phase

Zn-diffusion from the liquid phase was performed into $1.5 \times 1.5\ \mathrm{cm}^2$ n-GaSb : Te ($n \approx 3 \times 10^{17}\ \mathrm{cm}^{-3}$) (1 0 0) substrates from a Ga–Sb–Zn melt. A simple graphite one-melt one-substrate LPE boat was used. This boat can also be considered a "pseudo-closed box". The substrate was placed in a horizontal position. The melt depth was 4 mm. The process was performed in a H_2 atmosphere purified by a Pd cell.

It was found that the wetting of the substrate by the melt was always successful if the melt and the substrate had been baked at 600°C during 1 h prior to the diffusion process. The baking helped to reduce native oxides on the GaSb surface and to dissolve Sb and Zn in Ga homogeneously. The

process temperature was 550°C. The Ga–Sb–Zn melt was undersaturated with respect to Sb. The undersaturation level was chosen to cause a dissolution of roughly 20 μm of the GaSb substrate. Afterwards the Zn-diffusion into GaSb took place. The melt–substrate contact time was 1 h. The process was terminated by removing the melt from the substrate.

Minor changes took place on the GaSb surface after the etchback-diffusion process and it remained almost mirror like.

3. Results and discussion

3.1. Zn-diffusion from the vapour phase

It was assumed apriori that Zn profiles in GaSb are dependent on the following parameters of the diffusion process: (i) temperature of diffusion, (ii) diffusion time, (iii) type of the Zn vapour source and (iv) type of the Sb vapour source. In order to determine experimental dependencies, studies of each parameter with all others fixed were performed.

3.1.1. Temperature of diffusion

Fig. 2 shows SIMS profiles of Zn concentration from the vapour phase at different temperatures. It was found that a Zn-diffusion profile generally consists of 5 parts (see diffusion profiles for 480°C and 500°C in Fig. 2): (i) a part with a steep Zn concentration gradient near the surface, (ii) a first plateau with a relatively slow decrease of Zn concentration, (iii) a kink, (iv) a second plateau with a relatively slow change of Zn concentration and (v) a steep diffusion front. The first part was usually thinner than 0.1 μm. We consider that this part of the SIMS measurements is not reliable enough. Therefore, we did not take this part into consideration and in the following figures it will be omitted. Hereafter, we understand under the surface concentration the maximum concentration at the 1st plateau region. Similar Zn diffusion profiles in GaSb were obtained in Ref. [11], whereas in Ref. [12] diffusion profiles with only one plateau were reported. Zn diffusion profiles with a kink were reported in Ref. [13] for GaAs. These profiles could not be explained by the standard interstitial-substitutional–diffusion mechanism which is usually used to model Zn diffusion in III–V materials. Two different modifications of the interstitial-substitutional mechanism seem to explain the appearance of a kink in diffusion profiles in GaAs [13, 14]. No models of Zn diffusion were suggested for GaSb. However, it is reasonable to assume that the diffusion mechanisms of Zn in GaAs and GaSb are similar.

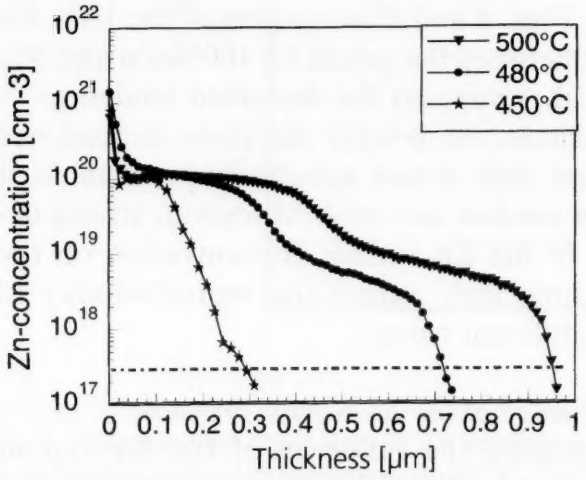

Fig. 2. SIMS profiles of Zn concentration after diffusion of Zn from the vapour phase at different temperatures for pure Zn and Sb as vapour sources. Diffusion time was 1 h. The dash-dot line shows the doping level in the n-GaSb : Te substrate.

It is noteworthy, that there is almost no difference in the Zn surface concentration at 450–500°C after 1 h diffusion. This shows, that the saturation of Zn concentration of GaSb in this time–temperature range takes place at the level of $\approx 1.7 \times 10^{20}\,cm^{-3}$. This value is very close to the GaSb : Zn solubility at 500°C ($1.5 \times 10^{20}\,cm^{-3}$) published in Ref. [15]. The fact that the surface concentration can be saturated is very important for the reproducibility and simplicity of the p-layer formation process. In general, the diffused p-layer thickness depends on the surface concentration, diffusion temperature and time. On the other hand, the surface concentration itself depends on temperature and time. This makes the temperature and time dependencies of the p-layer thickness complicated and hardly reproducible. Moreover, this does not allow to change the p-layer thickness without varying the surface concentration. If one can fix the surface concentration at the saturation level, the

p-layer thickness can be regulated either by diffusion temperature or diffusion time with more accuracy. If one needs to decrease the surface concentration, a precise anodic oxidation of the corresponding part of the diffused layer succeeded by selective etching can be used. This procedure is described below.

3.1.2. Diffusion time and Zn vapour sources

Zn–Ga [2, 11] or Zn–Sb [1] melts were always used as a Zn vapour source by other investigators of the Zn PCB diffusion process in GaSb. In this work we investigated application of both diluted Zn sources and of pure Zn. As the criterion of reproducibility of the diffusion process we have chosen the proportionality of the p-layer thickness on the square root of the diffusion time. In the case of such dependence, one can accurately regulate the p-layer thickness by changing the diffusion time.

Fig. 3 shows the Zn concentration profiles for different diffusion times and Zn vapour sources. In the case of the 3 wt% Zn + 97 wt% Ga sources, the source was used for only one diffusion. Two diffusions with a 10 wt% Zn + 90 wt% Ga source were also performed. Their results are shown in Figs. 4 and 5 .

The shapes of diffusion profiles at various diffusion times in Fig. 3a are quite different compared to Fig. 3b. For better understanding of the data from the large family of curves in Fig. 3, the time dependence of the Zn surface concentration is shown in Fig. 4 and the time dependence of the emitter thickness in Fig. 5. Several important conclusions can be drawn from these figures.

The use of a pure Zn source allows to reach the proportionality of the emitter thickness on the square root of the diffusion time (Fig. 5). The square-root dependence starts for the diffusion times equal or longer than 1 h. For shorter times one has to consider the influence of the 1.5 h heating time before reaching the diffusion temperature. For very short diffusion times (several minutes) the heating time becomes predominant in the diffusion process.

The emitter thickness diffusion time dependence for the diluted Zn vapour sources is much more complicated and therefore, as one can assume, less reproducible. For example, if a diluted 97 wt% Ga–3 wt% Zn source is regarded, no square-root dependence is observed (Fig. 5). Fig. 4 shows that for a pure Zn source, the Zn surface concentration slowly increases with diffusion time and reaches a saturation level in 1–2 h. Afterwards, one can change the emitter thickness taking into account the square-root time dependence only. Both, the heating effect and the increase of the surface concentration are of no importance for diffusion times longer than 1–2 h. This makes the process of the emitter thickness regulation easy and reproducible. On the contrary, in the case of a 3% Zn source, the Zn surface concentration: (a) increases more steeply and (b) after reaching a maximum begins to decrease. That means, the Zn vapour pressures produced by both 100% and 3% Zn sources are enough to reach the Zn saturation level in GaSb. However, the higher Zn vapour pressure in the case of the 100% Zn source allows to reach the level close to saturation within several minutes of diffusion time. Only a minor increase takes place during the following time before the 100% saturation is reached. In the case of a diluted source, more time is necessary to accumulate enough Zn in the boat and on the GaSb surface to reach the saturation level. Thus, one can see that during 1 h diffusion time less than 20% of the saturation level is reached when a 3% Zn source is used.

The effect (b) can be explained by a Zn depletion in the melt and a Zn out-diffusion from the diffused layer. This cannot happen with the pure Zn source which is practically infinite.

In both Figs. 4 and 5 two points of the 10% Zn source are between the points for 100% Zn and 3% Zn. Thus, they support the described tendency.

To conclude, the p-layer thickness dependence on diffusion time is not accurately predictable, if diluted Zn sources are used. Moreover, strong dependence of the Zn surface concentration on the diffusion time may reduce the reproducibility of results in different runs.

3.1.3. Influence of the Sb vapour pressure

To determine the influence of the Sb vapour pressure on the Zn diffusion parameter, several diffusions with and without Sb vapour sources were performed. Fig. 6 shows the SIMS profiles of the Zn concentration after diffusion from the vapour

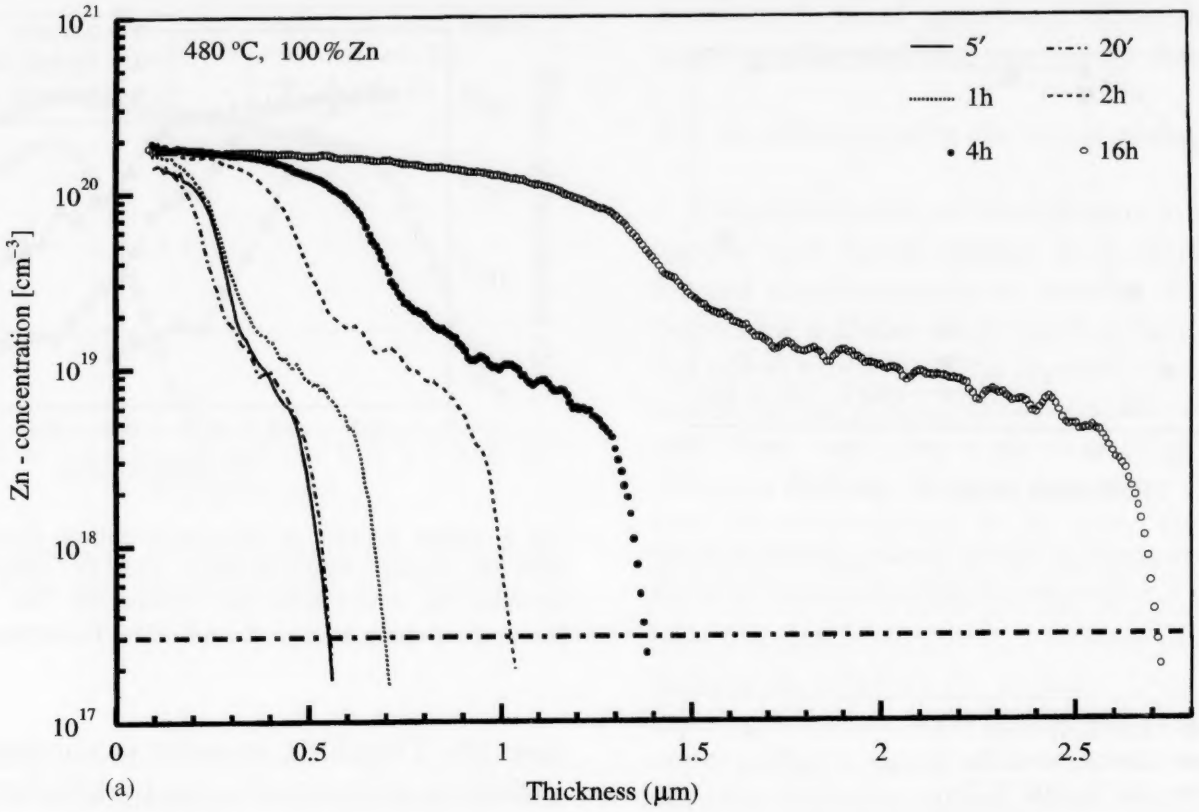

Fig. 3. Diffusion time dependence of Zn concentration profiles for the following diffusion parameters: (a) 480°C, pure Zn and Sb as corresponding vapour-phase sources, (b) 500°C, 3 wt% Zn + 97 wt% Ga, Sb, Zn and Sb vapour pressure sources were never mixed. The horizontal dash-dot lines show the doping level in the n-GaSb : Te substrate.

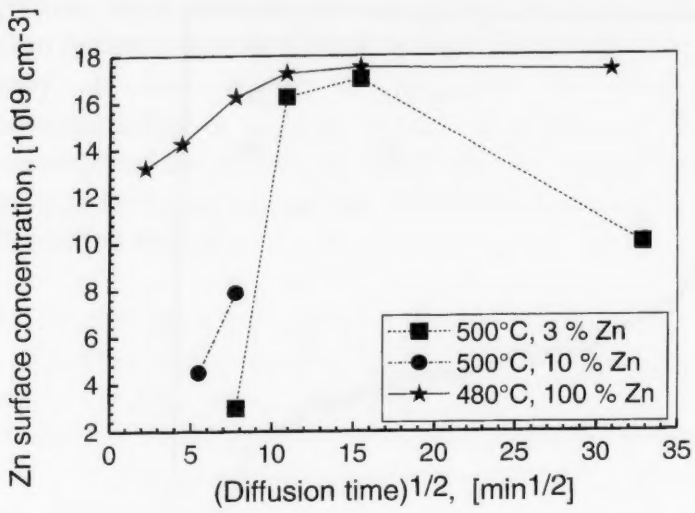

Fig. 4. Time dependence of the Zn surface concentration for 480°C – and 500°C – diffusions with different Zn vapour sources.

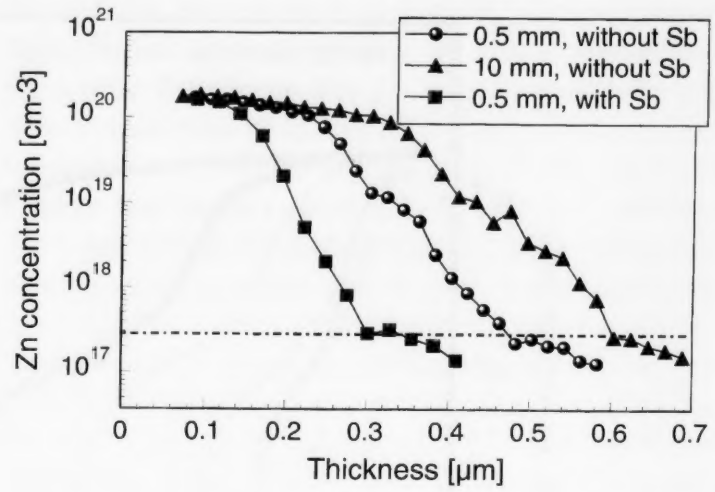

Fig. 6. SIMS profiles of Zn concentration after Zn-diffusion from the vapour phase at 450°C (1 h) for different distances between the wafers with and without Sb. The dash-dot line shows the doping level in the n-GaSb : Te substrate.

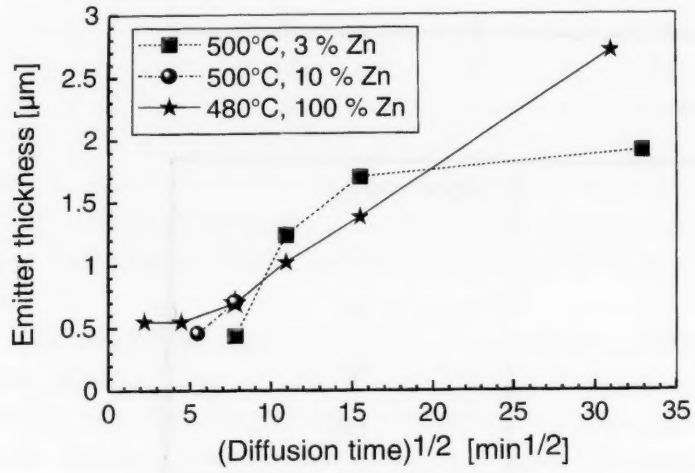

Fig. 5. Time dependence of the emitter thickness for 480°C – and 500°C – diffusions with different Zn vapour sources.

phase. Three combinations of the distances between the wafers and the presence of Sb sources were investigated. One can see that both, decreasing the distance between the wafers and adding Sb, decrease the Zn diffusion depth into the substrate. If one assumes the similar dependence of the Zn-diffusion in GaSb on the vapour pressure of V-element as in GaAs [16], the difference in the diffusion profiles can be explained by Sb desorption from the GaSb surface. The larger the distance between the wafers, the stronger is the desorption of Sb and the more Zn penetrates into GaSb. Addition of Sb into the boat decreases the Sb desorption from the wafer due to the high vapour pressure of pure Sb. Therefore, in order to eliminate possible variations in Zn profiles due to different conditions for Sb desorption from the GaSb surface, we always used Sb vapour sources and one and the same (0.5 mm) distance between the wafers.

As it was shown, by using pure Zn as Zn-vapour source one can reach the saturation Zn surface concentration level in GaSb. In this case, one can reproducibly regulate the p–n junction position by changing the diffusion time. However, a lower Zn surface concentration is necessary for some devices. Using anodic oxidation and selective etching of the oxide is a convenient, precise and reproducible way to reduce the surface concentration with a simultaneous decrease of the p-layer thickness [17]. The anodization technique used was essentially that reported for GaAs in Ref. [18]. The oxidation depth rate of GaSb in the range of an applied voltage of 10–100 V was determined as 2.0 nm/V [17]. Concentrated or diluted HCl was used as a selective etchant of the anodic oxide on GaSb.

3.1.4. Measurements of free-hole profiles

Free-hole profiles in p-GaSb were measured by Raman-spectroscopy and electrochemical *C–V* profiling methods.

In the case of Raman-spectroscopy measurements, the depth resolution was provided by a precise layer-by-layer anodic oxidation of GaSb and

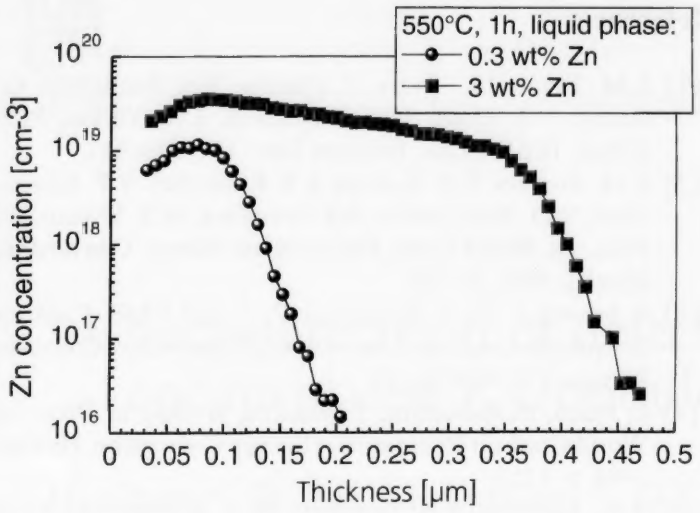

Fig. 7. SIMS profiles of Zn concentration after Zn-diffusion (550°C, 1 h) from two Ga–Sb–Zn melts with different Zn content.

corresponding selective etching of the oxide. Details of these measurements are described in Ref. [17]. The agreement of the SIMS and Raman-spectroscopy measurements for the Zn (hole) concentrations between 10^{19} and $10^{20}\,cm^{-3}$ was quite good. That means, that almost all Zn atoms are electrically active in that part of the diffused layer.

The electrochemical C–V profiling was performed with a 0.1 M tiron solution $[C_6H_2(OH)_2(SO_3Na)_2 \cdot H_2O]$ as an electrolyte. A relatively good agreement of free-hole and Zn-atom profiles was also proved by this method.

3.2. Zn-diffusion from the liquid phase

The experiments on Zn-diffusion into GaSb from vapour and liquid phases were started and performed simultaneously in parallel. From the very beginning, we have observed that the diffusion from the liquid phase was less reproducible with respect to the surface concentration and the emitter thickness. Now, on the basis of our understanding of the diffusion from the vapour phase, we can conclude, that the evaporation of Zn from the Ga–Sb–Zn melt is the main reason for the lower reproducibility. Fig. 7 shows SIMS profiles of Zn concentration after Zn-diffusion (550°C, 1 h) from two Ga–Sb–Zn melts with different Zn content. One can see that the Zn diffusion from the liquid phase results in lower surface concentration values compared to the diffusion from the vapour phase, and hence in "no-kink" profiles.

3.3. Device fabrication

In order to prove the applicability of the developed diffusion methods, approximately 600 cm^2 of the diffused structures for photovoltaic GaSb cells were fabricated. The parameters of the best

Table 1
Photovoltaic cells parameters (AM 1.5 Global, 25°C, 1 sun = 100 mW/cm^2)

Designated area (cm^2)	Concentration (suns)	Short-circuit current density (mA/cm^2)	Open-circuit voltage (mV)	Fill-factor (%)	Efficiency (%)
Zn diffusion from the vapour phase					
0.13	200	5871	456	74.0	9.9
0.92[b]	23	790	414	69.9	9.7
0.92[a]	1	34.4	357	69.9	8.2
3.61[a]	1	35.5	354	65.6	8.2
3.61[b]	8	275	410	70.0	10.2
Zn diffusion from the liquid phase					
0.13	62	2090	383	64.7	8.3

[a]All cell parameters were measured in the Calibration Laboratory of the Fraunhofer Institute for Solar Energy Systems, Freiburg, Germany.
[b]One-sun short-circuit current density was measured in the Calibration Laboratory of the Fraunhofer Institute for Solar Energy Systems, Freiburg, Germany.

cells with one-layer antireflection coatings, optimized for tandem and thermophotovoltaic application, are listed in Table 1. To our knowledge, GaSb cells with the designated area as large as 3.61 cm^2 were fabricated for the first time.

4. Conclusions

Two types of Zn diffusion into GaSb were studied. Both of them resulted in obtaining GaSb photovoltaic cells with good parameters. First cells with a designated area 3.61 cm^2 have been fabricated.

We have demonstrated that the reproducible formation of Zn diffusion profiles in n-GaSb is possible by the technologically simple pseudo-closed-box diffusion method. This method yields good control over Zn surface concentration and junction depth.

The results of this work have shown the applicability of the PCB method for a large-scale production of GaSb p–n structures.

Acknowledgements

The authors wish to thank Dr. B. Ber for SIMS measurements, Dr. A. Mintairov for Raman-spectroscopy measurements, R. Beckert for the solar cells parameter measurement, Professor W. Wettling, Professor V. Andreev and G. Stollwerck for fruitful discussions and Professor J. Luther for his permanent interest in the performed investigations. This work was partially financed by the Federal Ministry of Education, Science, Research and Technology (BMBF), Germany (contract 0328554D). The authors are responsible for the content of this publication.

References

[1] L.M. Fraas, J.E. Avery, J. Martin, V.S. Sundaram, G. Girard, V.T. Dinh, T.M. Davenport, J.W. Yerkes, M.J. O'Neil, IEEE Trans. Electron Dev. 37 (1990) 443.
[2] V.M. Andreev, L.B. Karlina, A.B. Kazantsev, V.P. Khvostikov, V.D. Rumyantsev, S.V. Sorokina, M.Z. Shvarts, in: Proc. 1st World Conf. Photovoltaic Energy Conversion, Hawaii, 1994, p. 1721.
[3] A. Schock, C. Or, V. Kumar, in: Proc. 2nd NREL Conf. on Thermophotovoltaic Generation of Electricity, Colorado Springs, CO, 1995, p. 81.
[4] L. Fraas, R. Ballantyne, J. Samaras, M. Seal, in: Proc. 1st World Conf. on Photovoltaic Energy Conversion, Hawaii, 1994, p. 1713.
[5] A.N. Baranov, A.N. Imenkov, M.P. Mikhailova, Yu.P. Yakovlev, SPIE 1724 (1992) 78.
[6] M.P. Mikhailova, A.N. Titkov, Semicond. Sci. Technol. 9 (1994) 734.
[7] L.M. Fraas, J.E. Avery, P.E. Grunbaum, V.S. Sundaram, in: Proc. 22nd IEEE Photovoltaic Specialists Conf., Las Vegas, 1991, p. 80.
[8] A.W. Bett, S. Keser, G. Stollwerck, O.V. Sulima, W. Wettling, in: Proc. 25th IEEE Photovoltaic Specialists Conf., Washington, 1996, p. 133.
[9] A. Baldus, A. Bett, U. Blieske, O.V. Sulima, W. Wettling, J. Crystal Growth 146 (1995) 299.
[10] V.M. Andreev, O.K. Salieva, V.A. Solov'ev, O.V. Sulima, A.M. Khammedov, Crystal Res. Tech. 23 (1988) 1531.
[11] V.S. Sundaram, P.E. Gruenbaum, J. Appl. Phys. 73 (1993) 3787.
[12] G.J. Conibeer, A.F.W. Willoughby, C.M. Hardingham, V.K.M. Sharma, Mater. Sci. Forum 143–147 (1994) 1427.
[13] S. Reynolds, D.W. Vook, J.F. Gibbons, J. Appl. Phys. 63 (1988) 1052.
[14] K.B. Kahen, Appl. Phys. Lett. 55 (1989) 2117.
[15] S.F. DaCunha, J. Bougnot, Phys. Status Solidi 22 (1974) 205.
[16] D. Shaw, Atomic Diffusion in Semiconductors, Plenum, New York, 1973.
[17] O.V. Sulima, N.N. Faleev, A.B. Kazantsev. A.M. Mintairov, A. Namazov in: Proc. 4th European Space Power Conf. Poitiers, 1995, p. 641.
[18] H. Hasegawa, H.L. Hartnagel, J. Electrochem. Soc. 123 (1976) 713.

ELSEVIER

Journal of Crystal Growth 181 (1997) 17–25

JOURNAL OF CRYSTAL GROWTH

Characterization of defect structures in magnetic liquid encapsulated Kyropoulos grown InP single crystals

H. Chung[a], W. Si[a], M. Dudley[a,*], D.F. Bliss[b], R. Kalan[c], A. Maniatty[c], H. Zhang[d], V. Prasad[d]

[a] *Department of Materials Science and Engineering, State University of New York at Stony Brook, Stony Brook, New York 11794-2275, USA*
[b] *USAF Rome Laboratory, Hanscom AFB, Massachusetts 01731, USA*
[c] *Department of Mechanical Engineering, Aeronautical Engineering and Mechanics, Rensselaer Polytechnic Institute, Troy, New York 12180,USA*
[d] *Department of Mechanical Engineering, State University of New York at Stony Brook, Stony Brook, New York 11794-2300, USA*

Received 5 December 1996; accepted 1 April 1997

Abstract

Synchrotron White Beam X-ray Topography (SWBXT) has been used as a nondestructive diagnostic technique for the characterization of defect structures in large wafers cut from S and Fe-doped InP single-crystal boules. Wafers cut both longitudinally and laterally with respect to the growth axis were studied in order to reveal the overall defect distribution in the boules. Studies carried out on longitudinally cut S-doped crystals enabled information to be obtained on interface shape, from the observation of growth striations, as well as defect distribution. The conditions for optimal visibility of the growth striations were determined and it was found that the morphology of the growth interface was a sensitive function of local growth conditions. The formation of extensive slip bands from peripheral regions was also observed. This indicates that large thermal stresses were generated during crystal growth leading to such significant plastic deformation processes. Studies carried out on a series of laterally sliced, Fe-doped wafers cut from the same boule revealed dislocations in well-defined fourfold symmetric distributions. A finite element thermal-elastic stress analysis was performed for an intermediate growth stage to investigate the nature of the stress which causes this fourfold distribution. The calculated excess shear stress from this analysis agrees qualitatively with the observed dislocation distribution and slip system activity. The influence of an applied magnetic field on precipitate distributions in InP boules was preliminarily studied by examining a longitudinal cut, heavily Fe-doped InP wafer, which was grown in the presence of an intermittent applied field. Topographs recorded from this wafer revealed that no formation of large precipitates was discernible in either the initial or intermediate growth stages when the magnetic field was applied. On the other hand, the formation of large precipitates was observed in regions near the final stage of crystal growth when the magnetic field was turned off. Further such investigations are underway.

Keywords: X-ray topography; InP; Growth striations; Slip bands; Dislocations and twins

* Corresponding Author: Fax: + 1 516 632 8052; e-mail: mdudley@ccmail.sunysb.edu.

0022-0248/97/$17.00 © 1997 Elsevier Science B.V. All rights reserved
PII S0022-0248(97)00271-6

1. Introduction

InP is an important semiconductor material for long-wavelength optoelectronic devices and high-frequency electronic devices. The performance of these devices is controlled by the structural and chemical uniformity of the epitaxial layers, which in turn, is strongly dependent on the structural perfection and compositional homogeneity of the substrates. It is, therefore, imperative to improve the crystalline quality and homogeneity of InP substrates. However, the relatively low yield stress of InP [1] makes it susceptible to deformation by stresses generated during crystal growth. It is, therefore, difficult to produce InP crystals with low dislocation density. On the other hand, temperature fluctuations imposed by turbulent convective flow give rise to uncontrolled variations in the local solidification rate and diffusion layer thickness, leading to microscopic and macroscopic chemical inhomogeneity. Improvements in the structural perfection of InP crystals has been demonstrated by using the magnetic liquid encapsulated Kyropoulos (MLEK) growth method [2]. The use of a magnetic field can dampen out the turbulent convective flow to improve the microscopic homogeneity of the crystal [3]. On the other hand, with the Kyropoulos process, where the solid–liquid growth interface is several millimeters below the encapsulating layer, the thermal stresses generated during growth can be reduced. A decrease of the dislocation density in GaAs crystals by using the liquid encapsulated Kyropoulos (LEK) growth method has been reported [4].

Defects in InP have been studied by means of optical microscopy (OM) of the etched surface [5], transmission electron microscopy (TEM) [6], and X-ray topography [7]. While OM is a quick and easy method, it can only reveal defects which create inhomogeneities as they intersect with the sample surface, yielding very little structural or crystallographic information. TEM can give detailed structural and chemical information at atomic scales, but sample preparation is difficult and destructive. In addition, only very small regions of a wafer can be examined at a time due to the extremely small field of view. By comparison, synchrotron white beam white X-ray topography (SWBXT) [8, 9] is nondestructive, and no special sample preparation is needed. It is complementary to TEM with respect to the field of view, since it can image whole wafers up to 4 in. in diameter in a single exposure. Also it is superior to conventional X-ray topography due to its high intensity, wavelength tunability, and good geometric resolution [9]. The purpose of this study is to characterize the structure, density, and distribution of defects in MLEK grown InP crystals using SWBXT. It extends our previous work [10] and presents investigations of structural defect configurations and their distributions in the different stages of crystal growth, which enables a correlation between observed defect structures and both the growth parameters and modeling predictions. The results can provide feedback to the crystal grower to enable optimization of these growth parameters.

2. Experimental procedure

All the crystals used for this study were grown with $\langle 0\,0\,1 \rangle$ pulling directions by the MLEK technique, at Rome Laboratory, Hanscom AFB. The crystals had a diameter of about 2–3 in. and all appeared macro-twin free to the naked eye. In the heavily Fe-doped InP crystal (wafer B), the magnetic field was turned off during part of the pulling process to investigate the effect of magnetic field on the dopant (precipitate) distribution.

SWBXT experiments were carried out at the Stony Brook Synchrotron Topography Station, Beamline X-19C, at the National Synchrotron Light Source (NSLS), Brookhaven National Laboratory. In this study, both transmission and reflection Laue geometries are employed. In the transmission topographic experiments, crystals were oriented in the beam so that the wavelengths selected for the reflections used were around 0.45 Å, which is just above the InK absorption edge (0.44 Å), to minimize photoelectric absorption. In addition, a scanning mechanism [11] comprising both vertical and horizontal translation stages is also employed to enable single-exposure imaging of these large-size wafers. To prevent possible surface deterioration of the crystals due to prolonged exposure to the intense radiation, the longer wavelength

components of the synchrotron radiation, which are most readily absorbed, were selectively removed by employing a filter consisting of a few hundred micrometers of aluminum. All images were recorded on 8″ × 10″ Kodak SR-1 high-resolution X-ray film.

3. Results and discussion

3.1. Wafer A (S-doped wafer)

3.1.1. The visibility of growth striations

In a previous paper [10], we reported on the observation of growth interface morphology in the S-doped ($1–2 \times 10^{18}$ at/cm^3) InP crystal using SWBXT. Systematic investigation of the contrast variations in the images of growth striations reveals that the visibility of growth striations is a sensitive function of diffraction geometry. Fig. 1a and Fig. 1b are transmission X-ray topographs recorded from the S-doped InP crystal showing the contrast variations in the images of growth striations in different reflections. Growth striations are clearly visible in Fig. 1a, where the lattice planes parallel to the (0 0 1) growth interface are chosen for the reflection. In contrast, growth striations are invisible in Fig. 1b, where the lattice planes perpendicular to the (0 0 1) growth interface are chosen for the reflection. The contrast variations strongly indicate that the lattice distortion arising from dopant segregation is primarily normal to the growth front. In other words, the displacement vector associated with the growth striations is perpendicular to the interface plane so that growth striations are invisible when the reflecting planes are parallel to the displacement vector. This result clearly indicates that the choice of correct orientation of the active reciprocal lattice vector with respect to the interface plane is important to optimize the visibility of growth interfaces.

3.1.2. The Morphology of growth interface vs. growth conditions

The morphology of growth interfaces is clearly delineated through the observation of growth striations (Fig. 1a). A significant change in the growth

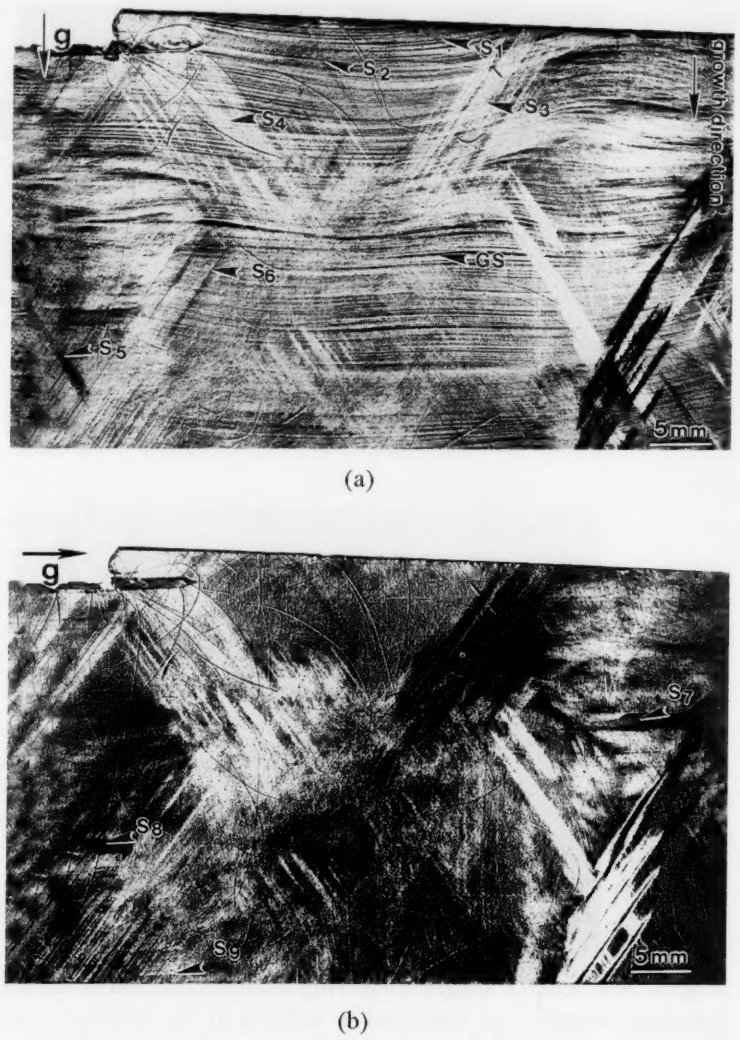

Fig. 1. Transmission X-ray topographs recorded by using (a) $\boldsymbol{g} = 0\,0\,\bar{4}$, $\lambda = 0.45$ Å and (b) $\boldsymbol{g} = 2\,\bar{2}\,0$, $\lambda = 0.45$ Å from a MLEK grown S-doped InP crystal showing the contrast variations in the images of growth striations (GS).

interface morphology was observed when the pulling process was initiated, with bimodal shape of growth interface, comprising a convex region in the center and two concave regions near the outer surface of the crystal being developed. The likely reasons for this lie in the fact that the convective flow in the melt due to both buoyancy and the combination of crucible and crystal rotation changes when the pulling process begins [12, 13]. At this point, as the shoulder of the crystal emerges from the melt into the encapsulant, the thickness of the encapsulant above the crystal decreases as the encapsulant moves into the region between the outer boule circumference and the crucible wall.

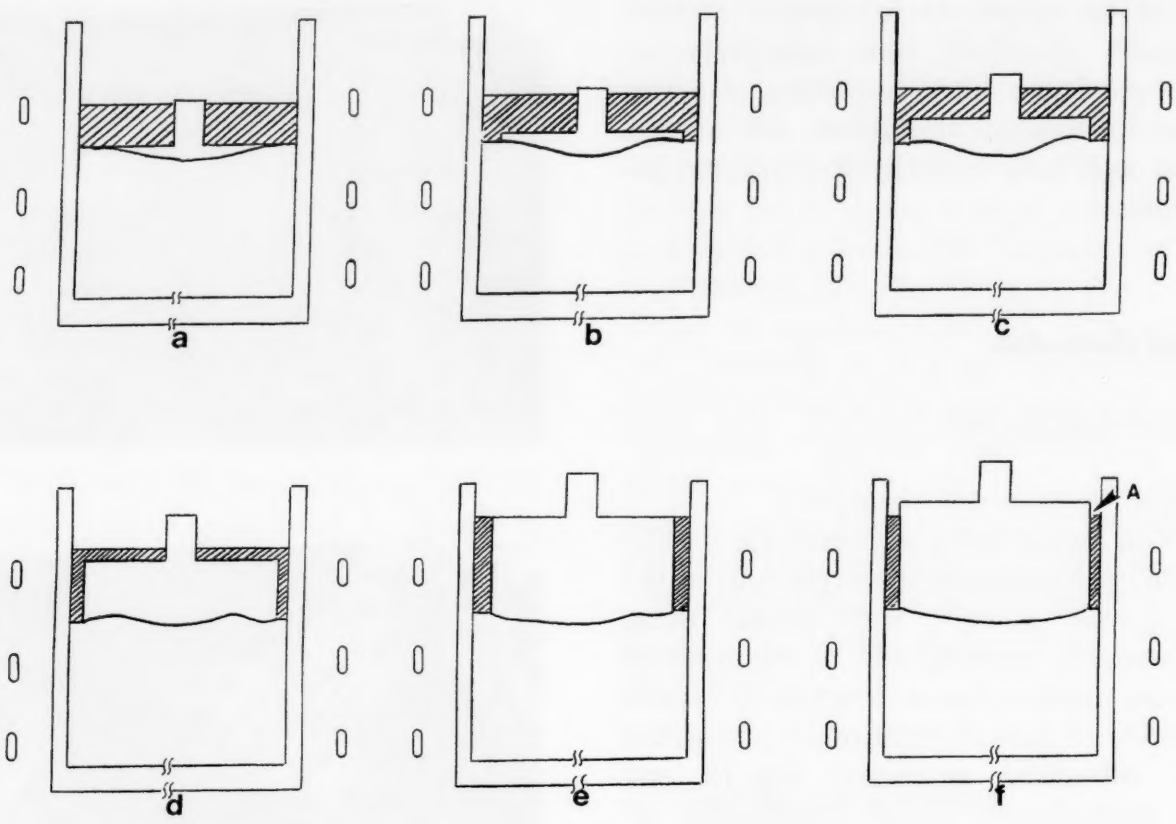

Fig. 2. A schematic diagram showing the modification of the geometric configuration of the encapsulant and the corresponding growth interface morphology observed in wafer A at the various stages of the growth process.

Fig. 2 is a schematic diagram showing the modification of the geometric configuration of the encapsulant and the corresponding growth interface morphology at various stages of the growth process. This change in the geometric configuration of the encapsulant during growth leads to a dramatic modification of the convective and radiative heat transfer from both the top and cylindrical outer surfaces of the boule. These effects modify the global heat transfer environment of the growth process and potentially cause a change in the flow pattern of the melt, which gives rise to a modification of the growth interface morphology. It is also worth noting that a well defined, slightly convex shape of growth interface was developed in the final stages of the growth process. Since the geometric configuration of the encapsulant remained the same after the flat shoulder of the boule emerged from the encapsulant, the heat transfer environment of the growth process after this point can be stable so that no significant temperature changes causing a modification of the growth interface morphology were observed in the subsequent stages of the growth.

3.1.3. The distribution of dislocations

In the growth of indium phosphide, boric oxide is used as an encapsulant to prevent the decomposition of the melt. The encapsulant also reduces the radiative heat loss from the outer surface of the crystal since B_2O_3 acts as a heat shield. The maximum heat loss, therefore, occurs at the point where the hot solid material emerges from the encapsulant (as indicated by region A in Fig. 2), which gives rise to maximum temperature gradients and thereby a large thermal stress in this region [13]. X-ray topographs revealed that the slip bands are most likely to be nucleated at this stage to relieve the large thermal stresses (Fig. 1). The diffuse

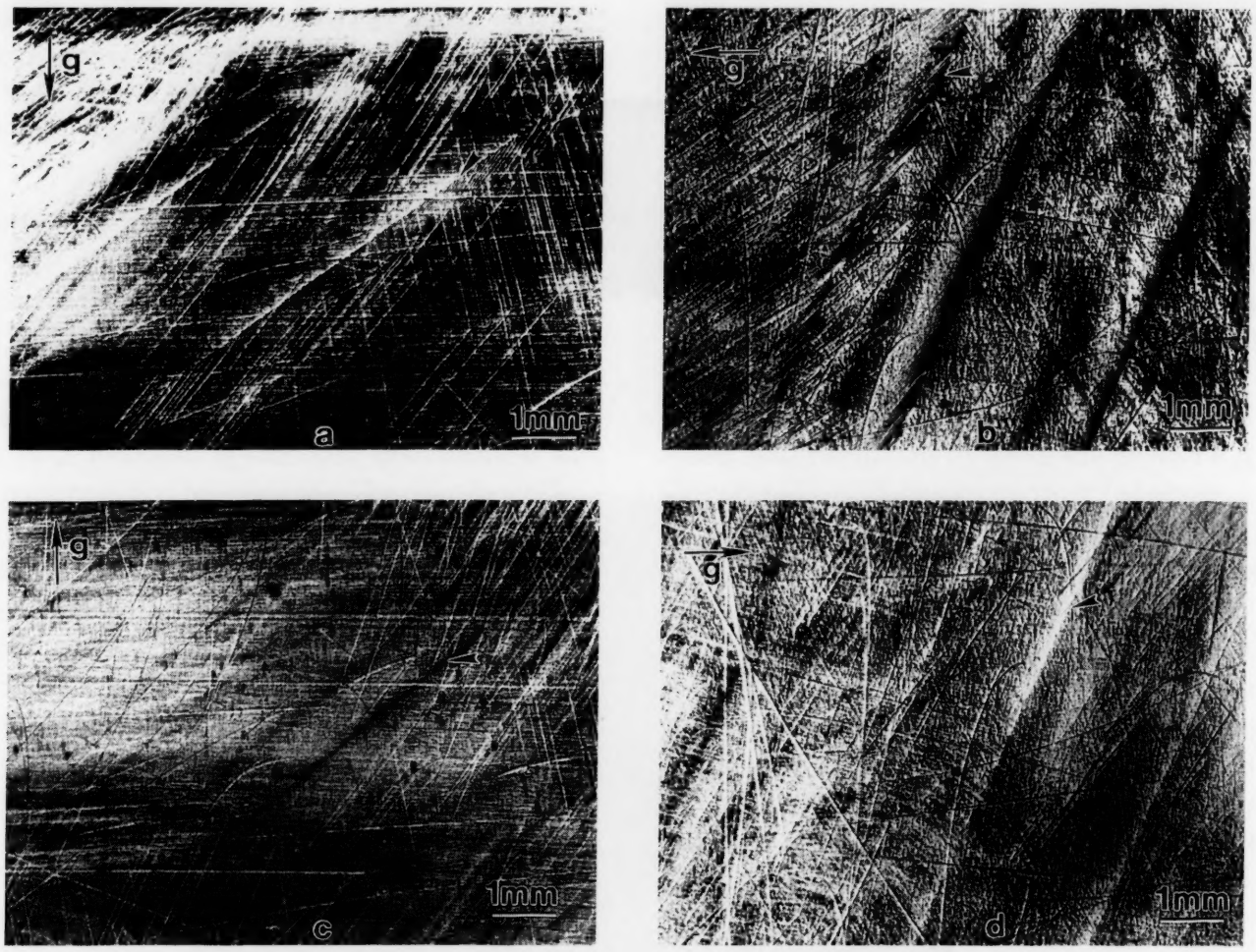

Fig. 3. Transmission X-ray topographs recorded from wafer A by using (a) $\boldsymbol{g} = (1\,1\,1)$, $\lambda = 0.45$ Å, (b) $\boldsymbol{g} = (0\,4\,0)$, $\lambda = 0.45$ Å, (c) $\boldsymbol{g} = (1\,1\,\bar{1})$, $\lambda = 0.45$ Å and (d) $\boldsymbol{g} = (4\,0\,0)$, $\lambda = 0.45$ Å showing the contrast variations of a slip band.

contrast in the slip bands and in their surrounding crystal volume revealed on X-ray topographs is due to the long-range strains associated with a high density of dislocations piling up on their slip planes [14, 15]. A judicious choice of proper projection and diffraction conditions enabled individual dislocations within a slip band to be clearly resolved. Fig. 3 are transmission X-ray topographs recorded from a slip band showing the contrast variations of slip dislocations in different reflections. It is worth noting that individual dislocations are clearly visible in both (1 1 1) and (0 4 0) reflections, while only faint contrast associated with the intersection of the slip band on the X-ray exit surface can be discerned in both (1 1 $\bar{1}$) and (4 0 0) reflections. The dislocation Burgers vector ($\boldsymbol{b}$) can, therefore, be determined by using the $\boldsymbol{g} \cdot \boldsymbol{b} = 0$ criterion [9], where $\boldsymbol{g}$ is the diffraction vector. The slip plane can also be determined by analyzing the projected direction and length of slip dislocations in different reflections. This slip band is, therefore, characterized to belong to the [0 1 1]/(1 $\bar{1}$ 1) slip system. Systematic characterization of all the slip dislocations in this sample reveals that nine out of twelve possible $\langle 1\,1\,0\rangle/\{1\,1\,1\}$ slip systems are activated at different stages of the crystal growth process.

Calculations of the distribution of excess resolved shear stresses in the crystal at various stages in the growth process have recently been carried out by using a three-dimensional anisotropic thermo-elastic finite element model for InP single crystals. Results also confirm that the maximum excess-resolved shear stresses are generated on the outer surface of the crystal at the point where the crystal emerges from the encapsulant (see Section 3.3).

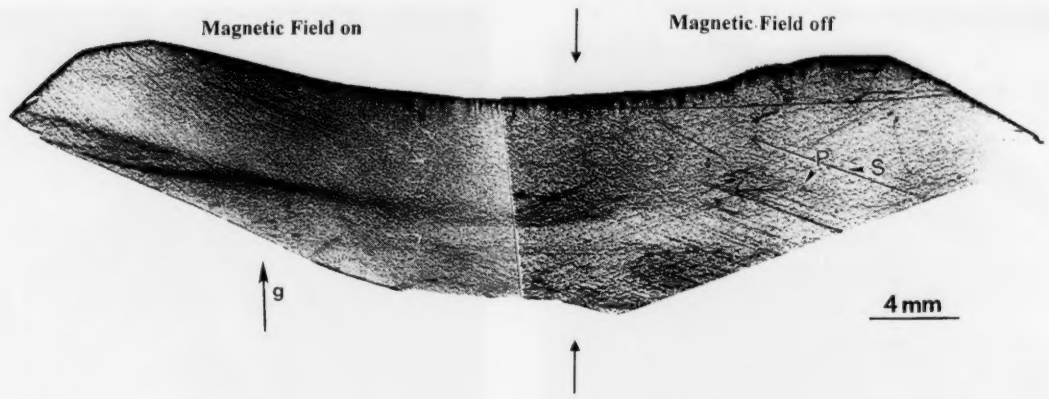

(a)

(b)

Fig. 4. (a) Reflection topographs of wafer B, $\boldsymbol{g} = 4\,4\,0$, $\lambda = 0.74$ Å, which shows slip bands (S), Fe precipitates (P), and dislocation segments (D); (b) a highly magnified reflection X-ray topograph enlarged from the final growth stage.

3.2. *Wafer B (Fe-doped wafer)*

In wafer B, a heavily Fe-doped ($1–2 \times 10^{19}$ at/cm^3) crystal, the applied magnetic field was switched off in the middle of the growth process to investigate the effect of magnetic field on dopant incorporation. The segregation coefficient of iron in indium phosphide is low (approximately 10^{-3}), so there is a strong tendency for the occurrence of macrosegregation during growth [3]. Fig. 4a is an X-ray topograph ($\boldsymbol{g} = 440$, $\lambda = 0.74$ Å) recorded in reflection geometry from this sample. Images of precipitates (P) consisting of two dark, kinematic lobes positioned in the $\pm \boldsymbol{g}$ directions, separated by a region of significant lattice rotation are clearly observed in the final growth stages. Fig. 4b is a highly magnified X-ray topograph recorded from this region to show the defect structures in a greater detail. It appears, therefore, that large precipitates were generated in the final growth stage when the applied magnetic field is turned off. On the other hand, no formation of large precipitates is evident in both the initial and intermediate growth stages when a magnetic field is applied. However, the presence of a very high density of dislocations in both the initial and intermediate growth stages obscured detailed observations of precipitate distributions in these regions. Therefore, studies of

dopant distributions in crystals with higher structural perfection are required to evaluate the effect of magnetic field on the homogeneity of dopant distributions in more detail.

3.3. Modeling the distribution of dislocations

The observation of dislocation distributions in a series of wafers sliced perpendicular to the [0 0 1] growth direction from a Fe-doped InP boule has been previously reported [10]. Results revealed the formation of a fourfold symmetric distribution of dislocations separated by regions of low dislocation density in the intermediate growth stages. The regions of high dislocation density are observed to lie near the periphery of the wafer along $\langle 1\,0\,0\rangle$ directions, while the density of dislocations reaches a minimum along $\langle 1\,1\,0\rangle$ directions. In addition, X-ray topographs recorded from wafers sliced longitudinally from MLEK grown InP crystals revealed the formation of extensive slip bands from the outer surface which have propagated into the interior of these crystals. In order to investigate the origin of the observed dislocation distributions in detail, a three-dimensional anisotropic, thermal-elastic finite element analysis of an InP single crystal at an intermediate growth stage was conducted. For a specified temperature field within the crystal, the finite element model calculates the corresponding stress field. The model incorporates room temperature values for the elastic parameters and a temperature-dependent thermal expansion coefficient. The values for three elastic parameters given by Ref. [16], are $c_{11} = 102$ Gpa, $c_{12} = 57.3$ Gpa and $c_{44} = 44.2$ Gpa. The thermal expansion coefficient for temperatures above 823 K is expressed by the following linear function [17]:

$$\alpha = 8.57 \times 10^{-9}\theta - 2.57 \times 10^{-6},$$

where θ is in Kelvin. For temperatures less than 825 K, the thermal expansion coefficient is constant, $\alpha = 4.5 \times 10^{-6}$.

The calculated stress is then projected onto the twelve primary crystallographic slip systems. This projected stress (resolved shear stress) is compared to the critical-resolved shear stress (CRSS) for a given temperature at representative points in the crystal. The temperature-dependent critically resolved shear stress for undoped InP is given by Jordan [18]. This relationship is

$$\sigma_{\mathrm{CRSS}} = 2.133 \times 10^{5736/\theta}.$$

If the stress on the slip system at that point is less than the CRSS, then the plastic deformation will not occur in that slip system at that point. If the projected stress is greater than the CRSS then plastic slip will occur.

An analysis was carried out using the temperature field predicted by the code MASTRAPP [12]. Comparing with the experimental observations for wafer A, ten active slip systems were predicted by the model on the (1 1 1) plane. Nine correspond to those found experimentally in wafer A as summarized in Fig. 4. The tenth predicted active slip system was the $[1\,\bar{1}\,0]/(1\,1\,1)$ which is symmetrically related to the $[1\,\bar{1}\,0]/(1\,1\,\bar{1})$ (S_9 in Fig. 1) system which was observed in the experiment.

The dislocation density is taken to be related to the total excess resolved shear stress σ^{ex} defined as

$$\sigma^{\mathrm{ex}} = \sum_{i=1}^{N} \langle |\sigma_i| - \sigma_{\mathrm{CRSS}} \rangle,$$

Where σ_i is the resolve shear stress on slip system i, N is the number of slip systems and the angle bracket indicates a singularity function. Fig. 5 a shows a plot of the total excess-resolved shear stress on the (1 1 0) plane. The highest stresses are found near the outside surface, where the crystal emerges from the B_2O_3 layer. The stress distribution on the (0 0 1) plane, shown in Fig. 5b, corresponds to the 90° periodicity of the cubic structure. The excessive shear stress is highest along the $\langle 1\,0\,0\rangle$ and $\langle 0\,1\,0\rangle$ directions and lowest along the $\langle 1\,1\,0\rangle$ directions. This agrees with the dislocation density distribution observed in laterally sliced Fe-doped InP crystals as shown in Fig. 6.

4. Conclusions

Synchrotron white beam X-ray topography has been successfully applied to the nondestructive characterization of defect structures in MLEK-grown InP crystals. The conclusions include,

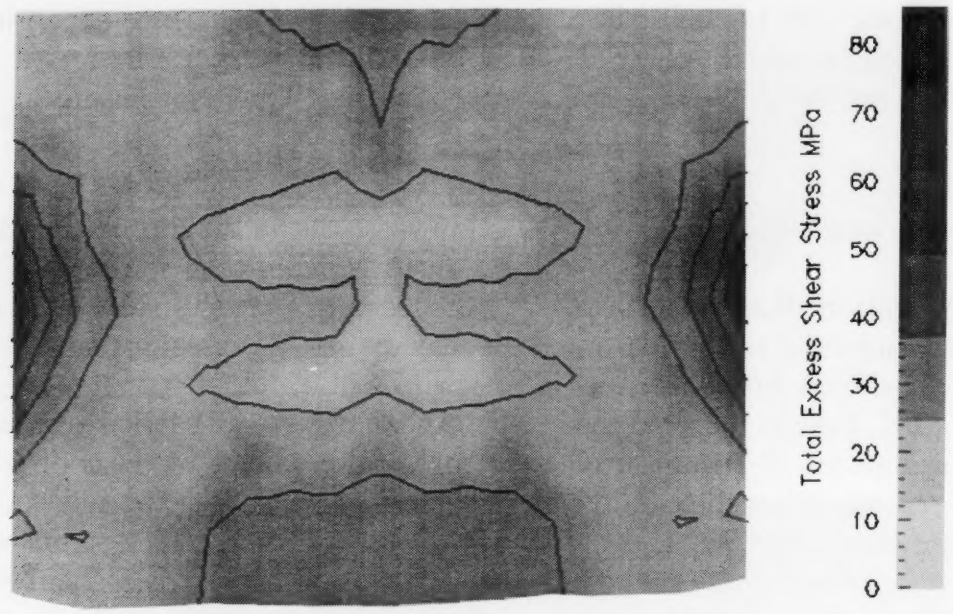

(a)

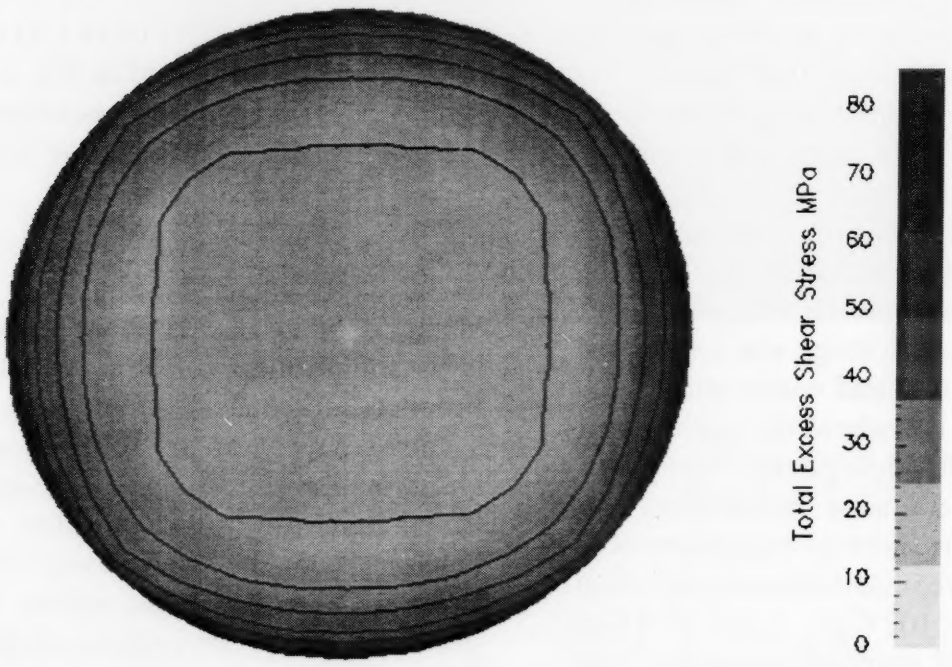

(b)

Fig. 5. (a) The distribution of the total excess resolved shear stress on the (0 1 0) plane through the center of the crystal subject to an intermediate growth stage temperature field; (b) The distribution of the total excess resolved shear stress on the (0 0 1) plane through the middle of the crystal subject to an intermediate growth stage temperature field.

1. X-ray topographs revealed that the lattice distortions associated with growth striations are normal to the growth front. The choice of correct orientation of the active reciprocal lattice vector with respect to the interface plane is important to maximize the visibility of growth interfaces.
2. The most likely origin for slip bands can be attributed to relieve large thermal stresses generated when the crystal is pulled from the encapsulant. X-ray topographic studies reveals that nine of the twelve possible $\langle 1\,1\,0\rangle/\{1\,1\,1\}$ systems are activated at different stages of the growth process.

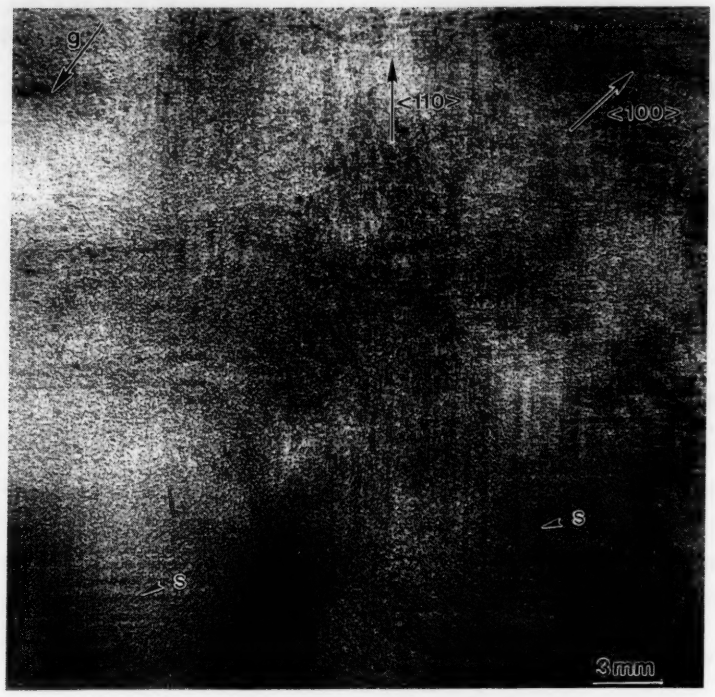

Fig. 6. Transmission X-ray topograph ($\boldsymbol{g} = \bar{4}\,0\,0, \lambda = 0.45$ Å) recorded from a wafer sliced laterally from a Fe-doped InP crystal showing the fourfold symmetric distribution of dislocations.

3. Large Fe precipitates were found when magnetic field used for melt stabilization was not applied. No formation of large precipitates was discernible in both the initial and intermediate growth stages. However, the formation of a very high density of dislocations in these regions obscured a detailed observation of precipitate distributions. Studies of dopant distributions in crystals with higher structural perfection are required to evaluate in more detail the effect of magnetic fields on dopant incorporation.
4. A thermal-elastic finite element stress analysis for an intermediate growth stage shows good agreement with the observed slip system activity and with the observed fourfold symmetry of the dislocation distribution.

Acknowledgements

This work was supported by DARPA/AFOSR Consortium of Crystal Growth Research under the contract F496209510407. Topography was carried out at the Stony Brook Synchrotron Topography Facility, Beamline X-19C, at the National Synchrotron Light Source, at Brookhaven National Laboratory, which is supported by the Department of Energy.

References

[1] M. Azzaz, J. Michel, A. George, Philos. Mag. A 69 (1994) 903.
[2] D.F. Bliss, R.M. Hilton, J.A. Adamski, J. Crystal Growth 128 (1993) 451.
[3] R.W. Series, D.T.J. Hurle, J. Crystal Growth 113 (1991) 305.
[4] G. Jacob, J. Crystal Growth 58 (1982) 455.
[5] A. Huber, N.T. Linh, J. Crystal Growth 29 (1975) 80.
[6] S. Mahajan, A.K. Chin, J. Crystal Growth 54 (1981) 138.
[7] S. Tohno, A. Katsui, J. Crystal Growth 74 (1986) 362.
[8] M. Dudley, Applications of synchrotron radiation techniques to materials science, in: D.L. Perry, R.L. Stockbauer, N.D. Shinn, K.L. D'Amico, L.J. Terminello (Eds.), Mater. Res. Soc. Symp. Proc., vol. 307, Pittsburgh PA, 1993, p. 213.
[9] M. Dudley, in: D. Bloor, R.J. Brook, M.C. Flemings, S. Mahajan (Eds.), Encyclopedia of Advanced Materials, vol. 4, Pergamon, Oxford, 1994, p. 2950.
[10] H. Chung, W. Si, M. Dudley, A. Anselmo, D.F. Bliss, A. Maniatty, H. Zhang, V. Prasad, J. Crystal Growth 174 (1997) 230.
[11] S. Wang, M. Dudley, W. Huang, C.H. Carter Jr, V.F. Tsvetkov, C. Fazi, in: W.M. Bullis, D.G. Seiler, A.C. Diebold (Eds.), Semiconductor Characterization Present Status and Future Needs, AIP, New York, 1996, p. 278.
[12] H. Zhang, V. Prasad, D.F. Bliss, J. Crystal Growth (1997), in press.
[13] Y.F. Zou, G.-X. Wang, H. Zhang, V. Prasad, D.F. Bliss, J. Crystal Growth, submitted.
[14] A. Authier, A.R. Lang, J. Appl. Phys. 35 (1964) 1956.
[15] J. Wu, T. Fanning, M. Dudley, V. Shastry, P. Anderson, Defect engineering in semiconductor growth, processing and device technology, in: S. Ashok, J. Chevallier, K. Sumino, E. Weber (Eds.), Mater. Res. Soc. Symp. Proc., vol. 262, Pittsburgh PA, 1993, p. 265.
[16] S. Adachi, J. Brice (Eds.), Properties of Indium Phosphide, INSPEC, The Institution of Electrical Engineerings, New York, 1991.
[17] V.M. Glazov, K. Davletov, A. Ya Nashel'skii, M.M. Mamedov, Russ. J. Phys. Chem. 51 (1977) 1496.
[18] A.S. Jordan, G.T. Brown, B. Cockayne, D. Brasen, W.A. Bonner, J. Appl. Phys. 58 (1985) 4383.

ELSEVIER

Journal of Crystal Growth 181 (1997) 26–32

JOURNAL OF CRYSTAL GROWTH

Silicon doping of InGaAs grown by MOVPE using tertiarybutylarsine

X.G. Xu[a,*], Ch. Giesen[a], J. Xu[b], M. Heuken[a], K. Heime[a]

[a] *Institut für Halbleitertechnik, RWTH Aachen, Templergraben 55, D-52056 Aachen, Germany*
[b] *Physikalisches Institut der RWTH Aachen, Templergraben 55, D-52056 Aachen, Germany*

Received 21 January 1997; accepted 19 March 1997

Abstract

Silicon doping of InGaAs with disilane by low pressure metalorganic vapor phase epitaxy (MOVPE) using tertiarybutylarsine (TBAs) as the group V source has been investigated. The dependence of carrier concentration on the substrate temperature, V/III ratio and reactor pressure was studied. The carrier concentration increases linearly with the ratio of molar fraction of disilane to group III sources. The doping efficiency depends not only on the substrate temperature, but also on the reactor pressure and on the carrier gas velocity. Apparent activation energies of 1.1, 1.4, 2.0 eV were observed at reactor pressures of 100, 40, 20 mbar for substrate temperatures between 590°C and 640°C. The doping efficiency increases with increasing V/III ratio at a substrate temperature of 590°C, and decreases slightly at 640°C. Possible dopant incorporation mechanism was discussed. Silicon doping efficiency is about two times higher by using TBAs instead of arsine.

PACS: 68.55.Ce; 81.15.Gh; 68.55.Ln

Keywords: MOVPE; InGaAs/InP; Si_2H_6; TBAs

1. Introduction

Alternative arsenic precursors used in MOVPE, mostly arsenic alkyls, have attracted increasing attentions in recent years [1, 2]. Among them, tertiarybutylarsine (TBAs) has shown to be a promising substitute for arsine, which is a highly toxic gas. Quantum wells, superlattices and laser diodes in the wavelength region of 1.3 μm have been grown by using TBAs and the results are comparable to those using arsine [3–7]. Compared with AsH_3, TBAs usually offers higher doping efficiency and better doping uniformity [8]. In addition, TBAs pyrolyzes more efficiently at low temperatures than AsH_3. The doping behavior in the low temperature region can be investigated using TBAs.

Silicon has been used as a n-type dopant in many binary, ternary, and quaternary semiconductors, such as GaAs, InP, AlGaAs, AlGaInP, and GaInAsP. Compared with other donor impurities,

* Corresponding author. Fax: + 49 241 8888 199; e-mail: mailbox@iht.rwth-aachen.de.

0022-0248/97/$17.00 © 1997 Elsevier Science B.V. All rights reserved
PII S0022-0248(97)00245-5

such as sulfur [9], selenium [10], tin [11], silicon has a low volatility in the vapor phase and a low diffusion coefficient in epilayers at typical MOVPE growth conditions, which are particularly suitable for device fabrication. The doping can be accomplished by using either silane (SiH_4) or disilane (Si_2H_6). Compared to silane, disilane decomposes at a lower temperature, and thus gives higher doping efficiency. Since the pioneering research of Kuech et al. [12] on the silicon doping of GaAs with disilane, a number of publications have been devoted to understand the doping mechanism, using either TBAs or AsH_3 [8, 13–19]. Recent results show that silicon incorporation is controlled by gas phase formation of silylene (SiH_2) and its subsequent diffusion to the surface. Homogeneous reactions dominate the doping process [8, 16].

Although there have been many reports on silicon doping of GaAs, there are only few reports on the silicon doping of InGaAs. Woelk and Beneking [20] reported the silicon doping of InGaAs using Si_2H_6 and AsH_3, and the doping efficiency of Si_2H_6 is more than a factor of 10 lower for InGaAs compared with InP. No systematic study of silicon doping of InGaAs using TBAs is available. Compared to GaAs, InGaAs lattice matched to InP offers another material system to study the doping process in MOVPE. The results may help to clarify the doping mechanism in MOVPE. n-type InGaAs layer is also an important material, which is usually used in microelectronics devices, such as high electron mobility transistors and heterojunction bipolar transistors. In this paper, we report the silicon doping of InGaAs lattice matched to InP grown by LP-MOVPE using TBAs. The effects of growth temperature, V/III ratio and reactor pressure on silicon doping efficiency were investigated.

2. Experimental procedure

Because the aim of this study was primarily to investigate the influence of growth parameters on silicon doping behavior, we concentrated in our experiments on the growth conditions to achieve doping concentrations greater than $\sim 10^{18}\,cm^3$. Lower doping levels could be achieved by reducing the ratio of gas-phase molar fraction of disilane to group III sources. Growth was carried out in a horizontal low pressure MOVPE system with a rectangular cross-section quartz reactor cell [21]. Pd-diffused hydrogen with a total flow of 6.8 SLM served as the carrier gas. A total flow of 3.6 SLM at a reactor pressure of 20 mbar was used to investigate the influence of carrier gas flow on doping efficiency, and the corresponding gas velocity is 1.20 m/s. Trimethylindium (TMIn), triethylgallium (TEGa), trimethylgallium (TMGa), TBAs, tertiarybutylphosphine (TBP), AsH_3 and PH_3 were used as source materials. TMGa, AsH_3 and PH_3 were used for comparison. n-type doping was accomplished by using disilane (100 ppm in H_2). The graphite susceptor was heated by means of five quartz halogen lamps. The substrate temperature was varied from 575°C to 640°C, which is the typical growth temperature region for InGaAs. Growth rate was about 1.3 μm/h. Substrates were exactly (0 0 1) oriented InP (Fe doped) wafers. They were cleaned in organic solutions, deionized water, etched in $H_2SO_4 : H_2O_2 : H_2O$ (3 : 1 : 1), and HF (4%). Immediately after cleaning, the substrate was transferred into the reactor.

The surface morphology was observed by phase-contrast optical microscopy and scanning electron microscopy (SEM). The structural quality of epilayers was characterized by high resolution X-ray diffraction. The layer mismatch was restricted to the range of less than $\pm 1 \times 10^{-3}$. Hall effect measurements of uniformly doped epilayers were carried out by using the standard van der Pauw method. In order to clarify the influence of growth conditions on silicon incorporation, epilayers with a multilayer structure were grown by varying either the gas phase mole ratio of disilane to group III sources, the substrate temperature, or the V/III ratio while keeping other parameters unchanged. Carrier concentration of those epilayers was measured by electrochemical C–V depth profiling. The etched depth was corrected by measuring the depth using a mechanical profile.

3. Results

All the layers grown in this study exhibit a smooth surface morphology. The growth rate of

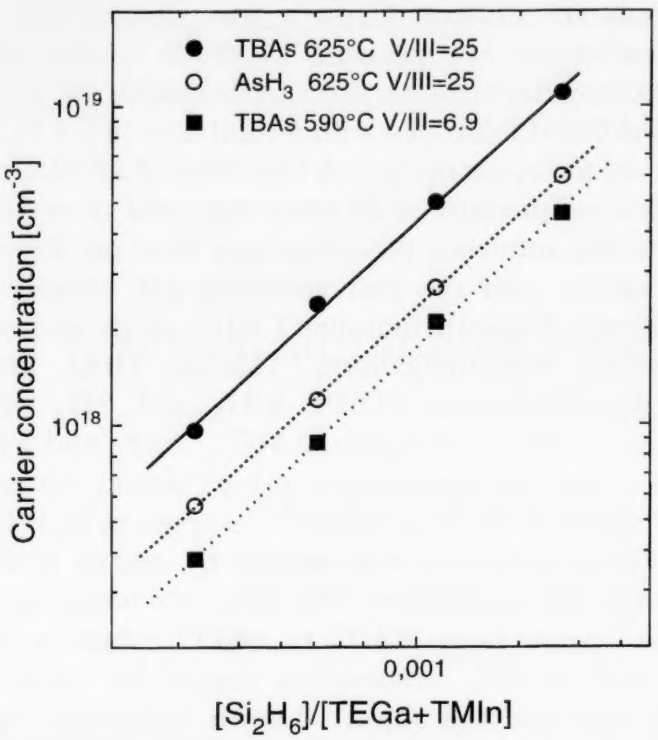

Fig. 1. The dependence of carrier concentration on the ratio of molar fraction of Si_2H_6 to group III sources.

bulk InGaAs layers does not depend on the substrate temperature in the region 530–650°C.

3.1. Dependence of silicon incorporation on the disilane flow rate

The dependence of carrier concentration on the ratio of gas-phase molar fraction of disilane to group III sources is shown in Fig. 1. The reactor pressure was 40 mbar with a total H_2 flow of 6.8 SLM. The lines are apparent linear fittings to the experimental results. The slopes are about one. The linear relationship does not change with the substrate temperature, V/III ratio, reactor pressure, group V sources, TBAs or arsine. This character is a common feature of silicon doping, and is also observed in GaAs and InP binary compounds [16, 22].

The efficiency of silicon doping can be described by using the distribution coefficient, which is the ratio of gas-phase and solid-phase atomic concentrations of silicon normalized to the group III atomic concentrations in the gas and solid phases, respectively. At a substrate temperature of 625°C and a V/III ratio of 25, the distribution coefficients of silicon using TBAs and arsine are about 0.2 and 0.1, respectively. Silicon doping efficiency is about two times higher by using TBAs instead of arsine. The distribution coefficient is reduced to 0.09 using TBAs at 590°C with a V/III ratio of 6.9. The influence of the V/III ratio and the substrate temperature is described separately in the following section.

3.2. Dependence of doping characteristic on the V/III ratio

Fig. 2 shows the dependence of carrier concentration on the V/III ratio. The ratio of molar fraction of disilane to group III sources was kept constant at 1.1×10^{-3}. The reactor pressure was 40 mbar, and the total H_2 flow was 6.8 SLM. At a substrate temperature of 590°C, the dependences on V/III ratio using TBAs and AsH_3 show a similar relationship. The doping efficiency increases with increasing V/III ratio for both TBAs and AsH_3.

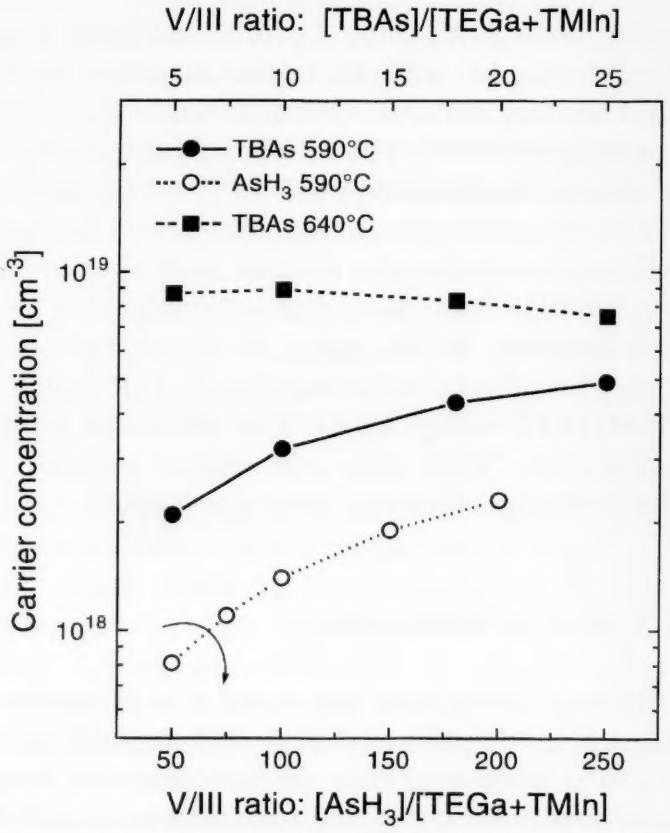

Fig. 2. The dependence of carrier concentration on the V/III ratios. AsH_3 was used for comparison at a substrate temperature of 590°C.

Although the V/III ratios using AsH_3 were ten times higher than that using TBAs, the distribution coefficient using AsH_3 was still about 2.5 times lower than those using TBAs. But it is more important that the dependence on V/III ratio using TBAs changes with substrate temperatures. At a substrate temperature of 640°C, the dependence becomes weaker, and a slight decrease of the carrier concentration from 8.7×10^{18} to 7.5×10^{18} cm^3 is observed. The distribution coefficient is about 0.37, which is comparable to disilane doping of GaAs [8, 13, 15–17]. The different dependences of doping efficiency on V/III ratios using TBAs imply that TBAs plays different roles at high and low substrate temperatures. The effective dopant reactants responsible for silicon incorporation must be related to TBAs. The influence of growth parameters on doping efficiency was investigated by using TBAs as the group V source in the following sections.

3.3. The influence of reactor pressure at the same carrier gas flow

Fig. 3 shows the dependence of carrier concentration on the substrate temperature at a reactor pressure of 100 and 20 mbar, respectively. V/III ratio and the ratio of molar fraction of disilane to the group III sources were kept at 13 and 1.1×10^{-3}, respectively. The total H_2 flow was 6.8 SLM. The higher the reactor pressure, the higher the doping efficiency. At a reactor pressure of 100 mbar, the distribution coefficient increases from 0.2 to 0.5 as the substrate temperature increases from 590°C to 640°C. But at a reactor pressure of 20 mbar, it changes from 0.04 to 0.2 as the substrate temperature increases. If the reactor pressure increases from 20 to 100 mbar, the doping efficiency increases by a factor of 4 at 590°C and a factor of 2.5 at 640°C. The difference increases in the low growth temperature region [16, 17]. The apparent activation energies estimated from the slopes in Fig. 3 are 1.1 and 2.0 eV for a reactor pressure of 100 and 20 mbar, respectively. The lines are the Arrhenius fitting to the experimental data except those data at 575°C, which are always higher than expected from the fitting.

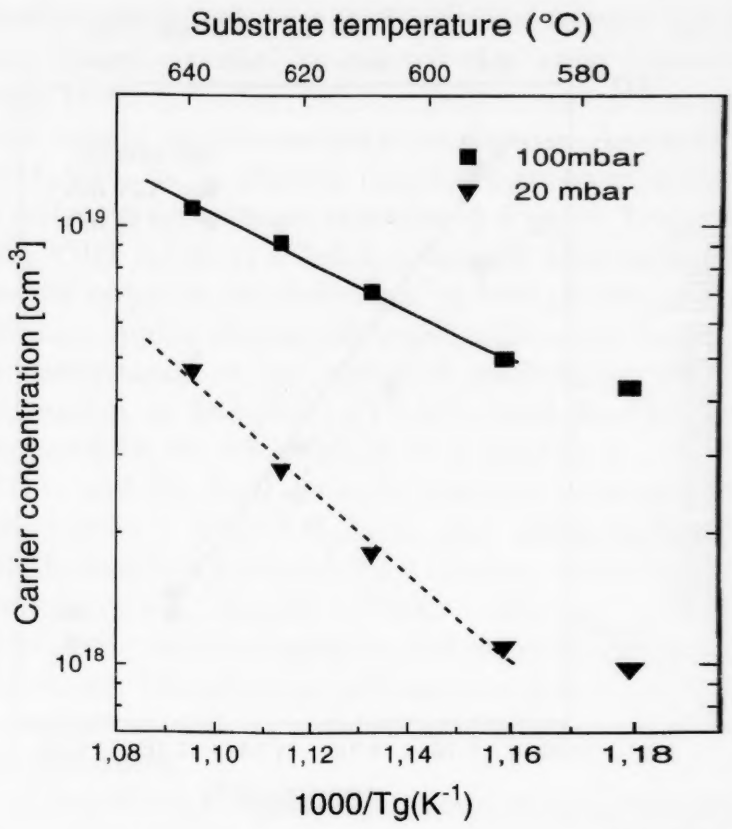

Fig. 3. The dependence of carrier concentration on the substrate temperature at reactor pressures of 100 and 20 mbar. Carrier gas flow is 6.8 SLM. TBAs is the group V source.

3.4. The influence of carrier gas velocity at the same reactor pressure

Both reactor pressure and carrier gas velocity have influence on the silicon doping efficiency [16]. Carrier gas velocity can be enlarged by either increasing the total carrier gas flow or by reducing the reactor pressure. It is necessary to identify the influence of the reactor pressure and the carrier gas velocity separately. In our reactor, the growth rate has a strong dependence on the total carrier gas flow. Growth rate increases as the carrier gas flow is reduced. Therefore, if the total gas flow was changed, the input molar flow of the source materials was adjusted to give a similar growth rate while the V/III ratio and the ratio of molar fraction of disilane to group III sources were kept unchanged.

Fig. 4 shows the dependence of carrier concentration on the substrate temperature at a reactor pressure of 20 mbar with a total carrier gas flow of 3.6 and 6.8 SLM, respectively. The corresponding

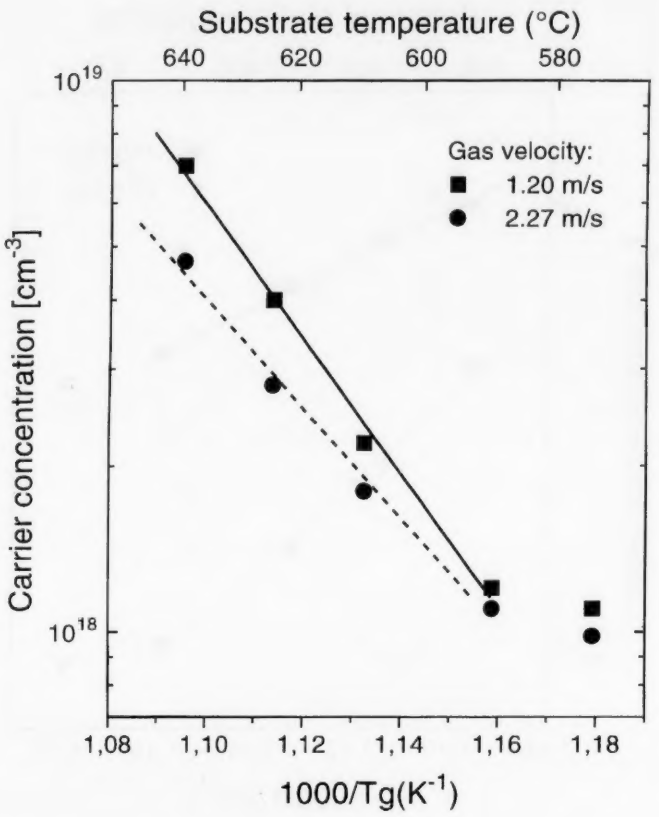

Fig. 4. The dependence of carrier concentration on the substrate temperature at a carrier gas velocity of 1.20 and 2.27 m/s. The reactor pressure is 20 mbar. TBAs is the group V source.

carrier gas velocities are 1.20 and 2.27 m/s, at room temperature. The apparent activation energy for the total gas flow of 3.6 SLM is 2.4 eV. The influence of carrier gas velocity on the doping efficiency shows different behaviors at a substrate temperature of 640°C and 590°C.

At a substrate temperature of 640°C, doping efficiency decreases with increasing gas velocity. This is a typical behavior of silicon doping with disilane which is determined by homogeneous reactions [8, 16]. As the carrier gas velocity increases, the residence time of reactants above the susceptor is reduced, and thus, the products of gas phase homogeneous reactions are reduced.

As the substrate temperature is reduced, the influence of gas velocity on doping efficiency becomes smaller. If the substrate temperature is reduced to 590°C, doping efficiency has little dependence on gas velocity. This implies that at a substrate temperature of 590°C, the doping process is mainly controlled by heterogeneous reactions, which is typically not sensitive to carrier gas velocity [8].

3.5. The influence of reactor pressure at similar carrier gas velocity

As mentioned above, both reactor pressure and carrier gas velocity have effects on doping efficiency. The results of the influence of reactor pressures at similar carrier gas velocity is displayed in Fig. 5. The reactor pressures are 20 and 40 mbar with a total carrier gas flow of 3.6 and 6.8 SLM, respectively. The corresponding carrier gas velocities are 1.20 and 1.13 m/s, at room temperature. The apparent activation energy for the reactor pressure of 40 mbar with total flow of 6.8 SLM is 1.4 eV. Similar apparent activation energies are obtained if TMGa is used instead of TEGa.

The influence of the reactor pressure on doping efficiency enhances at lower substrate temperatures. The absorption and desorption rates of effective reactants from the surface depend strongly on the reactor pressure. Thus, it indicates that surface process of silicon incorporation plays an important role in the low temperature region.

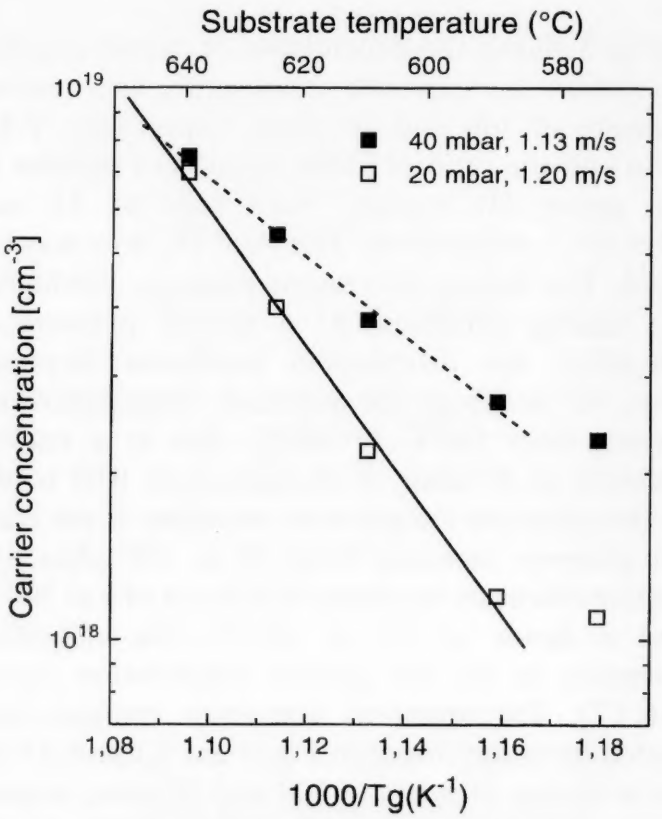

Fig. 5. The dependence of carrier concentration on the substrate temperature at a reactor pressure of 40 and 20 mbar with the carrier gas velocity of 1.13 and 1.20 m/s, respectively. TBAs is the group V source.

4. Discussion

Silicon doping efficient varies from 0.04 to 0.5 at different growth conditions, such as substrate temperature, V/III ratio and reactor pressure. Among them, the substrate temperature has a significant influence on silicon incorporation efficiency. At a substrate temperature of 640°C and a reactor pressure of 40 mbar, the distribution coefficient is about 0.37, which is comparable to silicon doping in GaAs with disilane [8, 13, 15–17].

Normally in MOVPE, the epitaxial growth process has different growth mechanisms in different temperature regions. At a moderate growth temperature, growth is controlled by mass transport, and at a lower growth temperature, it is controlled by kinetic processes. In our MOVPE reactor, the growth of InGaAs bulk layer is still mass transport limited at a substrate temperature of 530°C.

Silicon incorporation shows different behaviors at a substrate temperature of 640°C and 590°C. Doping efficiency shows a weaker relationship on the V/III ratio at 640°C. This is similar to those observed in silicon doping of GaAs with disilane [8, 12]. However, doping efficiency increases with increasing V/III ratio at 590°C. By comparing the differences of the apparent activation energies and carrier concentrations, it can be concluded that the gas velocity has a stronger influence on doping efficiency at 640°C than at 590°C, as shown in Fig. 4. In contrast, the reactor pressure has a much higher influence at 590°C than at 640°C, as shown in Fig. 5.

Comparing the results at a substrate temperature of 640°C with those at 590°C, we propose that there are two kinds of doping mechanism controlling the silicon incorporation process at high and low substrate temperature regions, respectively. At a substrate temperature above 640°C, silicon doping is mainly controlled by gas phase formation of SiH_2 and its subsequent diffusion to the surface. Homogeneous reactions dominate the doping process. This is similar to the doping process of GaAs with disilane. V/III ratio has no effects on the doping efficiency. At a substrate temperature below 590°C, another reactant, monosilylarsine (SiH_3AsH_2) dominates the silicon incorporation behavior. The formation rate of SiH_3AsH_2 near the substrate surface and its subsequent absorption to the growing layer by surface reaction is the rate limiting step. Heterogeneous reactions play a more important role in the low temperature region. Assuming SiH_3AsH_2 as an effective reactant can explain the V/III ratio dependence, as shown in Fig. 2. Increasing V/III ratios at a lower substrate temperature would enhance the formation of SiH_3AsH_2, thus giving a higher doping efficiency, although there is a discrepancy in the chemical pathway of the formation of SiH_3AsH_2 [13, 23]. SiH_3AsH_2 was detected in the co-pyrolysis of a mixture of 3% TBAs and 3% Si_2H_6 in a H_2 ambient using mass spectrometry [23]. SiH_3AsH_2 was detected after Si_2H_6 begins to pyrolyze and it reaches a maximum concentration around 550°C. Above 550°C, SiH_3AsH_2 becomes unstable and its concentration decreases. Therefore, its influence on silicon incorporation should be reduced at higher substrate temperatures.

From the above analysis, it is easy to explain the discrepancy in the apparent activation energies, shown in Figs. 3–5. The highest activation energy is 2.4 eV, observed at a reactor pressure of 20 mbar with a gas velocity of 1.20 m/s. In the temperature region from 640°C to 590°C, both homogeneous and heterogeneous reactions contribute to the doping process. The smaller the gas velocity at 640°C, the higher the doping efficiency. The lower the reactor pressure at 590°C, the lower the doping efficiency. Therefore, at a fixed reactor pressure, smaller gas velocities will give a higher activation energy. At the same gas velocity, higher reactor pressure will give a smaller activation energy. It is difficult to explain the nature of the activation energy since there are two kinds of effective reactants controlling the doping process.

The present model is not concerned with the group III precursors, and can also be applied to silicon doping in GaAs with disilane [8, 16].

5. Conclusion

In conclusion, silicon doping of InGaAs grown by MOVPE using TBAs as the group V source was studied. The dependences of carrier concentration on the substrate temperature, V/III ratio and

reactor pressure were investigated in detail. The carrier concentration increases linearly with the ratio of molar fraction of disilane to group III sources. The doping efficiency of silicon in InGaAs lattice matched to InP is comparable to that in GaAs. Si doping efficiency is about two times higher by using TBAs instead of arsine. The doping efficiency depends not only on the growth temperature but also on the reactor pressure and on the carrier gas velocity. The effective reactants in the silicon incorporation process depend on the substrate temperature. At a substrate temperature above 640°C, the doping process is mainly controlled by gas-phase formation and diffusion of SiH_2 and its succeeding incorporation into the growing layer, while at a substrate temperature below 590°C, silicon doping is mainly dominated by the formation of SiH_3AsH_2 and its subsequent surface reaction.

Acknowledgements

X.G. Xu would like to acknowledge the support from Alexander von Humboldt foundation. The financial support from the Bundesministerium für Bildung, Forschung und Wissenschaft (01 BM 406/8) is gratefully acknowledged.

References

[1] A.C. Jones, J. Crystal Growth 129 (1993) 728.
[2] J. Komeno, J. Crystal Growth 145 (1994) 468.
[3] A.L. Holmes, M.E. Heimbuch, G. Fish, L.A. Coldren, S.P. Denbaars, J. Electronic Mater. 25 (1996) 965.
[4] J. Weber, A. Nowitzki, I. Gyuro, J. Scherb, in: Proc. 8th Internat. Conf. on InP and Related Materials, Germany, April 1996.
[5] S. Ae, T. Terakado, T. Nakamura, T. Torikai, T. Uji, J. Crystal Growth 145 (1994) 852.
[6] Y. Sakata, T. Nakamura, S. Ae, T. Terakado, Y. Inomoto, T. Torikai, H. Hasumi, J. Electronic Mater. 25 (1996) 401.
[7] S.P. Watkins, M.K. Nissen, G. Haacke, E.M. Handler, J. Appl. Phys. 72 (1992) 2797.
[8] J.M. Redwing, H. Simka, K.F. Jensen, T.F. Kuech, J. Crystal Growth 145 (1994) 397.
[9] R.A. Logan, T. Tanbun-Ek, A.M. Sergent, J. Appl. Phys. 65 (1989) 3723.
[10] T. Tsuchiya, H. Nagai, T. Meguro, H. Sakaguchi, J. Crystal Growth 145 (1994) 403.
[11] A.R. Clawson, C.M. Hanson, J. Electronic Mater. 20 (1991) 365.
[12] T.K. Kuech, B.S. Meyerson, E. Veuhoff, Appl. Phys. Lett. 44 (1984) 986.
[13] T. Kikkawa, H. Tanaka, J. Komeno, J. Electronic Mater. 21 (1992) 305, and references therein.
[14] P.R. Hageman, X. Tang, M.H.J.M. de Croon, L.J. Giling, J. Crystal Growth 98 (1989) 249.
[15] H. Sakaguchi, R. Suzuki, T. Meguro, J. Crystal Growth 93 (1988) 602.
[16] Harry K. Moffat, T.F. Kuech, K.F. Jensen, P.J. Wang, J. Crystal Growth 93 (1988) 594.
[17] M. Shimazu, K. Kamon, K. Kimura, M. Mashita, M. Mihara, M. Ishii, J. Crystal Growth 83 (1987) 327.
[18] S. Chichibu, A. Iwai, S. Matsumoto, Appl. Phys. Lett. 60 (1992) 489.
[19] N. Furuhata, K. Kakimoto, M. Yoshida, T. Kamejima, J. Appl. Phys. 64 (1988) 4692.
[20] E. Woelk, H. Beneking, J. Appl. Phys. 63 (1988) 2874.
[21] R. Hövel, W. Brysch, N. Neumann, K. Heime, L. Pohl, J. Crystal Growth 124 (1992) 106.
[22] B. Rose, C. Kazmierski, D. Kobein, Y. Gao, J. Crystal Growth 94 (1989) 762.
[23] J.M. Redwing, T.F. Kuech, D. Saulys, D.F. Gaines, J. Crystal Growth 135 (1994) 423.

ELSEVIER

Journal of Crystal Growth 181 (1997) 33–40

JOURNAL OF CRYSTAL GROWTH

Carbon and silicon doping in GaAs and AlAs grown on (3 1 1)-oriented GaAs substrates by metalorganic chemical vapor deposition

Kouta Tateno*, Chikara Amano

NTT Optoelectronics Laboratories, 3-1 Morinosato-Wakamiya, Atsugi-shi, Kanagawa 243-01, Japan

Received 20 March 1997

Abstract

We have investigated carbon (C) and silicon (Si) doping characteristics in GaAs and AlAs grown on (3 1 1)A and (3 1 1)B-oriented GaAs substrates by metalorganic chemical vapor deposition (MOCVD) and compared them to those on (1 0 0)-oriented substrates. For C doping in both GaAs and AlAs with CBr_4, the order of the hole concentration is (3 1 1)A $\geqslant$ (1 0 0) > (3 1 1)B at V/III < 60. Hole concentration decreases with increasing V/III ratio for all the cases. It decreases with increasing growth temperature except for AlAs on (3 1 1)B, in which case it increases with increasing growth temperature. For AlAs on (3 1 1)B, surface morphology is improved by increasing growth temperature, decreasing V/III ratio and increasing CBr_4 flow rate due to the enhancement of the two-dimensional growth mode. For GaAs on (3 1 1)B, disk-like structures appear at $T_g = 750°C$ and V/III = 15. For Si doping in both GaAs and AlAs with SiH_4, the order of electron concentration is (3 1 1)B > (1 0 0) > (3 1 1)A. Electron concentration in AlAs on (3 1 1)B is about one order of magnitude higher than that on (1 0 0), while the Si-doped AlAs on (3 1 1)A exhibits p-type conductivity. For both dopants, AlAs shows apparent dependence compared with GaAs because of its reactivity but the tendencies are almost same as GaAs.

PACS: 61.72.Vv; 68.55. – a

Keywords: Carbon; Silicon; Doping; MOCVD; GaAs; AlAs; CBr_4; SiH_4

1. Introduction

GaAs-based growth on non-(1 0 0)-oriented substrates such as (3 1 1) and (1 1 1) substrates has been continuously investigated by many workers in order to improve device performance or to find some interesting phenomena. For example, vertical cavity surface emitting lasers (VCSEL) on (3 1 1)A and (3 1 1)B show stable polarization along $[\bar{2}\ 3\ 3]$ and $[\bar{2}\ 3\ \bar{3}]$ [1, 2]. Crystallographic orientation of the substrate changes not only physical characteristics such as the anisotropic optical gain in VCSEL on (3 1 1) substrates but also chemical

* Corresponding author. Fax: + 81 462 40 3259; e-mail: tateno@aecl.ntt.co.jp.

0022-0248/97/$17.00 © 1997 Elsevier Science B.V. All rights reserved
PII S0022-0248(97)00218-2

characteristics which are related to the growth mode or quality of epi-layers on the surface. This results from the different surface state; on (n 1 1) substrates, surface polarity, which designated A and B, exists and the number of single and double dangling bonds is different from that on (1 0 0) [3–10]. VCSEL growth on (n 1 1) substrates is expected to be difficult due to a large change of growth conditions compared to (1 0 0). Regarding VCSELs on (3 1 1) substrates, devices on (3 1 1)A and (3 1 1)B grown by molecular beam epitaxy (MBE) have been reported, but their lasing characteristics are not as good as those on (1 0 0) [1, 2]. Therefore, it is interesting to examine whether the performance of VCSELs on (3 1 1) substrates can be improved by metalorganic chemical vapor deposition (MOCVD). Furthermore, on a (3 1 1)B substrate, orderly InGaAs disks have recently been reported, which are formed during the growth interruption of MOCVD [3]. These disks offer the possibility of zeroth quantum confinement and are expected to improve laser characteristics.

Carbon has been widely used as a p-type dopant in GaAs-based optical and electronic devices. Owing to its low diffusion length and high doping efficiency, it is a useful dopant for the base layer of heterojunction bipolar transistors (HBTs) and for p-type distributed Bragg reflector (DBR) of VCSELs. There are typically two methods of carbon doping. One involves the use of alkyl radicals in group-III or V sources such as trimethylgallium (TMGa) and trimethylarsine (TMAs) and the other the introduction of C-contained species such as CCl_4 and CBr_4 independently. With the latter, it is easier to control the carbon concentration because it can be varied widely by adjusting the flow rate without changing other growth conditions such as the growth temperature or V/III ratio. For C doping in GaAs on non-(1 0 0)-oriented substrates, there have been several studies in which TMGa and TMAl [4, 5] and CCl_4 [6] were used. Recently, CBr_4 has been used more widely than CCl_4 because CBr_4 has fewer adverse environmental effects; however, the doping characteristics on (3 1 1) substrates have not yet been reported. On the other hand, for Si doping, a relatively large number of works on orientation dependence in GaAs have been reported [7–10]; however the doping characteristics of AlAs on (3 1 1) substrates have not yet been reported.

Previously, we have investigated C doping and the etching effects of CBr_4 on (1 0 0) substrates [11]. This time we have systematically examined C and Si doping of GaAs and AlAs grown on (3 1 1)A, (3 1 1)B and (1 0 0)-oriented substrates, and considered the doping mechanisms on these substrates.

2. Experimental procedure

The growth was carried out in a horizontal MOCVD reactor at 76 Torr [11, 12]. TMGa and trimethylaluminum (TMAl) were the group-III sources and 100% AsH_3 the group-V source. C and Si doping sources were CBr_4 and SiH_4, respectively. The carrier gas was palladium-diffused H_2 and the flow rate was 6.0 l/min. The growth rates for GaAs and AlAs were both about 3.0 μm/h. The CBr_4 bubbler was maintained at 30°C, where the flow was varied from 10^{-7} to 10^{-5} mol/min. One-hundred ppm SiH_4 was used for Si doping and its flow rate was varied from 10^{-8} to 10^{-6} mol/min. One-μm thick C-doped and Si-doped GaAs and AlAs layers were grown on undoped or CrO-doped semi-insulating GaAs(1 0 0), (3 1 1)A and (3 1 1)B substrates at the same time. Each AlAs layer was capped with a 200 Å non-doped GaAs layer in order to prevent surface oxidation. The growth temperature, V/III ratio and each flow rate were varied. The carrier concentration was measured at room temperature by the van der Pauw–Hall method. The surface morphology was measured by Nomarski interference contrast microscopy.

3. Results and discussion

3.1. C doping in GaAs and AlAs

3.1.1. CBr_4 flow rate dependence

Fig. 1a shows the hole concentration in GaAs and AlAs as a function of CBr_4 flow rate ([CBr_4]). The growth temperature (T_g) was kept at 650°C and the V/III at 60. The hole concentration increased linearly with increasing [CBr_4] in both

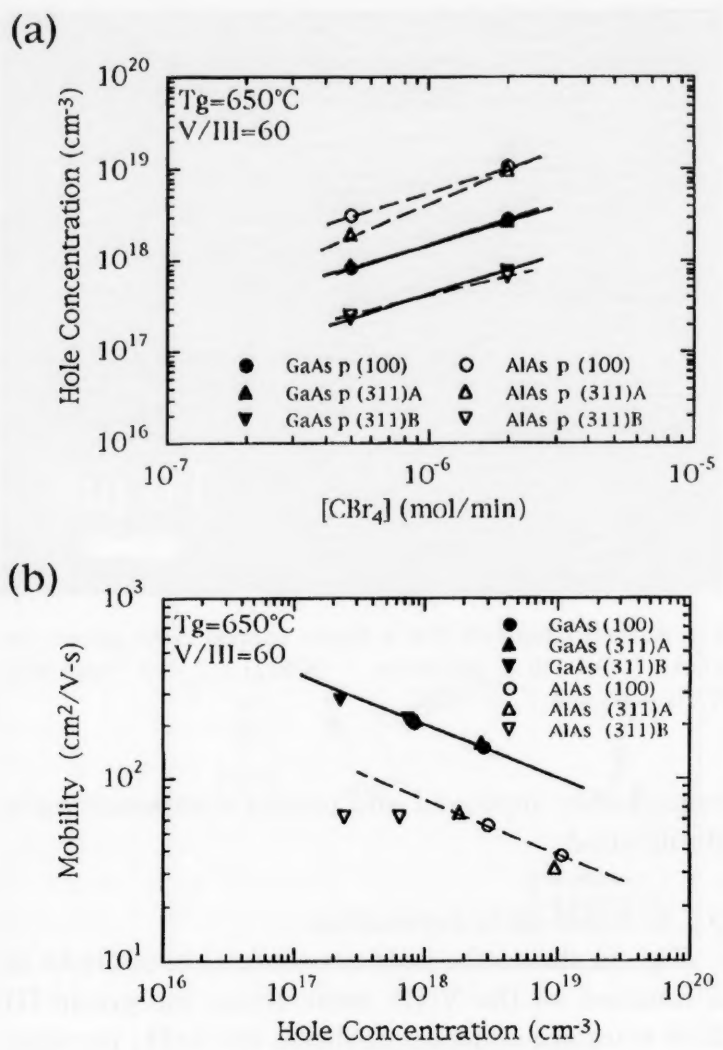

Fig. 1. (a) CBr_4 flow-rate ([CBr_4]) dependence of hole concentration in GaAs and AlAs. (b) Mobility as a function of hole concentration.

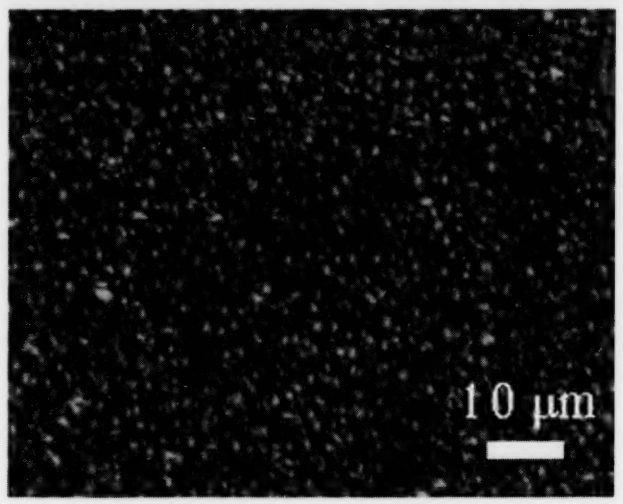

(a) [CBr_4] = 5×10^{-7} mol/min

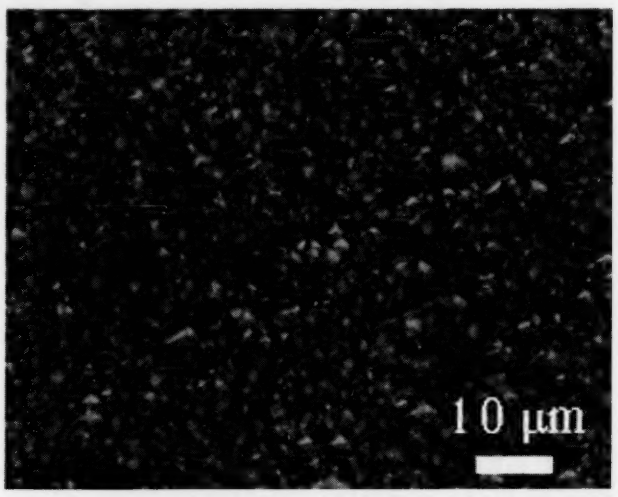

(b) [CBr_4] = 2×10^{-6} mol/min

Fig. 2. Photograph of 200 Å GaAs capped AlAs grown on GaAs (3 1 1)B substrate. V/III = 60 and $T_g = 650°C$.

GaAs and AlAs. In GaAs and AlAs, it is almost of the same order for both (1 0 0) and (3 1 1)A substrates. On the other hand, it is about $\frac{1}{4}$ for GaAs and $\frac{1}{10}$ for AlAs lower on (3 1 1)B substrate. It has been reported that p-type dopants such as Zn and C preferentially incorporate on A face regardless of their group [6, 9]. In our experiment, the hole concentration for (3 1 1)A was higher than for (3 1 1)B, which is consistent with the above findings. Fig. 1b shows mobility as a function of hole concentration. The results for GaAs are almost on the same line, while for AlAs, the results with (3 1 1)B are below those with (1 0 0) and (3 1 1)A. This suggests that the crystal quality of AlAs on (3 1 1)B was insufficient. Fig. 2 shows photographs of AlAs on (3 1 1)B at [CBr_4] of 5×10^{-7} and 2×10^{-6} mol/min. In this figure, laterally extended structures can be seen at the higher flow rate. A large increase of lateral growth rate by introducing CBr_4 has been reported by Kim et al. [13]. In a similar way, the two-dimensional growth mode is thought to be enhanced by increasing [CBr_4] owing to its etching effect. The promotion of two-dimensional growth is the key to improving surface morphology. As will be shown next, the most effective way to promote two-dimensional growth of AlAs on (3 1 1)B is to increase growth temperature.

3.1.2. Growth temperature dependence

Fig. 3a shows the hole concentration in GaAs and AlAs as a function of growth temperature at

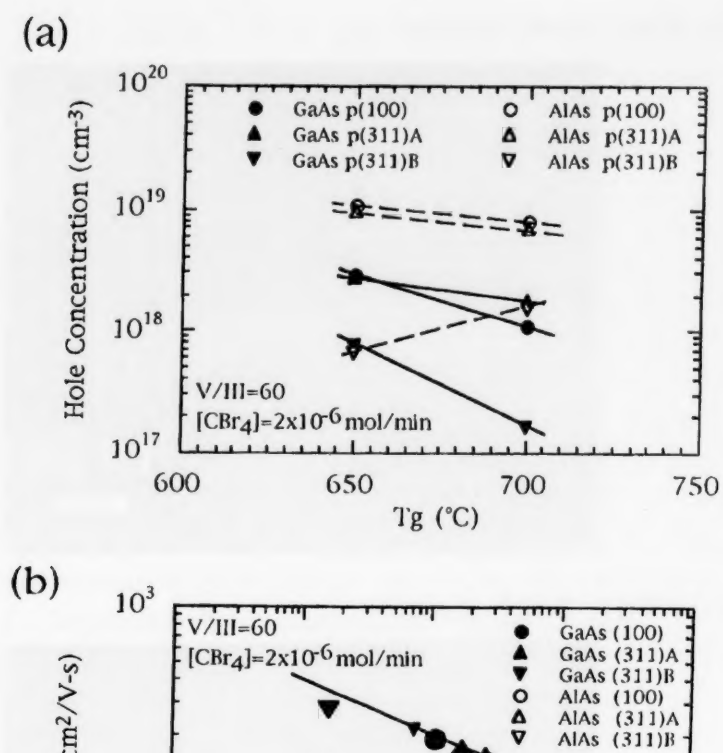

Fig. 3. (a) Growth temperature dependence of hole concentration in GaAs and AlAs. (b) Mobility as a function of hole concentration.

$[CBr_4]$ of 2×10^{-6} mol/min and V/III ratio of 60. For both (1 0 0) and (3 1 1)A, the hole concentration in GaAs and AlAs decreased similarly as the temperature was increased from 650°C to 700°C. For (3 1 1)B, it also decreased in GaAs, but it increased in AlAs. Fig. 3b shows mobilities as a function of hole concentration. The mobility of AlAs on (3 1 1)B locates below the level of AlAs on (1 0 0) and (3 1 1)A. Fig. 4 is a photograph of AlAs on (3 1 1)B at T_g of 700°C. Increasing the growth temperature considerably improved the AlAs surface morphology, although there are still some undulations. The reasons for the increase of hole concentration in AlAs on (3 1 1)B with increasing T_g are considered to be that the crystal quality is

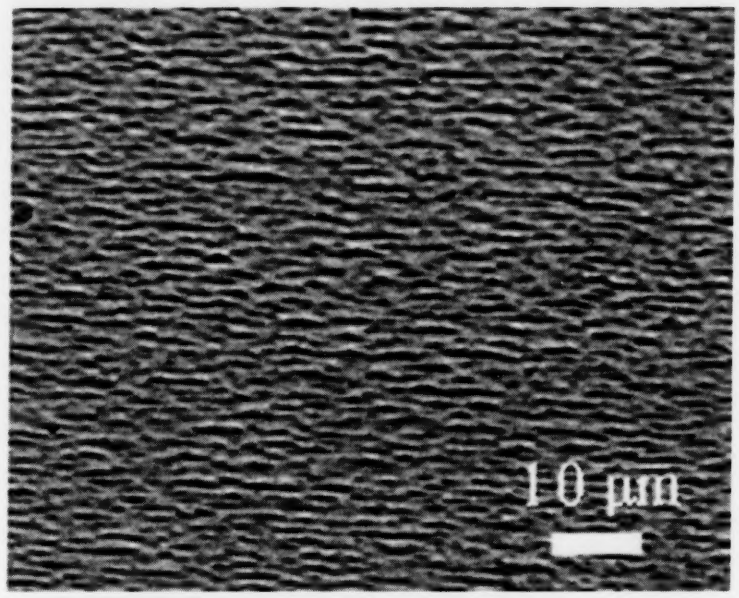

Fig. 4. Photograph of 200 Å GaAs capped AlAs grown on GaAs (3 1 1)B substrate. $[CBr_4] = 2 \times 10^{-6}$ mol/min, V/III = 60 and $T_g = 700°C$.

remarkably improved and carrier compensation is diminished.

3.1.3. V/III ratio dependence

Fig. 5a shows the hole concentration of GaAs as a function of the V/III ratio. Since the group-III flow rates are constant, it shows the AsH_3 pressure dependence. The $[CBr_4]$ was kept at 2×10^{-6} mol/min and the growth temperatures were 600–750°C. For all substrates, hole concentration increased with decreasing V/III ratio. This tendency is much more evident in GaAs on (3 1 1)A than on (1 0 0). At V/III = 15, GaAs on (3 1 1)B showed a drastical increase of hole concentration for T_g from 700°C to 600°C (about 50 times). Fig. 5b shows mobility as a function of hole concentration. For GaAs on (3 1 1)B, the mobility degraded with increasing T_g, which is contrary to the situation for AlAs on (3 1 1)B as mentioned above. Fig. 6 is a surface photograph of GaAs on (3 1 1)B at T_g of 750°C, V/III of 15 and $[CBr_4]$ of 2×10^{-6} mol/min. About 4 μm diameter disk-like structures can be seen in the photograph. They resemble the InGaAs disks on (3 1 1)B reported by Temmyo et al. [3]. These structures appear to influence the mobility of the GaAs epilayer on (3 1 1)B. And at higher temperature, GaAs is more thermodynamically stable and C atoms are excluded from

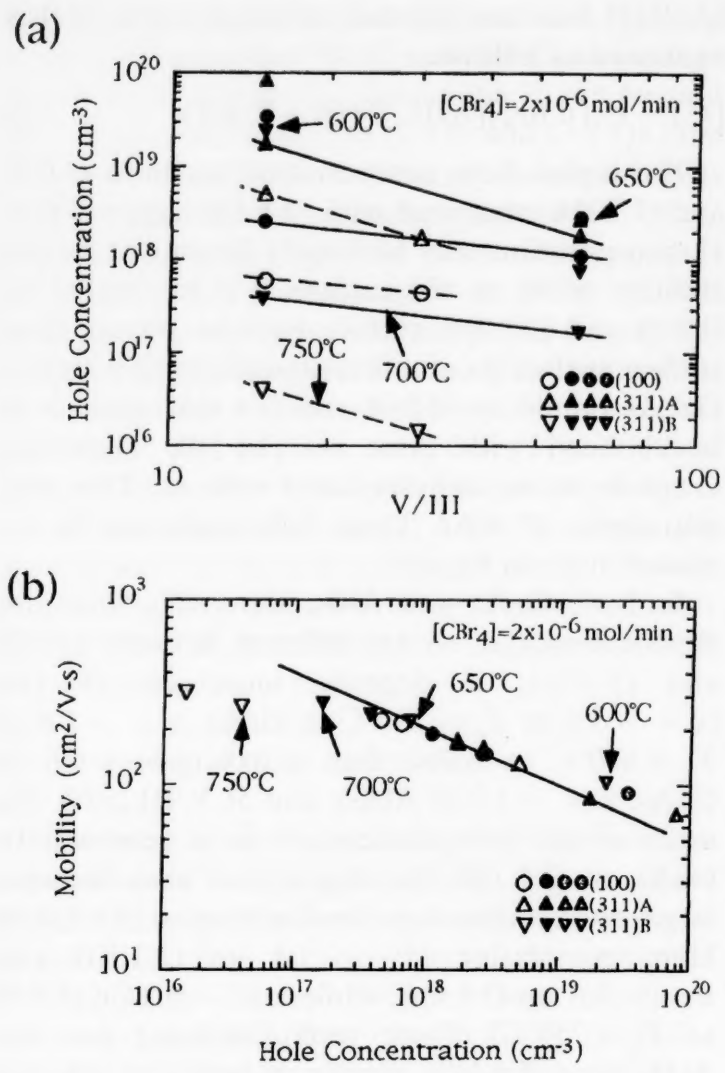

Fig. 5. (a) V/III ratio dependence of hole concentration in GaAs. (b) Mobility as a function of hole concentration.

As sites, which result in the large decrease of hole concentration. This explains the lower activation energy (negative value) as seen in Fig. 3. At 600°C, mobilities for all substrates distribute upward and are above the line for other temperatures. The reason for this is not clearly understood at present.

Fig. 7a shows the hole concentration in AlAs as a function of the V/III ratio. The $[CBr_4]$ was kept at 2×10^{-6} mol/min and the growth temperatures were 650°C, 700°C and 750°C. For (3 1 1)B, hole concentration increased with decreasing V/III ratio, which is similar to the situation on (1 0 0). Here, it is found that at V/III > 60, the hole concentration for (1 0 0) apparently becomes higher than that for (3 1 1)A. Fig. 7b shows mobilities as a function of hole concentration. From this figure, increasing the growth temperature is confirmed to be quite an

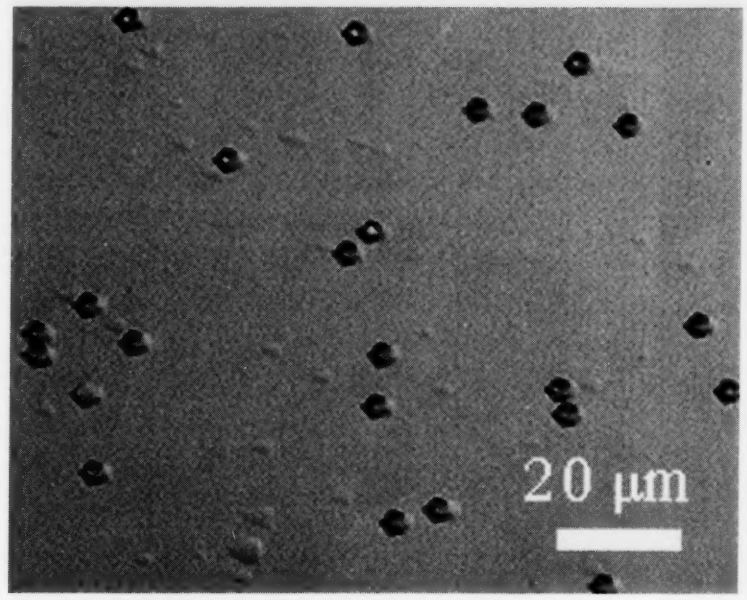

Fig. 6. Photograph of 200 Å GaAs capped AlAs grown on GaAs (3 1 1)B substrate. $[CBr_4] = 2 \times 10^{-6}$ mol/min, V/III = 15 and $T_g = 700°C$.

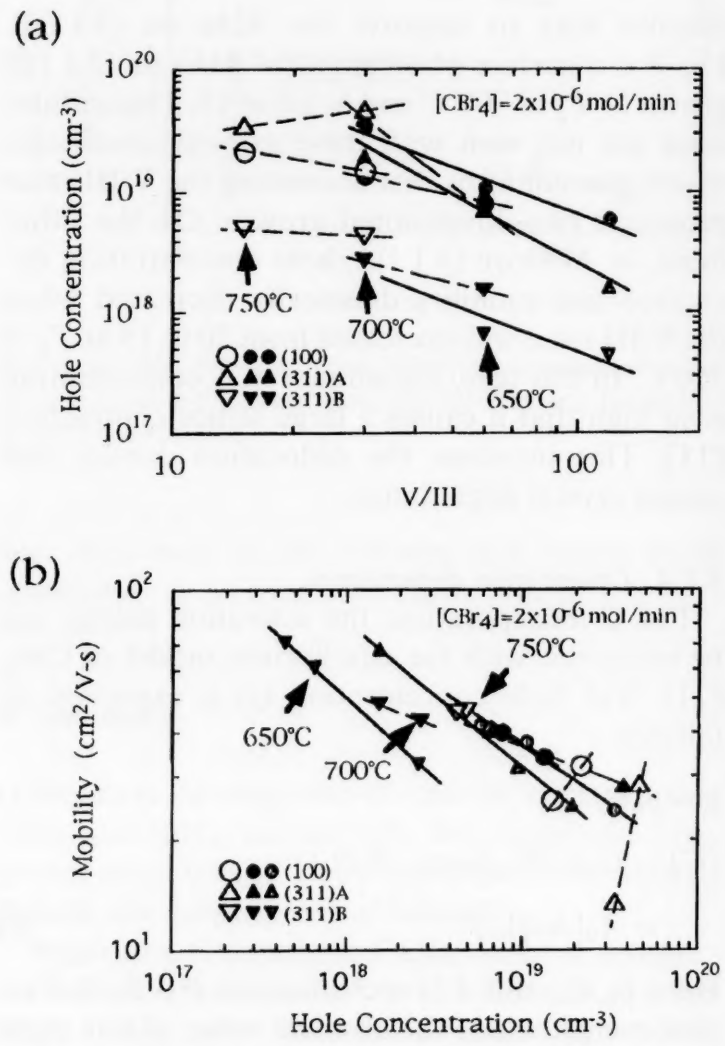

Fig. 7. (a) V/III ratio dependence of hole concentrations in AlAs. (b) Mobility as a function of hole concentration.

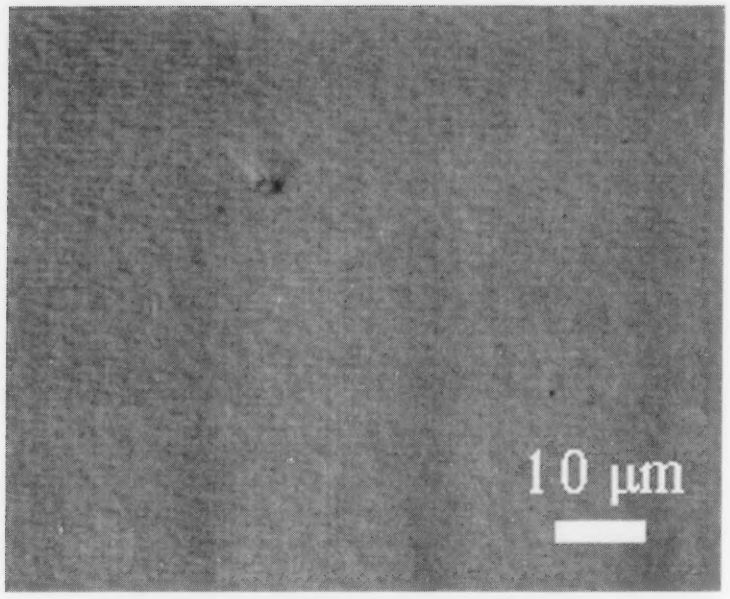

Fig. 8. Photograph of GaAs on (3 1 1)B substrate. $[CBr_4] = 2 \times 10^{-6}$ mol/min, V/III = 15 and $T_g = 750°C$.

effective way to improve the AlAs on (3 1 1)B. Fig. 8 is a surface photograph of AlAs on (3 1 1)B grown at T_g of 700°C and V/III of 15. The undulations are not seen with these growth conditions, which also confirms that decreasing the V/III ratio promotes two-dimensional growth. On the other hand, in AlAs on (3 1 1)A, hole concentration decreased and mobility drastically decreased when the V/III ratio was decreased from 30 to 15 at T_g of 750°C. In this case, the amount of C concentration is so high that it causes a large lattice contraction [11]. This increases the dislocation density and causes crystal degradation.

3.1.4. Orientation dependence

For C incorporation, the activation energy can be explained with the equilibrium model of CBr_x [11]. The hole concentration (p) is expressed as follows;

$$p = p_0[C], \tag{1}$$

$$[C] = C_0[CBr_4]\exp(-E/RT) = A_0[AsH_3]^x. \tag{2}$$

Here, p_0, C_0 and A_0 are coefficients, E is the activation energy, where the absolute value of E is equal to the Gibbs free energy of CBr_4 (1.3 eV [11]), and $[AsH_3]$ is the AsH_3 flow rate. Assuming that the $[AsH_3]^x$ does not depend on temperature, [C] is expressed as follows:

$$[C] = C_1[CBr_4][AsH_3]^x\exp(-E/RT). \tag{3}$$

The higher hole concentration on both (1 0 0) and (3 1 1)A compared with (3 1 1)B suggests that C incorporation may be largely dependent on the stability of As on the surface; it is less stable on (1 0 0) and (3 1 1)A surface because on an ideal surface, surface As atoms are backbonded with two Ga–As bonds on (1 0 0) and (3 1 1)A, while it is backbonded with three on (3 1 1)B. Therefore, C can be more easily replaced with As. This may also apply to AlAs. These differences can be included in C_1 in Eq. (3).

In both GaAs and AlAs, the AsH_3 flow-rate dependences (i.e., x) are different between (1 0 0) and (3 1 1)A; it depends more on (3 1 1)A ($x = -1.6$ at $T_g = 700°C$ in GaAs, $x = -1.8$ at $T_g = 650°C$ in AlAs) than (1 0 0) ($x = -0.6$ in GaAs, $x = -1.3$ in AlAs), and at V/III $\geqslant 60$, the order of the hole concentrations is reversed. In GaAs on (3 1 1)B, the dependence also becomes larger and reaches same level as that on (3 1 1)A at high temperature ($x = -1.4$ on (3 1 1)B and $x = -1.6$ on (3 1 1)A, while $x = -0.5$ on (1 0 0) at $T_g = 750°C$). These results indicate that the AsH_3 dependence is similar in both (3 1 1)A and (3 1 1)B when the surface As diffuses sufficiently on the surface at high temperature. It is considered that the step density, which must be largely different between (3 1 1) and (1 0 0), influences AsH_3 pressure; probably, C incorporation is much more sensitive to the desorption or adsorption of As at the step.

The activation energy of C incorporation is constant (-1.3– -1.4 eV) in both GaAs and AlAs on (1 0 0) [11]. In Fig. 3, for GaAs, the activation energies are estimated to be -2.4 eV in (3 1 1)B, -1.5 eV in (1 0 0) and -0.6 eV in (3 1 1)A. For AlAs, it is -0.5 eV in both (1 0 0) and (3 1 1)A. Possible explanations of the difference of the activation energy are (i) a change of the C activity as an acceptor (temperature dependence of p_0) or (ii) a change of the C incorporation rate at each T_g (temperature dependence of C_0), i.e., a change in the temperature dependence of x in $[AsH3]^x$. The AsH_3 dependences are almost the same at different

temperatures in GaAs on (1 0 0) and (3 1 1)A (x is not much changed at 700°C and 750°C), so (ii) does not seem to explain the results. So it can be said that for at least GaAs on (1 0 0) and (3 1 1)A, the reason for the difference of the activation energy is mainly (i), i.e., the temperature dependence of p_0. For GaAs on (3 1 1)A, the activation energy is above that of C incorporation on (1 0 0). In this case, the C activity is believed to be largely decreased at lower temperature owing to the increase of C occupation at sites other than As sites, which is apparently seen in AlAs on (1 0 0) [11]. While in the case of GaAs on (3 1 1)B, (ii), i.e., the temperature dependence of C_0 (x of $[AsH_3]^x$), may be the main reason for the low activation energy because C atoms may be excluded from As sites at higher temperatures as described above. AlAs on (3 1 1)B may be the extreme case.

3.2. Si doping in GaAs and AlAs

Here, we discuss the crystallographic orientation dependence of Si doping using SiH_4. Fig. 9a shows the carrier concentration as a function of the ratio of the SiH_4 flow rate to that of the group-III ($[SiH_4]/[III]$). Carrier concentration increased with increasing SiH_4 flow rate. In GaAs, the order of electron concentration is (3 1 1)B > (1 0 0) > (3 1 1)A. This is consistent with the tendency of n-type dopants to incorporate preferentially on B face [9]. Fig. 9b shows the mobility as a function of carrier concentration. All data for GaAs are almost on the same line, which indicates that their crystal quality is sufficient. In the case of AlAs, the orientation dependence is remarkably clear, that is, the carrier concentration for (3 1 1)B is one order of magnitude higher than for (1 0 0) and the conduction type on (3 1 1)A was reversed to p-type.

In the case of Si doping, because of the high-temperature growth ($T_g = 800°C$), the quality of the layer must be sufficient. However, the conduction type changes to p-type in AlAs on (3 1 1)A. In both GaAs and AlAs on (1 0 0), we have found that carrier concentration is about one order of magnitude lower than Si concentration from SIMS measurement. The activity of Si as a donor is so low that the change of the surface state may largely influence the rate of Si incorporation at group-III

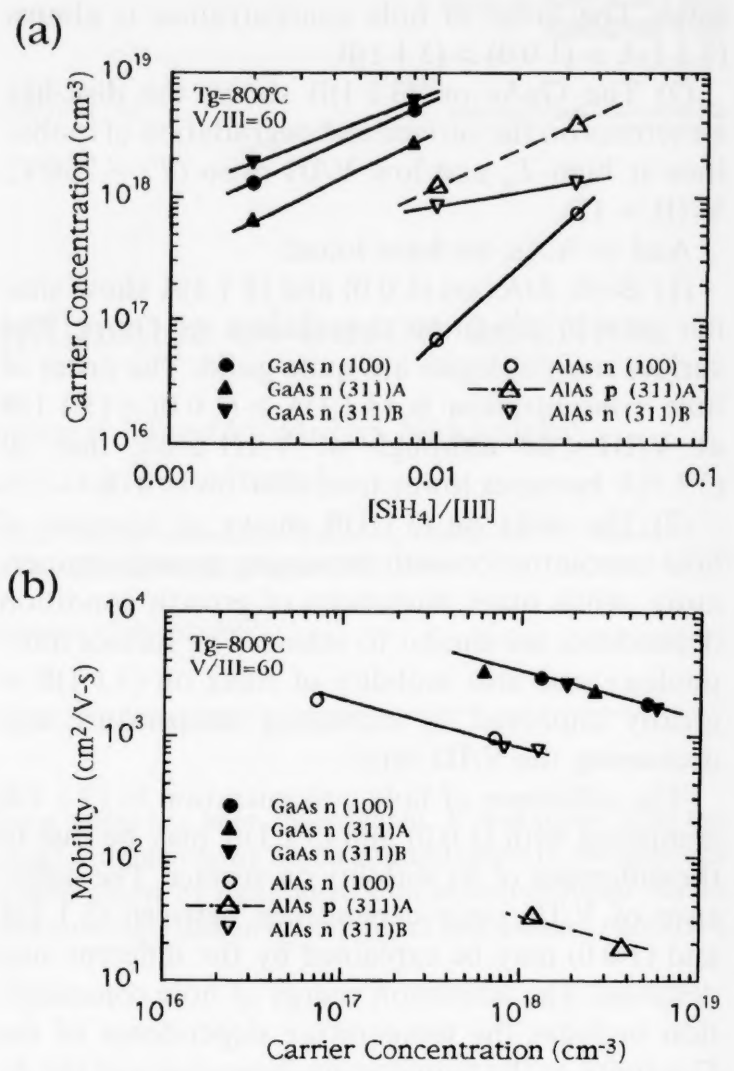

Fig. 9. (a) SiH_4 flow rate ($[SiH_4]/[III]$) dependence of carrier concentration in GaAs and AlAs. (b) Mobility as a function of carrier concentration.

site. AlAs may be the extreme case owing to its reactivity.

4. Summary

We have investigated C and Si doping using CBr_4 and SiH_4, respectively, for GaAs and AlAs grown on (1 0 0), (3 1 1)A and (3 1 1)B substrates. Results are summarized as follows.

Regarding C doping in GaAs, we have found:

(1) Both GaAs on (1 0 0), (3 1 1)A and (3 1 1)B show similar growth condition dependence; hole concentration increases with increasing $[CBr_4]$, decreasing growth temperature, and decreasing V/III

ratio. The order of hole concentration is almost (3 1 1)A > (1 0 0) > (3 1 1)B.

(2) The GaAs on (3 1 1)B shows the disk-like structures on the surface and degradation of mobilities at high T_g and low V/III ratio ($T_g = 750°C$, V/III = 15).

And in AlAs, we have found:

(1) Both AlAs on (1 0 0) and (3 1 1)A show similar growth condition dependence as GaAs. The surface morphologies are quite good. The order of hole concentration is (3 1 1)A $\geqslant$ (1 0 0) > (3 1 1)B at V/III < 60 although at V/III $\geqslant$ 60, that of (3 1 1)A becomes lower than that on (1 0 0).

(2) The AlAs on (3 1 1)B shows an increase of hole concentration with increasing growth temperature, while other tendencies of growth condition dependence are similar to others. The surface morphology and also mobility of AlAs on (3 1 1)B is greatly improved by increasing temperature and decreasing the V/III ratio.

The difference of hole concentration in (3 1 1)B compared with (1 0 0) and (3 1 1)A may be due to the difference of As stability on surface. The difference of V/III ratio dependence between (3 1 1)A and (1 0 0) may be explained by the different step densities. The activation energy of hole concentration includes the temperature dependence of the C activity or the temperature dependence of the As dependence. The former case may appear at least in GaAs on (3 1 1)A, while the latter case at least in GaAs on (3 1 1)B.

And for Si doping:

(1) The order of electron concentration at the same SiH_4 flow rate is (3 1 1)B > (1 0 0) > (3 1 1)A. Electron concentration in AlAs on (3 1 1)B is about one order of magnitude higher than that on (1 0 0). Conduction type is reversed to p-type in AlAs on (3 1 1)A.

For both C and Si doping, AlAs shows relatively apparent growth condition dependences of hole concentration compared with GaAs, maybe because of its reactivity.

Acknowledgements

The authors would like to acknowledge Dr. Yoshiaki Kadota and Dr. Jiro Temmyo for their helpful discussions. They also wish to thank Dr. Hidetoshi Iwamura and Dr. Takashi Kurokawa for their continuous encouragement.

References

[1] M. Takahashi, P. Vaccaro, K. Fujita, T. Watanabe, T. Mukaihara, F. Koyama, K. Iga, IEEE Photon. Lett. 8 (1996) 737.
[2] Y. Kaneko, S. Nakagawa, T. Takeuchi, D.E. Mars, N. Yamada, N. Mikoshiba, Electron. Lett. 31 (1995) 805.
[3] J. Temmyo, E. Kuramoti, M. Sugo, T. Nishiya, R. Nötzel, T. Tamamura, Mater. Sci. Eng. B 35 (1995) 7.
[4] K. Tamamura, J. Ogawa, K. Akimoto, Y. Mori, C. Kojima, Appl. Phys. Lett. 50 (1987) 1149.
[5] M. Kondo, T. Tanahashi, ICMOVPE VII, Conf. Digest, 1994, p. 40.
[6] C. Caneau, R. Bhat, M.A. Koza, J. Crystal Growth 118 (1992) 467.
[7] W.I. Wang, E.E. Mendez, T.S. Kuan, L. Esaki, Appl. Phys. Lett. 47 (1985) 826.
[8] K. Agawa, K. Hirakawa, N. Sakamoto, T. Ikoma, Appl. Phys. Lett. 65 (1994) 1171.
[9] R. Bhat, C. Caneau, C.E. Zah, M.A. Koza, W.A. Bonner, D.M. Hwang, S.A. Schwarz, S.G. Menocal, F.G. Favire, J. Crystal Growth 107 (1991) 772.
[10] W.Q. Li, P.K. Bhattacharya, S.H. Kwok, R. Merlin, J. Appl. Phys. 72 (1992) 3129.
[11] K. Tateno, Y. Kohama, C. Amano, J. Crystal Growth 172 (1997) 5.
[12] Y. Kohama, C. Amano, Y. Ohiso, T. Kurokawa, Jpn. J. Appl. Phys. 34 (1995) 3504.
[13] S.-I. Kim, M.-S. Kim, Y. Kim, C.S. Son, S.-M. Hwang, B.-D. Min, E.K. Kim, S.-K. Min, Appl. Phys. Lett. 69 (1996) 815.

ELSEVIER

Journal of Crystal Growth 181 (1997) 41–47

JOURNAL OF CRYSTAL GROWTH

Oxygen solubility in Si melts: influence of boron addition

Keisei Abe[a,*], Takeshi Matsumoto[a], Susumu Maeda[a], Hideo Nakanishi[a], Keigo Hoshikawa[b], Kazutaka Terashima[a]

[a] *Silicon Melt Advanced Project, Shonan Institute of Technology, 1-1-25 Tsujido-nishikaigan, Fujisawa, Kanagawa 251, Japan*
[b] *The Faculty of Education, Shinshu University, 6-Ro Nishinaganocho, Nagano 380, Japan*

Received 9 November 1996; accepted 17 March 1997

Abstract

The influence of boron addition on oxygen solubility in silicon melts has been investigated. It was found that the oxygen concentration increases from 2×10^{18} to 4×10^{18} atoms/cm^3 with increasing boron concentration in silicon melts from nondoped to 5×10^{20} atoms/cm^3. Boron atoms gather oxygen atoms by weak attraction in boron-doped silicon melts. The temperature dependence of oxygen concentration in boron-doped silicon melts is small and without definition in the experimental range investigated.

Keywords: Solubility; Oxygen; Molten silicon; Boron impurity

1. Introduction

Oxygen is one of the most important species in silicon single crystals, since the interstitial oxygen is precipitated during device processing and device yield is strongly dependent on the behavior of the oxygen. As semiconductor devices become more integrated, stricter control of oxygen concentration and distribution is needed.

Several recent papers have dealt with investigations of solubility of oxygen in liquid silicon in equilibrium with its oxide at elevated temperature [1–4]. Huang et al. investigated the influence of antimony addition on the oxygen solubility [5].

Recently highly conductive silicon wafers have been required for use in RAM devices. Especially heavily boron-doped silicon wafers are needed. Aoki et al. reported the iron gettering effect of P^+ substrates [6]. Choe reported that oxygen precipitation is different in boron-doped crystals compared to nondoped crystals [7]. But there is no data on the dependence of oxygen solubility on the concentration of boron in silicon melts in contact with SiO_2. This paper describes the oxygen solubility in silicon melts and the influence of boron addition.

2. Experimental procedure

Our experimental method is basically the same as Huang reported in Ref. [5].

* Corresponding author. Fax: + 81 466 36 1594.

0022-0248/97/$17.00 © 1997 Elsevier Science B.V. All rights reserved
PII S0022-0248(97)00244-3

2.1. Sample preparation

To measure the solubility of oxygen in a silicon melt in equilibrium contact with quartz, and to minimize the possible errors caused by the surrounding space, a combination of silicon and quartz was prepared so as to insure complete contact with each other at high temperatures. A silicon rod 13 mm in diameter and 33 mm in length was fixed in a 13 mm inner-diameter quartz ampoule with a flat bottom. The upper space in the ampoule was sealed with a quartz rod with a slightly smaller diameter and it was welded completely to the inside wall of the ampoule after evacuation to about 10^{-5} Torr. A cross section of the quartz ampoule in which nondoped or boron-doped silicon was sealed is shown schematically in Fig. 1a. The silicon sample used in nondoped experiments was cut from a polycrystal having an initial oxygen content of $< 10^{16}$ atoms/cm^3. The boron powder was put onto the ampoule bottom, then polycrystalline silicon was put in the quartz ampoule as shown in Fig. 1b. The boron powder size was below 44 μm and its purity was 2N (Koujundo Chemical Laboratory Co., Ltd.).

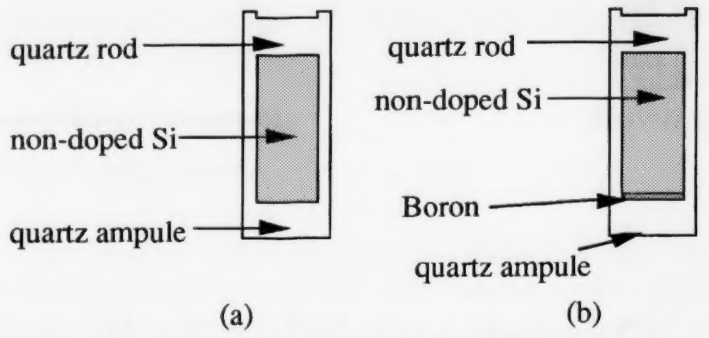

Fig. 1. Cross section of sample fixed tightly in a quartz ampoule: (a) nondoped silicon sample and (b) boron-doped silicon sample.

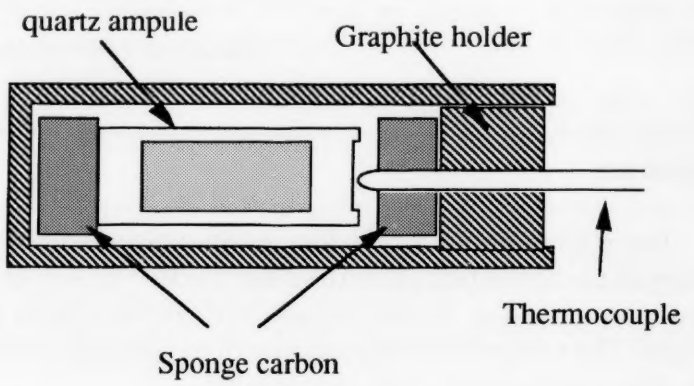

Fig. 2. Schematic of apparatus for melting the sample in the quartz ampoule held in a graphite holder.

2.2. Melting, resolidification and temperature measurement

The quartz ampoule with a pure silicon rod or silicon rod with boron powder inside was covered with a graphite holder, and heated to various temperatures in the range of 1430–1470°C for 120 min. in an Ar atmosphere. Ar flow rate was 1.5 l/min. The furnace used in this experiment was a horizontal three-zone type. The temperature and its variation were measured using 0.5 mm diameter Pt–PtRh B-type thermocouples placed along the outer wall of the graphite holder at the end of the silicon rod, as shown in Fig. 2. The sample was quickly drawn from the furnace for quenching, after equilibration has presumably been attained in 120 min. Quenching rates of the samples were about 20°C/s. The duration for holding the temperature was determined by calculating the diffusion of oxygen atoms in the melt from the quartz ampoule wall, using a diffusion coefficient of 1×10^{-4}cm^2 s. The employed value for calculation was chosen on the basis that most common dopant elements have larger diffusion coefficients than this value [3, 8]. According to the calculation, the degree of saturation after 120 min. was predicted to be 99.9%, even at the center of the melt, with the presently employed ampoule size.

2.3. Oxygen and boron concentration measurement

The size of specimen was $3 \times 3 \times 2.5$ mm^3. The samples were mirror polished. The oxygen and boron concentrations were measured using a SIMS (CAMECA, IMS-3f/4f) instrument.

Standard samples for the measurement were silicon wafers with oxygen concentrations of 1.16×10^{18}, 1.46×10^{18} and 1.73×10^{18} atoms/cm^3, which were measured by FT-IR with a conversion coefficient of 3.03×10^{17} atoms/cm [2, 9]. The

relative error of SIMS measurements was less than 5%.

3. Results and discussion

Oxygen concentration increases with increasing boron concentration as shown in Fig. 3. When the boron concentration is 5×10^{20} atoms/cm^3, the oxygen concentration is 4×10^{18} atoms/cm^3. This oxygen concentration is about twice as much as the value for nondoped silicon. The results of nondoped silicon in our laboratory showed good agreement with the reported value of Carlberg [1].

The dependence of the oxygen concentration on the silicon melt temperature in boron-doped silicon melts is given in Fig. 4. The dependence of oxygen concentration on temperature is small with no definite relationship.

According to our experimental data, oxygen concentration increases with increasing boron concentration independent of the silicon melt temperature. The cause of this phenomenon is discussed below.

To discuss the relation between boron atoms and oxygen atoms in a silicon melt, at first we assumed the generation of boron oxide species. If x atoms of boron react with one oxygen atom, the following chemical reaction occurs:

$$xB + O \leftrightarrow B_xO\,. \tag{1}$$

Equilibrium constant K, is expressed by the following expression:

$$K = \frac{[B_xO]}{[B]^x[O]}\,, \tag{2}$$

where [O], [B] and [B_xO] are the total oxygen concentration, the boron concentration and B_xO concentration in the boron- doped silicon melt, respectively.

It is assumed that there are two kinds of oxygen in a boron-doped silicon melt: one is uncombined or isolated oxygen atoms, the other is combined with boron atoms in the form of B_xO. Then the following calculation can be carried out:

$$[O] = [O]_{Si} + [B_xO] = [O]_{Si} + K[B]^x[O]\,, \tag{3}$$

$$\Delta[O]/[O] = K[B]^x\,, \tag{4}$$

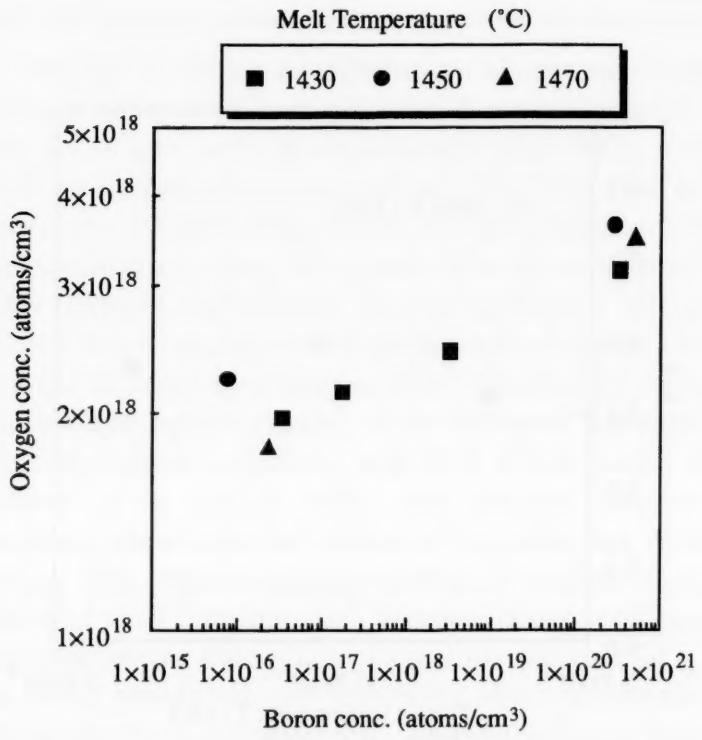

Fig. 3. Dependence of the oxygen concentration on the boron concentration in a boron-doped Silicon melt.

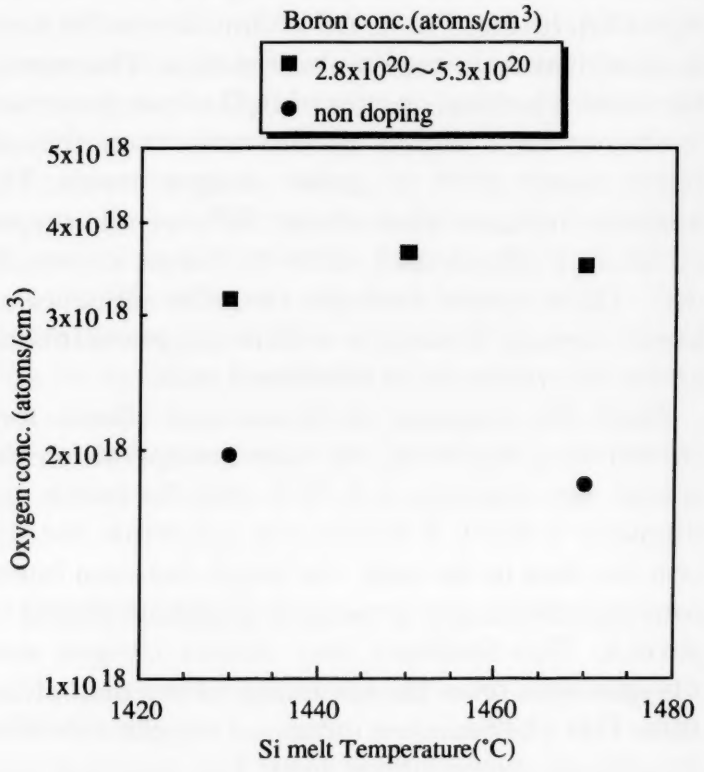

Fig. 4. Dependence of the oxygen concentration on the Si melt temperature in a boron-doped silicon melt.

$\Delta[O] = [O] - [O]_{Si}$ is the increased oxygen concentration due to boron addition in the silicon melt. Eq. (4) can be rewritten as follows:

$$\ln \{\Delta[O]/[O]\} = \ln K + x \ln \{[B]\} . \quad (5)$$

The values of x and K are calculated by using our results. x and K values are obtained from following process. The relationship between the increase of oxygen concentration and boron concentration in silicon melt is plotted in Fig. 5. The gradient corresponds to x. In Fig. 5, ln [B] being equal to 0, the value of ln(Δ[O]/[O]) expresses K. Table 1 shows x and K. According to Table 1, the ratio of boron to oxygen is 1 to 0.089 or 0.52. The dependence of K on the silicon melt temperature in boron-doped silicon melt is given in Fig. 6. The value of K is small and the dependence on the silicon melt temperature has no definite relationship. Activation energy of the boron oxygen reaction is discussed below. Activation energy ΔE, is expressed by the following expression.

$$\ln K = \frac{-\Delta E}{RT} + N, \quad (6)$$

where R is the gas constant and N is a constant unrelated to the silicon melt temperature. According to Eq. (6) and Fig. 6, ΔE is almost zero. So there is no activation energy in this reaction. This means the stable chemical species of B_xO is not generated by boron in a doped silicon melt, even though boron atoms seem to gather oxygen atoms. The analysis indicates that about 52% of all oxygen atoms in a silicon melt relate to boron atoms added. These results indicate that the influence of boron doping, involves a shift in oxygen solubility above the values for a nondoped melt.

Next, the diameter of boron and silicon ions should be considered. At room temperature, the silicon ion diameter is 0.39 Å and the boron ion diameter is 0.2 Å. If boron ions substitute the silicon ion sites in the melt, the length between boron ions and silicon ions at nearest neighbors should be shrunk. This tendency may attract oxygen ions. Oxygen ions relax the shrinkage of the melt structure. This phenomenon increased oxygen solubility in a boron-doped silicon melt. The structure variation of silicon melt with and without boron and oxygen atoms is now under investigation.

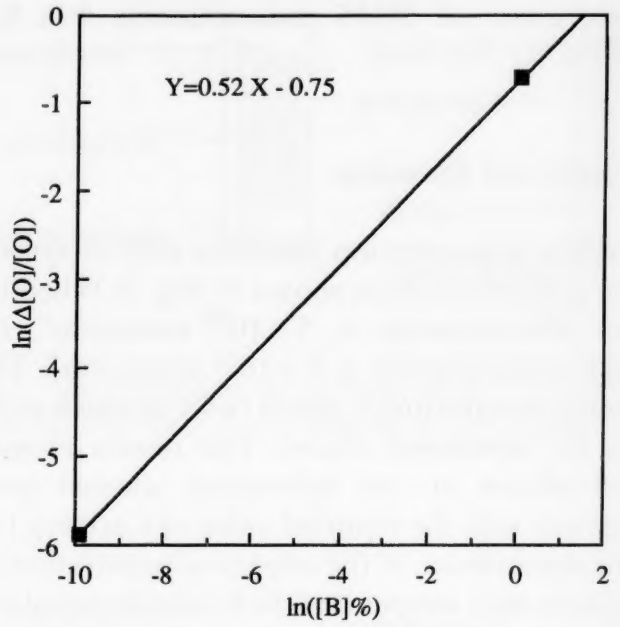

Fig. 5. Relationship between the increase of oxygen concentration and boron concentration in a silicon melt: Silicon melt temperature = 1470°C.

Table 1
Calculated x and the equilibrium constant K

Si melt temperature (°C)	x	Equilibrium constant K
1430	0.16	0.51
1450	0.089	0.54
1470	0.52	0.47

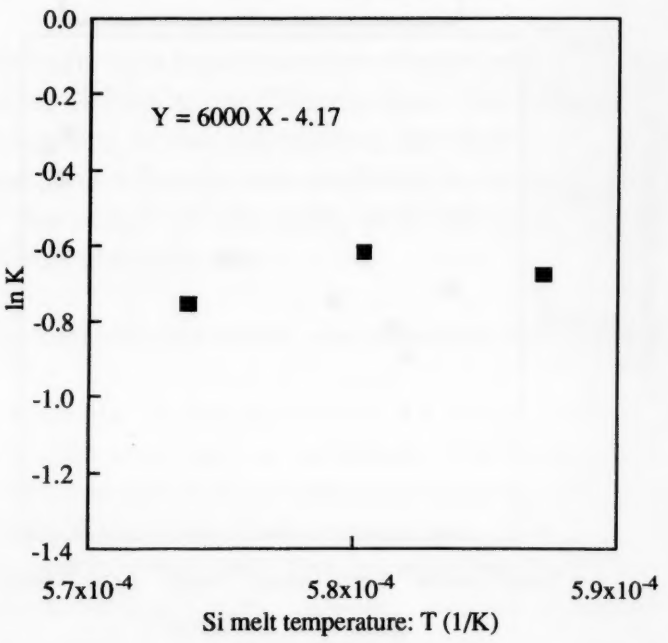

Fig. 6. Relationship between equilibrium constant and Si melt temperature in a boron-doped silicon melt.

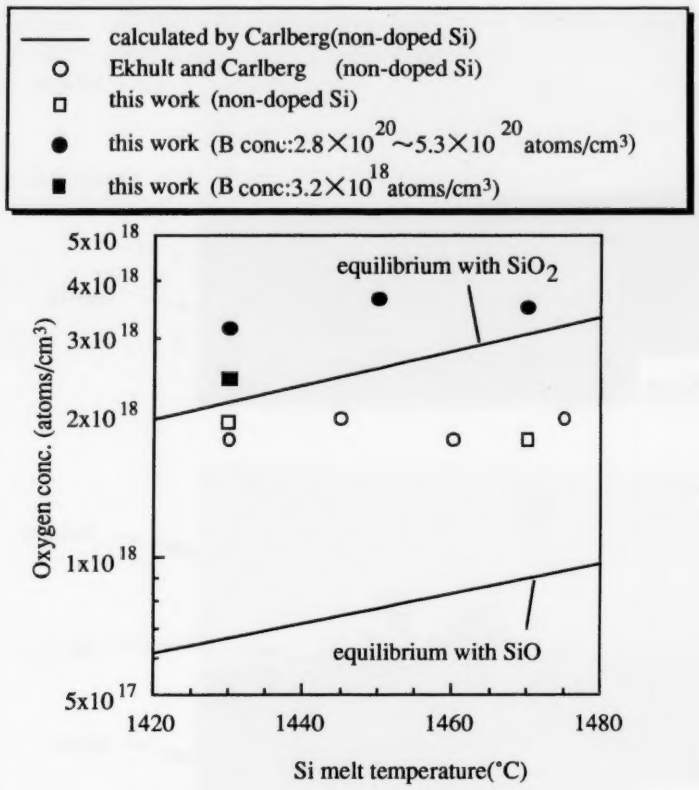

Fig. 7. Relationship between oxygen concentration and temperature (This work; closed circles and closed squares). Oxygen solubility in a boron-doped silicon melt is higher than nondoped silicon melt in equilibrium with SiO_2.

We next consider equilibrium of silicon melt with silicon oxide. Carlberg calculated oxygen solubilities in silicon melt in equilibrium with SiO_2 and SiO by thermo-dynamics calculation [10]. Our results are plotted in Fig. 7 with the calculated values in equilibrium with SiO_2 and SiO by solid lines. Our oxygen solubilities in boron-doped silicon melt are denoted by closed circles and a square. The results of nondoped silicon melt, denoted by open circles and open squares, all lie between the equilibrium values with SiO_2 and SiO. When boron is doped in a silicon melt, the oxygen concentrations approach the values of equilibrium with SiO_2. The boron concentration is higher than about 1×10^{18} atoms/cm^3, oxygen concentrations increase above the values of equilibrium with SiO_2. In other words, oxygen solubility shifts above the values for the nondoped case. And in the case where the boron concentration is 1×10^{20} atoms/cm^3, the oxygen concentration values approach the values of equilibrium with SiO_2 with increasing silicon melt temperature. So we observed the interface between the silicon and the quartz ampoule using an optical microscope. Fig. 8a is micrograph of a nondoped sample heated at 1430°C for 120 min. Fig. 8b is that of a boron-doped sample (boron concentration is 5×10^{20} atoms/cm^3) heated at 1430°C for 120 min. Fig. 8c is micrograph of a nondoped sample heated at 1470°C for 120 min. Fig. 8d is that of a boron-doped sample (boron concentration is 5×10^{20} atoms/cm^3) heated at 1470°C for 120 min. In the nondoped sample, a brown thin film between the silicon and quartz ampoule is clearly observed, and the interface was dendritic in form as shown in Fig. 8a and Fig. 8c. In a heavily boron-doped sample ($>1 \times 10^{18}$ atoms/cm^3) using a Si melt temperature of 1430°C, there is no brown thin film between silicon and the quartz ampoule as shown in Fig. 8b. In a heavily boron-doped sample ($>1 \times 10^{18}$ atoms/cm^3) and using a Si melt temperature of 1470°C, a brown thin film between silicon and quartz ampoule is observed. This brown-colored layer was reported as an $SiO_{2-\delta}$ layer by Carlberg [10]. The fraction of brown thin film area around the interface of the quenched silicon sample and the quartz was measured. Fig. 9 shows dependence of the ratio of brown thin film on the boron concentration in a boron-doped Si melt. Because the nondoped silicon melt corresponds with the equilibrium between SiO_2 and SiO at our experimental temperature range, an $SiO_{2-\delta}$ layer is observed between the silicon and the quartz ampoule. When boron is doped in a silicon melt, with increasing silicon melt temperature, the oxygen concentration approaches a value which is consistent with an equilibrium with SiO_2. The brown thin film was observed with increasing silicon melt temperature, but it is not observed at 1430°C as shown in Fig. 8b and Fig. 9.

4. Conclusions

The influence of boron addition on the oxygen solubility in silicon melts was studied. The main results are as follows: (1) Oxygen concentration increases with increasing boron concentration in a silicon melt. (2) Boron gathers oxygen by weak

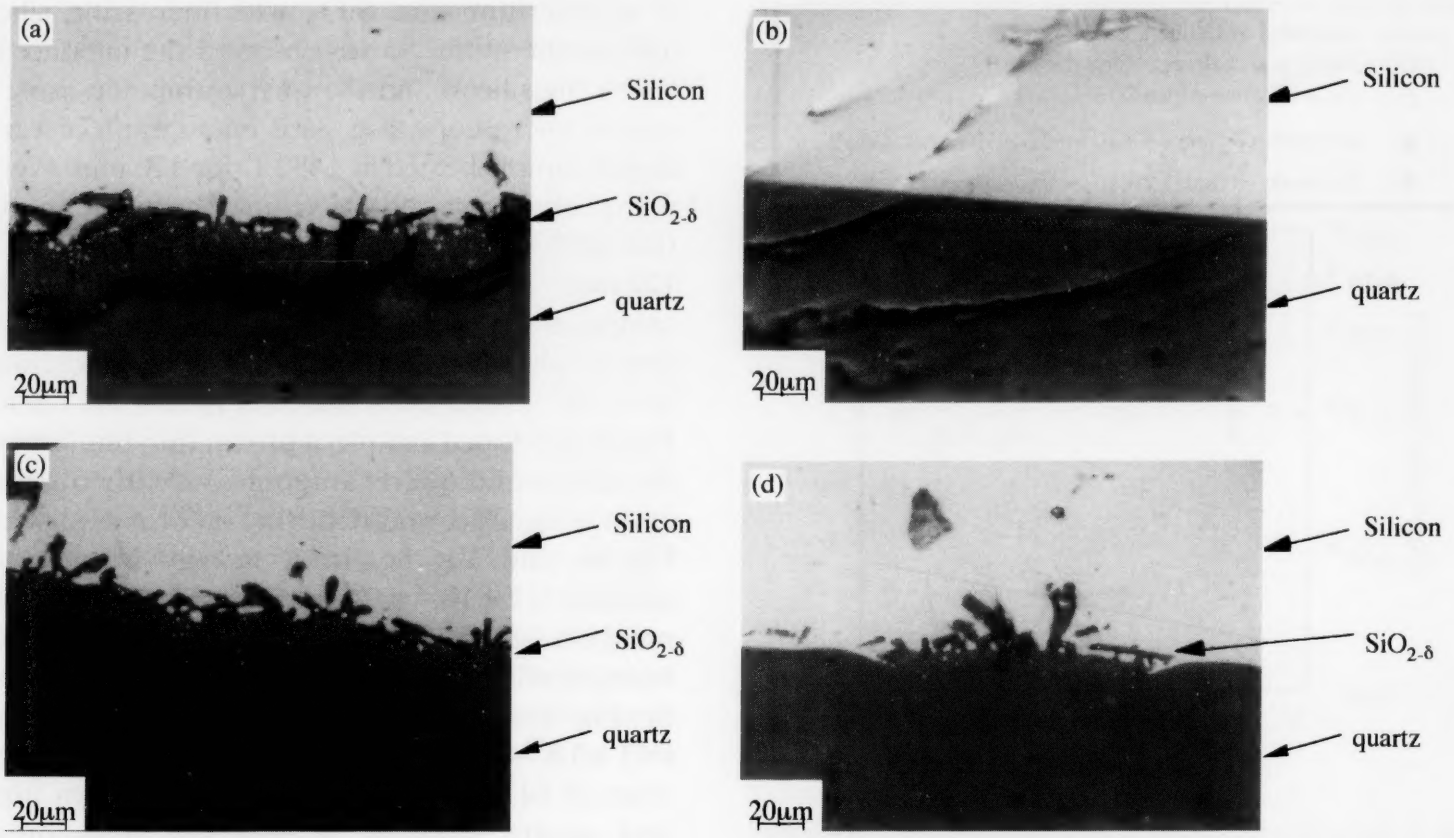

Fig. 8. A micrograph of a silicon sample heated for 120 min. (a) Non-doped silicon sample, Si melt temperature 1430°C (b) Heavily boron-doped silicon sample ($\sim 10^{21}$ atoms/cm^3), Si melt temperature 1430°C (c) Nondoped silicon sample, Si melt temperature 1470°C (d) Heavily boron-doped silicon sample ($\sim 10^{21}$ atoms/cm^3), Si melt temperature 1470°C.

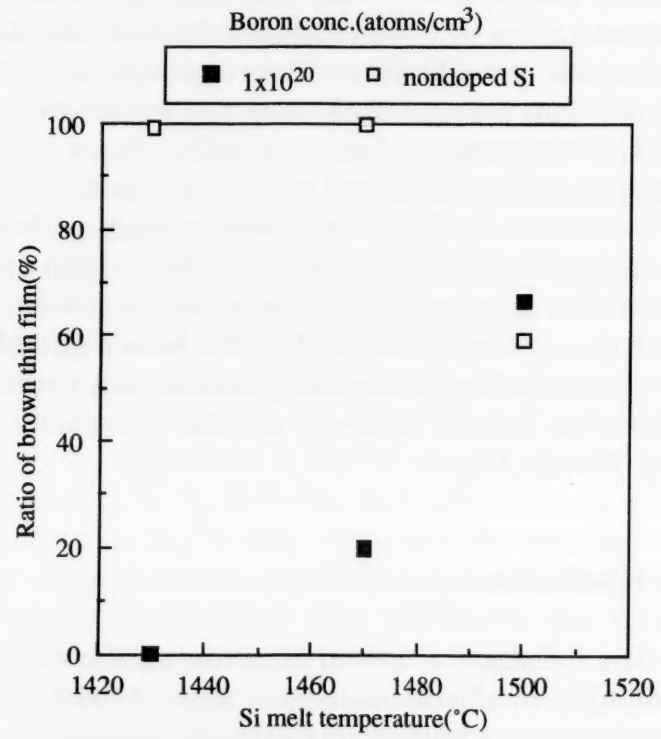

Fig. 9. Dependence of the ratio of brown thin film on the boron concentration in a boron-doped Silicon melt.

attraction in a boron-doped silicon melt. These results indicate that the influence of boron doping shifts the oxygen solubility above the values for the nondoped case. (3) The temperature dependence of oxygen concentration in boron doped silicon melts is small and has no definite relationship in the experimental range.

Acknowledgements

The authors deeply thank Dr. S. Kimura of National Institute for Research in Inorganic Materials for his fruitful suggestion, and also Drs. M. Kida and H. Sasaki of Mitsubishi Materials Silicon Co. Ltd. for their helpful discussion. The authors are much indebted to Mitsubishi Materials Silicon Co. Ltd., Komatsu Electronic Metals Co. Ltd. and Toshiba Ceramics Co. Ltd. for their positive support in this fundamental research on silicon melt. This work was conducted as JSPS Research for the

Future Program in the Area of Atomic-Scale Surface and Interface Dynamic.

References

[1] T. Carlberg, J. Electrochem. Soc. 133 (1986) 1940.
[2] U. Ekhult, T. Carlberg, J. Electrochem. Soc. 136 (1989) 551.
[3] H. Hirata, K. Hoshikawa, J. Crystal Growth 106 (1990) 657.
[4] A.E. Organ, N. Rilev, J. Crystal Growth 82 (1987) 465.
[5] X. Huang, K. Terashima, H. Sasaki, E. Tokizaki, S. Kimura, Jpn. J. Appl. Phys. 32 (1993) 3671.
[6] M. Aoki, T. Itakura, N. Sasaki, J. Appl. Phys. Lett. 66 (1995) 2709.
[7] K. Choe, J. Crystal Growth 147 (1995) 55.
[8] H. Kodera, Jpn. J. Appl. Phys. 2 (1963) 212.
[9] T. Iizuka, S. Takasu, M. Tajima, T. Arau, T. Nozaki, N. Inoue, M. Watanabe, J. Electrochem. Soc. 132 (1985) 1707.
[10] T. Carlberg, J. Electrochem. Soc. 136 (1989) 551.

ELSEVIER

Journal of Crystal Growth 181 (1997) 48–54

JOURNAL OF CRYSTAL GROWTH

Crystal growth and optical properties of $Ti^{3+}:YAl_3(BO_3)_4$ and $Ti^{3+}:GdAl_3(BO_3)_4$

Guofu Wang[1], T.P.J. Han, H.G. Gallagher*, B. Henderson

Department of Physics and Applied Physics, Optical Materials Research Centre, University of Strathclyde, North Portland Street, Colville Building, Glasgow G1 1XN, Scotland, UK

Received 7 April 1997; accepted 7 April 1997

Abstract

Large single crystals of Ti^{3+}-doped $YAl_3(BO_3)_4$ (YAB) and $GdAl_3(BO_3)_4$ (GAB) have been prepared by top-seeded solution growth (TSSG) from a $K_2Mo_3O_{10}$–B_2O_3 flux, using a cooling rate of 2.4°C/day and rotation rate of 6 rpm in a pure N_2 atmosphere. The optical properties of $Ti^{3+}:RAl_3(BO_3)_4$, where $R = Y^{3+}$ or Gd^{3+}, are quite similar to those of $Ti^{3+}:Al_2O_3$. However, the Ti^{3+}-doped aluminoborates have larger absorption coefficients than $Ti^{3+}:Al_2O_3$ and the peaks in the photoluminescence bands are shifted by ca. 20 nm to longer wavelengths compared to $Ti^{3+}:Al_2O_3$. The results suggest that Ti^{3+}-doped rare-earth aluminoborates have potential as tunable laser gain media in the near infrared region.

1. Introduction

Tunable solid state laser materials activated by Ti^{3+}-dopants are of much interest because of their broadband absorption and photoluminescence characteristics. Laser action has only been reported in $Ti^{3+}:Al_2O_3$ [1, 2], $Ti^{3+}:Y_3Al_5O_{12}$ (YAG) [3] and $Ti^{3+}:YAlO_3$ (YAP) [4, 5]. Indeed the Ti-sapphire laser, which is tunable over the wavelength range 660–1100 nm at room temperature [6], has become the most commercially successful solid state laser.

The Ti^{3+}-ion has the $3d^1$ electron configuration outside the closed shells, resulting in a ^2D ground state for the free ion. An octahedral crystal field splits ^2D into ^2E and $^2T_2$ states, separated in energy by the octahedral crystal field energy of 10 Dq. Titanium is the first of the transition metal elements in the periodic table: there are four valence electrons in the electron configuration $3d^24s^2$. Titanium (IV) is the most stable and common oxidation state. Compounds in lower oxidation states – I, II, III, are readily oxidised to titanium (IV) by air, water or other reagents [7]. In consequence, Ti^{3+}-doped crystals must be grown in mildly reducing or neutral atmospheres to prevent oxidation to the Ti^{4+}-state. The Ti^{3+}-ion substitutes for Al^{3+} in such crystals as Al_2O_3, $Y_3Al_5O_{12}$ and $YAlO_3$ in trigonally distorted, octahedral crystal field sites.

* Corresponding author. Fax: + 44 141 5534162.

[1] Permanent address: Fujian Institute of Research on the Structure of Matter, Chinese Academy of Science, Fuzhou, Fujian 350002, People's Republic of China.

0022-0248/97/$17.00 © 1997 Elsevier Science B.V. All rights reserved
PII S0022-0248(97)00272-8

The trigonal distortions in concert with spin–orbit coupling completely removes the five-fold orbital degeneracy of the $3d^1$ configuration [8, 9], and the consequent splittings of the ^2E and $^2T_2$ states are reflected in the optical properties as we discuss briefly in this paper.

2. Crystal growth

$YAl_3(BO_3)_4$ (YAB) and $GdAl_3(BO_3)_4$ (GAB) crystals melt incongruently at high-temperature decomposing into their constituent phases [10]. Single crystals of such compounds are grown from high-temperature solutions. Previously, the authors have reported the successful growth of Cr^{3+}-doped YAB and GAB by the top-seeded solution growth (TSSG) method using a $K_2Mo_3O_{10}$–B_2O_3 flux [11, 12].

In the experiments reported here, crystals of Ti-doped YAB and GAB were prepared in a nitrogen atmosphere to prevent oxidation of Ti^{3+} to Ti^{4+}. Crystal growth was performed using the TSSG method in a modified tubular muffle furnace regulated by a Eurotherm temperature controller/programmer. The growth atmosphere was maintained by passing N_2 gas through a silica tube insert enclosed at both ends with water cooled aluminium plates as shown in Fig. 1. Flowing gas was introduced at the base of the furnace and allowed to exit through the seed holder opening in the top plate. The crucible was charged with appropriate weights of 4N purity Y_2O_3 or Gd_2O_3, Ti_2O_3, Al_2O_3, B_2O_3, K_2CO_3 and MoO_4 and placed in the centre of the furnace. Oxygen was purged from the furnace and crucible by passing 200 cm^3/min of N_2 through the system for 1–2 h, before slowly heating the furnace. When the growth temperature was reached, the nitrogen flow rate was reduced to 50 cm^3/min and the crystals were grown using the procedure described previously [11, 12]. During growth, the temperature lowering rate and crystal rotation rate were maintained at 2.4°C/day and 4–5 rpm, respectively. At the end of the run, the crystal was withdrawn from the melt surface and cooled to room temperature at a rate of 50°C/h.

Crystals of both Ti^{3+} : YAB and Ti^{3+} : GAB have been grown from the $K_2Mo_3O_{10}/B_2O_3$ flux

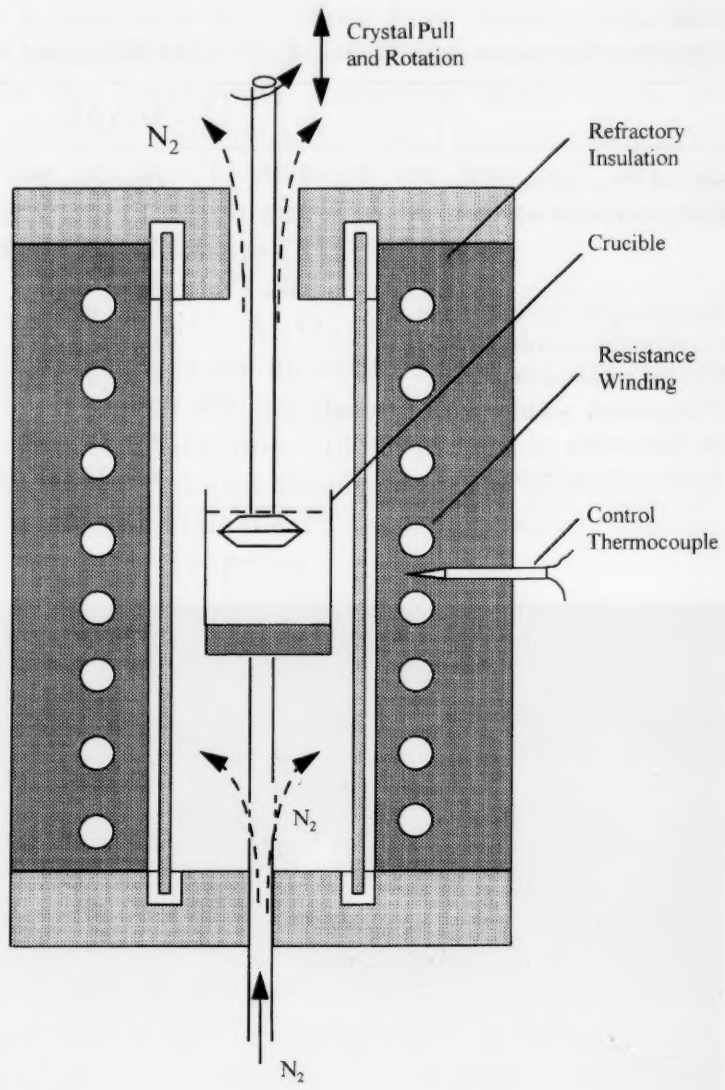

Fig. 1. A schematic diagram of the growth furnace showing the arrangement for controlling the growth atmosphere.

mixed in specific proportions for each compound. Details of the starting compositions and growth parameters for Ti^{3+} : YAB and Ti^{3+} : GAB are summarised in Table 1. The phase diagrams for the $RAl_3(BO_3)_4$–TiO_2–$K_2Mo_3O_{10}$–B_2O_3 system (where R = Y or Gd) are extremely complex, containing six constituents. Therefore, the composition of the growth solutions were determined empirically to achieve a careful balance between the competing factors of saturation temperature, solvent evaporation, solubility and viscosity. For the compositions used, cooling rates of < 4°C/day were necessary to avoid significant inclusions of flux. The optimum N_2 gas flow rate was found to be 50 cm^3/min. At flow rates greater than

Table 1
Experimental parameters for TSSG of $Ti^{3+}:YAl_3(BO_3)_4$ and $Ti^{3+}:GdAl_3(BO_3)_4$ crystals

	Ti : YAB	Ti : GAB
Size of Pt crucible	Diameter 75 × 75 mm high	Diameter 40 × 40 mm high
Composition of solution	21.3 wt% YAB with 0.5 at% Ti_2O_3, 71.4 wt% $K_2Mo_3O_{10}$ and 7.3 wt% B_2O_3	18.6 wt% GAB with 0.5 at% Ti_2O_3, 74.1 wt% $K_2Mo_3O_{10}$ and 7.3 wt% B_2O_3
Temperature growth range	1100–900°C	1030–952°C
Cooling rate during growth	2.4°C/day	2.4°C/day
Crystal rotation rate	4–5 rpm	4–5 rpm
Post growth cooling rate of crystal	50°C/h	50°C/h
N_2 flow rate	50 cm^3/min	50 cm^3/min
Typical crystal size	42 × 32 × 18 mm^3	10 × 9 × 7 mm^3

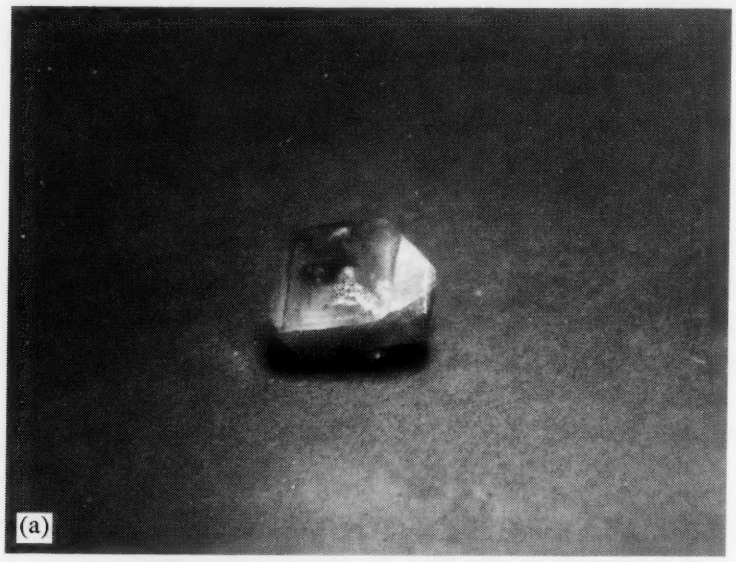

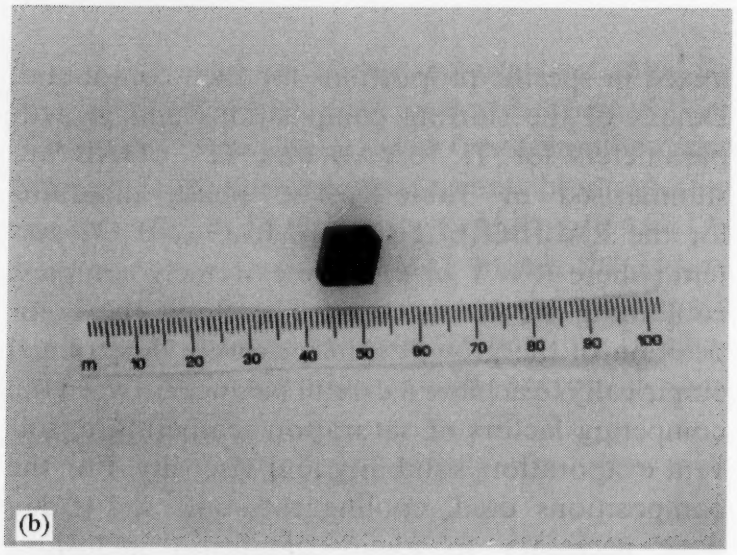

Fig. 2. The crystals of (a) $Ti^{3+}:YAl_3(BO_3)_4$ and (b) $Ti^{3+}:GdAl_3(BO_3)_4$.

100 cm^3/min, increased solvent evaporation and uncontrolled fluctuations in temperature resulted in the growth of crystals containing severe flux inclusions and striations. Slower flow rates were not employed to avoid in-diffusion of oxygen to the growth furnace.

The Ti^{3+} : YAB crystals had typical dimensions of ca. 42 × 36 × 24 mm^3 as shown in Fig. 2a and were pink in colour. Crystals of Ti^{3+} : GAB, Fig. 2b, with dimensions up to 22 × 18 × 12 mm^3 were a dark purple colour. Both compounds crystallise as rhombohedral prisms bounded by well-formed $\{1\,0\,\bar{1}\,0\}$ and $\{1\,\bar{2}\,1\,0\}$ facets. They are of high quality with no visible striations or flux inclusions, although some cracking was observed around the seed regions. In both crystals there is a gradual decrease in colour towards the periphery which is more pronounced for Ti^{3+} : YAB than for Ti^{3+} : GAB, indicating that the segregation coefficients of Ti^{3+} in YAB and GAB are greater than unity.

3. Optical characterisation of $Ti^{3+}:RAl_3(BO_3)_4$ crystals

Optical properties were measured on small single crystal, samples (2 × 2 × 5 mm^3) cut from the as-grown crystals and then polished on diamond-impregnated laps. Absorption spectra were recorded at room temperature and at 77 K using a CARY-AVIV 14DS spectrophotometer, which operated over the range 200–2500 nm. Photoluminescence

spectra were measured at room temperature and 14 K following excitation with the multi-line visible output of an Ar^+ laser. The light emitted by the sample was dispersed using a half-meter Spex grating monochromator and detected at the exit slit by a Hamamatsu R928 photomultiplier tube.

The $RAl_3(BO_3)_4$ crystals have huntite-like structures with space group R32, in which the R^{3+}-ions occupy trigonal prisms and Al^{3+}-ions are located in distorted oxygen octahedra [13, 14]. Ti^{3+}-ions substitute for Al^{3+}-ions in $RAl_3(BO_3)_4$ on sites which undergo strong trigonal distortions just as is the case for Ti^{3+} in Al_2O_3 and $Y_3Al_5O_{12}$ [8–10]. Fig. 3 shows the polarised optical absorption spectra of both Ti^{3+} : YAB and Ti^{3+} : GAB crystals measured at room temperature in the wavelength range of 300–750 nm. Two overlapping broad bands are observed for each crystal peaking at 514 and 576 nm for Ti^{3+} : YAB and 520 and 586 nm for Ti^{3+} : GAB. These bands correspond to transitions from the ground $^2T_2$ state to the excited ^2E state split by a static Jahn–Teller effect. This splitting is measured from the position of the peaks in the overlapping absorption bands to be ca. 2100 cm^{-1} for both crystals. The spin–orbit splitting of the ^2D state in the free Ti^{3+}-ion, ca. 150 cm^{-1}, is too small to be measured from the absorption spectra [8].

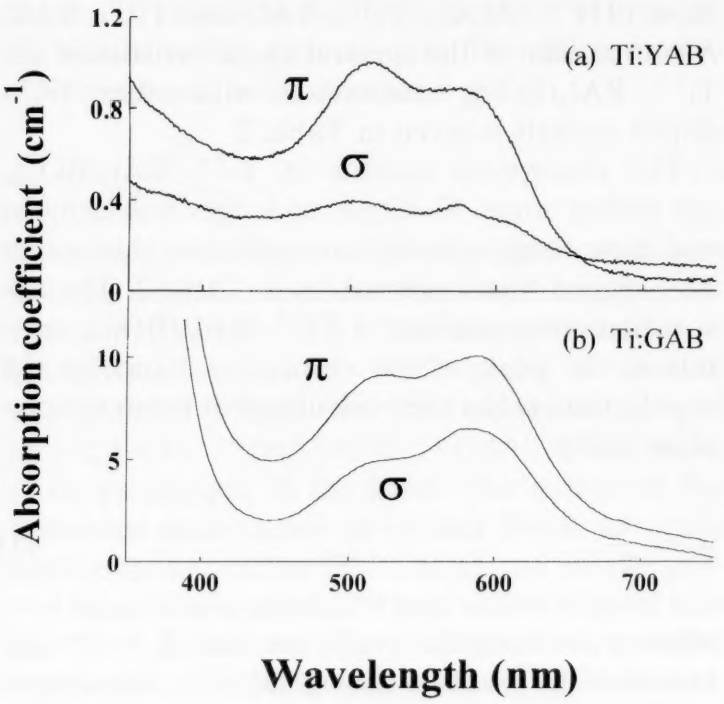

Fig. 3. The polarised optical absorption spectra of Ti^{3+}-ions in (a) $YAl_3(BO_3)_4$ and (b) $GdAl_3(BO_3)_4$, measured at 300 K. The polarisations are defined as follows: π polarisation has the ***E*** vector of the radiation parallel to the symmetry of the axis (in this case *c*-axis) and in σ polarisation ***E*** vector is perpendicular to the symmetry axis.

For other Ti^{3+}-doped materials such as Ti^{3+} : YAP [5], $Ti^{3+} : Al_2O_3$ [15] and $Ti^{3+} : Mg_2SiO_4$ [16], there is an unexpected, weaker absorption band at 700–900 nm due to Ti^{3+}/Ti^{4+} pairs [5]. No such absorption band is present in the spectra of the Ti^{3+}-doped aluminoborates suggesting that in these crystals the Ti^{3+}-ions are mainly isolated from other Ti-species.

The absorption spectra shown in Fig. 3, are strongly polarised with intensity ratios $\pi : \sigma = 3 : 1$ for Ti^{3+} : YAB and $\pi : \sigma = 3 : 2$ for Ti^{3+} : GAB, respectively. The polarised photoluminescence spectra of these Ti^{3+}-doped crystals measured at 300 K are shown in Fig. 4. The broad-band luminescence covers the wavelength range 650–1200 nm with peaks at 760 nm (π-polarisation) and 775 nm (σ-polarisation) for Ti^{3+} : YAB and 765 nm (π-polarisation) and 770 nm (σ-polarisation) for Ti^{3+} : GAB. The sharp emission lines near 684 nm are due to trace Cr^{3+} impurities, which emit into the weak vibronic sideband [11, 12].

The peaks in the photoluminescence bands shown in Fig. 4 shift to longer wavelengths with increasing temperature, the shifts amounting to ca. 10 nm between 14 K and room temperature for both crystals. The strong broad-band emission observed for Ti^{3+} : YAB and Ti^{3+} : GAB crystals is due to the $^2E \rightarrow {}^2T_2$ transition of Ti^{3+}-ions. The zero-phonon structure characteristic of low-temperature measurements on Ti^{3+}-doped Al_2O_3, $YAlO_3$ and $Y_3Al_5O_{12}$ [3–6, 9] are not observed in the photoluminescence of Ti^{3+} : YAB and Ti^{3+} : GAB even down to 14 K.

The fluorescence decay recorded at 780 nm and at 14 K is single exponential with a decay time of 7.9 μs for Ti^{3+} : YAB and 8.9 μs for Ti^{3+} : GAB. At room temperature the fluorescence decay time reduced to ca 1.0 μs for both Ti^{3+}-doped crystals. The lifetime of the luminescence is consistent with electric dipole transitions induced by odd-parity distortions of the crystal field. The luminescence

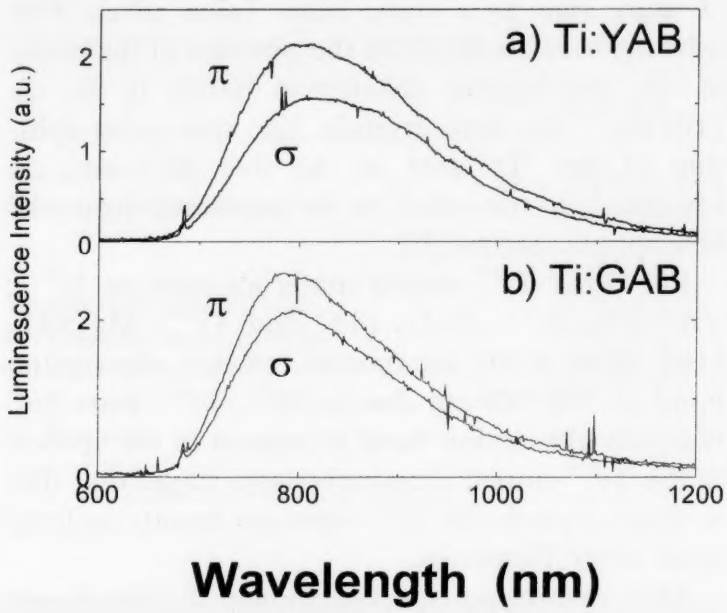

Fig. 4. Polarised photoluminescence spectra of Ti^{3+}-ions in (a) $YAl_3(BO_3)_4$ and (b) $GdAl_3(BO_3)_4$, measured at 300 K. Also revealed are the sharp R-lines near 685 nm due to trace amounts of Cr^{3+} impurity in the crystal.

decay may occur via pure radiative processes, which are independent of temperature, or by temperature-dependent radiative and nonradiative schemes. Appropriate temperature dependence measurements, required for a full analysis of the de-excitation process, have not been undertaken. Nevertheless it is apparent that the reduced lifetime at 300 K is due to the combined effects of phonon-induced radiative and nonradiative decay [5, 17].

4. Concluding remarks

Large crystals of $RAl_3(BO_3)_4$, where R = Y or Gd, were grown by TSSG in a nitrogen atmosphere. The use of a $K_2Mo_3O_{10}/B_2O_3$ flux combined with a slow cooling rate were effective in reducing problems of inclusions and striations normally encountered in the growth of these crystals. As a result there was a significant decrease in cracking, although minor fractures were found to persist in regions of crystal near the seed. A nitrogen gas flow successfully eliminated oxygen from the growth furnace, enabling Ti to substitute in the tripositive oxidation state for Al^{3+} with a segregation coefficient greater than one.

The Ti^{3+}-ion contains a single 3d electron, yielding a ^2D ground state for the free ion. The five-fold orbital degeneracy of the ^2D state is lifted by the crystal field of the host crystal. The dominant octahedral term splits the Ti^{3+} levels into an orbital triplet $^2T_2$ ground state and an orbital doublet ^2E excited state. The orbital degeneracy of the ground state is completely lifted by the combined effects of trigonal symmetry and spin–orbital coupling. The total splitting of the ground state is only ca. 100–200 cm^{-1}. The ^2E excited state is split by a static Jahn–Teller effect into two spin doublets separated by ca. 2000–2240 cm^{-1} [17]. The consequences of these splittings and the strong electron–phonon coupling are that two overlapping broad absorption bands separated by ca. 2000–2500 cm^{-1} are observed in the visible region. Luminescence transitions occur from the lower of the two exited states to the three spin doublets of the electronic ground state, overlap of these broad vibronic transitions resulting in a single broad luminescence band. The absorption and luminescence spectra shown in Figs. 2 and 3 are similar to those of$Ti^{3+}:Al_2O_3$, Ti^{3+} : YAG and Ti^{3+} : YAP. A comparison of the spectral characteristics of the $Ti^{3+}:RAl_3(BO_3)_4$ compounds with other Ti^{3+}-doped crystals is given in Table 2.

The absorption spectra of $Ti^{3+}:RAl_3(BO_3)_4$ are shifted some 30–40 nm to longer wavelengths and have larger absorption coefficient than other Ti^{3+}-doped hosts referred to in Table 2. The absorption cross-sections of $Ti^{3+}:RAl_3(BO_3)_4$ crystals at the peak of the absorption band for the π-polarisation has been calculated at room temperature using

$$\sigma_a = \frac{\alpha}{N_c}, \tag{1}$$

where α is absorption coefficient and N_c is concentration of Ti^{3+}-ions in the crystal [17]. The crystals of $Ti^{3+}:RAl_3(BO_3)_4$ contain ca. 0.5 at% Ti_2O_3, corresponding to Ti^{3+} concentrations of $N_c \cong 8.3\times10^{-19}\,cm^2$ in YAB and $\cong 8.8\times10^{-19}\,cm^2$ in GAB. The calculated absorption cross-section, σ_a are $\cong 1.2\times10^{-20}\,cm^2$ and $\cong 1.0\times10^{-20}\,cm^2$ for Ti^{3+}-doped YAB and GAB, respectively.

Table 2
Experimental spectral values and estimation of 10Dq for $Ti^{3+}:RAl_3(BO_3)_4$ compared with other materials

Crystal	YAB	GAB	YAG	Al_2O_3	YAP
E_a^- (cm^{-1})	17300	17100	16700	18200	20400
E_a^+ (cm^{-1})	19500	19200	20000	20400	23500
E_e (cm^{-1})	13160	13070	13300	13500	16400
Dq	1840	1815	1835	1930	2195
$\tau_{300\,K}$ (μs)	~1.0	~1.0	2.0	3.2	11.4
$\tau_{14\,K}$ (μs)	7.9	8.9	50	3.8	17.5
Half-width (cm^{-1}) ($^2E \rightarrow {}^2T_2$)	3850	3470	2800	3200	3310
ΔE_{stoke} (cm^{-1})	5240	5080	5050	5360	4360
σ_a (cm^2)	$\cong 1.2\times10^{-20}$	$\cong 1.0\times10^{-20}$	5×10^{-21}	4.3×10^{-20}	2.9×10^{-20}
σ_e (cm^2)	2.2×10^{-19}	2.4×10^{-19}	8×10^{-20}	3.2×10^{-19}	3.7×10^{-20}
Ref.			[3, 18]	[2, 18]	[4, 5, 18, 19]

The luminescence spectra of $Ti^{3+}:RAl_3(BO_3)_4$ shown in Fig. 3 have maxima near 803 nm and FWHM of 3850 cm^{-1} for $Ti^{3+}:YAl_3(BO_3)_4$ crystal and ~790 and ~3470 cm^{-1} for $Ti^{3+}:GdAl_3(BO_3)_4$. The bandwidth is very similar to that observed for $Ti^{3+}:Al_2O_3$ at room temperature and the corresponding transition is from the ^2E excited to $^2T_2$ ground state. The effective emission cross-sections, estimated from

$$\sigma_e = 3\frac{\lambda^2}{4\pi^2\tau n^2\,\Delta\nu} \tag{2}$$

in which the lifetime is τ, the transition wavelength is λ, the refractive index is n and the homogeneous linewidth (FWHM) is $\Delta\nu$. The refractive index n of $RAl_3(BO_3)_4$ crystals is ~1.75 giving a value of $\sigma_e = 2.2\times10^{-19}\,cm^2$ for $Ti^{3+}:YAl_3(BO_3)_4$ and $\sigma_e = 2.4\times10^{-19}\,cm^2$ for $Ti^{3+}:GdAl_3(BO_3)_4$ at the peak wavelength of the band. The measured fluorescence decay times at 14 and 300 K are quite similar to that of the $Ti^{3+}:Al_2O_3$, as are the general band characteristics. These results suggest that the Ti^{3+}-doped rare earth aluminoborates have significant potential as gain media in tunable near-infrared lasers.

Acknowledgements

The authors are indebted to the Rolling Grant GR/K04392, jointly funded by EPSRC and the Malvern MoD (DRA) of which this investigation forms a part. One of the authors, Guofu Wang, wishes to acknowledge the University of Strathclyde for their award of a John Anderson Research Scholarship.

References

[1] P. Moulton, Optics News 8 (1982) 9.
[2] P. Moulton, J. Opt. Soc. Am. B 3 (1986) 125.
[3] F. Bantien, P. Albers, G. Huber, J. Lumin. 36 (1987) 363.
[4] K.L. Schepler, in: A.B. Budgor, L. Esterowitz, L.G. DeShazer (Eds.), Tunable Solid-State Laser II, Springer, Berlin, 1986, p. 235.
[5] T. Wegner, K. Petermann, Appl. Phys. B 49 (1989) 275.
[6] P.F. Moulton, P. Lacovara, L. Esterowitz, R. Allen, in: P. Hammerling, A. Budgor, A. Pinto (Eds.), Tunable Solid State Lasers, Springer, Berlin, 1985, p. 4.
[7] A. Cotton, G. Wilkinson, Advanced Inorganic Chemistry, Part 3, Wiley, New York.
[8] R.M. Macfarlane, J.Y. Wong, M.D. Sturge, Phys. Rev. 166 (1968) 250.
[9] B.F. Gächter, J.A. Koningstein, J. Chem. Phys. 60 (1974) 2003.
[10] S.F. Akhmetov, G.L. Akhmetova, V.S. Kovalenko, N.I. Leonyuk, A.V. Pashkova, Sov. Phys. Dokl. 23 (1978) 107.
[11] G. Wang, H.G. Gallagher, T.P.J. Han, B. Henderson, J. Crystal Growth 153 (1995) 169.
[12] G. Wang, H.G. Gallagher, T.P.J. Han, B. Henderson, J. Crystal Growth 163 (1996) 272.
[13] E.L. Belokoneva, A.V. Azizov, N.I. Leonyuk, M.A. Simonov, N.V. Belov, Zhurnal Strukturnol Khimii 22 (1981) 196.

[14] H.Y.-P. Hong, K. Dwight, Mater. Res. Bull. 9 (1974) 1661.
[15] R.L. Aggarwal, A. Sanchez, M.M. Stuppi, R.E. Fahey, A.J. Strauss, W.R. Rapoport, C.P. Khattak, IEEE J. Quantum Electron. QE-24 (1988) 1003.
[16] S. Li, L. Liu, Z. Wang, Y. Tiang, X. Jiang, X. Wu, J. Crystal Growth 139 (1994) 327.
[17] B. Henderson, G.F. Imbusch, Optical Spectroscopy of Inorganic Solids, Oxford University Press, Oxford, 1989.
[18] M. Yamaga, Y. Gao, F. Rasheed, K.P. O'Donnell, B. Henderson, B. Cockayne, Appl. Phys. B 51 (1990) 329.
[19] C.P. Khattak, F. Schmid, K.F. Wall, R.L. Aggarwal, Growth, Characterisation and Applications of Laser Host and Nonlinear Crystals, SPIE, vol. 1104, 1989, p. 95.

ELSEVIER

Journal of Crystal Growth 181 (1997) 55–60

JOURNAL OF CRYSTAL GROWTH

Oxygen nonstoichiometry in copper iron oxide [$CuFeO_{2+\delta}$] single crystals

Tong-Rong Zhao[a,*], Masashi Hasegawa[b], Humihiko Takei[c]

[a] *The State Key Laboratory of High Performance Ceramics and Superfine Microstructures, Shanghai Institute of Ceramics, Chinese Academy of Sciences, 1295 Dingxi Road, Shanghai 200050, People's Republic of China*

[b] *The Institute of Solid State Physics, The University of Tokyo, 7-2-1 Roppongi, Minato-ku, Tokyo 106, Japan*

[c] *Faculty of Science, Osaka University, 1-16 Machikaneyama, Toyonaka, Osaka 560, Japan*

Received 21 December 1996; accepted 3 February 1997

Abstract

Compositional, structural, and density measurements have been carried out on $CuFeO_{2+\delta}$ single crystals grown under surrounding atmospheres of CO_2, Ar, and Ar containing oxygen (Ar + 0.5% O_2, Ar + 1% O_2, and Ar + 2% O_2) by means of the traveling Cu_2O-solvent floating-zone method. The crystal grown in Ar + 0.5% O_2 atmosphere shows the stoichiometric composition, while reducing and oxidizing atmospheres result in oxygen nonstoichiometry in $CuFeO_{2+\delta}$ single crystals, with the component changing either from $Cu_{1.00}Fe_{1.00}O_{1.86}$ to $Cu_{1.00}Fe_{1.00}O_{2.06}$ or from $Cu_{1.00}Fe_{1.00}O_{1.94}$ to $Cu_{1.00}Fe_{1.00}O_{2.08}$. With increase in oxygen content, the a_h-axis extends from 3.0311 to 3.0325 Å, and the c_h-axis compresses from 17.154 to 17.149 Å, while the structural symmetry does not change.

1. Introduction

Nonstoichiometry in metal oxides has been of great interest because it affects sensitively the chemical and physical properties of solid-state materials. In study of the transport properties of oxide materials, it is necessary to obtain accurate information concerning the metal/oxygen ratio as a function of temperature and oxygen pressure. So far, several techniques have been employed to determine the thermodynamic properties and nonstoichiometry of metal oxides [1–3].

Cuprous ferrite $CuFeO_2$ is one of the typical stable compounds in the Cu–Fe–O ternary system exhibiting the so-called delafossite structure [4–7]. As it is composed of two transition metal oxides of copper and iron, $CuFeO_2$ reveals a tendency to deviate from the stoichiometry, and the extent of deviation is dependent on the composition of the surrounding atmosphere.

The purpose of the present work was to investigate the oxygen nonstoichiometry in $CuFeO_{2+\delta}$ single crystals on the basis of knowledge of crystal chemistry and crystal structure.

* Corresponding author.

0022-0248/97/$17.00 © 1997 Elsevier Science B.V. All rights reserved
PII S0022-0248(97)00187-5

2. Experimental procedure

2.1. Preparation of $CuFeO_{2+\delta}$ single crystals

Powders of CuO (99.9%) and Fe_2O_3 (reagent grade) were used as starting materials. They were mixed in a molar ratio 2 : 1 and prefired at 800°C for 15 h in air to obtain a partial reaction of the mixed oxides. X-ray powder diffraction (XPD) examinations confirmed that $CuFe_2O_4$ and CuO were the constituent compositions. The prefired products were mixed again and heated to 950°C in an alumina furnace, and the solid-state reaction between $CuFe_2O_4$ and CuO was accomplished in 24 h under a flow of nitrogen. Single phase $CuFeO_2$ was confirmed by XPD and no extraneous composition was found. The cylindrical ceramic rods were hydrostatically formed from the synthesized $CuFeO_2$ powder and sintered again in argon 10–20 h at 1000°C to reduce further shrinkage and increase the density of the final rods.

Crystal growth was carried out in an infrared radiation furnace by means of the traveling Cu_2O-solvent floating-zone method, which has been described in detail elsewhere [8–10]. The surrounding atmospheres of CO_2, Ar, and Ar with excess of oxygen (Ar + 0.5% O_2, Ar + 1% O_2, and Ar + 2% O_2) were employed during crystal growth. XPD and X-ray precession examinations identified that the as-grown crystals are of the trigonal $CuFeO_2$ with good crystallinity.

2.2. Compositional and density measurement

Several samples were selected from the $CuFeO_{2+\delta}$ single crystals grown under CO_2, Ar, Ar + 0.5% O_2, Ar + 1% O_2, and Ar + 2% O_2, respectively. Compositions of the samples were measured by using a scanning electron microscope (SEM) together with electron probe microanalysis (EPMA) method with metal copper and iron (ASTIMEX Scientific Ltd.) as standards, and the unit-cell parameters for $CuFeO_{2+\delta}$ were determined by means of XPD with a cell refining program. The density of the single crystal samples was determined by using the following two methods.

(1) d_{cal} was obtained by the calculation from the chemical composition (or the formula) measured by EPMA, and from the volume of the unit cell determined by the XPD data according to the formula

$$d_{cal} = \frac{\text{Formula weight} \times Z \times 1.6603 \times 10^{-24}}{\text{Unit cell volume } (\text{Å}^3) \times 10^{-24}} \quad (\text{g/cm}^3), \tag{1}$$

where the formula weight is a sum of the mass of its constituent atoms or ions, Z is the number of molecules in one unit, and 1.6603×10^{-24} is the reciprocal of Avogadro's constant [11].

(2) d_{obs} was measured by using a buoyancy method based on the Archimedean principle. The weight of the sample crystals was measured by means of a microbalance (± 0.0001 g) in air and then in pretreated deionized water, for which density is precisely known and is corrected for any temperature. During the measurement the temperature and the dissolved gas in water were carefully controlled, because the former affects the density of water and the latter may cause the formation of bubble on the surface of specimen to reduce the apparent weight. By using measured d_{obs}, the formulae of the as-grown $CuFeO_{2+\delta}$ single crystals were obtained.

3. Results and discussion

As shown in Table 1, the molar ratio of metal copper to iron in either crystal is found 1 : 1, while the content of oxygen composition changed systematically with increasing oxygen partial pressure in the surrounding atmosphere. The chemical formulae of the as-grown single crystals under different surrounding atmospheres are written either from the EPMA measurement or density measurement as in Table 1. In either case, the crystal grown in Ar + 0.5% O_2 is very close to the stoichiometric composition, while reducing (CO_2 and pure Ar) and oxidizing (Ar + O_2) atmospheres with oxygen content more than 1% result in the deviation from the stoichiometric composition. Oxygen ratio in chemical formulae F_2 is more precise than in F_1 because of the high accuracy of buoyancy method.

Table 1
XPD and EPMA results for $CuFeO_{2+\delta}$ single crystals

Sample	Lattice parameters			Density (g/cm^3)		Chemical formulae	
	a (Å)	c (Å)	V (Å^3)	d^a_{cal}	d^b_{obs}	F^c_1	F^d_2
CO_2	3.0311	17.154	136.50	5.44	5.489	$CuFeO_{1.86}$	$CuFeO_{1.939}$
Ar	3.0312	17.154	136.50	5.46	5.509	$CuFeO_{1.89}$	$CuFeO_{1.974}$
Ar + 0.5% O_2	3.0314	17.154	136.51	5.52	5.532	$CuFeO_{1.99}$	$CuFeO_{2.014}$
Ar + 1% O_2	3.0317	17.150	136.51	5.54	5.565	$CuFeO_{2.03}$	$CuFeO_{2.070}$
Ar + 2% O_2	3.0325	17.149	136.58	5.56	5.580	$CuFeO_{2.06}$	$CuFeO_{2.085}$

[a] d^{cal} denotes the data calculated from the unit-cell parameters.
[b] d^{obs} denotes the data measured by means of buoyancy method.
[c] F^1 represents the formulae from EPMA measurement.
[d] F^2 represents the formulae from observed density.

3.1. Defect chemistry

From the knowledge of solid-state chemistry, nonstoichiometric compounds contain point defects which are formed thermodynamically. Point defects are atomistic in nature and the principal types are vacant sites, interstitial atoms or ions and substitutional impurity atoms or ions. In the case of oxides, defects can be considered as the result of an oxidation or a reduction reaction [12]. The defects contained in $CuFeO_{2+\delta}$ single crystals are caused by deficiency or excess of oxygen content, which is a function of oxygen partial pressure in the surrounding atmosphere. The Kröger–Vink notation [13] is employed in our discussion.

In reducing atmosphere, such as CO_2 and Ar, the deficiency of oxygen results in O^{2-} anion leaving its normal lattice position with a formation of anion vacancies in the crystal structure. In order to maintain the charge neutrality within the bulk of crystal, a part of the valence state of irons are considered as a change from Fe^{3+} to Fe^{2+} cations by the defect interaction,

$$2Fe_{Fe} + O_O^x \leftrightarrow 2Fe'_{Fe} + V_O^{\cdot\cdot} + \tfrac{1}{2}O_2, \quad (2)$$

which means a formation of the oxygen anion vacancy $V_O^{\cdot\cdot}$ resulting from its normal lattice site O_O. The Fe^{3+} cations in the normal site Fe_{Fe} catch electrons from the anion vacancy to form compensated defects. Eq. (2) can also be expressed as

$$O_O^x \leftrightarrow V_O^{\cdot\cdot} + \tfrac{1}{2}O_2 + 2e', \quad (3)$$

from which the equilibrium constant is obtained as

$$K = \frac{[V_O^{\cdot\cdot}][P_O]^{1/2}[e']^2}{[O_O^x]}. \quad (4)$$

Thus, the stoichiometry and hence the defect concentration is seen to depend on the oxygen partial pressure. The oxygen vacancy defects also result in a decrease of crystal density, as shown in Table 1.

On the other hand, the oxidizing atmosphere like Ar + 1% O_2 and Ar + 2% O_2 results in oxygen anions which then enter the interstices of the normal lattice sites. As a result, a part of Cu^+ cations changes their valence state to Cu^{2+},

$$2Cu_{Cu} + \tfrac{1}{2}O_2 \leftrightarrow 2Cu^{\cdot}_{Cu} + O_i''. \quad (5)$$

Eq. (5) can also be written as

$$\tfrac{1}{2}O_2 \leftrightarrow 2h^{\cdot} + O_i''. \quad (6)$$

The oxygen anions take up the interstitial position with the formation of $2h^{\cdot}$ and the overall charge neutrality is, therefore, preserved. Application of the law of mass action gives

$$[O_i''] \propto P_{O_2}^{1/2}. \quad (7)$$

The concentration of interstitial oxygen anion is therefore in proportion to the partial pressure of

oxygen, which is in agreement with the results in Table 1.

3.2. Crystal structure

The hexagonal lattice constants of the crystals calculated from the following (0 0 3), (0 0 6), (1 0 1), (0 1 2), (1 0 4), (0 1 5), (0 0 9), (0 1 8), (1 1 0), (1 0 $\overline{1}$ 0), (0 0 $\overline{1}$ 2), (0 1 $\overline{1}$ 1), (2 0 2), (2 0 8), and (0 1 $\overline{1}$ 4) diffraction lines in the XPD spectra are listed in Table 1, and the variations of the cell parameters with increasing oxygen are shown in Fig. 1. In reducing atmospheres, the unit-cell parameters almost unchanged. On the other hand, in oxidizing atmospheres, the a_h-axis extends from 3.0314 to 3.0325 Å with increasing δ, while c_h-axis shrinks from 17.154 to 17.149 Å, and the volume from 136.51 to 136.58 Å^3.

According to the close-packing principle, the structure of the space group R$\bar{3}$m is in the form of closest packing, of which the packing index is usually 74.05% [14]. On the other hand, the actual packing index for $CuFeO_2$ of the delafossite structure, based on the data listed in Table 2, is calculated about 53.50%. Considering that the space occupied by Cu^+, Fe^{3+} cations and O^{2-} anions is about 20% less than the theoretical occupation rate, it is possible to introduce excess oxygen without changing the structural symmetry [15], although a departure from the stoichiometry can cause a deformation of the unit-cell parameters, as shown in Table 1. The changes in the unit-cell parameters caused by the oxygen non-stoichiometry are explained as follows.

In reducing atmosphere, a part of Fe^{3+} cations of radius 0.76 Å changes to Fe^{2+} cations of radius 0.83 Å because of the deficiency of oxygen anions and the change results in the extension of the crystal structure (Fig. 2). As there is almost no change in the cell parameters, it is estimated that the change of the cation radius possibly compensates for the structural shrinkage caused by the oxygen deficiency. In the case of $CuFeO_{1.939}$, for example, the shrinkage caused by oxygen deficiency is approximated to $r_{O^{2-}} \times \delta \approx 0.080$ Å, while the actual volume increased from the change of Fe^{3+} cations is proportional to $(r_{Fe^{2+}} - r_{Fe^{3+}}) \times 2\delta \approx 0.020$ Å, which is only about a fourth of the value of the

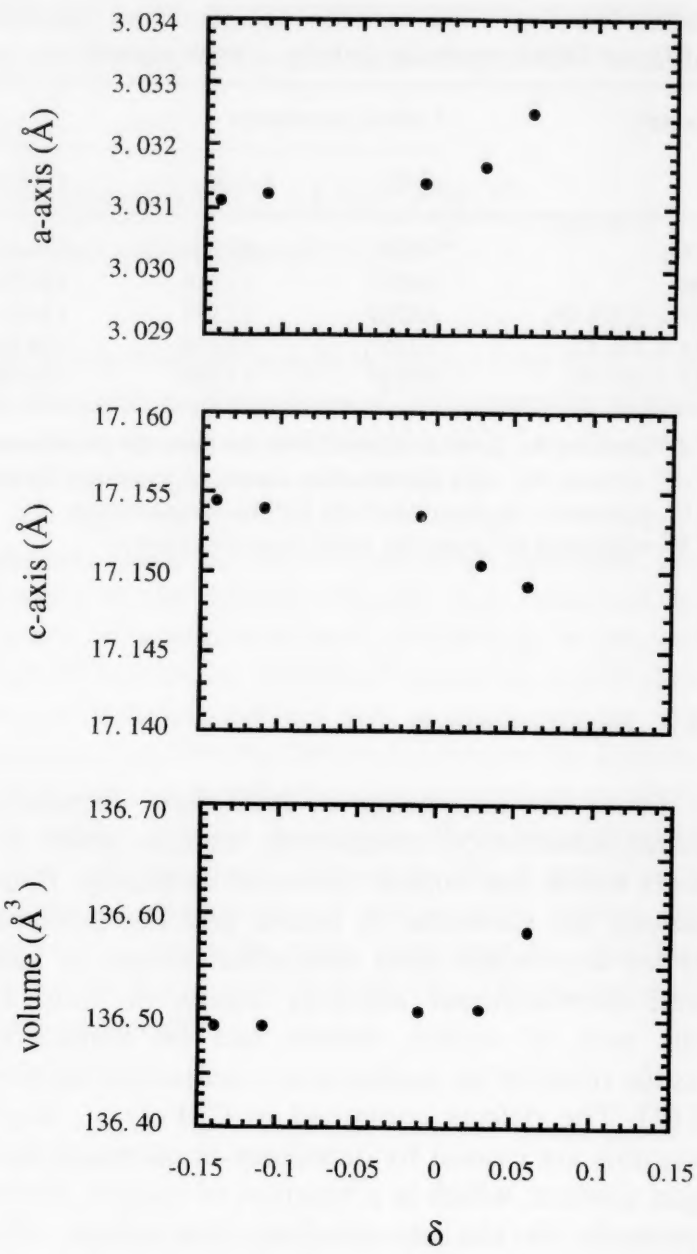

Fig. 1. Dependence of unit-cell parameters on the change of oxygen content δ.

Table 2
Structural parameters for $CuFeO_2$ (after Pabst [7] and Jaff [11])

Ionic radii (Å)		Distances ($u = \frac{1}{9}$) (Å)	
Fe^{3+}	0.67	Cu^+–Cu^+	3.035
Fe^{2+}	0.83	Fe^{3+}–Fe^{3+}	3.035
Cu^+	0.96	Cu^+–O^{2-}	1.899
Cu^{2+}	0.72	Fe^{3+}–O^{2-}	1.991
O^{2-}	1.32	O^{2-}–O^{2-}	2.583

shrinkage. As a result, both of the a_h- and c_h-axis should shrink. However, as shown in Table 1, the observed unit-cell parameters are almost unchanged. The reason is probably that the repulsive force among the cations around oxygen vacancy counteracts the structural shrinkage.

On the other hand, the oxidizing atmosphere introduces excess oxygen anions which presumably enter the interstices, as shown in Fig. 2. In order to eep the charge neutrality, a part of Cu^+ cations of radius 0.96 Å changes to Cu^{2+} cations of radius 0.72 Å and is supposed to result in the shrinkage of the c_h-axis in crystal structure (Fig. 2), where a vacant site can be structurally provided for oxygen in the Cu^{2+}-packed layers. Taking account of the cross-section of the Cu^{2+} cation triangular plane in Fig. 2, when an excess oxygen anion of 1.32 Å radius is inserted in, the distance between Cu^{2+} cations, i.e., the unit-cell parameter a_h, has to be enlarged. As a result, the crystal structure in the a_h-direction should be extended. In the case of $CuFeO_{2.085}$, for example, the shrinkage in the c_h-direction is roughly estimated according to the relation $(r_{Cu^+} - r_{Cu^{2+}}) \times 2\delta$ as 0.041 Å. However, the XPD result shows only 0.005 Å shrinkage. The reason is probably that the Coulombic repulsive force between the interstitial and lattice-site oxygen anions counteracts the shrinkage in the c_h-direction and results only in the extension in the a_h-direction, as shown in Table 1 and Fig. 2. Such anisotropic behavior in the a_h- and c_h-axis has also been observed in a high pressure experiment [16], where the a_h-axis has been found to shrink 3.9 times in comparison with the c_h-axis. This indicates that the packing feature along the a_h-axis in $CuFeO_2$ is much looser and that along the c_h-axis is tight.

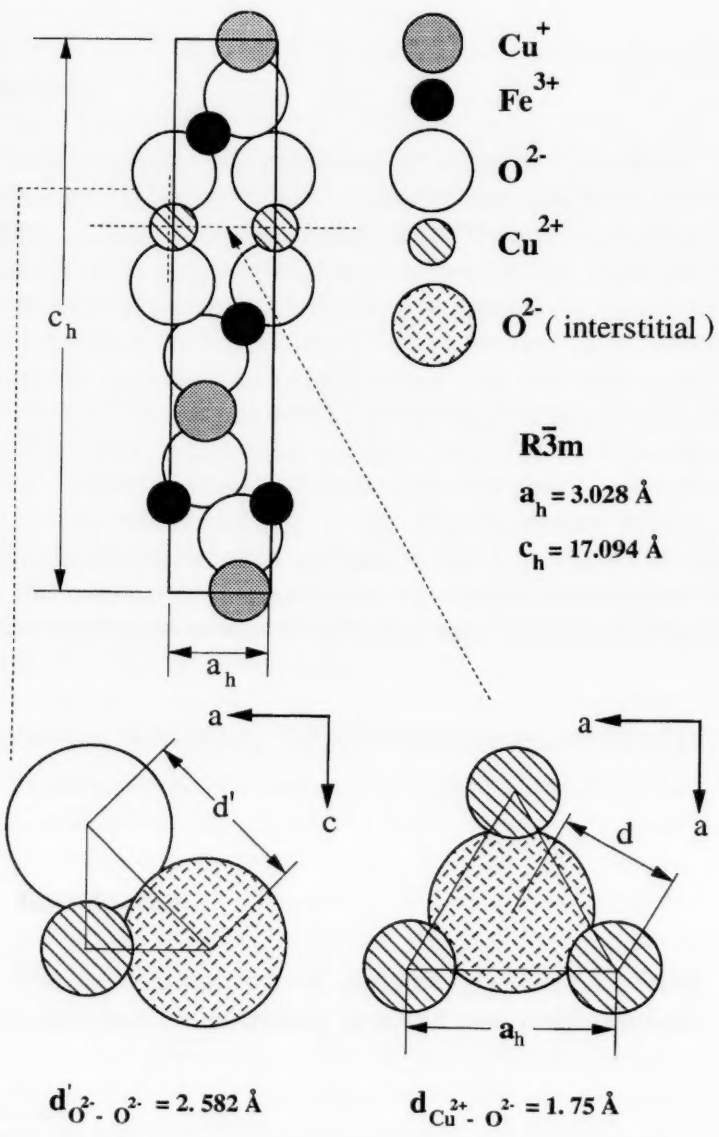

Fig. 2. Defect chemistry in $CuFeO_{2+\delta}$ single crystal.

4. Conclusion

EPMA and X-ray analyses on the crystals grown under different surrounding atmospheres indicate that $CuFeO_{2+\delta}$ shows non-stoichiometric compositions changing from $\delta = -0.14$–0.06 to $\delta = 0.06$–0.09 with increasing oxygen partial pressure. The crystal grown under Ar + 0.5% O_2 shows the stoichiometric composition. X-ray diffraction study on the $CuFeO_2$ single crystals indicates that the departure from the stoichiometry causes deformation of the crystal lattice without changing the structural symmetry. With the increase of oxygen partial pressure, the a_h-axis extends from 3.0311 to 3.0325 Å, while the c_h-axis compresses from 17.154 to 17.149 Å.

Acknowledgements

The authors would like to express their appreciation to Mrs. F. Sakai of the University of Tokyo for her help in the SEM-EPMA measurement, and to Mr. M. Koike of the University of Tokyo for his help in taking care of the equipment.

References

[1] K.J. Bachmann, H.L. Hwang, C. Schwab (Eds.), Nonstoichiometry in Semiconductors, Part I, Elsevier, Amsterdam, 1992.

[2] J. Nowotny, W. Weppner (Eds.), Nonstoichiometric Compounds, ch. 1, Kluwer, Dordrecht, 1989.

[3] L. Mandelcorn (Ed.), Nonstoichiometric Compounds, ch. 3, Academic Press, New York, 1964.

[4] Rogers, Amer. J. Sci. 35 (1964) 290.

[5] W. Soller, A.J. Thompson, Phys. Rev. 47 (1935) 644.

[6] A. Pabst, Amer. Mineralogist 23 (1938) 175.

[7] A. Pabst, Amer. Mineralogist 31 (1946) 539.

[8] T.R. Zhao, M. Hasegawa, M. Koike, H. Takei, J. Crystal Growth 148 (1995) 189.

[9] T.R. Zhao, M. Hasegawa, H. Takei, J. Crystal Growth 154 (1995) 322.

[10] T.R. Zhao, M. Hasegawa, H. Takei, J. Mater. Sci. 31 (1996) 5657.

[11] H.W. Jaff, Crystal Chemistry and Refractivity, ch. 4, 10, Cambridge University Press, New York, 1988.

[12] C. Monty, in: A.V. Chadwick, M. Terenzi (Eds.), Defect in Solids, ch. 1, Plenum, New York, 1986.

[13] F.A. Kröger, H.J. Vink, in: F. Seitz, D. Turnbull (Eds.), Solid State Physics III, Academic Press, New York, 1956, p. 307.

[14] B.K. Vainshtein, V.M. Fridkin, V.L. Indenbom, Modern Crystallography II, Springer, Berlin, 1982, p. 104.

[15] R.J. Cava, H.W. Zandbergen, A.P. Ramirez, H. Takagi, C.T. Chen, J.J. Krejewski, W.F. Peck Jr., J.V. Waszczak, G. Meigs, R.S. Roth, L.F. Schneemeyer, J. Solid State Chem. 104 (1993) 437.

[16] T.R. Zhao, M. Hasegawa, H. Takei, T. Kondou, T. Yagi, Jpn. J. Appl. Phys. 35 (1996) 3535.

ELSEVIER

Journal of Crystal Growth 181 (1997) 61–69

JOURNAL OF CRYSTAL GROWTH

Diffusion and cluster formation in aqueous solutions of potassium aluminum sulfate

Soojin Kim, Allan S. Myerson*, Michael Kohl

Department of Chemical Engineering, Chemistry, and Materials Science, Polytechnic University, 6 Metrotech Center, Brooklyn, New York 11201, USA

Received 5 August 1996; accepted 17 March 1997

Abstract

The property and structure of aqueous $KAl(SO_4)_2 \cdot 12H_2O$ solutions were investigated by the measurements of diffusion coefficients and concentration gradients developed in vertical columns of supersaturated solutions. The diffusion coefficients decreased linearly with increasing concentration up to the saturation point and decreased more rapidly with increasing concentration in the supersaturated region. This drastic decrease of diffusion coefficient at supersaturated concentrations was similar to that observed in other supersaturated aqueous solutions which was attributed to the formation of solute clusters in metastable solutions. A cluster diffusion model employing the solution viscosity and thermodynamic data can provide a good correlation between predicted and experimental diffusion coefficients in undersaturated solutions, but fails to provide a reasonable prediction of the much lower values of diffusion coefficients in supersaturated solutions. The average size of the diffusing entities estimated from the diffusion coefficient data showed a steady growth with increasing concentration in the undersaturated region and a faster growth with increasing concentration in the supersaturated region. The average cluster sizes in supersaturated solutions were estimated from the data of concentration gradients in vertical columns and solution thermodynamics using the concept of the number and weight average molecular weights. The estimated cluster size increased with increasing degree of supersaturation as well as solution "age", and showed good agreement with those estimated from the diffusion coefficient data.

Keywords: $KAl(SO_4)_2 \cdot 12H_2O$; Supersaturated solutions; Diffusion; Cluster

1. Introduction

The crystallization of $KAl(SO_4)_2 \cdot 12H_2O$ from solution has been widely studied not only because it is an important material in the chemical industry, and but also because it is easy to work with in the laboratory, making it a desirable model system for crystallization research. In addition, its relatively wide metastable zone width makes it an ideal system for the study of supersaturated solution properties. Although $KAl(SO_4)_2 \cdot 12H_2O$ has been studied extensively for the kinetics of crystal

* Corresponding author. E-mail: amyerson@roebling.poly.edu.

0022-0248/97/$17.00 © 1997 Elsevier Science B.V. All rights reserved
PII S0022-0248(97)00221-2

growth and crystal morphology [1–3], few investigations into its supersaturated solution properties have been performed.

The study of supersaturated solution structure is important to the fundamental understanding of the nucleation process and crystal growth mechanism. Researchers have investigated the solution structures of many supersaturated solutions using a variety of experimental techniques. Among the major efforts in this area, measurements of solution properties such as density, refractive index, diffusivity, and viscosity have been conducted by some investigators [4–6]. Others have implemented spectroscopic techniques to compare the solution structure of a supersaturated solution to that of an undersaturated solution [7, 8]. In addition, concentration gradients developed in long vertical columns of isothermal supersaturated solutions have been investigated to study the solution structure under the influence of gravitational fields [9–12]. In many of the experiments, the presence of solute clusters has been indirectly observed, confirming the classical nucleation theory based on the assumption that concentration fluctuations in supersaturated solutions give rise to clusters which can coalesce to form nuclei.

It is the purpose of this work to investigate the supersaturated solution properties of $KAl(SO_4)_2 \cdot 12H_2O$ through the experimental investigation of diffusivity and concentration gradients developed in vertical columns, and to consider the solution structure in relation to cluster formation and solution thermodynamic properties.

2. Experimental procedure

2.1. Diffusivity

Measurement of diffusion coefficients was carried out using Göuy interferometry, monitoring free diffusion across a sharp boundary between two solutions of slightly different concentration in an isothermal diffusion cell. The change of concentration due to bulk diffusion between the two solutions was traced optically by observing interference fringes with respect to time. Details of the experiment can be found elsewhere [13]. Measurements were conducted at 25°C using aqueous solutions of $KAl(SO_4)_2 \cdot 12H_2O$ at the concentration range of entire undersaturation and up to the supersaturation of 15%.

2.2. Column experiments

Column experiments were conducted using a jacketed glass column with two sampling ports at top and bottom, 60 cm apart. After the column was filled with $KAl(SO_4)_2 \cdot 12H_2O$ solution of a desired concentration, maintained at 45°C by a circulating water bath, it was cooled uniformly to 25°C to make the solution supersaturated. The solution was then left stationary and isothermal for several days. The densities of the sampled solution from the top and bottom of the column were measured at 30°C by a Mettler–Paar density meter accurate to 1×10^{-5} g/cm^3. Density values were converted to concentration using a calibration curve obtained from separate measurements. A series of experiments were conducted using solutions of different degree of supersaturation at 25°C.

3. Results and discussion

3.1. General trend of diffusion coefficients

Diffusion coefficient is important information for a quantitative analysis in the studies of crystal growth and dissolution. Despite extensive research into the crystallization kinetics of $KAl(SO_4)_2 \cdot 12H_2O$, there have been few reports about its diffusion coefficients in solutions. Few data of diffusion coefficients in undersaturated solution reported in the literature [14, 15] show a wide discrepancy between themselves, with the difference being an order of magnitude. There has been almost no reliable data of diffusion coefficients in the wide range of concentration that we investigated.

Fig. 1 shows the diffusion coefficient measured as a function of solution concentration at 25°C. Diffusion coefficient declined slowly but continuously with concentration in the undersaturated region and declined more rapidly in the supersaturated region. This rapid decrease of diffusion coefficient with concentration after the saturation point is

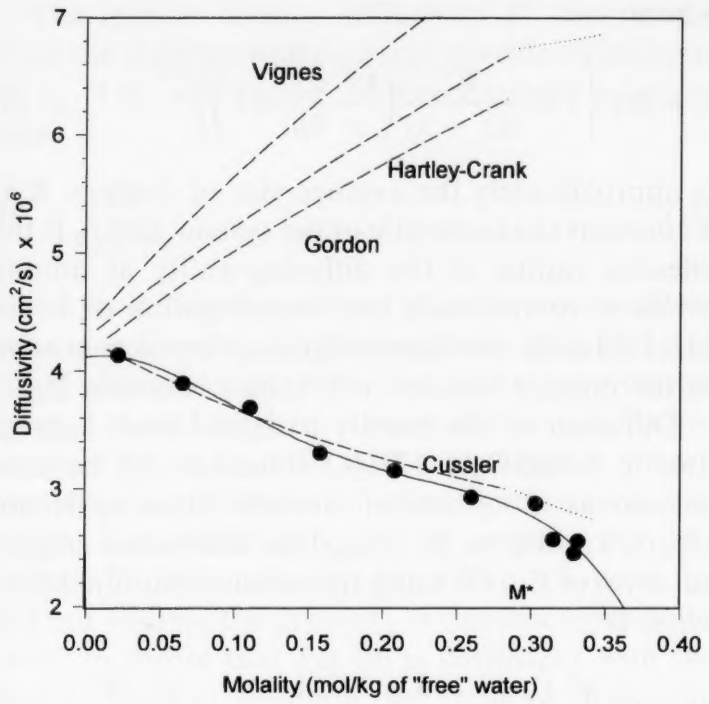

Fig. 1. Experimental data points of the diffusion coefficients and theoretically predicted diffusion coefficients in aqueous solutions $KAl(SO_4)_2 \cdot 12H_2O$ at 25°C. M* indicates the saturation point.

analogous to the cases of many other aqueous systems previously investigated (urea, glycine, NaCl, and KCl) [13, 16, 5, 17]; it has been attributed to the formation of solute clusters in supersaturated solutions. The decreasing trend of diffusion coefficient in undersaturated concentration region is distinct from the general trend of diffusion coefficients in the other electrolyte solutions (NaCl and KCl), which showed a maximum near saturation point. This behavior of continuously decreasing diffusion coefficient is more similar to that of nonelectrolyte solutions such as urea and glycine.

3.2. Diffusivity and solution thermodynamic properties

Numerous efforts of investigators to theoretically calculate diffusion coefficient with predictive equations have been hindered by the lack of thermodynamic data of many solutions, especially in high-concentration range, since most of the theoretically derived equations involve the infinite dilution diffusivity term and a thermodynamic correction term. Thus, most of the theoretical attempts to calculate diffusion coefficient have been limited to solutions of very low concentration or ideal solutions.

The activities of concentrated and supersaturated $KAl(SO_4)_2 \cdot 12H_2O$ solutions have been recently reported [18], based on the measurements of water activity of $KAl(SO_4)_2 \cdot 12H_2O$ using electrodynamic microparticle levitator [19, 20]. The water activity data at 25°C can be extrapolated to lower-concentration range and represented by the polynomial equations:

$$a_w = 1.0 - 0.01842m - 0.03707m^2 \quad (1)$$

for $0 < m < 1.2$ mol/kg of "free" water, and

$$a_w = 1.04 - 1.702 \times 10^{-1} m + 2.788 \times 10^{-2} m^2 - 2.443 \times 10^{-3} m^3 + 1.055 \times 10^{-4} m^4 - 1.757 \times 10^{-6} m^5 \quad (2)$$

for $1.2 < m < 20$ mol/kg of "free" water.

Many predictive equations such as the Gordon equation [21]

$$D = D^0 \left(\frac{\mathrm{d} \ln a}{\mathrm{d} \ln x} \right) \frac{\eta^0_{\mathrm{slv}}}{\eta}. \quad (3)$$

Hartley–Crank equation [22]

$$D = (x_{\mathrm{slv}} D^0 + x D^0_{\mathrm{slv}}) \left(\frac{\mathrm{d} \ln a}{\mathrm{d} \ln x} \right) \frac{\eta^0_{\mathrm{slv}}}{\eta} \quad (4)$$

and Vignes equation [23]

$$D = (D^0)^{x_{\mathrm{slv}}} (D^0_{\mathrm{slv-slt}})^x \left(\frac{\mathrm{d} \ln a}{\mathrm{d} \ln x} \right) \quad (5)$$

use the thermodynamic correction term, $\mathrm{d} \ln a / \mathrm{d} \ln x$, which can be calculated using the Gibbs–Duhem relation as follows:

$$\frac{\mathrm{d} \ln a}{\mathrm{d} \ln x} = -\frac{1000}{18.02m} \frac{\mathrm{d} \ln a_w}{\mathrm{d} \ln m} \left(1 + \frac{18.02m}{1000} \right), \quad (6)$$

where a and m are the activity and molality of the hydrated solute in "free" water. Throughout this paper, we use the activity and molality of hydrated

solute in "free" water without considering separate ionic quantities, because we treat solute molecules each with 12 molecules of bound water as the diffusing entities. This is justified by the fact that the motion of ions in electrolyte solutions is restricted by the condition of electrical neutrality, hence, the oppositely charged ions move in the same direction at equal speeds. Furthermore, there is strong reason to believe that the majority of the ions in these solutions are associated into a neutral molecular form. Moreover, it is well known that most ions in aqueous solutions have a firmly attached group of water molecules which act as a part of the diffusing solute entity [22]. Detailed discussions of this issue follow in the next sections.

The calculation of $\mathrm{d}\ln a/\mathrm{d}\ln x$ using Eq. (6) yields an increasing function of concentration in the concentration range of our diffusion coefficient data but approaches zero as the concentration is increased to very high supersaturation nearing the limit of metastability. Hence, the diffusion coefficient is expected to approach zero nearing the spinodal point. Fig. 1 illustrates the calculated diffusion coefficients from the Eqs. (3)–(5) using the thermodynamic correction term computed using Eq. (6). In using the above equations, D^0, the infinite dilution diffusivity, was determined empirically by extending our diffusion coefficient data at very low concentration, and the solution viscosity data were adapted from the literature [14]. As shown in the figure, the calculated values of diffusion coefficient are in poor agreement with the experimental data, due to the large influence of the thermodynamic term increasing with concentration. Although these equations theoretically predict that diffusion coefficient should reach zero at the limit of metastability, they cannot predict all aspects of diffusion and are quite inadequate in the description of $KAl(SO_4)_2 \cdot 12H_2O$ diffusion.

3.3. *Diffusion of clusters*

Diffusion in concentrated, non-ideal solutions as movement of clusters was described by Cussler [24] using the equation

$$D = \frac{kT}{2\pi\eta\xi}, \tag{7}$$

where

$$\xi = 2r_0 \left\{1 + \frac{K}{x(1-x)}\left(\frac{kT}{x}\frac{\partial x}{\partial \mu} - 1\right)\right\}^{1/2} \tag{8}$$

is approximately the average size of clusters. K is a constant characteristic of the system, and r_0 is the effective radius of the diffusing entity at infinite dilution. At infinitely low concentration or in an ideal solution the thermodynamic correction term in the bracket reduces to 1, thus ξ becomes $2r_0$.

Diffusion of the heavily hydrated ionic aggregates in $KAl(SO_4)_2 \cdot 12H_2O$ solutions can be considered as a motion of clusters. Since r_0 is not clearly known, we have used the alternative empirical form of Eq. (7) using the infinite dilution diffusivity, D^0

$$D = D^0 \frac{\eta^0}{\eta}\left\{1 + \frac{K}{x(1-x)}\left(\frac{\mathrm{d}\ln x}{\mathrm{d}\ln a} - 1\right)\right\}^{-1/2}. \tag{9}$$

As illustrated in Fig. 1, the calculated values of diffusion coefficient fit the experimental data very well in the entire undersaturated concentration range but fail to predict the more rapid decline of diffusion coefficient after the saturation point. It appears that the use of only the solution thermodynamic data and viscosity data in the calculation is insufficient to accurately describe the pattern of diffusion coefficient in supersaturated solutions, where the average cluster sizes should be much greater. Furthermore, the assumption of a constant value of D^0 in Eq. (9), which implies that the solute size is unchanged as the supersaturation increases, is probably not valid because highly complex salts such as this usually have varying degrees of hydration as supersaturation increases [22]. Regardless of whether the hydration number increases or decreases as supersaturation increases, it probably affects the way the molecules form clusters. Therefore, consideration of some structural details of the solution is essential for a more complete theoretical treatment of diffusion coefficients in supersaturated solutions. Nevertheless, employment of the cluster diffusion model in undersaturated concentrations seems to provide a good estimate of diffusion coefficient for $KAl(SO_4)_2 \cdot 12H_2O$, despite the fact that it remains highly empirical due to the required estimation of the parameters K and D^0.

The infinite dilution diffusivity D^0 determined from the experimental data can provide an estimate of r_0. The well-known Stokes–Einstein equation gives

$$D^0 = \frac{kT}{6\pi\eta^0 r_0}, \tag{10}$$

which is widely known to be accurate for dilute solutions. Cussler's original equation [Eq. (7)] is in slight disagreement with the above expression, since it would lead to numerical constant 4π instead of 6π in Eq. (10). Although Cussler himself empirically modified his original derivation of ξ to make his expression of D reduce to the Stokes–Einstein equation for dilute solutions, he did not address the problem of this discrepancy. In order to insure that Eq. (9) is consistent with the Stokes–Einstein equation, we propose to modify Eq. (7) so that

$$D = \frac{kT}{3\pi\eta\xi}. \tag{11}$$

This is justified by the fact that a few authors, including Cussler, mentioned the uncertainty and unimportance of the numerical constant (2π or 3π) which was often used differently depending on models and systems [24, 22].

r_0, Stokes law radius, calculated from Eq. (10) using the value of infinite dilution viscosity – by extrapolation from viscosity data of undersaturated solutions – was 6 Å. Calculation of the radius of one molecular unit of $KAl(SO_4)_2 \cdot 12H_2O$ crystal (from the crystal density value), with the assumption of spherical shape, gave 4.7 Å. Considering that solute molecules in liquid phase are in the form of looser aggregates of ions rather than tightly ordered crystal state, the estimate of 6 Å is reasonable for the radius of one molecular unit at infinite dilution. This can be compared to the empirical relation suggested by Robinson and Stokes [22] for the radius of individual clusters of heavily hydrated complex ions in dilute aqueous solutions:

$$r = 0.72V^{1/3}, \tag{12}$$

where r is in Å and V in cm^3/mol. This estimation was demonstrated to be adequate for many hydrated ionic clusters, especially where the particles are relatively large (> 5 Å in radius) [22]. The radius calculated from Eq. (12), using the molar volume of $KAl(SO_4)_2 \cdot 12H_2O$ crystal, came out to be 6.3 Å, which is in adequate agreement with the value of r_0 from Eq. (10).

3.4. Cluster size estimation from diffusivity

An approximate relation of diffusion coefficient with the average cluster size was developed by Myerson and coworkers [16, 4] taking into account the general form of viscosity variation in the supersaturated region

$$n \cong \left(\frac{D_s}{D}\right)^{1.5}, \tag{13}$$

where D_s is the diffusion coefficient at saturation. The average numbers of molecules in clusters calculated according to Eq. (13) from the diffusion coefficients of $KAl(SO_4)_2 \cdot 12H_2O$ in supersaturated solutions are listed in Table 1.

Eq. (13) is based on an assumption that no clustering occurs at saturation, thus average cluster size at saturation is one molecular. However, this supposition is incompatible with the considerably large values of the radius (6–6.3 Å) of one diffusing entity at infinite dilution, calculated by Eqs. (10) and (12), which are big enough to be one molecular radius. If an average diffusing entity is already one molecular unit at infinite dilution, it is probable that the entity grows bigger as the solution becomes much more concentrated. When we used the originating Eq. (11) to directly estimate average cluster diameter (or correlation length ξ) using the solute diffusion coefficients and solution viscosity data, the values of the correlation length (equivalent to cluster diameter) came out to be almost constant – approximately 12 Å – at low concentrations ($0 < m < 0.1$ mol/kg), but to increase continuously at higher concentrations, as shown in Table 1. This indicates, consistently with our speculation, that the diffusing entities are predominately one molecular unit of ionic clusters, with diameter of 12 Å, in the low concentration range, but their sizes increase with increasing concentration even before saturation point, and more rapidly after that. The average numbers of molecules in

Table 1
Estimation of cluster sizes from the diffusivity data of $KAl(SO_4)_2 \cdot 12H_2O$ solutions

Molality (mol/kg of "free" water)	Supersaturation $\sigma = m/m^* - 1$	Ave. no. of molecules in clusters $n = (D/D_s)^{1.5}$	Correlation length, ξ (approximate cluster diameter) (Å)	Ave. no. of molecules in clusters[a] $n = (\xi/2\ r_0)^3$
0.021	− 0.93 (undersat)	–	12.01	1.00
0.065	− 0.77 (undersat)	–	11.91	0.98
0.111	− 0.62 (undersat)	–	11.81	0.95
0.159	− 0.45 (undersat)	–	12.42	1.11
0.208	− 0.28 (undersat)	–	12.31	1.08
0.261	− 0.09 (undersat)	–	12.57	1.15
0.303	0.054	1.00	12.18	1.04
0.315	0.095	1.19	13.37	1.38
0.329	0.143	1.27	13.70	1.49
0.332	0.153	1.20	13.09	1.30

[a] r_0 is assumed to be 6 Å.

clusters, calculated from the cluster diameters using the relation

$$n = \left(\frac{\xi}{2r_0}\right)^3 \tag{14}$$

are also listed in Table 1.

Our view that most $KAl(SO_4)_2 \cdot 12H_2O$ solute ions form clusters of one molecular unit even at very low concentration is also supported by the conductivity measurements carried out in our laboratory [25]. Conductivities of $KAl(SO_4)_2 \cdot 12H_2O$ solutions were much lower than those of other simple electrolyte solutions (such as NaCl, $(NH_4)_2SO_4$, and KBr) at equivalent concentrations in undersaturated solutions, thus indicating low ionic mobilities and/or low ionic dissociation (or analogously, high ionic association). This leads to our justification that the solute is mostly in neutral form, and might be an explanation for the trend of the diffusion coefficient (shown in Fig. 1), which is similar to that of nonelectrolyte solutions.

3.5. Cluster size estimation from column density gradient

For most supersaturated solutions in which the concentration gradients had been observed, i.e., glycine, citric acid, sodium nitrate, potassium sulfate, and urea, [10, 11, 26, 27] the time required to develop a measurable concentration gradient was typically 1–2 days. In our experiments, no detectable density difference between the top and bottom could be measured within 2 days. Table 2 shows the results of the column experiments using solutions of various supersaturation. The results generally show that the higher the supersaturation, the greater the density gradient which increased with time. This is consistent with the view that the density increase at the bottom of the column is caused by cluster formation, which should be a time-dependent process.

Ginde and Myerson [12] used the concept of number and weight average molecular weights to calculate solute cluster sizes from concentration gradient data, assuming that the supersaturated solution column kept under isothermal condition established a quasi-equilibrium. The weight average molecular weight, M_w, of the solute cluster

$$M_w = \frac{RT}{(1 - \rho v)gH} \frac{(C_B - C_T)}{C_0} \tag{15}$$

is related to the extent of association, p, and the number average molecular weight, M_n, hence, the number average cluster size n [12]. Eq. (15) was originally derived based on the assumption that the activity coefficient remains constant at all supersaturation ranges. However, it was found that supersaturated $KAl(SO_4)_2 \cdot 12H_2O$ solutions are

Table 2
Estimation of cluster sizes from the density gradients of supersaturated $KAl(SO_4)_2 \cdot 12H_2O$ solution columns

Supersaturation $\sigma = m/m^* - 1$	Time (h)	Density gradient $\Delta\rho$ ($\times 10^5$ g/cm^3)	M_w weight ave. mol. wt.	p degree of association	n, Ave. no. of molecules in clusters	Ave. diameter of clusters (Å)
0.082	67	5.95	2306	0.66	2.93	16.09
0.130	144	28.6	1.09×10^4	0.92	11.98	26.99
0.135	43	9.52	3628	0.77	4.32	18.71
0.135	67	11.9	4536	0.81	5.28	20.15
0.195	72	97.7	3.64×10^4	0.97	38.89	40.36
0.195	144	267	9.88×10^4	0.99	104.72	56.29

highly nonideal with their nonideality increasing with supersaturation [18]. Thus, we have reformulated the expression for M_w to include the thermodynamic term as follows, so that the equation can be applicable to nonideal solutions. The original expression for the derivative of Gibbs free energy with respect to height [12]

$$\frac{dG}{dh} = 0 = -\rho g M_0 v + RT\left(\frac{d\ln a}{dc}\right)_P \frac{dc}{dh} + M_0 g \tag{16}$$

can be written with summation over all clusters of j molecules, retaining the thermodynamic term

$$\sum_{j=1}^{N} \frac{dc_j}{dh} + \sum_{j=1}^{N} \frac{dc_j}{dh}\left(\frac{\partial \ln \gamma_j}{\partial \ln c_j}\right)_P = -\frac{(1 - v\rho)g}{RT} \sum_{j=1}^{N} M_j c_j . \tag{17}$$

Since activity is the same whether molecules are associated or dissociated [28], i.e., $\partial \ln \gamma_j / \partial \ln c_j = \partial \ln \gamma / \partial \ln c$, Eq. (17) becomes

$$\frac{dc}{dh} + \frac{dc}{dh}\left(\frac{\partial \ln \gamma}{\partial \ln c}\right)_P = -\frac{(1 - v\rho)g}{RT} M_w C_0 . \tag{18}$$

Integrating Eq. (18) from $h = 0$ to H and $c = C_B$ to C_T gives

$$M_w = \frac{RT}{(1 - \rho v)gH} \times \frac{[(C_B - C_T) + \int_{C_T}^{C_B} (\partial \ln \gamma / \partial \ln c)_P \, dc]}{C_0} . \tag{19}$$

The value of the integral can be numerically calculated from our data of solute activity, using Eq. (6).

The calculated values of M_w, p, and n are listed in Table 2. The result shows that the average cluster size and the extent of association increase with increasing supersaturation and time. The time effect is shown to be more pronounced at higher supersaturation, as indicated by the drastic increase of n as time extended at the highest supersaturation level in Table 2. These results confirm the generally accepted theory of concentration fluctuations in supersaturated solutions, which should increase with supersaturation degree and time, and thereby result in the formation of nuclei. Calculation of M_w excluding the thermodynamic term results in much lower values of n. This indicates that the assumption of solution ideality (or constant activity coefficient) in supersaturation would lead to the significant underestimation of cluster sizes. Fig. 2 shows the cluster sizes, n, plotted with respect to initial solution concentration. The average cluster sizes estimated from the column experiments are much greater than those estimated from the diffusion coefficient data of supersaturated solutions. This is attributed to the supersaturated solution "age" since the solution columns were allowed enough time to develop clusters big enough to be detected by density changes.

Calculation of the weight average cluster diameter using the relation

$$d_w = 2\left(\frac{3}{4}\frac{M_w}{\pi\rho N_{Avo}}\right) \tag{20}$$

gave the values listed in Table 2. The values of d_w were used as correlation length in estimation of the diffusion coefficients using Eq. (11). The calculated diffusion coefficients are plotted in Fig. 3

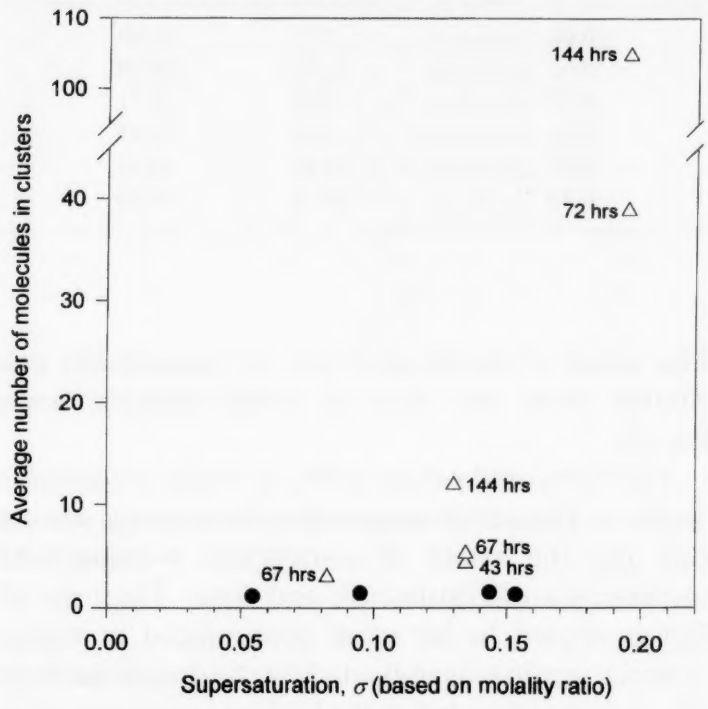

Fig. 2. Cluster sizes estimated from the column density gradients (△) and diffusion coefficients (●).

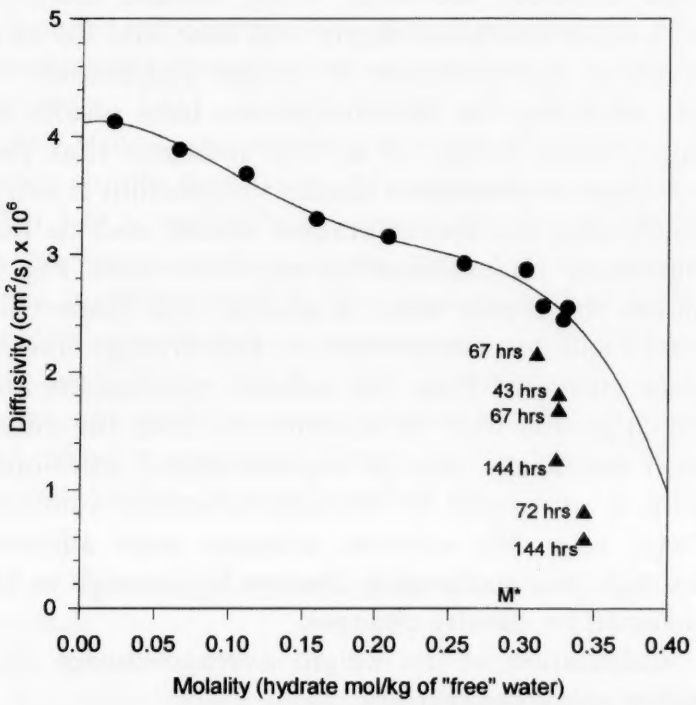

Fig. 3. Diffusion coefficients calculated from cluster sizes estimated from column density gradients (▲) and those measured experimentally (●).

with respect to concentration along with the measured diffusion coefficients reported in the earlier section. It shows that the calculated diffusion coefficients of the clusters whose sizes were estimated from the column density gradient are much lower than the measured diffusion coefficients of the "fresh" solutions. This demonstrates the effect of decreasing diffusion coefficient with extended solution "age," as was previously observed for the diffusion in supersaturated glycine and urea solutions [16].

4. Conclusions

Indirect evidences of ionic association and cluster formation in concentrated and supersaturated solutions of $KAl(SO_4)_2 \cdot 12H_2O$ were found from the measurements of diffusion coefficients and concentration gradients in vertical columns. Strong ionic association was suspected even in the solutions of low concentration, and the sizes of the clusters increased with increasing concentration. The clusters in the supersaturated region increased much more drastically with increasing concentration and extended time. The theoretical prediction of the diffusivity and the analysis of column concentration gradients in the supersaturation range require consideration of structural details of the solution, as well as the thermodynamic solution properties.

Nomenclature

a	activity of solute, mol/kg of "free" water
a_w	activity of water in aqueous solution, mol/kg of "free" water
c	concentration of solute
C_B	concentration at the column bottom
C_0	initial concentration of column solution
C_T	concentration at the column top
D	diffusion coefficient of solute
D^0	diffusion coefficient of solute at infinite dilution
D_s	diffusion coefficient of solute at saturation
D^0_{slv}	self-diffusion coefficient of solvent molecules

$D^0_{slv-slt}$ diffusion coefficient of solvent molecules in solute
d_w weight average cluster diameter
G Gibbs free energy
g gravitational acceleration
h height
H distance between top and bottom of column
K a constant
k Boltzman's constant
m molal concentration of solute, mol/kg of "free" water
M_n number average molecular weight of clusters
M_0 molecular weight of nonclusters
M_w weight average molecular weight of clusters
N maximum number of molecules in a cluster
N_{Avo} Avogadro's number
n average number of molecules in clusters
P pressure
p degree of association into clusters
R gas constant
r radius of a unit ionic cluster at dilute concentration
r_0 Stokes law radius
T temperature
V molar volume
x mole fraction of the solute
γ activity coefficient
η solution viscosity
η^0 solution viscosity at infinite dilution
η^0_{slv} solvent viscosity
ρ cluster density
v specific volume of clusters
ξ correlation length
slv of solvent
slt of solute

References

[1] P. Bennema, J. Crystal Growth 1 (1967) 287.
[2] E.G. Denk, G.D. Botsaris, J. Crystal Growth 6 (1970) 241.
[3] J.W. Mullin, J. Garside, Trans. Inst. Chem. Eng. 45 (1967) T285.
[4] R.M. Ginde, A.S. Myerson, AIChE Symp. Ser. 87 (1991) 124.
[5] Y.C. Chang, A.S. Myerson, AIChE J. 3 (1984) 820.
[6] E.V. Khamskii, Crystallization from Solutions, Consultants Bureau, New York, 1969.
[7] G.A. Hussman, M.A. Larson, K.A. Berglund, in: Industrial Crystallization, Elsevier, Amsterdam, 1984, p. 21.
[8] P.M. McMahon, K.A. Berglund, M.A. Larson, in: Industrial Crystallization, Elsevier, Amsterdam, 1984, p. 229.
[9] J.M. Mullin, C.L. Leci, Phil. Mag. 19 (1969) 1075.
[10] A.T. Allen, M.P. McDonald, W.M. Nicol, R.M. Wood, Nature 235 (1972) 36.
[11] M.A. Larson, J. Garside, J. Chem. Eng. Sci. 41 (1986) 1285.
[12] R.M. Ginde, A.S. Myerson, J. Crystal Growth 116 (1992) 41.
[13] L.S. Sorrell, A.S. Myerson, AIChE J. 28 (1982) 772.
[14] J.W. Mullin, J. Garside, R. Unahabhokha, J. Appl. Chem. 15 (1965) 502.
[15] A.A. Zatout, M.Z. El-Abd, G.H. Sedahmed, R.S. Khalil, Ann. Chim. 64 (1974) 587.
[16] A.S. Myerson, P.Y. Lo, J. Crystal Growth 99 (1990) 1048.
[17] Y.C. Chang, A.S. Myerson, AIChE J. 32 (1986) 1747.
[18] S. Kim, A.S. Myerson, Ind. Eng. Chem. Res. 35 (1996) 1078.
[19] M.D. Cohen, R.C. Flagen, J.H. Seinfeld, J. Phys. Chem. 91 (1987) 4563.
[20] H.S. Na, S. Arnold, A.S. Myerson, J. Crystal Growth 139 (1994) 104.
[21] A.R. Gordon, J. Chem. Phys. 5 (1937) 522.
[22] R.A. Robinson, R.H. Stokes, Electrolyte Solutions, 2nd ed., Butterworths, London, 1959.
[23] A. Vignes, Ind. Chem. Eng. Fund. 5 (1966) 189.
[24] E.L. Cussler, AIChE J. 26 (1980) 43.
[25] O. Karger, S. Kim, A.S. Myerson, 1995, unpublished data.
[26] A.S. Myerson, P.Y. Lo, J. Crystal Growth 110 (1991) 26.
[27] R.M. Ginde, A.S. Myerson, J. Crystal Growth 126 (1993) 216.
[28] O. Söhnel, J.W. Mullin, Chem. Eng. Sci. 33 (1978) 1535.

ELSEVIER

Journal of Crystal Growth 181 (1997) 70–78

JOURNAL OF CRYSTAL GROWTH

Transition of octacalcium phosphate to hydroxyapatite in solution at pH 7.4 and 37°C

Mayumi Iijima*, Hideo Kamemizu, Nobukazu Wakamatsu, Takayasu Goto, Yutaka Doi, Yutaka Moriwaki

Asahi University, School of Dentistry, Dental Materials and Technology, 1851-1 Hozumi, Hozumi-cho, Motosu-gun, Gifu 501-02, Japan

Received 28 December 1996; accepted 15 March 1997

Abstract

Transition of octacalcium phosphate (OCP) to apatite was studied under the condition where Ca^{2+} ions were continuously supplied to the reacting solution at pH 7.4 and at 37°C. OCP crystals were grown and subsequently converted into apatite by discontinuing of Ca addition. The rectangular (1 0 0) blades of OCP crystals developed notches on their short edges in the early stage of transition. The depth of the notches increased along the *c*-axis direction with the progress of the reaction, giving rise to a slit-like texture. The direction of the slit formation seemed to relate to the spatial configuration of H_2O molecules in the OCP lattice, which are released during the transition from OCP to apatite.

1. Introduction

Octacalcium phosphate (OCP; $Ca_8H_2(PO_4)_6 \cdot 5H_2O$, $P\bar{1}$, $a = 19.692(4)$ Å, $b = 9.523(2)$ Å, $c = 6.835(2)$ Å, $\alpha = 90.15(2)°$, $\beta = 92.54(2)°$, $\gamma = 108.65(1)°$ [1]) is thermodynamically metastable phase of hydroxyapatite ($Ca_5(PO_4)_3OH$, $P6_3/m$, $a = 9.418(2)$ Å, $c = 6.884(2)$ Å [2]) and it transforms to apatite spontaneously and topotaxially, keeping both the *b*- and *c*-axes and the plate-like morphology of the original OCP crystal [3, 4]. Moreover, in this process, impurities, strain field and defects, which have been detected in biological apatites, are able to be incorporated in the lattice of apatite [5–7]. Thus, mechanisms of biological apatite formation that involved OCP as an intermediate phase have been proposed [8–12]. Topotactic transition of OCP into apatite and subsequent epitaxial growth of OCP on the apatite is one of the plausible mechanisms of biological apatite formation, as originally proposed by Brown [8, 9]. Recent high resolution electron microscopic studies have provided another formation mechanism of tooth enamel apatite, e.g., the epitaxial overgrowth of apatite on a thin template of OCP-like precursor crystal [10–13]. Indeed, nucleation and overgrowth of apatite on a thin OCP template was shown in vitro, and was proposed to represent the same phenomenon as seen in tooth enamel apatite formation [12–14]. Although OCP has not been detected as a stable phase in vivo, analyses of matrix vesicles [15], tooth enamel [16] and

* Corresponding author. Fax: +81 58 329 1439; e-mail: iijima@dent.asahi-u.ac.jp.

0022-0248/97/$17.00 © 1997 Elsevier Science B.V. All rights reserved
PII S0022-0248(97)00230-3

enameloids [17] have shown peak shifts of PO_4 bands in their infrared spectra and the decrease of the HPO_4 content, suggesting the transition of OCP-like precursors into apatite.

Thus, transition of OCP into apatite is biologically of importance. However, almost of all the previous experiments of transition of OCP have been carried out at temperatures other than 37°C (boiling temperature [3], 85–95°C [6], 70°C [18]) or in solutions of rather high F concentrations [4] using previously prepared OCP at room temperature [6] or at 50°C [18]. The present study was therefore undertaken to investigate the process of subsequent transition of the grown OCP at 37°C and at pH 7.4, focusing on the morphological change of OCP crystals during transition.

2. Experimental procedure

2.1. Precipitation and hydrolysis of OCP

Reaction was carried out under a continuous Ca addition into reacting solution with low Ca/PO_4 at pH 7.4 and 37°C in a pH-stat system. The Ca addition played a key role in the formation of OCP [19]. Under the present experimental condition, OCP kept growing so long as Ca addition was maintained and discontinuance of the Ca addition caused transition of OCP to apatite, therefore, made it possible to investigate the subsequent change of the grown OCP to apatite.

All solutions were prepared with deionized and double distilled water. 200ml of metastable calcium phosphate solutions (0.55–0.60 mM Ca; 13.3–13.9 mM PO_4; $Ca/PO_4 = 0.04$) were prepared by mixing reagent grade $Ca(NO_3)_2 \cdot 4H_2O$ and KH_2PO_4 solutions. After the solution reached 37°C, the pH was adjusted to 7.40 with 0.5 N KOH. The pH of solution was kept at 7.40 ± 0.01 during the reaction using a pH-stat assembly (TOA, AUT-1) by the addition of 0.25 N KOH solution. The metastable calcium phosphate solution was placed in a water-thermostatted double-walled vessel and gently stirred with a magnetic stirrer. Immediately after the reaction started, which was indicated by drastic KOH solution consumption, a $Ca(NO_3)_2 \cdot 4H_2O$ solution (25 mM) was supplied at a rate of 2.85 ml/h for 15 hours using a titrater. Reactions were terminated when the transition from OCP to apatite completed: 152 h: 0.6 mM Ca and 13.9 mM PO_4; 219 h: 0.55 mM Ca and 13.3 mM PO_4.

2.2. Analysis of solid and solution

The phase change from OCP to apatite was studied by X-ray powder diffractometry (Rigaku, RINT2000, 56 kV, 200 mA, monochrometer, Cu Kα). 5 ml of the suspension was removed at regular intervals during the reaction, filtered through a 200 nm milipore filter, and the solid phases were quenched by dry ice and subsequently freeze-dried. At the same time, a droplet of fresh suspension was transferred onto a Cu grid coated with formval and carbon. After a few seconds, water was removed by filter paper and the morphology of the products were observed by transmission electron microscopy (JEOL, 1200EX, 80 kV). Selected area electron diffraction patterns were taken, using an objective aperture of 50 μm in diameter and a selected area aperture of 20 μm in diameter.

The lattice constants of resultant apatites were determined using the least squares method. The 2θ values of about 10 reflections in the range of 10–60° (2θ) were used for the calculation. The lattice constant of tooth enamel apatite of adult human was also calculated for comparison. The peak positions were corrected using Si powder.

The Ca concentration of the filtrate was analyzed using an atomic absorption spectrophotometer (Shimadzu, AA-670) with the addition of 5000 ppm La_2O_3 solution. PO_4 concentration was analyzed spectrometrically at the wavelength of 881 nm with molybdenum blue method.

The degree of supersaturation to OCP (DS(OCP)) of the solution was estimated as follows:

$$DS(OCP) = [AP(OCP)/Ksp(OCP)]^{1/8},$$

$$Ksp(OCP) = 10^{-49.3},$$

where Ksp is the solubility product [20] and AP is the activity product for OCP as

$$AP(OCP) = (Ca^{2+})^4(PO_4^{3-})^3(H^+).$$

The activity of each ion at pH 7.4 and 37°C was calculated from the measured Ca and PO_4 concentrations, volume and concentration of added KOH solution, using the method of Eanes and Meyer [21]. According to the calculation, the DS(OCP) of the initial solutions were between 3.9 and 3.7, and solutions were supersaturated to OCP but undersaturated to ACP [22].

3. Results

Fig. 1 is XRD patterns (between 8 and 13° in 2θ) of the intermediate products of 219 h reaction. OCP grew as long as the Ca addition was maintained. Soon after the Ca addition was stopped, decomposition of OCP started. It was indicated by a decrease in the XRD intensity of the 100, 200, and 110 reflections at 4.7, 9.4 and 9.7° in 2θ (after around 30 h). Appearance of the 100 reflection at 10.8° (in 2θ, arrow in Fig. 1) indicated that apatite was formed. With the progress of reaction, the intensity of the OCP reflections decreased and that of the apatite reflections increased, finally giving rise to an XRD pattern of apatite. Neither a combination peak of the OCP and apatite [6] nor the 16.5 Å reflection [18] was observed during the transition under the present condition. Instead of those peaks, a very broad peak ranging from about 9° (2θ) to 11.5° (2θ) was seen between 189–200 h in 219 h reaction (Fig. 1). As the reaction progressed, the intensity of this peak decreased in the lower angle region and increased in the higher angle region. The XRD pattern of the final product showed a single 100 reflection of apatite at about 10.75° tailing toward the lower angle (Fig. 1 bottom).

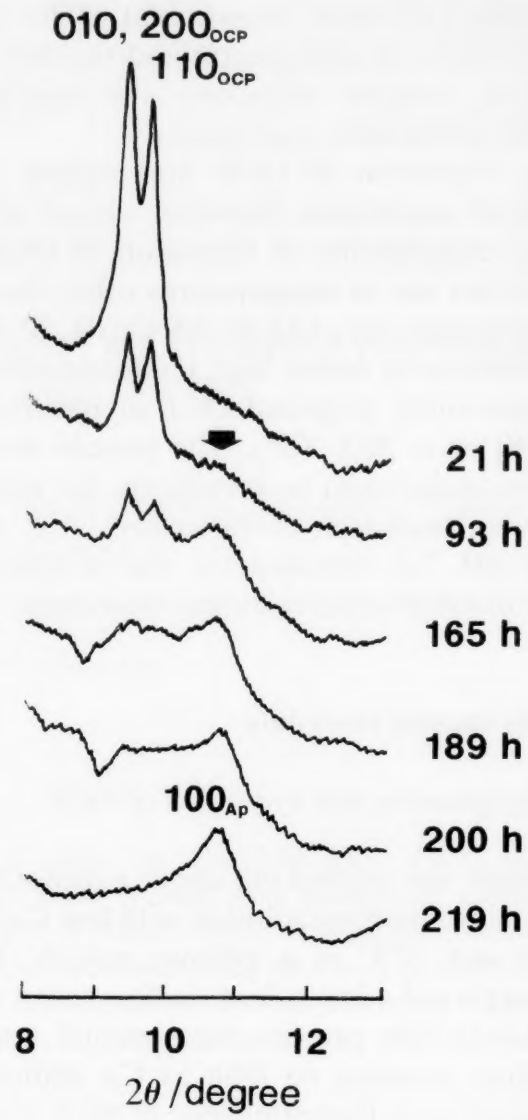

Fig. 1. X-ray diffraction patterns of the products during the 219 h reaction, where Ca-solution was added for 15 h. Each numeral indicates the reaction time. The arrow indicates the position of the 100 reflection of apatite (about 10.8°). Note that a broad peak (9–11.5°) appeared in the intermediate stage of the transition (189–200 h in the 219 h reaction).

The lattice constants of the resultant apatite after 152 and 219 h of reactions were $a = 9.450(1)$ Å and $c = 6.874(1)$ Å. Those of human tooth enamel of adult were $a = 9.442(1)$ Å and $c = 6.876(1)$ Å. The a-axis dimension of the resultant apatites was slightly larger than that of tooth enamel, while the c-axis dimension was almost the same.

Unique changes of the morphology were observed during the transition of OCP. Fig. 2a–Fig. 2d show the morphological change during 219 h reaction. The growing OCP crystals were plate-like with straight edges (Fig. $2a_1$) and showed a clear electron diffraction pattern (Fig. $2a_2$). Soon after the Ca addition was stopped, the rectangular OCP crystals exhibited notches along their short edges (Fig. 2b), indicating that the collapse of the OCP structure had started. The notch-like texture was observed after about 30 h in 219 h reaction. The time coincided with the time at which the decrease in the crystallinity of OCP was detected by X-ray diffractometer. The depth of the notches increased along the c-axis direction as the transition progressed (Fig. 2b–Fig. $2d_1$). The final products, which exhibited an XRD pattern of

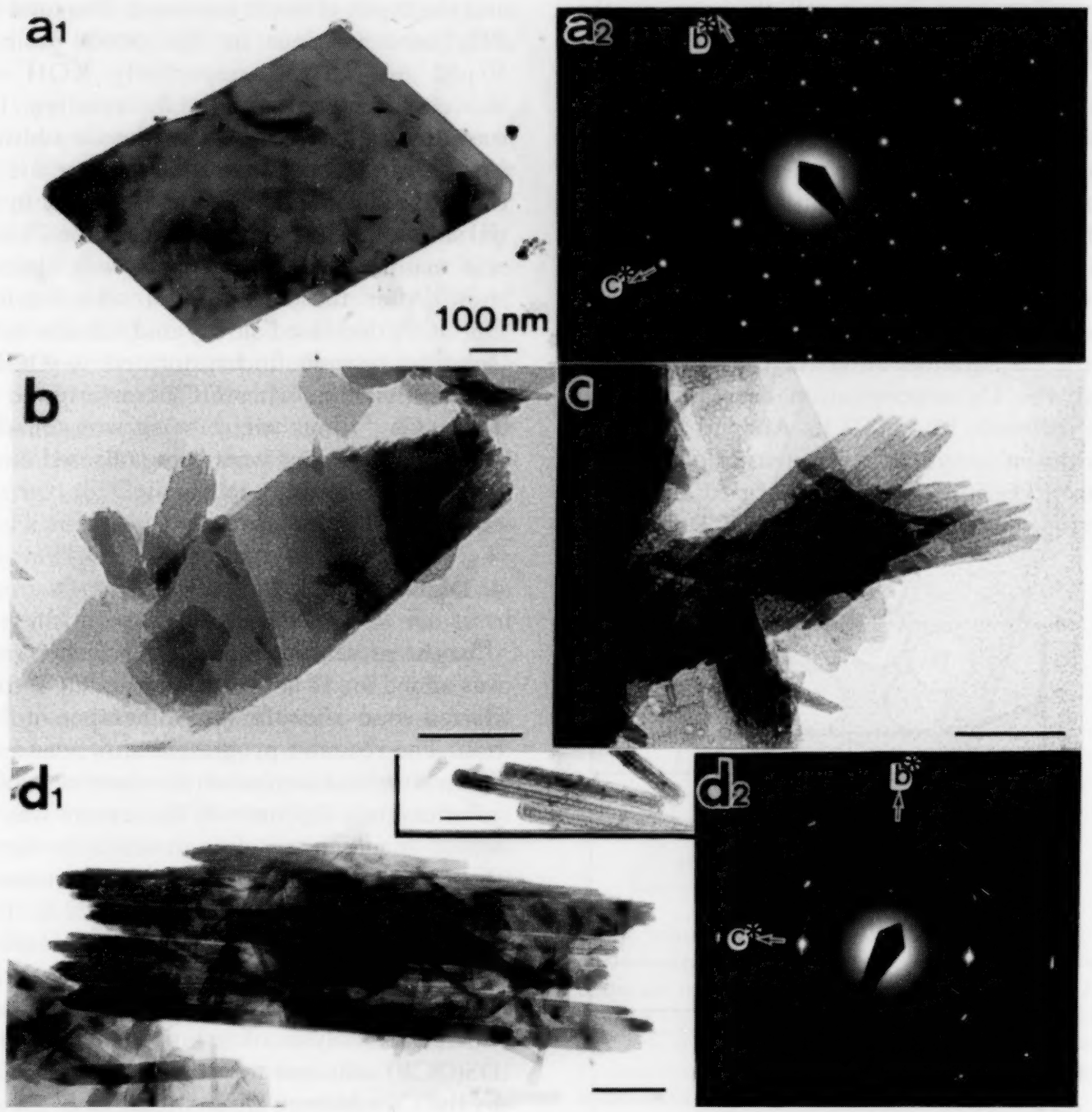

Fig. 2. Morphological changes during the transition from OCP to apatite in the 219 h reaction. (a) Growing OCP crystal (8 h) and its electron diffraction pattern. Crystals in the intermediate stages of transition: (b) 30 h; (c) 93 h. (d) Final product (219 h) and corresponding electron diffraction pattern, which is that of apatite. Note that the depth of the notches increased with reaction time and the resultant apatite crystals have a slit-like texture on the short edges. Insert is long rod-like crystals with a central translucent line running along their length. Scale bars represent 100 nm.

apatite, mainly contained of plate-like crystals with deep slits along the *c*-axis direction and tape-like crystals (Fig. $2d_1$). In addition, long rod-like crystals with a central translucent line running along their length were observed (insert in Fig. $2d_1$). The tape-like crystals may have resulted from crystals with slits, mechanically weaken along the slits, to split in the *c*-axis direction. The electron diffraction pattern of a crystal with deep slits was apatitic and the *c*-axis was in the long axis of the crystal (Fig. $2d_2$). The typical width of a slit and a translucent line was about 0.7–2.5 nm,

corresponding to 1–3 unit cell thickness in the *b*-axis direction.

Fig. 3 shows the changes in total Ca and PO_4 concentrations in solution, the DS(OCP) and the volume of KOH consumed during 152 h reaction. The arrow indicates the time when the Ca addition was stopped (15 h). After the initial drastic decrease in both Ca and PO_4 concentrations, total PO_4 concentration continued to decrease rather rapidly, while total Ca concentration was almost constant. This indicated that Ca consumption almost balanced the Ca addition. After the Ca addition was stopped, the Ca concentration decreased rather rapidly (between 16 and 31 h). After 31 h, the Ca concentration continued to decrease slowly, while the total PO_4 concentration increased slowly. In this period, the ratio of apatite to OCP increased and the depth of notch increased. The total Ca and PO_4 concentrations in this period were about 50 μM and 7.5 mM, respectively. KOH solution was consumed throughout the reaction. Its consumption rate decreased after the Ca addition was stopped, indicating that the reaction rate slowed down. The DS(OCP) decreased rapidly in the initial stage of the reaction. As long as the Ca addition was maintained, the DS(OCP) was almost constant. After the Ca addition was stopped, the DS(OCP) decreased slowly and became below 1.0 (solution became undersaturated to OCP) after 152 h of reaction, when OCP converted to apatite. Thus, Ca^{2+} ions were being consumed, while H^+ and PO_4^{3-} ions were being released during the transition from OCP to apatite.

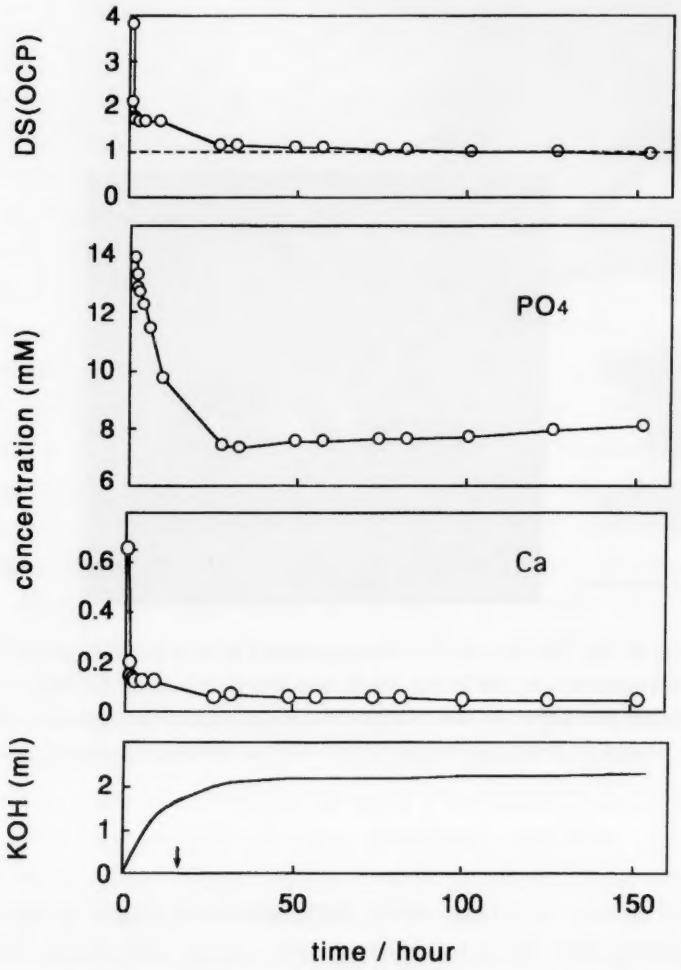

Fig. 3. Changes in solution Ca and PO_4 concentrations, degree of supersaturation to OCP, and KOH consumption during 152 h reaction. Arrow indicates the time when Ca-addition was stopped (15 h).

4. Discussion

In the present experiment in which Ca solution was added for 15 h, transition from OCP to apatite started soon after the discontinuance of Ca addition. The reaction progressed slowly and the slit-like texture was formed on the short edge of rectangular crystals. In contrast, the texture was not observed during the reaction in which the duration of the Ca addition was 9 h and the phase transition to apatite terminated earlier (around 20 h). Thus, the morphology of the resultant crystal was affected by the speed of the phase transition, and the transition speed related to the duration of Ca-addition. Chemical analysis of solution revealed that the DS(OCP) sufficient to grow OCP was maintained by the Ca-addition. Discontinuance of Ca-addition caused the decrease in the DS(OCP). The DS(OCP) became insufficient to grow OCP, as a result, conversion of OCP was initiated. Thus, the Ca-addition played an important role to maintain the DS(OCP) level. Although the solution conditions were different from that of biological fluids, this finding has an important implication to the biological apatite formation. Since the duration and activity of Ca and PO_4 inflow into the calcifying regions are changing during the process of the tooth enamel and dentin and bone formation [23, 24], it is probable that in vivo transition of initial precipitate(s) (presumably, ACP and/or

OCP) into apatite and concomitant morphological changes are affected by the mode of Ca and PO_4 inflow.

The very broad XRD peak at about 9–11.5°, which was observed in the later stage of reaction (189–200 h in Fig. 1), is probably ascribed to the overlapping of the broadened XRD peaks of OCP (0 1 0, 2 0 0, 1 1 0) and apatite (1 0 0). Generally, broadening of a line profile suggests that a number of small diffraction domains (smaller than 1000 $Å^2$ in case of Cu Kα) are formed and/or defects and distortion are incorporated into crystal lattice. As shown by the chemical formulas, when OCP converts to hydroxyapatite, the most remarkable change is the release of the H_2O molecules from OCP structure. Crystal structure of OCP is composed of a portion with apatitic structure and a potion where H_2O molecules are concentrated [1, 3]. Therefore, when H_2O molecules are released from OCP crystal, apatitic portions would be remained and empty regions would be formed inevitably. Thus, it is probable that OCP crystal split into small domains and small domains with apatitic structure were formed in the process of conversion. The change of the wide broad peak into the single 1 0 0 peak of apatite (219 h in Fig. 1) suggests that apatitic portions became small domains with apatitic structure, and then became larger domains of apatite with less lattice imperfection.

Since solution was supersaturated to OCP during conversion reaction, the mechanism of the conversion from OCP to apatite may be in situ reorganization of the lattice ions and/or apatitic clusters rather than dissolution of OCP and reprecipitation. The apatitic portion of OCP is structurally related to hydroxyapatite [3]. The projection onto the (0 0 1) plane of the structure of OCP and hydroxyapatite [1] clearly shows their close relationship. Therefore, it is well understood that OCP transforms to apatite topotaxially shearing their *b* and *c* axes directions with each other [3, 4]. When transition from OCP to apatite proceeds topotaxially and slowly, OCP may collapse in a manner somehow reflects its crystal structure. The direction of the slit formation seems to relate to the distribution of H_2O molecules in its crystal structure. In Fig. 4, ten water molecules in a unit cell of OCP are drawn schematically as circles with

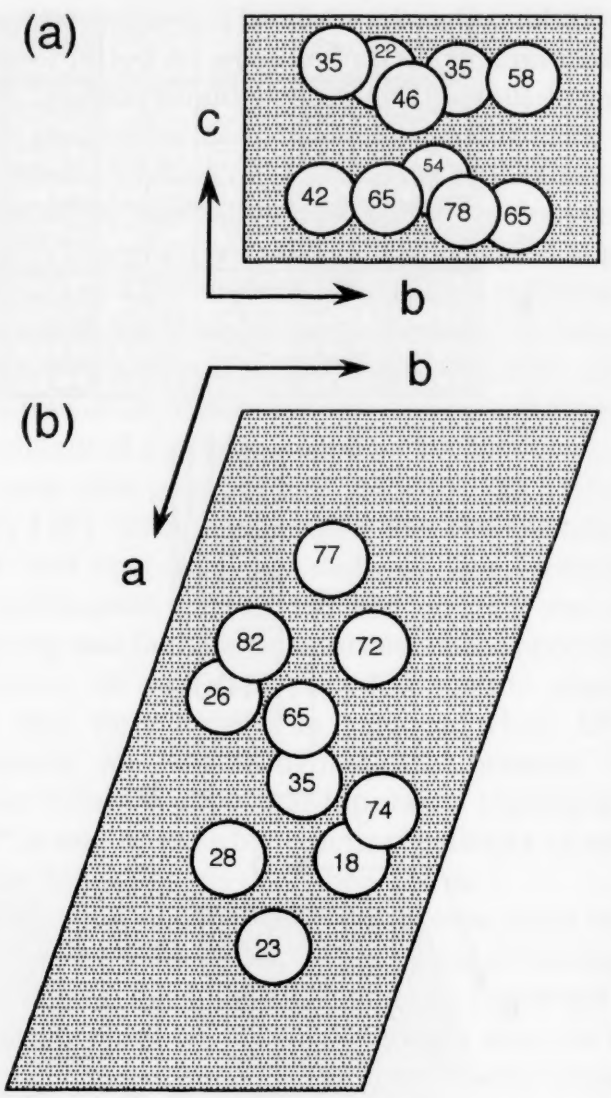

Fig. 4. Schema of the location of water molecules in a unit cell of OCP. (a) *a*-axis projection. (b) *c*-axis projection. Water molecules are represented as circles with a diameter of 2 Å. Each numeral represents the *x*-coordinate in (a) and *z*-coordinate in (b) .These show that a group of water molecules extend in the *a**-direction in a unit cell and they form water molecule columns in the *c*-axis direction.

2 Å diameter, based on crystallographic data [3]. A unit cell of OCP is projected along the *a*-axis (Fig. 4a) and the *c*-axis (Fig. 4b). In these figures, the x and z coordinates are indicated numerically. The locations of the H_2O molecules in the OCP crystal are projected along the *a*-axis in Fig. 5a and along the *c*-axis direction in Fig. 5b, with a schema for the texture of a crystal after transition. Figs. 4 and 5 indicate that water molecules arrange in the *a**-axis direction and form water columns in the *c*-axis direction. Since OCP crystallizes as a thin

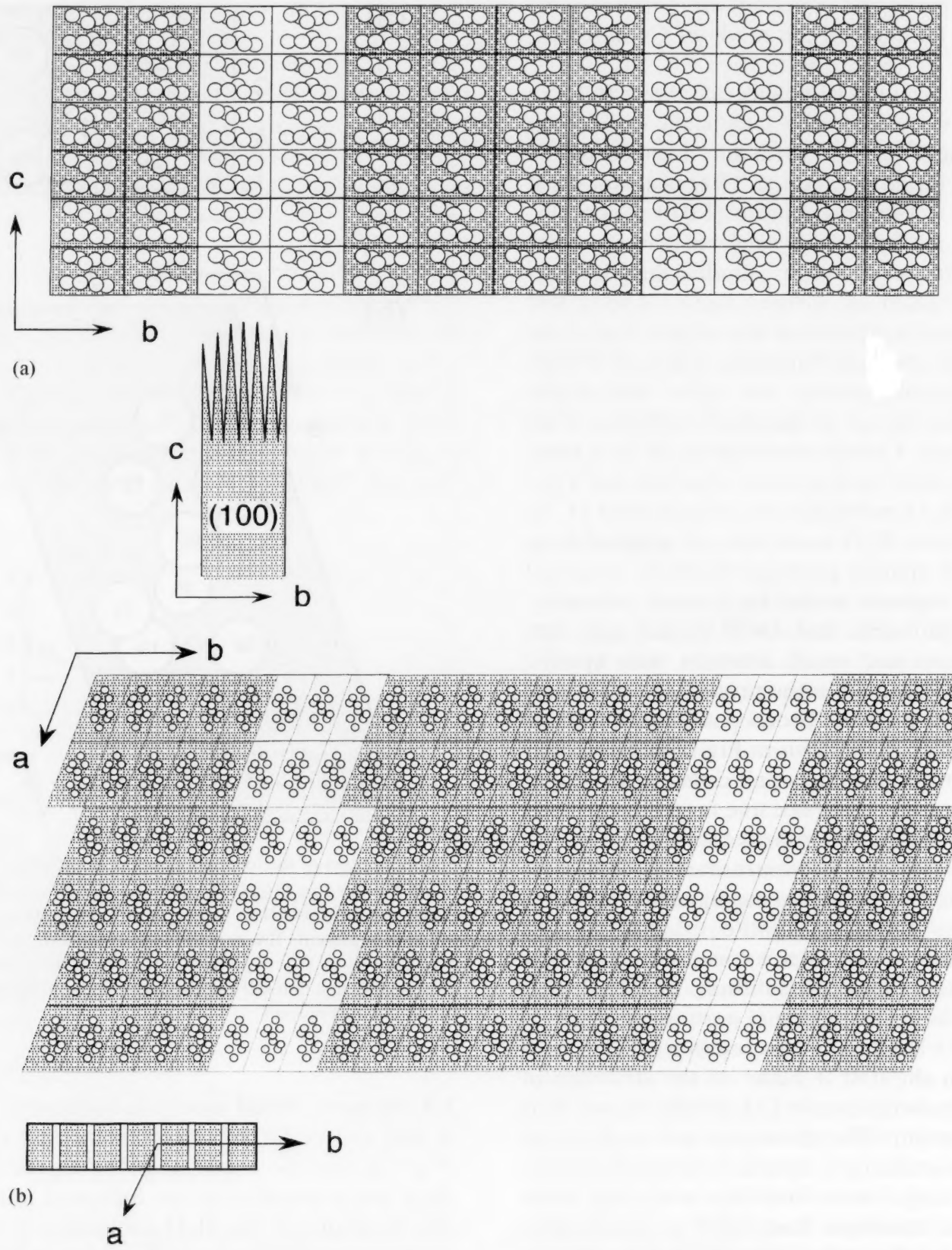

Fig. 5. Schematical drawings of the location of water molecules in an OCP crystal and the slit-like texture of a crystal as projected along (a) the *a*-axis and (b) *c*-axis direction. These depict the hypothesized relationship between the location of the water molecules (open circles) and the slit-like texture formation. Collapse of OCP started on the (0 0 1) plane by loss of H_2O molecules, remaining apatitic portions. Some of the apatitic portions (dotted regions) acted as nuclei to form domains of apatite and lattice components of others (white region) were used to construct the apatite domains, resulting in the solid region with apatite structure and the empty region. Small region of OCP crystal (white region) are thus lost along the *a**-axis direction, forming notches on the (0 0 1) plane (b). The notches grow in the *c*-axis direction as water molecules are lost along the water columns, giving rise to slits (a).

(1 0 0) blade and grows actively in the *c*-axis direction, the (1 0 0) is the most stable face and the (0 0 1) is a rather unstable one. Nelson et al. found that the collapse of OCP crystal was caused by the loss of H_2O molecules in the OCP [18]. It is therefore probable that the collapse started on the (0 0 1) plane by losing H_2O molecules. Since water molecules arrange rather densely in the a^*-axis and the *c*-axis directions (Figs. 4 and 5), diffusion and release of H_2O and other lattice components would progress favorably in these directions. TEM observation revealed that width of a slit and interval of the slits were almost regular in a crystal (Fig. 2b–Fig. 2d). It was deduced therefore that some of the apatitic portions acted as nuclei to form domains of apatite and other ones and/or their lattice ions shifted to construct the apatite domains, following the release of H_2O molecules. Whether an apatitic portion acts as a nuclear or shifts may be understood in terms of probability. Thereby, notches along the a^*-axis direction were formed and the notches grew in the *c*-axis direction with the progress of transition from OCP to apatite, resulting in slits parallel to the (0 1 0) plane on short edges. The formation of the translucent channel of the rod-like crystals (insert in Fig. $2d_1$) may be explained by this mechanism. The characteristic platy shape and the *c*-axis direction of original OCP crystal were preserved in the resultant apatite crystal (Fig. 2d). This could be taken as evidence that the transition of OCP to apatite was topotaxial.

The slit-like texture on the short edges of plate-like crystal has been observed in reaction products from solution [25–30] and in the early stage of enameloid formation of skate [17]. In contrast to the present assumption, crystal growth of skate enameloid was described as the elongation of projections perpendicular to the (0 0 1) plane and their subsequent lateral fusion into a single crystal domain. The mechanism of the slit-like texture formation may depend on whether or not OCP is involved in the reaction pathway of apatite formation, furthermore, how does OCP convert to apatite, as described above. OCP precipitation depends, in part, on the DS(OCP) of the fluid surrounding the mineral. The solubility product (Ksp) of OCP at 37°C [20] is larger than that of hydroxyapatite [31]. Therefore, when the solution is supersaturated to apatite but undersaturated to OCP, apatite would precipitate without forming OCP as an intermediate phase. In this case, the formation and the elongation of the projections are explained by nucleation and growth of apatite on the (0 0 1) plane [26]. When a solution is supersaturated to OCP and the DS(OCP) is sufficient to grow OCP, OCP would grow. However, when the DS(OCP) becomes insufficient to grow OCP, phase transition of OCP may take place. In a calcification experiment of a collagenous matrix, plate-like crystals with slits grew on and between the collagen fibrils [28]. Since the product was the mixture of OCP and apatite, it was deduced that formation and subsequent phase transition of OCP was undergoing and the slits were formed in the process of transition. In case that plate-like apatite crystals with slits were formed in solution where OCP formation was thermodynamically possible, the texture would suggest that topotaxial transition of OCP is one of possible reaction pathway of such apatite formation, as described above.

In conclusion, when OCP was grown under condition where Ca solution was supplied to the reacting solution for 15 h, OCP crystals converted to apatites subsequently and slowly soon after the Ca addition was stopped. The resultant apatite crystals retained slits on the short edges of the rectangular crystals and had lattice dimensions similar to that of human tooth enamel apatite. The slits were formed along the *c*-axis direction perpendicular to the (1 0 0) plane of OCP. The direction of the slit formation was deduced to relate to the direction of the arrangement of H_2O molecules which are released from OCP during transition.

Acknowledgements

This study was partly supported by the Miyata Grant of Asahi University.

References

[1] M. Mathew, W.E. Brown, L.W. Schroeder, B. Dickens, J. Cryst. Spectrosc. Res. 18 (1988) 235.

[2] K. Sudarsanan, R.A. Young, Acta Crystallogr. B 29 (1972) 3668.
[3] W.E. Brown, J.P. Smith, J.R. Lehr, A.W. Frazier, Nature 196 (1962) 1048.
[4] T. Aoba, T. Ishida, T. Yagi, K. Hasegawa, Y. Moriwaki, Jpn. J. Oral Biol. 17 (1975) 1.
[5] W.E. Brown, L.W. Schroder, J.S. Ferris, J. Phys. Chem. 83 (1979) 1385.
[6] N.S. Chickerur, M.S. Tung, W.E. Brown, Calcif. Tissue Int. 32 (1980) 55.
[7] D.G.A. Nelson, G.I. Wood, J.C. Barry, J.D.B. Featherstone, Ultramicroscopy 19 (1986) 253.
[8] W.E. Brown, in: M.V. Stack, R.W. Fearnhead (Eds.), Tooth Enamel II, Wright, Bristol, 1965.
[9] W.E. Brown, Clin. Orthop. 44 (1966) 205.
[10] D.G.A. Nelson, J.C. Barry, Anat. Rec. 224 (1989) 265.
[11] Y. Miake, S. Shimoda, M. Fukae, T. Aoba, Calcif. Tissue Int. 53 (1993) 249.
[12] M. Iijima, H. Tohda, H. Suzuki, T. Yanagisawa, Y. Moriwaki, Jpn. J. Oral Biol. 33 (1991) 495.
[13] M. Iijima, H. Tohda, Y. Moriwaki, J. Crystal Growth 116 (1992) 319.
[14] M. Iijima, H. Tohda, H. Suzuki, T. Yanagisawa, Y. Moriwaki, Calcif. Tissue Int. 50 (1992) 357.
[15] G.R. Sauer, R.E. Wuthier, J. Biol. Chem. 263 (1988) 13718.
[16] S. Shimoda, T. Aoba, E.C. Moreno, J. Dent. Res. 70 (1991) 1516.
[17] Y. Miake, T. Aoba, E.C. Moreno, S. Shimoda, K. Prostak, S. Suga, Calcif. Tissue Int. 48 (1990) 204.
[18] D.G.A. Nelson, J.D. McLean, Calcif. Tissue Int. 36 (1984) 219.
[19] M. Iijima, H. Kamemizu, N. Wakamatsu, T. Goto, Y. Doi, Y. Moriwaki, J. Crystal Growth 112 (1991) 467.
[20] L.J. Shyu, L. Perez, S.L. Zawcki, J.C. Heughehaert, G.H. Nancollas, J. Dent. Res. 62 (3) (1981) 398.
[21] E.D. Eanes, J.L. Meyer, Calcif. Tissue Res. 23 (1977) 259.
[22] J.L. Meyer, E.D. Eanes, Calcif. Tissue Res. 25 (1978) 59.
[23] T. Kawamoto, M. Shimizu, Calcif. Tissue Int. 46 (1990) 406.
[24] T. Kawamoto, M. Shimizu, Jpn. J. Oral Biol. 36 (1994) 365.
[25] T. Aoba, C. Yoshioka, T. Yagi, E.C. Moreno, J. Dent. Res. 63 (1984) 1348.
[26] Y. Doi, E.D. Eanes, Calcif. Tissue Int. 36 (1984) 39.
[27] K. Ishikawa, E.D. Eanes, J. Dent. Res. 72 (1993) 474.
[28] M. Iijima, K. Iijima, Y. Moriwaki, Y. Kuboki, J. Crystal Growth 140 (1994) 91.
[29] M. Okazaki, J. Takahashi, Dent. Mater. 14 (1995) 186.
[30] T. Takagi, R. Fujisawa, M. Akao, M. Kikuchi, N. Nagai, T. Sasaki, J. Hard Tissue Biol. 5 (1996) 15.
[31] H. McDowell, T.M. Gregory, W.E. Brown, J. Res. Natn. Bur. Stands. 78A (1977) 667.

ELSEVIER

Journal of Crystal Growth 181 (1997) 79–96

JOURNAL OF CRYSTAL GROWTH

Crystallogenesis studies in microgravity with the Advanced Protein Crystallization Facility on SpaceHab-01

Madeleine Riès-Kautt[a,*], Isabelle Broutin[a], Arnaud Ducruix[a], William Shepard[b], Richard Kahn[1,b], Naomi Chayen[c], David Blow[c], Klaus Paal[2,d], Walter Littke[d], Bernard Lorber[e], Anne Théobald-Dietrich[e], Richard Giegé[e]

[a] *Laboratoire d'Enzymologie et de Biologie Structurales, CNRS, Bâtiment 34, F-91198 Gif-sur-Yvette, France*
[b] *Laboratoire d'Utilisation du Rayonnement Électromagnétique (LURE), Bâtiment 209D, F-91405 Orsay, France*
[c] *Blackett Laboratory, Imperial College, Prince Consort Road, London SW7 2BZ, UK*
[d] *Chemisches Laboratorium, Albert-Ludwig Universität, 21 Albertstrasse, D-78000 Freiburg-im-Breisgau, Germany*
[e] *Institut de Biologie Moléculaire et Cellulaire du CNRS, 15 rue René Descartes, F-67084 Strasbourg Cedex, France*

Received 6 December 1996; accepted 28 March 1997

Abstract

The Advanced Protein Crystallization Facility (APCF), a new protein crystallization device developed by ESA for the IML-2 Mission in 1994, was tested in its maiden flight on STS-57 Mission in SpaceHab-01 with a physico-chemical experiment on lysozyme crystallization. In pre-flight ground experiments, prior to the Shuttle Mission, the protocol for lysozyme crystallization with NaCl was based on its solubility diagram at 18°C and pH 4.5. Crystallization was conducted under microgravity in 25 APCF reactors using vapor diffusion, dialysis, and free liquid interface diffusion, with control on earth in 25 identical reactors. Identical supersaturation values were tested by the three crystallization techniques. Values of supersaturation derived from *ground* experiments allowed for conditions that yielded crystals in microgravity. The average number and size of crystals from the flight experiment and the earth control showed no significant difference; however many crystals were not free floating and grew on the walls of some of the protein chambers. The dialysis technique proved to be suitable, since no additional nucleation was generated by the membrane. Protein concentration measurements indicated that 13 days after activation of the experiment as much as 70–90% of the protein in supersaturated state had already crystallized. Data indicated differences in the crystallization behavior depending upon the crystallization set-up. Images of the protein chamber of 6 reactors, recorded during the flight, allowed us to evaluate the early stage of crystallization, to verify that recovered crystals had actually grown under microgravity conditions, and showed motions of crystals during the Mission. Using synchrotron radiation, resolution and rocking curve measurements of *ground* and *space* lysozyme crystals grown in APCF reactors showed no significant

* Corresponding author. Fax: + 33 1 69 82 31 29.
[1] Present address: IBS, CNRS, 41 avenue des Martyrs, F-38027 Grenoble Cedex 1, France.
[2] Present address: Institut für Molekular Biologie und Biochemie, Herman Herder Strasse 7, D-79104 Freiburg-im-Breisgau, Germany.

0022-0248/97/$17.00 © 1997 Elsevier Science B.V. All rights reserved
PII S0022-0248(97)00280-7

differences, although the values are much better than previously recorded diffraction limits and mosaicity data obtained with tetragonal lysozyme crystals grown in other set-ups and under different conditions. All controls foreseen throughout the microgravity experiment proved to be essential for the interpretation of the flight data, as concerning the effect of microgravity.

Keywords: Microgravity; Protein; Lysozyme; Solubility; Nucleation; Crystallization; Crystallography; Mosaicity

1. Introduction

Protein crystallization is influenced by numerous parameters which must be controlled if large single crystals of high diffraction quality are to be produced repeatedly [1–3]. The understanding of protein crystallogenesis has made significant progress over the last four years after efforts to gather quantitative data on a few model proteins concerning solubilities, nucleation and growth (e.g. Refs. [4–8]). As to the effects of reduced gravity, the question was first addressed by Littke and John in 1982 [9]. Since then a number of microgravity experiments were performed, some of them showing larger, more uniformly shaped and/or better diffracting crystals (e.g. Refs. [10–18]). On earth, density gradients resulting from concentration changes lead to convection, generating nondiffusive material transport that may affect crystal growth [19]. Density differences between crystals and solution can induce crystal sedimentation or flotation. These effects are expected to be minimized in microgravity, but despite data on a large number of proteins, no definitive answer can be given to many basic questions. Reasons for this unsatisfactory situation are many: limited availability of microgravity experiments, lack of documentation with respect to the preparation of both microgravity and earth experiments, and confounding the effects of larger and better diffracting crystals attributed to microgravity.

It can be reasonably assumed that microgravity will not affect protein solubilities, but more likely equilibration, nucleation and growth kinetics, since these phenomena imply mass transport which becomes limited by diffusion in the absence of convection [19]. Therefore, the metastable zone in solubility diagrams may become broader in microgravity and the nucleation zone may shift towards higher supersaturation. For a given supersaturation, fewer crystals would nucleate and be larger in microgravity than on earth. To verify *the hypothesis of a shift of the nucleation zone* and its implications, an international joint experiment involving four European laboratories was organized. Resources were pooled to dedicate the largest number of crystallization reactors to a single project, rather than to spread efforts on separate problems with only a few reactors per protein. We explored a solubility diagram of hen egg-white lysozyme in microgravity, at pH 4.5 and 18°C. This temperature was chosen because data on lysozyme crystallization were already available under this condition [20–22] and also for organizational reasons, i.e. during the storage, trans-atlantic transportations and the microgravity mission. The prerequisite for microgravity crystal growth is the availability of specialized microgravity hardware (e.g. Refs. [9–18, 23–27]). This paper describes results obtained with the Advanced Protein Crystallization Facility (APCF) built by Dornier GmbH (Friedrichshafen, Germany) [25] and sponsored by the European Space Agency (ESA). Beside the major goal of our experiment, it was also a first opportunity to assay the APCF hardware and to optimize organizational aspects in view of the forthcoming IML-2 and other microgravity missions. In preliminary ground experiments, the nucleation range of lysozyme was determined for the different APCF reactor types in the four laboratories. For a better reproducibility and comparison of the results, all procedures were standardized, each laboratory working with the same chemicals and protein batch. From these results the protocol of the microgravity, and parallel ground, experiments were designed including a maximum of accurate

controls to avoid the misinterpretation of microgravity effect. Some measurements were foreseen to characterize the quality of some crystals in order to set a benchmark for future crystallographic investigations.

The experiment flew during the 10 day STS-57 Mission of the Shuttle Endeavour in June 1993. The APCF unit was embarked in the SpaceHab-01 mid-deck module. The 25 reactors dedicated to our experiment were divided in 10 hanging drop (HD), 10 dialysis (DIA) and 5 free interface diffusion (FID) reactor type, allowing comparison of crystal growth in reactors based on different crystallization methods. The volume of the protein chamber was 67 μl in the DIA reactors and 470 μl in the FID reactors (Fig. 1). Four out of the five FID reactors were used in dialysis mode and only one reactor was used in the free interface diffusion mode because its control experiment was difficult to perform on ground. A second set of reactors was used in parallel for ground controls with APCF reactors and crystallizing solutions identical to those run in microgravity. Part of the results originating from this joint mission are described in different articles [28–30]: they concern analyses of the video images of some protein chambers recorded in microgravity [28], crystallographic analyses of microgravity and earth grown crystals [29], and crystallographic refinement of the best diffracting lysozyme crystals obtained during this mission [30].

2. Instrumentation and experimental procedures

2.1. The APCF reactors

APCF is a versatile hardware which allows crystallization by either of the three main crystallization methods (Fig. 1): vapor diffusion (HD), dialysis (DIA) and liquid–liquid free interface diffusion (FID). FID reactors can also be used in dialysis mode by inserting a membrane between the protein chamber and the rubber seal of the plug. For details see Ref. [25]. The thermoregulated APCF flight unit accommodates 48 reactors of the three types in 4 rows of 12. Temperature of the microgravity experiments was set to $18 \pm 0.1^{\circ}C$.

2.2. Lysozyme crystallization

The reasons for the choice of lysozyme as the model protein were multiple: it is easily available (as 100 g preparations), it crystallizes within a short time span compatible with the duration of the US Shuttle flights, its solubility diagram on earth is known at various temperatures [20–22, 31, 32], its structure is known at high resolution [33], and it is one of the most extensively studied protein in crystallogenesis (e.g. Ref. [20–22, 31–39]). The protein was a single batch of three-times crystallized hen egg-white lysozyme chloride (Cat. No. L-2879, lot 51H7150, Sigma) containing about 90% (w/w)

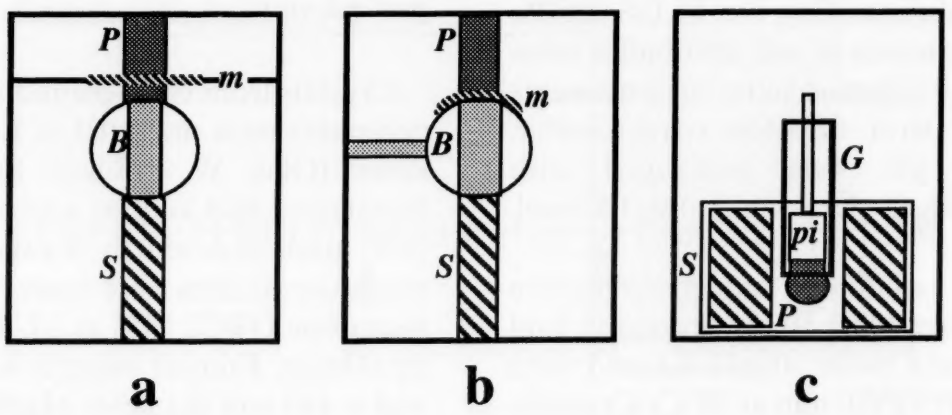

Fig. 1. Schematic drawing of the three types of reactors used in APCF. (a) DIA, (b) FID, (c) HD vapor diffusion reactors in activated positions. The FID reactor can be used in dialysis mode by inserting a membrane between the rotating plug and the protein chamber. In HD reactors, the salt solution is maintained in absorbent blocks. Abbreviations used: *B* buffer solution, *P* protein solution, *S* salt solution, *m* semi-permeable membrane, *G* glass tube of the syringe, *pi* piston.

protein balanced with sodium acetate and sodium chloride. According to the manufacturer, its specific activity was 57 000 units/mg protein. Using denaturing gel electrophoresis and high performance size exclusion chromatography, it was found that it contains less than 0.3% w/w foreign proteins. Therefore it was used without further purification for all experiments throughout this study. Control crystallization assays were performed to verify the reproducibility and the quality of the crystals (i.e. the absence of polycrystalline material or twinned crystals that would appear in contaminated batches [40–42]). Lysozyme concentrations were calculated from absorbance measurements at 280 nm, assuming that the absorbance of a 1 mg/ml lysozyme solution is 2.66 for an optical path length of 1 cm, and were confirmed by colorimetric Bradford micro-assays in 96-well microtitration plates [43]. Residual lysozyme concentrations in crystallization solutions were measured after centrifugation for 2 min over microporous Ultrafree-MC membranes (0.22 μm, Cat. No. UFC3 OGV00, Millipore) to remove crystalline material prior to dilution with buffer.

"Pro analysis" grade sodium acetate trihydrate (Cat. No. 6267.0500), NaCl (Cat. No. 6404), and acetic acid (Cat. No. 63) were purchased from Merck. Acetate buffer was prepared by adjusting a 50 mM sodium acetate solution to pH 4.5 with acetic acid. A 4 M NaCl solution in buffer was used as a stock solution. All solutions were prepared with three-times distilled sterile water (Cat. No. 30631, Biosedra, France) and filtered over 0.22 μm sterile membranes (Cat. No. SLGS 025BS, Millipore). Concentrations of salt and buffer solutions were verified by refractive index measurements performed at 20°C with an Abbe refractometer. Measurements of pH were performed with a MIXC410 glass micro-electrode (Solea-Tacussel, France).

Lysozyme stock solutions for crystallization were prepared by dissolving 50 mg protein in 1 ml of 50 mM Na acetate buffer at pH 4.5 and were centrifuged at 10 000 × g (20 min at 20°C). Crystallization assays were set up after appropriate dilutions with buffered 4 M NaCl and 50 mM buffer solutions according to the conditions of Alderton et al. [2, 44].

2.3. Methodological aspects

The ground control experiment was simultaneously subjected to the same sequence of events as the microgravity experiment. Both sets of 25 reactors were filled at the same time and handled in the same way during the experiment. This is especially important after the end of the microgravity period (during Shuttle landing and reactor manipulations) when the protein solutions are most probably still supersaturated because several weeks to months are required for reaching solubility (equilibration between crystals and solution) in undisturbed protein solutions. At the return of the two sets of reactors in Strasbourg, each reactor was observed, crystals were counted, and their sizes measured. The operators in charge of the evaluations were not told whether the reactor belonged to the ground or microgravity set. Crystals larger than 0.2 mm, which had not grown on a surface and did not present apparent defects (cracks or twinning) were mounted in Lindeman glass capillaries for further X-ray investigations. Aliquots of each of the 50 protein solutions were withdrawn for absorbance measurements to determine the residual lysozyme concentration. In addition, refractive index and pH measurements of the buffer and the reservoir solutions were measured. The data of this study are compiled in 37 tables and 5 figures, available upon request from the corresponding author. For the sake of clarity, only the major results and the conclusions are presented here.

2.4. Crystallographic methods

Crystals from both ground and microgravity experiments were mounted in Lindeman glass capillaries (Glas W. Müller, Berlin, Germany) in Strasbourg and kept at a constant temperature of 18°C until exposed to X-rays. Measurements for resolution studies were made at 6°C on the wiggler beam-line DW32 [45] at LURE synchrotron facility (Orsay, France) using a wavelength of 0.901 Å and a 180 mm diameter MarResearch image-plate detector. Since no larger image plate system was available at the DW32 station at the time of recording, the detector was offset (50 mm) to collect the high resolution data sets. X-ray data were processed

with the program MOSFLM [46] adapted by P. Gouet to take into account the translation.

For each mounted crystal a partial data set was recorded in order to analyze statistically the difference of diffraction quality between them. Then a complete data set was recorded for the two apparently best crystals (one from the ground experiment and the other from space) in order to compare the quality of the data sets in real space. To collect a complete data set, one *ground* crystal and one *space* crystal of lysozyme were sufficient [30].

Rocking curve measurements were performed on the instrument located on the D23 beam line at LURE. The system consists of an Eulerian cradle with a two dimensional detector (Mark II), the whole instrument being rotated so that the ω axis was in the horizontal plane because of the horizontal polarization of the synchrotron beam [47]. Beam monochromatization was achieved by double Si(1 1 1) crystal monochromator with sagittal focusing. The X-ray beam was analyzed by the first crystal which selects the wavelength. The second crystal, which can be translated on a rail, focalizes the beam in the horizontal way. The crystal to detector distance was 580 mm with the detector swung from the symmetric position to reach appropriate resolution. Beam residual divergence was 5.41 mrad horizontally and 0.058 mrad vertically. The crystals were not crystallographically oriented and Bragg reflections were randomly picked. Rocking curves were measured by steps of 1/1000° from Bragg reflections chosen into two orthogonal area of the reciprocal space.

3. Results and discussion

3.1. Preliminary ground experiments

Preliminary experimentation was necessary to define precisely the experimental conditions in the APCF reactors on the basis of the data known for lysozyme crystallization at 18°C on earth and to take into account the overall time schedule of the SpaceHab-01 Mission (see Fig. 2). The total time was estimated to be about 20 days: 9 days at 18°C for forwarding the reactors to Cape Canaveral (Florida) and for integration into the Shuttle, $6\frac{1}{2}$ days for the foreseen time of the microgravity mission and 4 additional days for recovery of the reactors from APCF module, photographs and delivery back to Strasbourg. Because of the duration of the pre-flight steps, it was necessary to verify that the crystallization of lysozyme was not affected by aging of the undersaturated solutions during this time span or for a longer dormant period in case of a delayed Shuttle launch. It was found that lysozyme solutions, stored for three weeks at 18°C, yield crystallization results identical to those of fresh lysozyme (within the limits of reproducibility).

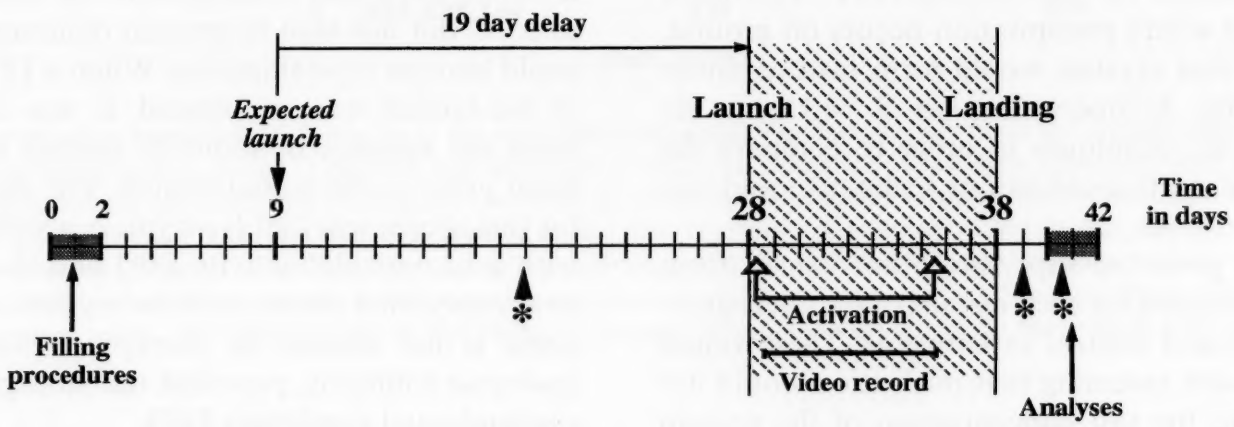

Fig. 2. Timetable of the SpaceHab-01 Mission. The actual microgravity phase is emphasized (hatched region). Temperature was recorded throughout the mission (see text). Filling procedures included also the measurements of pH, absorbance and refractive index of all the solutions. Analyses after landing consisted in measurements of pH, absorbance and refractive index of the recovered crystallizing solutions. *Indicates when photographs of the protein chambers were taken on earth.

In the training experiments, reactors were therefore activated immediately after filling in order to save time and to run more experiments. They were deactivated after $6\frac{1}{2}$ days and results were analyzed 4 days later, so that a whole cycle lasted 11 days.

The nucleation zone was determined on earth for two lysozyme concentrations (10 and 30 mg/ml) as a function of NaCl concentration for the three types of reactors. Supersaturation regimes (supersaturation being defined as $\sigma = c/S$, with c the protein concentration and S the solubility) leading to the growth of increasing numbers of crystals (less than 20 crystals, from 20 to 100 crystals, and more than 100 microcrystals) were defined. During the six months of the preparatory phase, each laboratory involved in the project has run ten times the flight conditions for each type of reactor at two protein concentrations as indicated in Fig. 3. Note that the frequency of nucleation events is dependent upon the crystallization device (technique, volume, geometry) used and that under certain conditions (those symbolized by hatched boxes) the range of nucleation was quite large and could vary from one experiment to another. From the output of these preparatory tests, we selected the conditions outlined in the gray parts of Fig. 3 for the microgravity mission. Since a shift of the nucleation zone toward a higher supersaturation was expected under microgravity, the lowest supersaturation chosen for the microgravity experiment corresponded to conditions yielding at least 20–100 tetragonal crystals on earth. The highest supersaturation ($\sigma \approx 30$) chosen for the microgravity experiment are located where precipitation occurs on ground, expecting that crystals would form instead under microgravity. A supersaturation of ≈ 15 was selected for all techniques in order to compare the influence of starting conditions, techniques and volumes.

Table 1 gives the supersaturation values (from 5.4 to 33) selected for each reactor of the microgravity and ground control experiments. These values are calculated assuming that nucleation would not start before the salt concentration of the protein solution would have completely equilibrated with the reservoir solution. This assumption is a rough approximation, necessary for comparing different techniques, but the benefit expected from dialysis and vapor diffusion is the occurrence of nucleation during the equilibration, otherwise all techniques would only be delayed batch methods. The FID *space* reactors 114A and 112A contained identical solutions ($\sigma = 16$) but the first one had no dialysis membrane in order to compare results of free interface diffusion and dialysis techniques in microgravity. The corresponding ground controls (FID113A and FID115A) were both equipped with a dialysis membrane. Reproducibility of the hanging drop method showed to be poor during the pre-flight experiments and was therefore checked with duplicates (10 mg/ml, $\sigma = 26$) in both microgravity and ground control experiments.

3.2. Overview of the mission experiment and control outcomes

The timetable of SpaceHab-01 experiment is summarized in Fig. 2. After the two-day filling of the 50 reactors in Strasbourg, they were sent to Cape Canaveral and stored until integration into the APCF module and the Shuttle launch. The temperature recorded over the whole period of the mission and during transportation of the reactors in the containers was within 18 ± 0.3°C, except in one container (the 12 HD reactors from the 101–116 and 133–145 series, see Table 1) in which it rose accidentally to 33°C for a period of 12 h during the transport to the USA, thus before activation of these reactors in microgravity. Lysozyme is thermostable up to 60°C, as shown by NMR spectroscopy [48], and consequently the heating cycle to 33°C did not lead to protein denaturation that could hamper crystallization. When a 19 day delay of the launch was announced, it was decided to leave the samples in stand-by instead of refilling them prior to the actual launch. The main reason for this choice was that lysozyme is a stable protein with a bactericidal activity [49] and that preliminary assays had shown that the crystallization outcome is not altered by storage of concentrated lysozyme solutions, provided the storage is in uncontaminated conditions [42].

Each of the 50 reactors was observed and photographed 9 days before launch to check for possible crystals and/or bubbles. DIA and FID reactors containing bubbles below the dialysis membrane

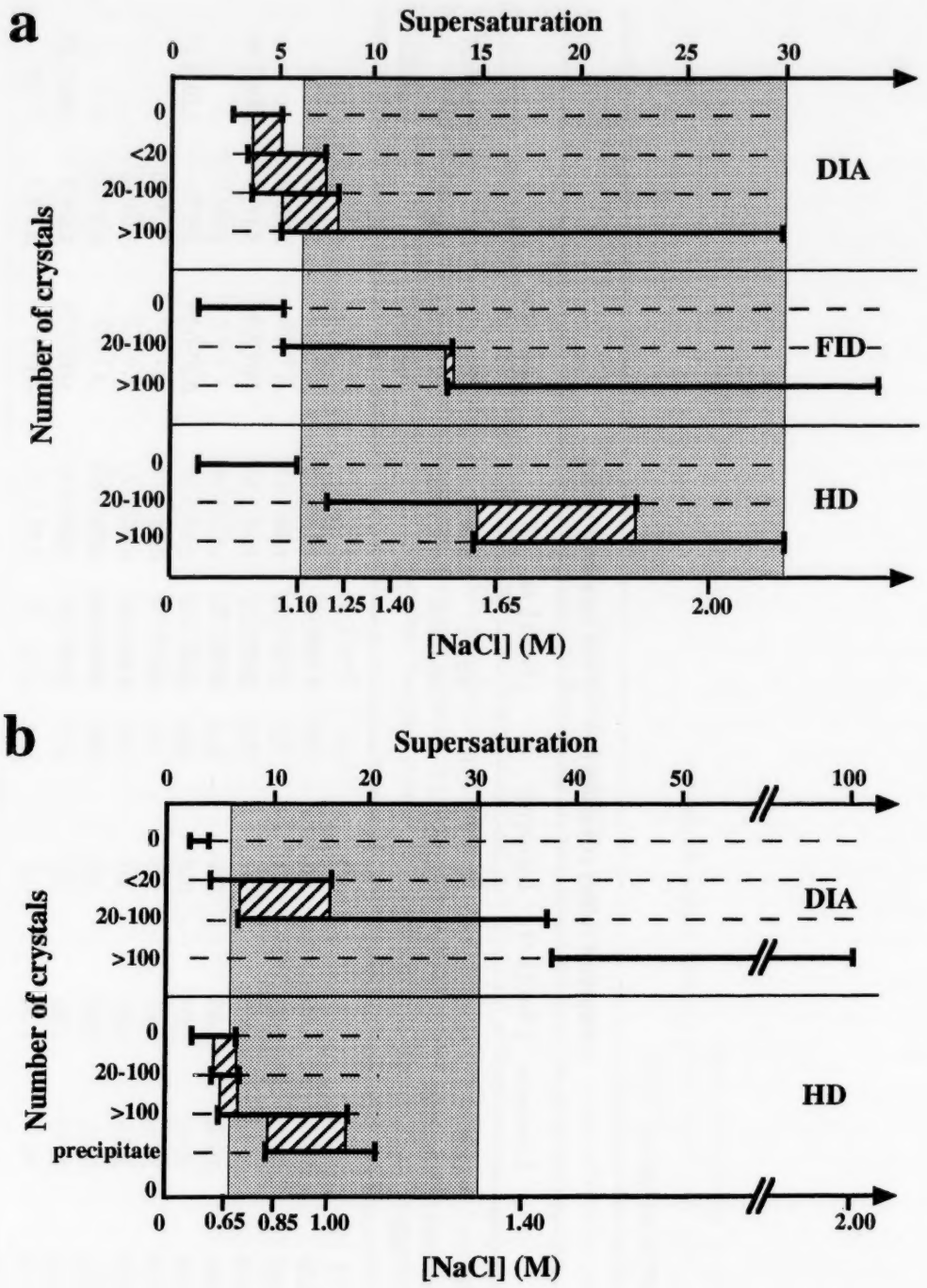

Fig. 3. Crystallization conditions for lysozyme in the pre-flight experiments. The data correspond to the average number of crystals counted in the crystallization set-ups 11 days (6 $\frac{1}{2}$ days activation + 4 days for simulation of post-flight operations) after activation and for two initial lysozyme concentrations (10 mg/ml in panel (a) and 30 mg/ml in panel (b). For each type of reactor, sets of solid lines indicate the supersaturation range in which (i) no crystals, (ii) less than 20 crystals, (iii) from 20 to 100 crystals, and (iv) more than 100 crystals are observed. Molarity of NaCl and corresponding supersaturation are indicated. The hatched boxes indicate the conditions where the variability of results was largest in duplicated experiments (e.g. where solid lines overlap). The dotted lines visualize the range of supersaturation tested. The grey zones (in (a) and (b) mark the supersaturation range chosen for the mission experiments.

were assigned to the ground control set. No crystallization had occurred during the dormant pre-flight phase in these reactors. On the contrary, HD reactors containing solutions with supersaturation ranging from 1.5 to 3.4 before activation (see Table 1) contained, unexpectedly at these low supersaturations, a small number of crystals (1–10). Thus, for each reactor pair, the one containing the

Table 1
Initial and final solution conditions in the APCF reactors

Reactor number (**space**/ground)	**Initial conditions**				**Expected values at equilibrium**[a]			**Final measured values**				
	[NaCl] *M*			Lysozyme	[NaCl] *M*	Lysozyme		[NaCl] *M*		Lysozyme		
	Protein chamber (67 µl)	Buffer reservoir (85 µl)	Salt reservoir (257 µl)	*c* (mg/ml)		*S* (mg/ml)	σ	Buffer reservoir	Salt reservoir	S^e (calculated) (mg/ml)	*c* (mg/ml)	Residual σ^e (calculated)
DIA												
101I/102I	0.1	1.10	1.36	10	1.10	1.6	6.3	**1.13**/0.91	**1.16**/1.35	**3.16**/-	**5.6**/11.1	**1.77**/-
103I/104I	0.1	1.25	1.55	10	1.25	1.2	8.5	**1.30**/1.35	**1.44**/1.42	-/-	**13.3**/10.6	-/-
105I/106I	0.1	1.40	1.74	10	1.40	0.9	11.0	**1.42**/1.16	**1.42**/1.55	**1.07**/1.34	**3.1**/3.9	**2.89**/2.90
109I/107I	0.1	1.65	2.05	10	1.65	0.6	16.0	**1.79**/1.79	**1.92**/1.88	-/-	**15.6**/13.3	-/-
110I[d]/111I	0.1	2.00	2.50	10	2.00	0.4	26.0	**2.01**/1.82	**2.11**/2.21	**0.67**/0.79	**3.5**/3.3	**5.20**/4.17
112I/113I	0.1	0.65	0.79	30	0.65	5.5	5.4	**0.67**/0.73	**0.81**/0.74	-/-	**32.3**/33.2	-/-
116I/117I	0.1	0.75	0.92	30	0.75	3.9	7.6	**0.80**/0.87	**0.95**/0.91	-/-	**30.4**/34.4	-/-
119I[d]/120I	0.1	0.85	1.05	30	0.85	2.9	10.0	**0.91**/0.89	**0.93**/1.10	-/-	**5.3**/36.2	-/-
124I[d]/127I	0.1	1.00	1.23	30	1.00	2.0	15.0	**0.98**/0.92	**1.00**/1.06	**1.94**/2.78	**3.6**/6.2	**1.86**/2.23
128I/130I	0.1	1.40	1.74	30	1.40	0.9	33.0	**1.34**/1.38	**1.59**/1.56	-/3.19	**3.3**/4.1	-/1.28
FID[f]	(450 µl)	(235 µl)	(598 µl)									
101A/105A	0.1	1.25	2.12	10	1.25	1.2	8.5	**1.29**/1.29	**1.31**/1.35	**1.42**/1.58	**2.9**/2.2	**2.06**/1.42
106A/108A	0.1	1.40	2.38	10	1.40	0.9	11.0	**1.40**/1.56	**1.57**/1.66	**1.36**/2.13	**2.8**/2.9	**2.08**/1.38
112A[d]/113A	0.1	1.65	2.82	10	1.65	0.6	16.0	**1.67**/1.71	**1.79**/1.77	**0.82**/0.81	**1.9**/2.5	**2.38**/3.10
114A[d]/115A	0.1	1.65	2.82	10	1.65	0.6	16.0	**1.68**/1.68	**1.71**/1.72	**0.70**/0.71	**2.0**/1.8	**2.86**/2.48
118A/119A	0.1	2.00	3.43	10	2.00	0.4	26.0	**2.04**/1.99	**1.93**/2.05	**0.35**/0.41	**0.8**/1.1	**2.29**/2.65

Reactor number (**space**/ground)	Initial conditions (50 µl drop)			Expected values at equilibrium[a,b]				Final measured values			
	[NaCl] *M*	Lysozyme		[NaCl] *M*	Lysozyme			[NaCl] *M*	Lysozyme		
		c (mg/ml)	σ		*c* (mg/ml)	*S* (mg/ml)	σ		*S* (calculated) (mg/ml)	*c* (mg/ml)	Residual σ (calculated)
HD											
101/102	0.70	5	1.1	1.40	10	0.9	11	**1.42**/1.43	**0.87**/0.85	**7.9**/3.6	**9.10**/4.22
107/104	0.78	5	1.4	1.55	10	0.7	14	**1.59**/1.68	**0.66**/0.58	**3.1**/2.5	**3.76**/5.32
112[d]/116[e]	0.83	5	1.6	1.65	10	0.6	16	**1.85**/1.70	**0.46**/0.57	**1.9**/2.2	**4.10**/3.88
122/118[e]	1.00	5	2.5	2.00	10	0.4	26	**1.99**/1.99	**0.39**/0.39	**3.7**/2.0	**9.48**/5.13
126/124[e]	1.00	5	2.5	2.00	10	0.4	26	**2.01**/2.00	**0.38**/0.39	**1.5**/2.7	**3.94**/7.00
128/129	0.38	15	0.7	0.75	30	3.9	8	**0.82**/0.82	**3.19**/3.19	**6.8**/4.9	**2.13**/1.54
136/133	0.43	15	1.0	0.85	30	2.9	10	**0.94**/0.95	**2.31**/2.25	**4.6**/4.4	**1.99**/1.95
140/141	0.45	15	1.1	0.90	30	2.6	12	**1.03**/0.95	**1.86**/2.25	**3.4**/3.9	**1.83**/1.73
145/143[e]	0.50	15	1.5	1.00	30	2.0	15	**1.09**/1.11	**1.63**/1.56	**4.0**/3.7	**2.46**/2.38
22/15[e]	0.70	15	3.2	1.40	30	0.9	33	**1.49**/1.44	**0.77**/0.84	**2.8**/3.4	**3.61**/4.05

Note: Bold and normal characters are used to indicate results obtained with *space* and *ground* reactors, respectively. Values at equilibrium must be taken as expected values in the protein solution after equilibration with the reservoir and before crystallization. The columns labeled 'Final measured values' include the measurements of the salt concentration of the buffer and piston reservoirs, and the protein concentration in the protein solution. The corresponding calculated *S* and σ values are also reported. *S* and σ values were calculated from the measured salt concentration in the buffer and piston reservoirs, under the assumption that these concentrations are descriptive of the protein-salt mixtures.

[a]Supersaturation values σ are calculated for indicated nominal salt concentrations and corresponding solubility data published in [20].

[b]The drops had an initial volume of 50 µl and were expected to shrink by half after complete equilibration.

[c]Missing data correspond to poorly or not equilibrated reactors

[d]Video pictures of these reactors have been taken during the flight.

[e]Crystals were already present in both *ground* and *space* reactors of the pair before activation.

[f]All FID reactors except one (114A) were used in the dialysis mode.

smallest number of crystals was chosen for the flight. Final assignments are given in Table 1.

The duration of the STS-57 Mission was prolonged and lasted 234 h ($9\frac{1}{2}$ days) of which the reactors were activated during 178 h. Endeavour landed on July 1st, the 50 reactors were photographed on July 2nd at Cape Canaveral. All reactors were again photographed as they arrived at Strasbourg, two days after landing. No significant difference of the number and size of the crystals could be observed when comparing the latest video images recorded on board, the photographs taken after landing in Florida and those taken in Strasbourg. Of course this comparison concerns especially the crystals grown on the quartz walls (60% and 40% of the total number of crystals in the DIA and FID reactors, respectively) as they remain exactly at the same position. The free floating crystals were more difficult to compare as they are hardly observable on the photographs.

The next day the reactors were opened, crystals counted, measured, and mounted for X-ray analyses, and the solutions analyzed. The final salt concentration of the reservoirs measured in the HD reactors were identical (within 0.05 M) to their initial values in 10 reactors, showed a deviation of only 0.06–0.10 M in 6 reactors, but had increased by more than 0.11 M in HD107, 112, 140 and 143, as shown in Table 1. These exceptions were attributed to leaking of the reactors during the experiment. Another problem of evaporation or leaking was noticed in 6 among the 10 DIA reactors in which no crystallization occurred, and in which the protein concentration appeared to have increased by more than 10%.

Refractive index measurements of buffer and reservoir solutions indicated that only 2 out of the 20 DIA reactors had equilibrated correctly. Among the remaining ones, 8 had equilibrated only partially and 10 very poorly because of bubbles trapped in the channel of the rotating plug. The 10 DIA reactors which had equilibrated poorly contained no crystals. Equilibration of the salt solutions in the different compartments was satisfactory in 9 out of the 10 FID reactors (except for FID108A), probably because of the larger diameter of the plug channel (when compared to DIA reactors) which makes equilibration possible even in the presence of small bubbles. The problem of poor equilibration of the DIA reactors should be solved by using a larger piston diameter (5 mm instead of 3 mm). The presence of traces of salt around the rotating plug of some DIA reactors was attributed to a misalignment of the plug between the protein and reservoir chambers during the assembly of the parts. This was not the case for the FID reactors.

Among the 29 DIA and FID reactors equipped with a dialysis membrane, a slight protein leaking through the membrane was noticed only in DIA102I, as 7.6% of the protein from the protein chamber was present in the plug channel. In FID 114A, which had no dialysis membrane, about 30% of the protein had diffused toward the buffer and reservoir chambers.

The pH of solutions in contact with the DIA and FID quartz reactors did not vary but that of reservoirs in HD reactors increased by 0.5–1.0 unit, likely because of traces of chemicals contained in the absorbent blocks. Consequently, this strongly suggests to wash extensively and to dry the polyethylene blocks in a desiccator in future experiments.

3.3. Comparative lysozyme crystallizations in space and on ground

The total number of crystals grown in each type of reactors are listed in Table 2 for the microgravity experiment and the ground controls. The data of the microgravity experiment are within the reproducibility range of the ground controls for the comparable FID reactors: a total number of 329 and 359 crystals were counted, respectively. Their size is also similar, respectively, 0.54 and 0.57 mm in average for microgravity and ground grown crystals. The comparison of the number and size of crystals grown in the DIA reactors is not possible because it was decided to keep the reactors presenting bubbles in the piston before the flight for the ground control set. Therefore they presented a lack of proper equilibration implying a different supersaturation in the reactors of a given pair. Among the HD reactors, only the pair HD101/102 can be compared and they both contained 50 crystals measuring between 0.05 and 0.10 mm, but they could not be observed directly in the syringe. The

Table 2
Number, size, and FWHM of lysozyme crystals obtained in space and on earth

	Reactor number	Number of crystals	Size of selected crystals (mm)	Mosaicity at 2 orthogonal positions (degrees)
DIA	**101I**	11 (0)		
	105I	**6 (0)**	**0.6×0.4×0.3**	**0.014–0.015**
	106I	32 (5)	0.4 × 0.4 × 0.3	0.013–0.008
	110I	**27 (0)**		
	111I	25 (4)		
	119I	**44 (4)**		
	124I	**26 (4)**	**0.6×0.6×0.6**	**0.011–0.012**
	127I	> 65 (5)		
	128I	**> 50 (20)**		
	130I	> 65 (15)		
FID	**101A***	**36 (12)**	**0.7×0.5×0.5**	**0.030–0.011**
	105A	58 (18)	0.6 × 0.6 × 0.5	0.012–0.015
	106A	**35 (0)**	**0.8×0.7×0.4**	**nd**
	108A	44 (10)		
	112A	**31 (2)**	**0.7×0.4×0.2**	**0.013–0.012**
	113A	63 (11)	0.8 × 0.4 × 0.4	nd
	114A	**105 (5)**		
	115A*	67 (6)	1.1 × 1.2 × 0.6	0.016–0.032
	118A	**29 (0)**		
	119	45 (4)	0.6 × 0.4 × 0.2	0.011–0.014
HD	**101**	50		
	102	**50**		
	118	5		
	122	**2**		
	124	26		
	126	**3**		
	128	**8**		
	133	6	0.5 × 0.5 × 0.3	0.013–0.006
	15	15		
	22	**20**	**0.5×0.5×0.3**	**0.016–0.024**

Note: Data of the space and ground experiments having yielded crystals are in bold and normal characters, respectively. The table displays the total number of crystals counted in each reactor including those free floating which are given in parenthesis.
* For selected crystals originating from these reactors, complete diffraction data sets were collected for the structure refinement at high resolution (see text). nd = not determined.

other HD reactors were not pairwise at identical supersaturation, and in addition the syringes had to be opened to withdraw their content for evaluation. This did not allow an accurate evaluation since several crystals were damaged during handling. The addition of a mirror and a window for enabling a better observation of the drops were suggested to the manufacturer to avoid these problems in future experiments.

The residual lysozyme concentrations in the crystallizing chamber of the three types of reactors from both the microgravity and ground sets, measured 3 days after the Shuttle landing, are given in Table 1. However, in some reactors the protein

solutions present a residual supersaturation up to ≈ 9, meaning that such high conditions of supersaturation may be sensitive to reentry vibrations of the Shuttle which may induce nucleation. In Fig. 4 the residual protein concentration (corresponding to the "final lysozyme concentration measured" in Table 1) are plotted together with the previously published [18] solubility curve of lysozyme, obtained under similar conditions of pH and temperature but after a period of 3–6 months to reach complete equilibration between the liquid and the solid phase. When comparing the amount of protein remaining in supersaturation (for calculation see legend of Table 3), most data of the *space* assays and of their *ground* controls superimpose with each other within the limits of experimental errors, for a given reactor type and initial lysozyme concentration (10 or 30 mg/ml) as given in Table 3. Surprisingly, 70–90% of the initial supersaturated material had already crystallized 14 days after activation of

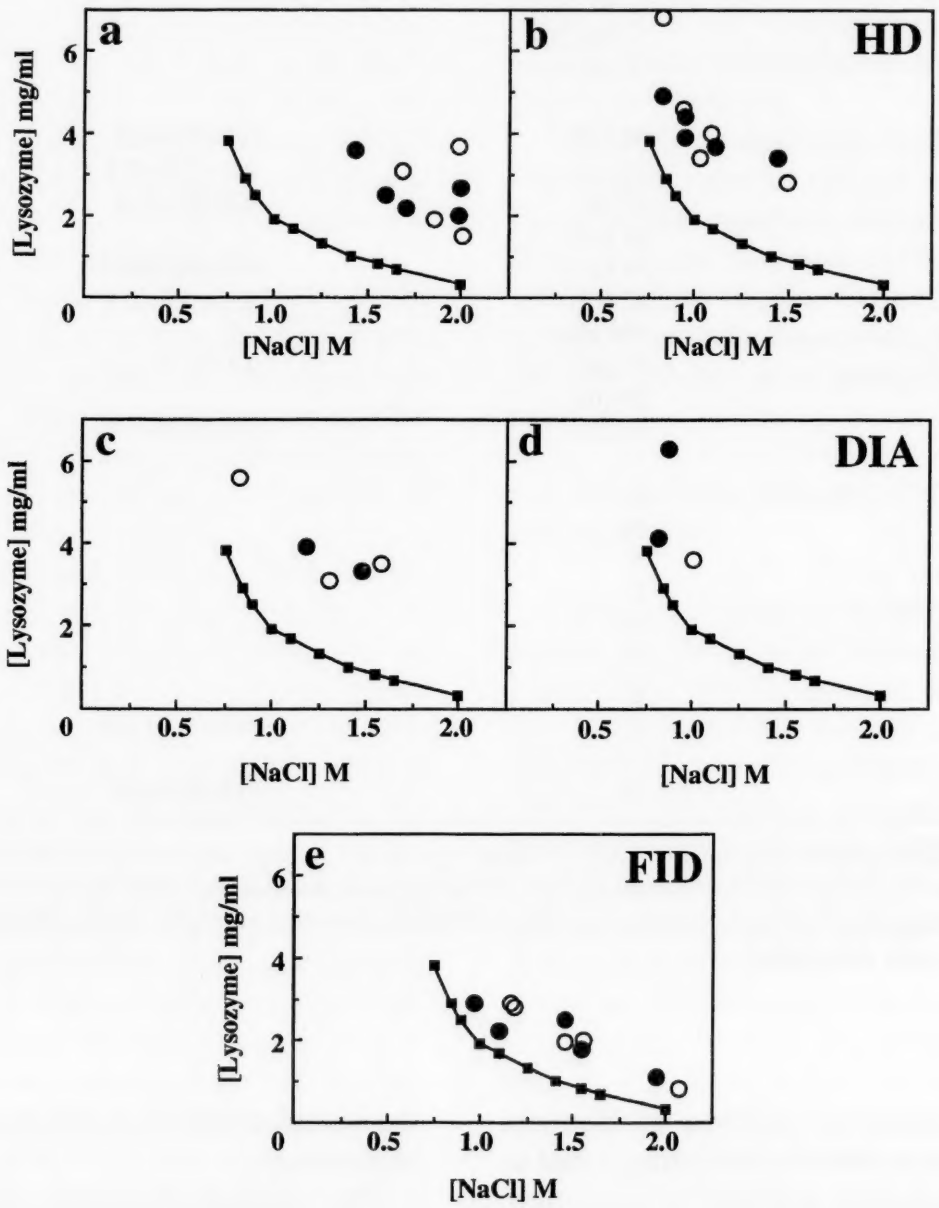

Fig. 4. Residual lysozyme concentration in space experiments (o) and ground controls (●), and comparison with the protein solubility curve (■) at 18°C. The residual lysozyme concentrations are displayed in solubility diagrams of lysozyme concentrations versus NaCl concentration, the crystallizing agent. (a,b) HD reactors, (c,d) DIA reactors and (e) FID reactor used in the dialysis mode. Initial lysozyme concentrations were 10 mg/ml (in a,c,e) and 30 mg/ml (in b,d).

Table 3
Average residual lysozyme concentrations in supersaturation for the three types of reactors containing two initial protein concentrations; percentages were calculated as: $\% = 100 \times [\text{Prot}]_{\text{final}} - S)/([\text{Prot}]_{\text{initial}} - S$, S being determined for the calculated salt concentration in the protein chamber; percentages are given with the standard deviation, except for DIA with 30 mg/ml initial protein concentration, for which only one value could be taken into account

Type of reactor	[Lysozyme] (mg/ml)	Volume of protein (μl)	Residual protein concentration in supersaturated state	
			Space (%)	Ground (%)
HD	10	50	**22±5**	22 ± 9
HD	30	50	**8±3**	7 ± 1
DIA	10	67	**30±5**	28 ± 2
DIA	30	67	**6**	8 ± 5
FID	10	450	**13±4**	11 ± 4

the experiment. A major observation is the differential crystallization behavior depending on the initial protein concentrations, as shown in Table 3. The percentage of residual protein concentration in supersaturation in the HD and DIA reactors is about 2–3 times higher when starting with an initial protein concentration of 10 mg/ml than with 30 mg/ml. Although a definitive interpretation of these effects cannot yet be given, it is likely that the observed differences reflect different kinetic behaviors of the overall crystallization process.

3.4. Motions occurring during the STS-57 Mission

During the flight video pictures of 2 FID, 1 HD, and 3 DIA reactors (see Table 1 for reactor numbers) were taken every 9 h for a given reactor, each time a series of 8 pictures was taken at a different focus so that the whole depth of the protein chamber could be observed. The images were stored in a tape drive together with the facility's housekeeping data and were supplied on CD-ROM pictures after the flight. They have been analyzed in detail independently [28]. The appearance of the first crystals could be estimated between 30 and 38 h after activation for DIA124I, 35 and 44 h for DIA119I, 49 and 58 h for FID112A and 64 and 72 h for DIA110I.

Video imaging of the growing crystals provided in particular useful information about the stability of the microgravity environment, as important motions of bubbles and/or floating crystals were observed twice during the STS-57 flight. In the first case (illustrated in Fig. 5a), one small free floating lysozyme crystal seen in DIA 124I moved toward the glass wall between 57h45 and 66h17 APCF elapsed time (i.e. elapsed time since activation of APCF reactors in microgravity). This displacement did not have any major consequence since the crystal continued to grow on the wall. Between 85h40 and 85h44 APCF elapsed time, the pictures of FID112A showed a second, more drastic motion. It is illustrated by FID114A (the second row of pictures in Fig. 5b taken at 84h09 and at 92h48 APCF elapsed time) in which most crystals were projected against one wall of the protein chamber. This must be due to a severe shock aboard the Shuttle, probably during the retrieval of the EURECA satellite which took place during the STS-57 Mission. Video images of the later IML-2 Mission also showed motion of the crystals during the microgravity phase in a HD reactor [50]. Detection of such phenomena convincingly showed that video imaging is essential during a microgravity mission; without monitoring, such events would have escaped our knowledge.

3.5. Crystallographic characteristics of microgravity and ground grown lysozyme crystals

The crystallographic characterization of the crystals detailed hereafter has not been optimized

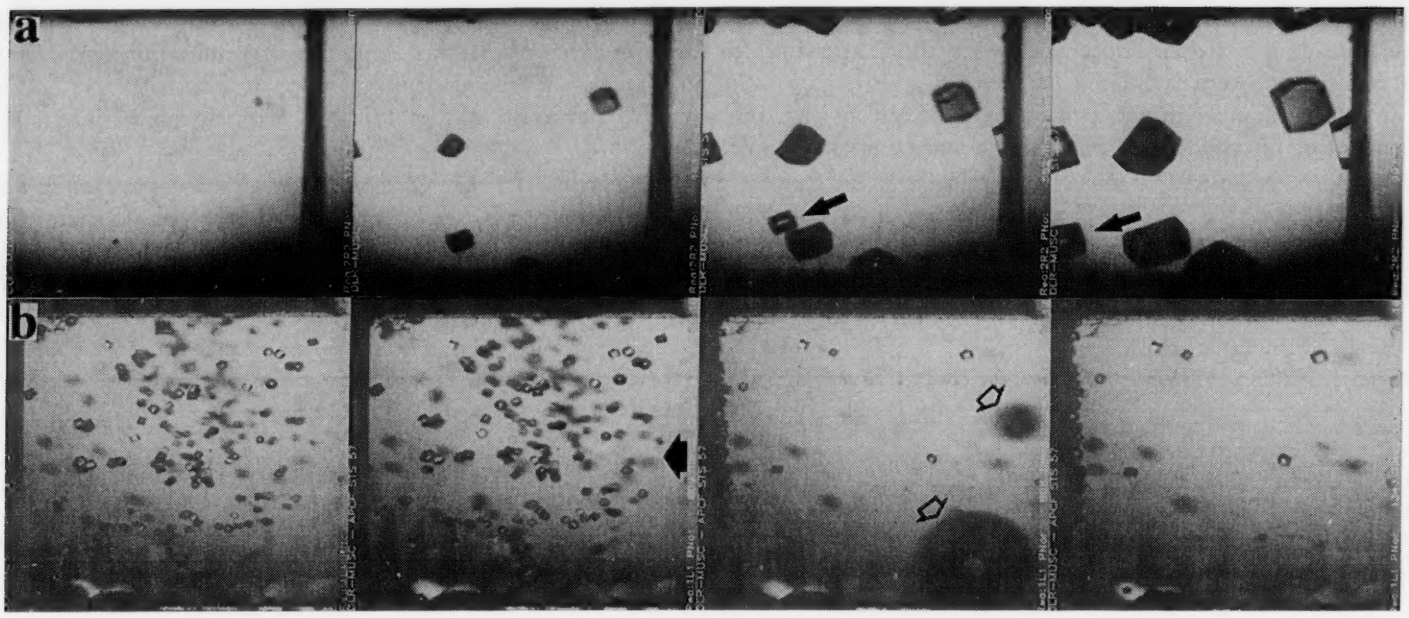

Fig. 5. Sequence of video images of tetragonal lysozyme crystals grown in microgravity. (a) Crystals growing in DIA 124I (30 mg/ml lysozyme, $\sigma = 15$) recorded at 38h51, 48h07, 57h23, and 103h42 APCF elapsed time, respectively, from left to right. Arrows point toward a moving free floating crystal. (b) Crystals growing in FID114A operating in the actual free interface mode (10 mg/ml lysozyme, $\sigma = 16$) at 74h53, 84h09, 93h24, and 139h07 APCF elapsed time, respectively, from left to right. The black arrow indicates the motion of most of the crystals toward one side of the chamber (as seen in the third and fourth images from the left). The two open arrows in the third image point towards the two bubbles that appeared in the field of view. Both types of events are indicative of strong perturbations that occurred on board. All pictures in one sequence are at the same magnification and cover a field of 3.5×5.5 mm^2 in (a) and 6.2×6.5 mm^2 in (b).

by preliminary tests as performed for crystal growth since the experiment aimed at comparing the number and size of microgravity and ground grown lysozyme crystals, and at checking possible difficulties and artefacts in the overall protocols in order to prepare future flights. However, since the SpaceHab-01 experiment yielded a large number of large crystals, some were subjected to crystallographic characterizations in order to define a benchmark and to optimize the investigations of crystals of future microgravity experiments such as IML-2. The crystals selected for these characterizations were chosen among the free-floating ones (except 105I and 106A which were loosely attached onto the top membrane) in different reactors as given in Table 2.

3.5.1. Resolution

Among the crystals grown in the different reactors with different techniques, six from each set (ground control and microgravity experiment) were chosen according to their morphological quality and their size. The crystals were analyzed by *space/ground* pairs. The choice of pairs was decided upon size criteria. For each crystal, a partial data set was recorded (see Table 2 for the list of tested crystals and [29] for details) in order to analyze statistically the difference of diffraction quality between them. All twelve crystals belong to the tetragonal system $P4_32_12$ with 1 molecule in the asymmetric unit and have the same cell parameters, except FID119A whose parameters are $a = b = 78.53$ Å and $c = 38.37$ Å. The average values are $a = b = 78.60$ Å (with a standard deviation of 0.4 Å) and $c = 37.81$ Å (with a standard deviation of 0.06 Å).

First of all, it should be noticed that using synchrotron radiation instead of a rotating anode is generally a major parameter towards improving resolution. In general, visual inspection of two orthogonal diffraction frames gave a fairly close approximation of the maximum resolution. In the

range of experimental conditions used, we have not observed any significant improvement of resolution or signal to noise ratio for *space* crystals, as compared to the *ground* crystals. Detailed analyses of these data and comparison with other data from the PCF Mission and the IML-2 Mission are given in the accompanying paper [29].

However, diffraction limits of both *ground* and *space* crystals were found to be better (1.3 Å) than any previously published tetragonal crystals of lysozyme. Therefore refinement of the high resolution structure of hen egg-white lysozyme from the best *ground* crystal grown in FID115A (1.33 Å resolution data) and the comparison with the data and structure from the best *space* crystal grown in FID101A (1.40 Å resolution data) were completed [30]. The two structures are nearly identical with the root mean square difference on all protein atoms being 0.13 Å. Four residues in the *ground* crystal and three residues in the *space* crystal show multiple alternative conformations. The quality of the new electron density allowed the localization of two ions in the maps of both structures: one Cl^- ion at the interface between two symmetry-related molecules and one Na^+ ion stabilizing the loop Ser_{60}-Leu_{75}. The Na^+ ion is surrounded by 6 ligands which form a bipyramid around it, with distances of 2.2–2.6 Å. Coordinates were deposited at the Protein Data Bank under entries 193L and 194L.

3.5.2. Mosaicity

As underlined above, the measurements of the experimental rocking width are aimed at defining technically the strategy for future characterization of the crystals grown either on earth or in microgravity. For the crystals originating from our set of experiments, these measurements were performed after the resolution limit analyses, for which exposure times to X-rays were short to minimize radiation damage. In the case of the two crystals from FID reactors 101A and 115A, complete diffraction data sets had been previously collected. As a consequence the very large values of the rocking width, up to 0.03° as shown in Table 2, do not reflect the crystal quality but rather the damage resulting from irradiation.

No significant difference of the rocking width (given as the full width at half maximum, FWHM, of a Bragg reflection) between *space* and *ground* crystals was observed as shown in Table 2. On average the microgravity grown crystals present a FWHM of $0.015 \pm 0.004°$, the average for the ground grown crystals being $0.011 \pm 0.004°$. Results with lysozyme crystals obtained by Helliwell and co-workers [51] during the same mission are in the same range with an average FWHM of 0.0091 ± 0.0025 and $0.0130 \pm 0.0049°$, respectively, for 11 microgravity and 9 ground grown crystals, using the same experimental set-up at LURE. As a matter of fact, for all microgravity and ground lysozyme crystals originating from SpaceHab-01 Mission, characterized in an identical way and with the same instrument, the average FWHM is $0.011 \pm 0.004°$ and $0.012 \pm 0.004°$, respectively. The best values observed are 0.006° for *ground* crystal HD133 in our study (Table 2), and 0.007° for a *space* crystal in Helliwell's data set [51]. Therefore it is difficult to demonstrate a significant effect of microgravity when comparing statistically the overall results of both teams.

The experimental rocking width Φ_h, given by FWHM, of a particular reflection h, is a convolution of the sample reflecting width ψ_h and the geometric and spectral parameters (divergence of the incident beam and spectral resolution) [51, 52]. For the experimental set up on station D23, the vertical divergence of the incident beam as determined from the source size and collimation is $\approx 0.0033°$, somewhat larger than intrinsic rocking curve or Darwin width of the Si (III) crystals in the monochromator, 0.00198°. The sample reflecting width ψ_h is itself a convolution of the intrinsic rocking width ω_h of each domain of the crystal and the mosaic spread η, the extent of the angular misalignment of each domain with respect to every other domain [52]. As a consequence of the above considerations, the experimental values presented here should be taken on a qualitative basis and do not contradict the claim of Snell and co-workers of substantially reduced mosaic spread η calculated for microgravity-grown crystals [53]. Profiles of Bragg reflections have since been directly recorded with a monochromatic quasi-planar X-ray wave [54] leading to quantitative values and also allowing for making topographs [52].

4. General conclusions and perspectives

This paper is a comprehensive description of a crystallogenesis experiment done under microgravity conditions with a model protein and performed in a large number of reactors. No significant shift of crystallization conditions was observed with lysozyme when analyzing comparable data of *space* and *ground* crystals. Resolution and mosaicity of *space* and *ground* crystals were comparable within the limit of the techniques used. This is in agreement with the model proposed by Rosenberger et al. [55] which suggests a limited effect of microgravity for lysozyme crystals as their growth would be dominated by growth kinetics rather than by mass transport. Since the highest resolution of the tetragonal crystal form [33] of hen egg-white lysozyme available in the Brookhaven Protein Data Bank was 1.8 Å, the two best *ground* and *space* crystals have been used to refine the structure to 1.33 and 1.40 Å resolution, respectively [30].

The performance of APCF hardware was satisfactory for a maiden experiment. The results were successful for the FID reactors; equilibration (final salt concentration in piston, reservoir and protein chamber) failed in some DIA reactors due to trapped bubbles in the narrow piston volume. However the dialysis technique proved to be suitable for microgravity experiments, the membrane triggering no additional nucleation. The dialysis technique confines the protein in its chamber, whereas in the free interface technique protein diffuses toward the reservoir, especially in case of small proteins, long duration missions, and occurrence of shocks originating from activities on board during the mission. Problems of interpreting the data were encountered with the HD reactors, mostly due to difficulties in their handling and for crystal observation of the drops. With some minor improvements as suggested above, APCF is potentially a good device allowing scientists to perform well controlled experiments, versatile in respect of techniques and volumes, with a controlled and recorded temperature, and the possibility of monitoring. These expectations were indeed fulfilled in the following IML-2 and USML-2 Missions.

More than the results of microgravity on lysozyme crystallization themselves, this work describes a strategy for a microgravity experiment from which conclusions can only be drawn with the knowledge of the data from a maximum number of controls throughout the experiment:

- Microgravity experiments must be prepared on earth in the flight identical hardware, as volumes and geometry of the hardware affect the nucleation zone.
- The effects of aging of the protein solutions should be checked in case of prolonged pre-flight periods occurring in the case of launch delay. Ideally experiments like these should be prepared on the launch site, but it would necessitate to have a laboratory at the scientists' disposal for preparing and analyzing the solutions.
- The knowledge of solubility diagrams helps controlling supersaturation at each step of the experiment and to monitor temperature. Nucleation can be induced in supersaturated solutions by vibrations as well during the launch than during the reentry. The effect of temperature on solubility is absolutely crucial for the solutions stored at 4°C during the pre-process period, as solutions which are undersaturated at 18°C may become supersaturated at lower temperatures inducing nucleation before the activation under microgravity conditions.
- Measurements of final salt and protein concentrations tell if foreseen crystallization conditions were actually achieved, and if comparison with ground controls are allowed.
- Video observation during the flight is essential since it allows not only to monitor nucleation and growth, but also to reveal unexpected perturbations during the flight, and ensure that recovered crystals have actually grown under microgravity and that their nucleation has not been induced during the reentry of the Shuttle.

Acknowledgements

The authors thank H. Walter, O. Minster, K. Fuhrmann, R. Berkeljon and M. Chofflet from European Space Agency (ESA) and the European Space Research and Technology Center (ESTEC, Noordwijk, The Netherlands); J. Stapelmann, R. Bosch, P. Lautenschlager, and K. Bockstahler

(Dornier GmbH, Friedrichshafen, Germany); the APCF coordinator G. Wagner (Giessen, Germany) for help and support in preparing this collaborative experiment. We also acknowledge commander R.J. Grabe, copilot B. Duffy, payload commander D. Low and mission specialists N.J. Sherlock, P.J.K. Wisoff and J. Voss. We wish to thank the National Agencies (CNES and CNRS in France, DARA in Germany, and the Medical Research Council in the UK) for financial support. We are indebted to S. Maignan (Gif-sur-Yvette) for technical assistance in crystal mounting.

References

[1] A. McPherson, Eur. J. Biochem. 189 (1990) 1.
[2] A. Ducruix, R. Giegé (Eds.), Crystallization of Nucleic Acids and Proteins, IRL, Oxford, 1992.
[3] L.F. Kuyper, C.W. Carter Jr., J. Crystal Growth 168 (1996) 155.
[4] R.S. Feigelson, J. Crystal Growth 76 (1986) 535.
[5] R. Giegé, A. Ducruix, J.C. Fontecilla-Camps, R.S. Feigelson, R. Kern, A. McPherson, J. Crystal Growth 90 (1988) 1.
[6] K.B. Ward, J. Crystal Growth 110 (1989) 1.
[7] J.J. Stetowski, W. Littke, J. Crystal Growth 122 (1992) 1.
[8] J.P. Glusker, Acta Crystallogr. D 50 (1994) 337.
[9] W. Littke, C. John, Z. Flugwiss, Weltraumforschung 6 (1982) 325.
[10] W. Littke, C. John, Science 225 (1984) 203.
[11] L.J. DeLucas, F.L. Suddath, R. Snyder, R. Naumann, M.B. Broom, M. Pusey, V. Yost, B. Herren, D. Carter, B. Nelson, E.J. Meehan, A. McPherson, C.E. Bugg, J. Crystal Growth 76 (1986) 681.
[12] V.A. Erdmann, C. Lippmann, C. Betzel, Z. Dauter, K. Wilson, R. Hilgenfeld, J. Hoven, A. Liesum, W. Saenger, A. Müller-Fahrnow, W. Hinrichs, M. Düvel, G.E. Schulz, C.W. Müller, H.G. Wittmann, A. Yonath, G. Weber, K. Stegen, A. Plaas-Link, FEBS Lett. 259 (1986) 194.
[13] L.J. DeLucas, C.D. Smith, H.W. Smith, V.-K. Senadhi, S.E. Senadhi, S.E. Ealick, D.C. Carter, R.S. Snyder, P.C. Weber, F.R. Salemme, D.H. Ohlendorf, H.M. Einspahr, L. Clancy, M.A. Navia, B.M. McKeever, T.L. Nagabhushan, G. Nelson, A. McPherson, S. Koszelak, G. Taylor, D. Stammers, K. Powell, G. Darby, C.E. Bugg, J. Crystal Growth 110 (1991) 302.
[14] L.J. DeLucas, C.D. Smith, D.C. Carter, R.S. Snyder, A. McPherson, S. Koszelak, C.E. Bugg, J. Crystal Growth 109 (1991) 12.
[15] S.D. Trakhanov, A.I. Grebenko, V.A. Shirikov, A.V. Gudkov, A. Egorov, I.N. Barmin, B.K. Vainstein, A.S. Spirin, J. Crystal Growth 110 (1991) 317.
[16] R.K. Strong, B.L. Stoddart, A. Arrott, G.K. Farber, J. Crystal Growth 119 (1992) 200.
[17] J. Day, A. McPherson, Protein Sci. 1 (1992) 1254.
[18] L.J. DeLucas, M.M. Long, D.M. Moore, W.M. Rosenblum, T.L. Bray, C. Smith, M. Carson, S.L.V. Narayana, M.D. Harington, D. Carter, A.D. Clark Jr., R.G. Nanni, J. Ding, Jacobo-Molina, G. Kamer, S.H. Hughes, E. Arnold, H.M. Einspahr, L.L. Clancy, G.S.J. Rao, P.F. Cook, B.G. Harris, S.H. Munson, B.C. Finzel, A. McPherson, P.C. Weber, F.A. Lewandowski, T.L. Nagabhushan, P.P. Trotta, P. Reichert, M.A. Navia, K.P. Wilson, J.A. Thomson, R.N. Richards, K.D. Bowersox, C.J. Meade, E.S. Baker, S.P. Bishop, B.J. Dunbar, E. Trinh, J. Prahl, A. Sacco Jr., C.E. Bugg, J. Crystal Growth 135 (1994) 183.
[19] H.U. Walter (Ed.), Fluid Sciences and Materials Science in Space, A European Perspective, Springer, Berlin, 1987.
[20] M. Riès-Kautt, A. Ducruix, J. Biol. Chem. 264 (1989) 745.
[21] E. Caccioppo, S. Munson, M.L. Pusey, J. Crystal Growth 113 (1991) 385.
[22] J.-P. Guilloteau, M. Riès-Kautt, A. Ducruix, J. Crystal Growth 122 (1992) 223.
[23] B.L. Stoddard, R.K. Strong, G.K. Farber, A. Arrott, G.A. Petsko, J. Crystal Growth 110 (1991) 312.
[24] R.S. Snyder, K. Fuhrmann, H.U. Walter, J. Crystal Growth 110 (1991) 333.
[25] R. Bosch, P. Lautenschlager, L. Potthast, J. Stapelmann, J. Crystal Growth 122 (1992) 310.
[26] M. Hennig, M. Visanji, W. Weber, H. Janczikowski, A. Plaas-Link, C. Betzel, J. Crystal Growth 135 (1994) 513.
[27] R. Giegé, J. Drenth, A. Ducruix, A. McPherson, W. Saenger, Progr. Crystal Growth and Characterization 30 (1995) 237.
[28] F. Otalara, J.-M. Garcia-Ruiz, J. Crystal Growth, in press.
[29] I. Broutin, M. Riès-Kautt, A. Ducruix, J. Crystal Growth 181 (1997) 97.
[30] M.C. Vaney, S. Maignan, M. Riès-Kautt, A. Ducruix, Acta Crystallogr. D 52 (1996) 505.
[31] M. Ataka, M. Asai, J. Crystal Growth 90 (1988) 86.
[32] S.B. Howard, P.J. Twigg, J.K. Baird, E.J. Meehan, J. Crystal Growth 90 (1988) 94.
[33] K.P. Wilson, B.A. Malcolm, B.W. Matthews, J. Biol. Chem. 267 (1992) 10842.
[34] G. Feher, Z. Kam, Meth. Enzymol. 114 (1985) 77.
[35] M. Ataka, M. Asai, Biophys. J. 58 (1990) 807.
[36] V. Mikol, E. Hirsch, R. Giegé, J. Mol. Biol. 213 (1990) 187.
[37] R.C. DeMattei, R.S. Feigelson, J. Crystal Growth 122 (1992) 21.
[38] L.A. Monaco, F. Rosenberger, J. Crystal Growth 129 (1993) 465.
[39] E. Forsythe, M.L. Pusey, J. Crystal Growth 139 (1994) 89.
[40] B. Lorber, M. Skouri, J.-P. Munch, R. Giegé, J. Crystal Growth 128 (1993) 1203.
[41] M. Skouri, B. Lorber, R. Giegé, J.-P. Munch, J.S. Candau, J. Crystal Growth 152 (1995) 209.
[42] N.E. Chayen, J. Radcliffe, D. Blow, Protein Sci. 2 (1993) 113.
[43] M. Bradford, Anal. Biochem. 72 (1976) 248.

[44] G. Alderton, W.H. Ward, H.L. Fevold, J. Biol. Chem. 157 (1945) 43.
[45] R. Fourme, P. Dhez, J.-P. Benoit, R. Kahn, J.-M. Dubuisson, P. Besson, J. Frouin, Rev. Sci. Instrum. 63 (1992) 982.
[46] A.G.W. Leslie (1987) Profile fitting, in: Computational aspects of protein crystal data analysis, Proc. Daresbury Study Weekend, SERC, Daresbury, Warrington, UK, pp. 39–50.
[47] R. Kahn, R. Fourme, R. Bosshard, V. Saintagne, Nucl. Instrum. Methods 246 (1986) 596.
[48] C.R. Dobson, P.A. Evans, Biochemistry 23 (1984) 4267.
[49] H.A. McKenzie, F.H. White Jr., Adv. Prot. Chem. 41 (1991) 173.
[50] N.E. Chayen, E.H. Snell, J.R. Helliwell, P.F. Zagalsky, J. Crystal Growth 171 (1997) 219.
[51] J.R. Helliwell, E. Snell, S. Weisgerber, in: L. Ratke, H. Walter, B. Feuerbacher (Eds.), Lecture Notes in Physics, Materials and Fluids under Low Gravity, Proc. of the IXth Eur. Symp. on Gravity Dependent Phenomena in Physical Sciences, Berlin, Germany, 1995, pp. 155–170, Springer, Berlin.
[52] R. Fourme, A. Ducruix, M. Riès-Kautt, B. Capelle, J. Synchrotron Rad. 2 (1995) 136.
[53] E.H. Snell, S. Weisgerber, J.R. Helliwell, Acta Crystallogr. D 51 (1995) 1099.
[54] J.C. Boulliard, B. Capelle, D. Ferret, A. Lifchitz, C. Malgrange, J.F. Pétroff, A. Taccoen, Y.L. Zheng, J. Phys. I (France) 2 (1992) 1215.
[55] F. Rosenberger, P. G. Vekilov, H. Lin, J.I.D. Alexander, Microgravity Science and Technology, in press.

ELSEVIER

Journal of Crystal Growth 181 (1997) 97–108

JOURNAL OF CRYSTAL GROWTH

Crystallographic analyses of lysozyme and collagenase microgravity grown crystals versus ground controls

I. Broutin, M. Riès-Kautt*, A. Ducruix

Laboratoire d'Enzymologie et Biochimie Structurales, CNRS, Bâtiment 34, F-91198 Gif sur Yvette Cedex, France

Received 6 December 1996; accepted 28 March 1997

Abstract

Hen egg white lysozyme and collagenase from *Hypoderma lineatum* larvae have been used as model proteins of known physical and chemical properties to study the influence of microgravity on crystal quality. This was performed using the Advanced Protein Crystallization Facility instrument during two successive missions of the US Space Shuttle. Lysozyme crystals were grown during the SpaceHab-01 mission and are compared with those obtained during the six months Eureca mission using the Protein Crystallization Facility instrument. Collagenase crystals were produced during the IML-2 mission. Space grown crystals as well as grounds controls were analyzed using synchrotron radiation to assess their diffraction limits. For lysozyme crystals, a large number of ground and microgravity grown crystals were analyzed and showed nearly equivalent maximum resolution (best one is 1.3 Å). Collagenase crystals from IML-2, although presenting a marginal increase of resolution (1.7 Å), display a better signal to noise ratio than ground crystals.

Keywords: Microgravity; Synchrotron radiation; X-ray; Crystal quality

1. Introduction

Due to the multiparametric aspect of protein crystallization [1], it is somewhat difficult to quantify the influence of one particular parameter on protein crystal growth and crystal perfection. Important biophysical parameters such as pH and temperature can be analyzed by measuring their effectiveness on protein solubility [2]. Similarly, one must find a way to quantify the influence of microgravity on crystal quality. Two parameters are good candidates: mosaicity and resolution. In both cases, the use of synchrotron radiation appears to be crucial but results are quite dependent on experimental setup. Mosaic spread, describing crystal perfection, is experimentally measured by rocking curves [3] or by topography [4]. Resolution gives the crystal diffraction limit. However the operational definition of resolution limit varies depending on authors: it is sometimes related to the ratio $\langle I \rangle / \langle \sigma(I) \rangle$ as a function of resolution shells or on values of R_{sym} (the relative disagreement between intensities of symmetry equivalent reflections) as a function of S.

* Corresponding author. Fax: + 33 1 69 82 31 29.

0022-0248/97/$17.00 © 1997 Elsevier Science B.V. All rights reserved
PII S0022-0248(97)00281-9

In order to perform appropriate comparison between microgravity and ground grown crystals, one may either compare the microgravity grown crystals to the ever best ground crystal or use rigorously the same experimental conditions such as protein concentration, pH, temperature, volume or transportation conditions, time of storage, etc. In the present work, we have used both approaches to study Hen egg white lysozyme (14306 Da molecular weight) and *Hypoderma lineatum* collagenase (25223 Da).

Lysozyme is a monomeric enzyme of 129 amino-acids (pI 11.1) which has been used systematically as a model for protein crystal growers over the last decade. Its physical-chemistry properties [5–7] and three dimensional structure [8–11] have been thoroughly described. Crystals are polymorphic but only the tetragonal form is treated here. Solvent content of the crystals is 33%. At the time of the SpaceHab-01 mission, the highest resolution so far recorded in the Protein Data Bank [12] was 1.7 Å for a recombinant lysozyme tetragonal crystal form [10].

Collagenase from *Hypoderma lineatum* is a member of the serine protease family. It is a monomeric enzyme of 230 amino-acid residues (pI 4.1) which degrades collagen under physiological conditions. The solvent content of the crystals is 50%. The 1.8 Å X-ray structure has been solved [13] and solubility diagrams as a function of salt concentration have been measured [14].

In the present paper, we will compare the resolution obtained with ground and microgravity crystals using different crystallization techniques and protocols.

2. Material and methods

2.1. Instruments

PCF (Protein Crystallization Facility) was developed [15] by ESA to fly on board the Eureca satellite. Two reactors using the liquid–liquid interface technique were used for lysozyme crystallization. ESA then replaced PCF by the APCF (Advanced Protein Crystallization Facility), a more versatile instrument [16, 17]. APCF permits crystallization using vapor diffusion, dialysis, or free interface diffusion methods. Volume of cells (from 30 to 500 μl) are adapted to the availability of proteins. One APCF flight unit contains 48 cells of either type with thermal regulation. Photographs of 12 cells/unit are recorded during flight, one series of images being taken every 9 h.

2.2. Microgravity missions

2.2.1. Eureca

Lysozyme crystals were obtained in PCF reactors during the Eureca (EUropean REtrievable CArrier) STS-46 mission which was launched on July 1992. On August 2nd, Eureca platform was released from Atlantis Shuttle. Reactors have been activated from August 10 of 1992 until the end of December of the same year. On December 25, following successive failures of the thermal regulation system, reactors were submitted to a temperature increase (less than 48 hrs) from 20° (nominal value) to 40°C. At that point, the Peltier temperature control was deactivated and temperature of reactors dropped down to 16°C and remained at this level with a variation of ± 2°C until January 26, 1993 when the Eureca Freon loop was deactivated. Since this time, the reactor temperature was free floating with the Eureca structure temperature at 20 ± 2°C until retrieval. Eureca was grappled by Endeavour and berthed into cargobay during the SpaceHab-01 mission on 24 June 1993. Crystals obtained during Eureca mission were mounted by Professor Littke and given to us in order to compare them to the crystals we obtained from SpaceHab-01 mission.

2.2.2. SpaceHab-01

Full details of the experiments are published in Ref. [18]. A complete set of 25 reactors containing lysozyme solutions flew during the 10 day STS-57 mission of the Shuttle Endeavour which was launched on June 21, 1993. Lysozyme crystallization experiments were activated for seven and a half days but remained for an additional two days under microgravity before landing. Two days after landing, reactors were recovered and analyzed in France. Temperature was continuously recorded in the APCF unit and in the transport containers

from the time of reactor filling to that of crystal recovery in Europe. Temperature was continuously monitored throughout the transportation and mission, and was kept constant at 18 ± 0.3°C.

2.2.3. IML-2

IML-2 (International Microgravity Laboratory) flew during the 15 days (July 8–23, 1994) of the STS-65 mission. Five hanging drop reactors were activated at board of the Columbia Shuttle for twelve and a half days. Temperature was continuously monitored throughout the mission and stayed constant at 20 ± 0.3°C.

2.3. Samples

The water used to prepare the solutions was a commercially available deionized and three-times distilled water for injectable purpose (Biosedra). $NH_4H_3C_2O_2$ (acetate) was purchased from Merck, and $(NH_4)_2SO_4$, Trizma Base (ACS reagent) from Sigma.

2.3.1. Lysozyme

For the Eureca mission, lysozyme was from Boehringer (Mannheim). Crystals were grown using NaCl and acetate buffer at pH 4.5 by free interface diffusion. Lysozyme used for the SpaceHab-01 mission came from a single Sigma batch of lysozyme chloride and was used without further purification for *ground* and *microgravity* experiments (Cat. No. L-2879, lot 51H7150, Sigma). Solubility diagrams were previously determined [19–21] and allowed for the calculation of supersaturation (from 5 to 33). Crystals were grown using either the hanging drop (HD) technique or the dialysis (DIA) technique. Temperature was 18 ± 0.3°C throughout the microgravity experiment. The pH of solutions in HD reservoir increased by 0.5–1.0 unit, due to traces of chemicals in the absorbent blocks. Ground control experiments (25 reactors, identical to the flight reactors) were subjected to the same sequence of events as the microgravity experiment. Nominal conditions of crystallization for the crystals which were X-ray analyzed are given in Table 1. More details concerning the design and the preparation of the experiments are given in the accompanying paper [18].

Furthermore, we added two more ground controls. First, to check the effect of the crystal size on resolution, we selected a series of calibrated crystals. They were grown using the batch method with deionized lysozyme [22] and NaCl as a crystallizing agent at pH 8. Second, some microcrystals obtained in APCF reactors in microgravity and on ground were used in parallel as seeds to grow lysozyme crystals on earth from metastable solutions. This aimed at uncoupling microgravity effects on nucleation and growth, in case a difference would be observed between crystals obtained on ground and in microgravity. Crystals obtained are mainly of small size.

2.3.2. Collagenase

Collagenase was purified [23] from Hypoderma lineatum larvae and crystallized [24] according to previously described procedures. Purity and homogeneity of the protein sample were analyzed by gel electrophoresis (SDS-PAGE and IEF), *N*-terminal sequencing and electrospray ionization mass spectrometry. Solubility of collagenase in the presence of ammonium sulfate was previously determined [14] and allowed for supersaturation calculation. Known crystallization conditions of collagenase [24] were adapted to APCF HD reactor, taking into account supersaturation. Five hanging drop cells of 80 μl were used for the crystallization of collagenase under microgravity. Temperature was 20 ± 0.3°C throughout the experiment. Supersaturation range was 11–12. Again a shift of pH occurred due to a desorption of a chemical from the APCF reactors absorbent blocks. Reference crystals were grown at 18 ± 1°C using either Linbro boxes with hanging drops (hlmarkII) or FID APCF reactors (protein chamber of 175 μl) equipped with a dialysis membrane (hlips). Crystallization conditions of all of the analyzed crystals are given in Table 1.

2.4. Selection of crystals

2.4.1. Lysozyme

Four crystals (Eureca A to D) from the Eureca mission were selected. From the SpaceHab-01 mission, six crystals (DIA110, DIA105, DIA124, HD22, FID112, FID101) grown in the different

Table 1
Nominal crystallization conditions of analyzed crystals. Lysozyme crystallizations were performed in 50 mM sodium acetate at pH 4.5, for collagenase crystals it was 50 mM Tris, HCl, 60 mM NaCl pH 7.2. For seeded crystals, the values in brackets indicate the reactor from which the seed was produced

	[Salt] (M)	[Protein] (mg/ml)	Super-saturation	Final pH (initial pH)
Lysozyme	Nacl			
DIA 105 space	1.40	10	9.8	4.3 (4.3)
DIA 106 ground	1.21	10	7.3	4.3 (4.3)
DIA 110 space	1.51	10	11.3	4.3 (4.3)
DIA 124 space	1.04	30	16.4	4.3 (4.3)
FID 101 space	1.19	10	7.1	4.3 (4.3)
FID 105 ground	1.12	10	6.3	4.3 (4.3)
FID 112 space	1.46	10	10.6	4.3 (4.3)
FID 113 ground	1.45	10	10.5	4.3 (4.3)
FID 115 ground	1.55	10	11.9	4.3 (4.3)
FID 119 ground	1.92	10	18.1	4.3 (4.3)
HD 22 space	1.48	30	32.6	5.03 (4.3)
HD 133 ground	0.93	30	13.2	5.10 (4.3)
size E ground	0.40	39	3.0	8.7 (8.0)
size F ground	0.60	22.5	2.6	8.6 (8.0)
size G ground	0.60	22.5	2.6	8.6 (8.0)
size H ground	0.60	22.5	2.6	8.6 (8.0)
seed space I (DIA119 space)	0.85	6	2.5	4.3 (4.3)
seed ground J (DIA127ground)	1.00	4	2.2	4.3 (4.3)
seed ground K (DIA130ground)	1.40	2.5	2.5	4.3 (4.3)
seed space L (DIA105 space)	1.40	2.5	2.5	4.3 (4.3)
Collagenase	Ammonium sulfate			
hl128 a space	1.24	15	11	6.12 (7.0)
hl128 b space	1.24	15	11	6.12 (7.0)
hl128 c space	1.24	15	11	6.12 (7.0)
hl129 e space	1.39	10	12	5.60 (7.0)
hlmarkII ground	1.23	20	9.5	not determined (7.2)
hlips ground	1.21	10	4.5	7.0 (7.0)

reactors with different techniques and six crystals (DIA106, HD133, FID119, FID113, FID105, FID115) from the corresponding ground control experiment were chosen according to their aspect (smooth faces, sharp edges) and their size. Four crystals (Size E-H) of increasing size were also selected as well as four crystals (Seed I-L) obtained from microgravity and ground seed experiments.

2.4.2. Collagenase

Within the range of reproducibility, the number and size of collagenase crystals grown in micro-

gravity are similar to those grown prior to the flight during preliminary ground experiments and using APCF HD reactors. Crystals from IML-2 mission, suitable for X-ray analysis, were all obtained from two (hl128 and hl129) out of the five HD reactors. The four largest ones (hl128a-c and hl129e) were subjected to X-ray analysis. HlmarkII crystal was previously characterized [25]. One crystal of very large size (hlips), grown in APCF reactor by dialysis on ground, was selected.

2.5. Data collection and processing

All the crystals were analyzed at 6°C on the wiggler beam line DW32 [26] at LURE (Synchrotron, Orsay, France) using a wavelength of 0.901 Å and a Mar-Research image plate system (IPS). The crystal-to-detector distances were 160 and 211 mm for lysozyme and collagenase crystals, respectively. Between the SpaceHab-01 and IML-2 missions, the IPS detector of LURE was replaced by a new one. The differences lie in the diameter of the plates, the new one being larger (300 mm) than the previous one (180 mm). The dynamic property went from a maximum intensity of 65535 per pixel (small plate) to 130 000 (large plate). The pixel size is 150 μm. For the Eureca and SpaceHab-01 crystals, because only the small plate of 180 mm was available, the detector was offset vertically (50 mm) to allow data collection at higher resolution. Because the IML-2 crystals were recorded on the large plate of 300 mm, installed in 1994, the detector remained centered.

The SpaceHab-01 crystals were analyzed by microgravity/ground pairs. The choice of pairs was decided on size criteria. For each crystal a partial data set was recorded (column 2 of Table 2) in order to analyze statistically the difference of diffraction quality between them. Initially, the range of the reciprocal space recorded was 10° in two perpendicular directions. The chosen rotation step was 2°, and so only 5 successive images were available to refine all the parameters (crystal–detector distance, position of the beam center, mosaicity, orientation, etc). During treatment of the data set, the 10° interval proved to be too small. Finally, as lysozyme crystals proved to be homogenous in function of the analyzed orientation, a continuous range of reciprocal space was recorded for the lasting crystals. This considerably reduced the treatment difficulties. The rotation step and exposure time per image (column 3 of Table 2) were determined first to use the complete dynamic of the IPS and secondly in function of beam time available for the analysis of all the crystals. Data treatment convinced us that it is better to perform a continuous rotation rather than sampling with small rotations in different zones of reciprocal space. Because crystals were randomly oriented, completeness (column 8 of Table 2) varies from 30% to 67% for lysozyme and upper for collagenase. After analysis of all the pairs, the two apparently best crystals (one ground and one microgravity) were completely recorded [11].

IML-2 collagenase crystals were analyzed in a different way because collagenase crystals had been extensively used as reference crystals on various detectors and experimental set-up [25]. For the five selected microgravity crystals, a partial data set was recorded and it was decided to compare them to one APCF ground crystal (hlips in Table 2) and to what was previously considered as our best ground data set (hlmarkII). The later was used for the refinement of the 1.8 Å structure [13]. It was collected at LURE using the prototype MarkII detector located at the D23 beam line. The largest microgravity grown crystal (hl129e) was fully recorded in order to obtain a complete data set to be used for a new refinement [27].

3. Results and discussion

3.1. Isomorphism

It has sometimes been claimed [28] that microgravity could induce polymorphism for protein crystals. It must be recalled that great care should be taken before assigning this change to microgravity because chemical or physico-chemical changes can often be the source [29]. No polymorphism was observed for either lysozyme nor collagenase in this work. All lysozyme crystals belong to the tetragonal system, space group $P4_32_12$, with one molecule in the asymmetric unit. Collagenase crystals are tetragonal, space group I 422, with two molecules

Table 2

Summary of results for data recording and treatment of lysozyme and collagenase crystals analyzed after the SpacehHab-01 and IML-2 missions, and of the ground controls; crystals in bold correspond to those fully X-ray recorded.

	1 Volume (10^{-2} mm^3)	2 Range of reciprocal space recorded (degree)	3 (°/s)	4 nb of unique reflections	5 $\langle I \rangle$	6 d_{max} (Å)	7 $\langle I/\sigma \rangle$ at 1.6 Å	8 Completeness (%) at d_{max}	9 d (Å) at $I/\sigma = 2$	10 R_{sym} (%) at $I/\sigma = 2$	10′ R_{sym} (%) at 1.6 Å	11 Scale to F101	12 R_{merge} to F101 (%)	13 Cell (Å)	14 $\langle$Cell$\rangle$ (Å)
(*a*) *Lysozyme*															
Eureca A space	56.0	30	1.5/45	8275	6890	1.30	5.8	30	1.41	3.6	3.3	1.3	4.8	78.63 37.78	
Eureca B space	18.0	30	1.5/45	5696	7178	1.30	5.9	43	1.40	3.3	3.2	1.7	13.6	78.40 37.87	$a = 78.56$
Eureca C space	16.0	30	1.5/45	8971	4589	1.33	4.6	43	1.42	3.3	3.0	1.8	7.9	78.61 37.87	$c = 37.82$
Eureca D space	14.0	30	1.5/45	6209	5850	1.32	5.5	40	1.39	3.3	3.2	1.9	6.0	78.59 37.74	
DIA 106 ground	4.8	10 + 10 + 10 + 10 2/60		8168	2947	1.40	2.7	52	1.56	5.1	5.0	4.4	4.5	79.22 37.75	
DIA 110 space	4.8	10 + 6 + 10	2/60	5258	3190	1.40	2.7	53	1.56	4.5	4.4	4.0	4.0	78.86 37.74	
FID 119 ground	4.8	18	2/60	4941	4000	1.30	4.1	31	1.50	3.8	3.5	2.4	18.1	78.53 38.37	ground
FID 112 space	5.6	20	2/60	6185	4587	1.30	4.9	39	1.45	3.3	3.1	2.0	9.1	78.45 37.93	$a = 78.63$
DIA 105 space	7.2	10 + 10 + 10	2/60	7124	7046	1.30	5.6	54	1.41	3.3	3.0	1.5	3.2	78.85 37.80	$c = 37.81$
HD 22 space[a]	7.5	28	1/30	6711	4105	1.30	3.5	48	1.50	3.3	3.1	2.6	8.8	78.41 37.79	
HD 133 ground	7.5	20	2/60	6006	5188	1.30	4.3	35	1.45	3.1	2.8	1.6	3.4	78.58 37.63	
FID 113 ground	12.8	16	2/60	4922	5165	1.30	5.1	32	1.41	3.5	3.0	1.6	4.4	78.51 37.70	space
FID 101 space	17.5	20	1/30	4746	6225	1.28	5.4	43	1.40	2.6	2.5	1.7	1.9	78.55 37.72	$a = 78.61$
FID 105 ground	18.0	20	2/60	3027	9062	1.30	7.5	30	1.41	2.0	1.9	1.4	9.5	78.47 37.75	$c = 37.81$
DIA 124 space	21.6	18	2/60	5339	5546	1.30	4.4	35	1.45	2.6	2.4	1.6	5.3	78.55 37.85	
FID 115 ground	79.2	20	2/60	5456	8775	1.30	6.8	42	1.37	3.1	2.9	1.3	3.6	78.44 37.64	
size E ground	112.5	20	2/60	2195	25010	1.37	3.7	31	1.53	3.3	3.3	1.3	30.2	77.92 38.25	
size F ground	72.0	5 + 5 + 5	2/60	7579	7633	1.45	3.5	57	1.50	3.6	3.4	1.1	19.8	78.02 38.08	$a = 77.97$
size G ground	10.8	5 + 5 + 5	2/60	5364	6009	1.60	2.0	67	1.65	4.4	4.4	1.7	24.0	77.97 38.20	$c = 38.80$
size H ground	3.6	30	1.5/90	7658	6502	1.50	2.6	53	1.54	6.6	6.4	1.4	21.6	77.95 38.17	
Space Seed I	19.6	5 + 5 + 5	2/60	5564	3051	1.40	3.2	62	1.54	3.4	3.3	4.4	5.6	78.79 37.87	
Ground Seed J	1.6	5 + 5 + 5	2/60	4425	999	1.60	0.7	62	1.79	5.5	5.7	15.9	6.8	78.82 37.88	$a = 78.74$
Ground Seed K	1.35	5 + 5 + 5	2/60	6188	825	1.55	1.5	58	1.73	5.1	5.6	16.4	3.8	78.67 37.77	$c = 37.81$
Space Seed L	1.35	5 + 5 + 5	2/60	4387	849	1.55	0.7	60	1.79	5.1	5.7	21.7	4.9	78.66 37.72	

[a] Nucleation started before flight.

	1 Crystal volume (10^{-2} nm^3)	2 Range of reciprocal space recorded (degree)	3 (°/min)	4 nb of unique reflections	5 $\langle I \rangle$	6 d_{max} (Å)	7 $\langle I/\sigma \rangle$ at 1.6 Å	8 Completeness (%) at d_{max}	9 d (Å) at $I/\sigma = 2$	10 R_{sym} (%) at $I/\sigma = 2$	10′ R_{sym} (%) at 1.6 Å	11 scale X/hlm arkII	12 R_{merge} to hlmarkII (%) at 1.9 Å	13 Cell (Å)	14 ⟨Cell⟩ (Å)
(*b*) *Collagenase*															
hl128a space	43.2	10 + 10	1/4	24111	13495	1.65	3.9	67.9	1.72	6.7	6.5	62.12	5.8	111.4 165.5	
hl128b space	7.2	20 + 20	1/4	32085	6397	1.90	1.6	94.7	1.95	6.6	6.9	19.16	4.8	111.4 165.6	
hl128c space	27.0	20	1/4	23849	14624	1.80	4.9	67.9	[a]	4.5[b]	4.4	60.46	4.8	111.4 165.9	$a = 111.5$
hl129e space	76.8	53	1/3	53047	16343	1.70	4.1	96.3	1.74	4.6	4.1	73.31	6.7	111.3 165.7	$c = 165.9$
hlips ground	1120.0	22	1/2.5	20735	19685	1.92	4.5	78.4	[c]	3.1[a]	3.1	61.73	6.9	111.8 166.5	
hlmarkII ground	25.6	94 + 96	0.05/0.5	29614	249	1.70	2.1	79.7	1.90	3.7	3.7	1.00		111.8 166.0	

[a] I/σ is still 3.2 at the highest resolution.
[b] As I/σ is still upper 2 at the resolution limit, this is the R_{sym} at d_{max}.
[c] I/σ is still 4.5 at the highest resolution.

(1) The important parameter is usually the cross section of the crystals, but as lysozyme and collagenase crystals grow with a prismatic shape, this parameter can be replaced by the volume of the crystal.
(2) When two values are specified, this means the crystal was analyzed in two orthogonal directions.
(3) The exposure time was optimized in order to use the complete dynamic of the image plates.
(4) Number of reflections obtained at the resolution limit after reduction to a unique data set.
(5) Mean value of intensity on the whole data set.
(6) Resolution limit at which the crystal diffracts. In the case of collagenase this parameter is determined visually.
(7) Mean value of the ratio of intensity over sigma over the whole data set. The estimated standard deviation of the intensity $\sigma(I)$ is a very important parameter to qualify a data set. In a first estimation, it is considered to be proportional to the root square of the intensity. It is then reevaluated taking into account the fluctuation of the background and systematic instrumental errors, and finally during the reduction to a unique data set, it is corrected in order to normalize the following distribution

$$I_n = \frac{I_{hkl} - \langle I_{hkl} \rangle}{\sigma(I_{hkl})}.$$

(8) Ratio of the number of reflections recorded over the number of theoretical reflections that can be recorded after reduction to a unique data set. In practice crystals were not oriented, thus the completeness is very different from one crystal to another.
(9) I/σ is one of the most important characteristic of a data set. We consider part of data set with I/σ above 2 of good quality although all the reflections are used during a structure refinement. As none of the data sets has the same I/σ value in their last resolution range, we consider as resolution limit the one at which this ratio is 2.
(10) The quality of a data set is also given by the R_{sym} factor that indicate the coherence between equivalent reflections. $I(hkl)_i$ is the ith measure of the hkl reflection and $\bar{I}(hkl)$ the mean value of the N considered equivalent reflections:

$$R_{sym} = \frac{\sum_{hkl} \sum_{i=1}^{n} |\bar{I}(hkl) - I(hkl)_i|}{\sum_{hkl} \sum_{i=1}^{n} I(hkl)_i}.$$

(11) Before comparing two data sets they have to be scaled together.
(12) When different data sets are compared, the quality of the agreement is given by the same formula as the R_{sym} factor, but in this case the average is done with the different values of a given reflection for the different data sets.
(13) This is given to verify the isomorphism of the different crystals. Two crystals are considered as isomorphous when the difference of each of their cell parameters to the mean value is lower than 0.5%.
(14) Mean values of the cell parameters.

in the asymmetric unit. Cell dimensions are given in Table 2.

The average unit cell of the SpaceHab/Eureca lysozyme crystals is $a = b = 78.60$ Å, $c = 37.81$ Å. It is to be noted that some of the crystals deviate slightly from perfect isomorphism ($\pm 0.5\%$ on each cell parameter [30]). This is demonstrated by scaling all partial data sets to the complete data set of FID101 (scale is given in column 12 in Table 2). Such small variations have been observed when changing the nature of the crystallizing salt [19] or changing H_2O to D_2O [31]. Corresponding Rmerge are given in column 13 of Table 2. FID119 ground crystal shows a defect of isomorphism as indicated by the high value of Rmerge (19.1%). This is clearly related to the larger "c" unit cell parameter (38.37 Å) when compared to the mean one (37.81 Å). Seed crystals (I to L) are isomorphous whereas size crystal (E to H) are not, probably because of the pH of crystallization.

Collagenase crystals do not show any deviation from isomorphism.

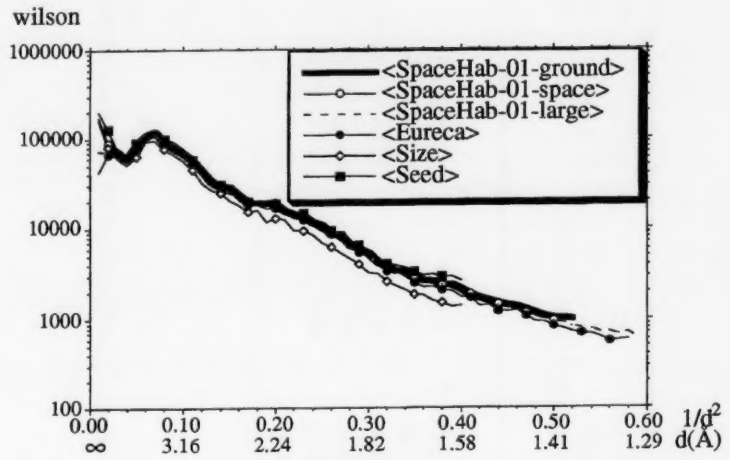

Fig. 1. Mean Wilson curves of the different groups of SpaceHab analyzed crystals. ⟨SpaceHab-01-ground⟩: mean of the 6 crystals SpaceHab-01 ground made; ⟨SpaceHab-01-space⟩: mean of the 6 crystals SpaceHab-01 microgravity made; ⟨Eureca⟩: mean of the 4 Eureca crystals; ⟨Size⟩: mean of the 4 crystals of different size; ⟨Seed⟩: mean of the 4 crystals obtained by seeding; ⟨SpaceHab-01-large⟩: mean of the 4 crystals SpaceHab-01 with volume upper 14×10^{-2} mm^3.

3.2. Size effect

As shown by Table 2 (column 1), the effect of the size of the crystals is rather complex to analyze and one cannot correlate crystal volume with maximum resolution. Rsym values tend to be higher for the smallest crystals. Furthermore, values higher than 4% (columns 10 and 10′ of Table 2) are generally associated with higher dmax values. It is known that up to a threshold value of the diffracting volume, the diffraction limit and signal-to-noise ratio are clearly proportional to the size of the crystal. This can be clearly observed for the small seeded lysozyme crystals (seed J, K, L). Above a critical crystal size, which varies from one protein crystal form to another, other parameters appear to be as much or more important as far as crystal diffraction limit is concerned. For instance, lysozyme FID115 ground crystal which is four times larger than FID105 crystal has an average intensity quite similar. This is also the case for collagenase hlips crystal which is 15 times larger than hl129e crystal but has close $\langle I \rangle$ values. We have not reported the maximum intensity of each data set because the limited completeness of each sample prohibits the use of this parameter.

3.3. Wilson plot as a function of resolution

Wilson plots [32] of lysozyme, shown in Fig. 1, are all superimposed. For the clarity of the figure, we have averaged data sets of ground, microgravity, Eureca, size and seeds crystals in subgroups and created a new subset with the four largest microgravity grown crystals. The values of the temperature factors B estimated from the Wilson plot (in the range 3–1.4 Å) for the two fully recorded data sets are, respectively, 14.7 and 17.4 Å^2 for FID115 and FID101 ground and microgravity grown crystals. At the end of the crystallographic refinement of these two data sets [11] the average temperature factor of the protein atoms are 16.7 and 18.6 Å^2, respectively. This may suggest that for crystals diffracting at high resolution, the diffracting limit is not only associated with the Debye–Waller temperature factor but also to packing and static disorder and therefore to crystal perfection. A recent refinement of ground grown crystals of Crambin [33] is in favor of this observation.

Wilson plot of collagenase crystals are shown in Fig. 2. Close inspection reveals a group formed of

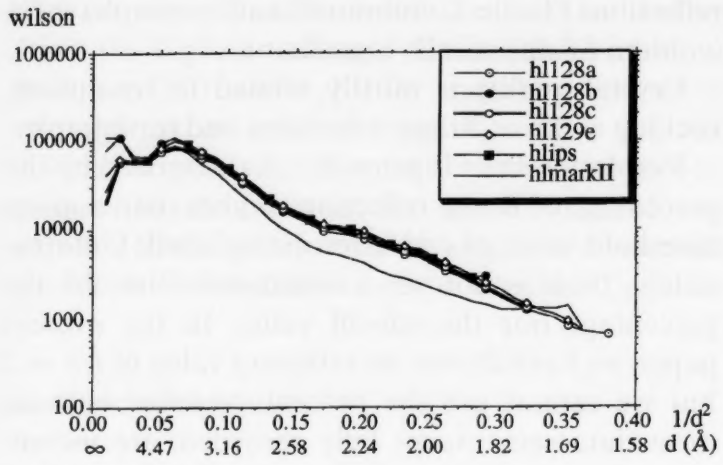

Fig. 2. Wilson plot of collagenase data sets.

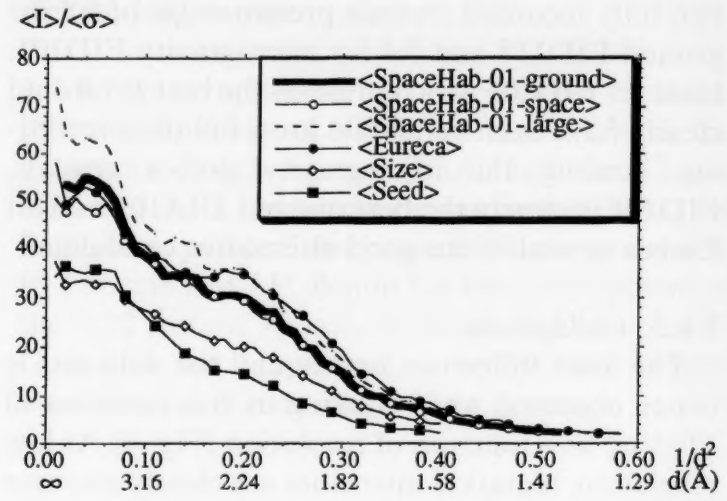

Fig. 3. Variation of $\langle I \rangle / \langle \sigma \rangle$ with $1/d^2$ for each group of SpaceHab analyzed crystals.

data sets hl128a, b, c, e and hlips whereas hlmarkII is isolated. The first group was recorded with a wiggler beam line and IPS whereas hlmarkII data was recorded with a non-wiggler synchrotron beam and MarkII detector [13]. As shown by Table 2b, the difference can be correlated to the diffraction power of each crystal. The low $\langle I \rangle$ (column 5) of crystal hlmarkII is linked to the detector response. As a matter of fact, this prototype detector could not withstand strong intensities (the maximum count rate is about 3.5×10^5 cps) without provoking flashing of the gas inside the detector. Temperature factor B values estimated from the Wilson plots for the two fully recorded data sets hlmarkII and hl129e are 24 and 23 Å^2, respectively. The values are somewhat more difficult to extract because the plot is not as linear as for lysozyme data sets. This may reflect different B factors for the two molecules which compose the asymmetric unit of the crystal of collagenase. This is however compatible with the values of the average B factors calculated from the refinement of the two independent molecules of the asymmetric unit from hlmarkII [13] (23 and 26 Å^2) and hl129e [27] (22 and 26 Å^2).

3.4. I/σ as a function of resolution

σ is a function of the accuracy of measurement and therefore I/σ is a good indicator of crystal quality. Because I/σ decreases with resolution (Figs. 3 and 4) a cut-off value must be defined in order to be able to compare the various data sets of

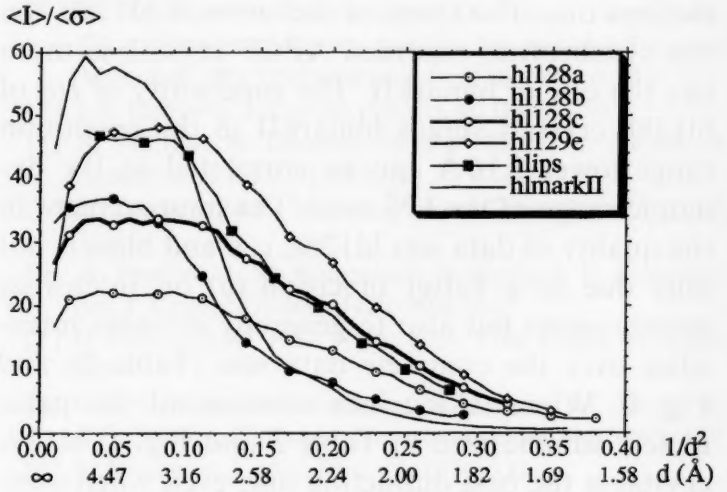

Fig. 4. Variation of $\langle I \rangle / \langle \sigma \rangle$ with $1/d^2$ for collagenase crystals.

a protein at the same resolution. I/σ values correlate with Rsym and crystal size. In the case of hlmarkII, the quality of the prototype detector probably explains the low Rsym value despite a low I/σ.

3.4.1. Lysozyme

For lysozyme data sets, a cut-off value of 1.6 Å has been arbitrary chosen so that all I/σ values could be calculated with all data set presenting a large enough number of data for a significant analysis. Crystals presenting the largest I/σ (Table 2, Fig. 3) do not always correspond to the largest crystals. Eureca crystals are rather homogeneous with values ranging from 4.6 to 5.9. The

two fully recorded crystals present a I/σ of 6.8 for ground FID115 and 5.4 for microgravity FID101. Data set FID105 which presents the best I/σ would clearly have been candidate for a full data recording. Among the microgravity grown crystals, FID101 is clearly the best one but DIA105 and all Eureca crystals were good alternative candidates.

3.4.2. Collagenase

The main difference between all the data sets is better observed when looking at the variation of $\langle I\rangle/\langle\sigma\rangle$ as a function of resolution (Fig. 4). At low resolution, hlmarkII intensities are clearly stronger than any of the others, but at resolution better than 3.16 Å, data sets hl128a, c, e and hlips have a completely different behavior and are clearly of better quality, hl129e which has been fully recorded being the best one. The shape of the curve of hl128b, the last synchrotron recorded APCF crystal, is more like the one of hlmarkII. The superiority of I/σ of hl128b crystals versus hlmarkII in the resolution range lower 3.16 Å can be correlated to the dynamic range of the IPS used. The improvement in the quality of data sets hl128a, c, e and hlips is not only due to a better precision (σ) on intensities measurement but also to generally stronger intensities over the complete data sets (Table 2b and Fig. 4). When taking into account all the parameters summarized in Table 2 and Fig. 4, hl129e crystal is the best diffracting one, even when compared to hlips which has comparable mean intensity and was our best ground grown crystal of collagenase until now. Consequently, even if the detector response and the intensity of the source are an obvious reason of improvement, our reference crystal of collagenase is now hl129e.

3.5. Maximum resolution and crystal quality

First of all, it should be noticed that using synchrotron radiation instead of a rotating anode is generally a major parameter improving resolution. This is true for both lysozyme and collagenase. Because synchrotron beam time allowance is limited, it is not possible to record full data sets for all crystals and one should make sure that for partial data sets the quantity of data recorded in reciprocal space is large enough to give a number of unique reflections (Table 2, column 4) and a completeness (column 8) statistically significant.

Crystal quality is mostly related to resolution, rocking width of Bragg reflections and topography.

Resolution limit is generally characterized by the percentage of Bragg reflections higher than a given threshold value of σ in a resolution shell. Unfortunately, there is not yet a consensus value for the percentage nor the cut-off value. In the present paper, we have chosen an arbitrary value of $I/\sigma = 2$ but we cannot use the percentage value because most data sets, except fully recorded, are incomplete. It is to be noted that visual inspection of digitized images of diffracted intensities give a fairly close approximation of resolution limit.

Mosaicity of lysozyme crystals from SpaceHab-01 is addressed in the accompanying paper. Collagenase hl129e microgravity crystal was tested using the standing wave station D25B at LURE-DCI [4] and presents a rocking curve of 0.0030° for a reflection at 3 Å resolution. The best rocking curve value of several ground grown collagenase crystals was 0.0016° for a strong Bragg reflection at the same resolution. Because only one microgravity crystal has been tested, it is not reasonable to draw conclusions from this observation.

3.5.1. Lysozyme

Results from PCF and APCF are quite similar (Table 2, columns 6, 7, 9). Based on visual inspection of a preliminary data recording, FID101 microgravity and FID115 ground were fully recorded. After analysis of all data, it is clear that FID105 ground would have been an other choice with an $\langle I/\sigma\rangle$ of 7.5 (column 7).

3.5.2. Collagenase

In term of resolution limit (Table 2 column 6) data set hl128a is slightly better (1.65) but not significantly different from hlmarkII or hl129e (1.70). The difference is enhanced when comparing the resolution at which I/σ ratio is greater than 2 (column 9), but the improvement in resolution is still rather small and far from what was observed [34] for elastase microgravity grown crystals. In term of accuracy, the best diffracting crystals seem to be hl128c and hlips as the value of I/σ is still 3.2

(4.5, respectively) at the resolution limit and as they have the highest values of I/σ at 1.9 Å resolution (column 7). However, hl128c and hlips data set do not diffract at a better resolution than 1.8 and 1.92 Å, respectively. For hl128c this can be explained by the fact that the crystal decayed very rapidly. For hlips this may be linked to absorption problems due to the size of the crystal.

4. Conclusions

Microgravity experiments dealing with protein crystal growth under reduced gravity show that some protein crystals seem to benefit from microgravity. Sometimes, the microgravity grown crystals are larger and provide a better signal to noise ratio with eventually a better resolution for X-ray analyses. Although there is often a lack of documentation with respect to solution preparation, statistics show [35] that 20% of the protein crystals grown in microgravity gave a better resolution of about 0.2–0.3 Å. Of these, 15% had a better signal to noise ratio, i.e. a higher number of observed reflections than their earth-grown counterpart. 20% of the crystals grown in microgravity are worse and 60% did not show any improvement. It has been proposed [36] that protein crystals would benefit or not from microgravity depending on either interfacial kinetics or transport dominating the control of the crystallization process.

As far as tetragonal crystals of HEW lysozyme are concerned, after testing a dozen of crystals, we have not observed any improvement on signal over background ratio nor on resolution limit either with crystals from APCF reactors or with PCF reactors. Of course this does not preclude any change for the better in other crystallization conditions, for instance at low supersaturation or associated to the gel technique. On the other hand, all lysozyme crystals obtained in APCF or PCF reactors, either ground or microgravity grown, diffract at higher resolution than any tetragonal crystal of HEW lysozyme published up to now, whatever the crystallization conditions were.

Concerning collagenase, one of the crystals grown under reduced gravity present a better signal to noise ratio although not a better resolution limit.

Acknowledgements

I.B. was supported by the Centre National d'Etudes Spatiales (CNES). We thank CNES, the European Space Agency (ESA) and the Centre National de la Recherche Scientifique (CNRS) for financial support of this project. We are grateful to R. Fourme and J.P. Benoit for the development of the W32 station. At last, we thank A. Leslie and P. Gouet for the adaptation of the MOSFLM software for the off-axis image-plate system.

References

[1] R. Giegé, B. Lorber, A. Théobald-Dietrich, Acta Crystallogr. D 50 (1994) 339.
[2] M. Riès-Kautt, A. Ducruix, in: A. Ducruix, R. Giegé (Eds.), Crystallization of Protein and Nucleic Acids: A Practical Approach, IRL/Oxford Press, Oxford, 1992, p. 195.
[3] J.R. Helliwell, J. Crystal Growth 90 (1988) 259.
[4] R. Fourme, A. Ducruix, M. Riès-Kautt, B. Capelle, J. Synchrotron Rad. 2 (1995) 1.
[5] C. Tanford, M.L. Wagner, J. Am. Chem. Soc. 76 (1954) 3331.
[6] W. Fredericks, M. Hammonds, S. Howard, F. Rosenberger, J. Crystal Growth 141 (1994) 183.
[7] H.A. McKenzie, F.H. White, Adv. Prot. Chem. 41 (1991) 173.
[8] C.C.F. Blake, D.F. Koening, G.A. Mair, A.C.T. North, D.C. Phillips, V. Sarma, Nature (London) 206 (1965) 757.
[9] R. Diamond, J. Mol. Biol. 82 (1974) 371.
[10] K.P. Wilson, B.A. Malcolm, B.W. Matthews, J. Biol. Chem. 267 (1992) 10842.
[11] M.C. Vaney, S. Maignan, M. Riès-Kautt, A. Ducruix, Acta Crystallogr. D 52 (1996) 505.
[12] F.C. Bernstein, T.F. Koetzle, G.J.B. Willias, E.F. Meyer, M.D. Brice, J.R. Rodgers, O. Kennard, T. Shimanouchi, M. Tasumi, J. Mol. Biol. 112 (1977) 535.
[13] I. Broutin, B. Arnoux, C. Riche, A. Lecroisey, B. Keil, C. Pascard, A. Ducruix, Acta Crystallogr. D 52 (1996) 380.
[14] C. Carbonnaux, M. Riès-Kautt, A. Ducruix, Protein Sci. 4 (1995) 2123.
[15] H.P. Schmidt, W. Koerver, B. Pätz, J. Crystal Growth 122 (1992) 317.
[16] R.S. Snyder, K. Fuhrmann, H.U. Walter, J. Crystal Growth 110 (1991) 333.
[17] R. Bosch, P. Lautenschlager, L. Potthast, J. Stapelmann, J. Crystal Growth 122 (1992) 310.
[18] M. Riès-Kautt, I. Broutin, A. Ducruix, W. Shephard, R. Kahn, N. Chayen, D. Blow, K. Paal, W. Littke, B. Lorber, A. Théobald-Dietrich, R. Giegé, J. Crystal Growth 181 (1997) 79.
[19] M. Riès-Kautt, A. Ducruix, J. Biol. Chem. 264 (1989) 745.

[20] M. Ataka, M. Asai, J. Crystal Growth 90 (1988) 86.
[21] S.B. Howard, P.J. Twigg, J.K. Baird, E.J. Meehan, J. Crystal Growth 90 (1988) 94.
[22] M.M. Riès-Kautt, A.F. Ducruix, A. Van Dorsselaer, Acta Crystallogr. D 50 (1994) 366.
[23] A. Lecroisey, C. Boulard, B. Keil, Eur. J. Biochem. 101 (1979) 385.
[24] A. Ducruix, B. Arnoux, C. Pascard, A. Lecroisey, B. Keil, J. Mol. Biol. 151 (1981) 327.
[25] I. Broutin, Thèse de Doctorat de l'Université de Paris XI, 1993.
[26] R. Fourme, P. Dhez, J.-P. Benoit, R. Kahn, J.-M. Dubuisson, P. Besson, J. Frouin, Rev. Sci. Instrum. 63 (1992) 982.
[27] I. Broutin, K. Merigeau, B. Arnoux, A. Ducruix, submitted.
[28] L. DeLucas, F. Suddath, R. Snyder, R. Nauman, M. Broom, M. Pusey, V. Yost, B. Herren, D. Carter, B. Nelson, E. Meehan, A. Mc Pherson, C. Bugg, J. Crystal Growth 76 (1986) 681.
[29] M. Riès-Kautt, A. Ducruix, in: C. Carter, R. Sweet (Eds.), Methods in Enzymology 276, Academic Press, New York, 1997, p. 23.
[30] F. Crick, B. Magdoff, Acta Crystallogr. 9 (1956) 901.
[31] I. Broutin, M. Riès-Kautt, A. Ducruix, J. Appl. Crystallogr. 28 (1995) 614.
[32] A.J.C. Wilson, Acta Crystallogr. 2 (1949) 318.
[33] B. Stec, R. Zhou, M. Teeter, Acta Crystallogr. D 51 (1995) 663.
[34] L.J. DeLucas, C.D. Smith, H.W. Smith, S. Vijay-Kumar, S.E. Senadhi, S.E. Ealick, D.C. Carter, R.S. Snyder, P.C. Weber, F.R. Salemme, D.H. Ohlendorf, H.M. Eisnpahr, L.L. Clancy, M.A. Navia, B.M. McKeever, T.L. Nagabhushan, G. Nelson, A. McPherson, S. Koszelak, G. Taylor, D. Stammers, K. Powell, G. Darby, C.E. Bugg, Science 246 (1989) 651.
[35] L.J. DeLucas, M.M. Long, K.M. Moore, W.M. Rosenblum, T.L. Bray, C. Smith, M. Carson, S.L.V. Narayana, M.D. Harington, D. Carter, A.D. Clark Jr., R.G. Nanni, J. Ding, A. Jacobo-Molina, G. Kamer, S.H. Hughes, E. Arnold, H.M. Einspahr, L.L. Clancy, G.S.J. Rao, P.F. Cook, B.G. Harris, S.H. Munson, B.C. Finzel, A. McPherson, P.C. Weber, F.A. Lewandowski, T.L. Nagabhushan, P.P. Trotta, P. Reichert, M.A. Navia, K.P. Wilson, J.A. Thomson, R.N. Richards, K.D. Bowersox, C.J. Meade, E.S. Baker, S.P. Bishop, B.J. Dunbar, E. Trinh, J. Prahl, A. Sacco Jr., C.E. Bugg, J. Crystal Growth 135 (1994) 183.
[36] F. Rosenberger, P.G. Vekilov, H. Lin, J.I.D. Alexander, Microgravity Sci. Technol., in press.

ELSEVIER

Journal of Crystal Growth 181 (1997) 109–116

JOURNAL OF CRYSTAL GROWTH

Primary spacing selection of Cu–Mn alloy under laser rapid solidification condition

Q.Y. Pan*, W.D. Huang, X. Lin, Y.H. Zhou

State Key Laboratory of Solidification Processing, Northwestern Polytechnical University, Xi'an 710072, People's Republic of China

Received 7 April 1997; accepted 7 April 1997

Abstract

In order to investigate the primary spacing selection under rapid solidification conditions, laser surface rapid resolidification experiments have been performed on Cu–26.6 wt.% Mn alloy. By taking transverse and then longitudinal sections of the directional growth dendrites/cells in the laser traces, the average primary spacing, spacing distribution range as well as the corresponding growth rate are quantitatively measured by SEM and image analyser. It has been found that there exists a wide distribution range in primary spacing under rapid solidification condition. As the growth rate increases, both the distribution range and the average spacing decrease. The maximum, $\lambda_{1\max}$, minimum, $\lambda_{1\min}$, and average primary spacing, $\bar{\lambda}_1$, as functions of growth rate, V_s, can be given by $\lambda_{1\max} = 10.68V_s^{-0.28}$, $\lambda_{1\min} = 2.42V_s^{-0.22}$, and $\bar{\lambda}_1 = 510V_s^{-0.33}$, respectively. Our experimental results are compared with the current KGT model for rapid dendritic growth, and a good agreement is found.

PACS: 68.70. + w; 81.30.Fb; 61.50.Cj; 42.62.Hk

Keywords: Primary spacing; Laser rapid solidification; Cellular/dendritic growth; Cu–Mn alloy

1. Introduction

Cellular/dendritic spacing, as one of the most important solidification microstructural scales, has been extensively studied in the past three decades. In recent years, several important developments have been made in understanding the selection mechanism of the celluar/dendritic spacing [1–10]. It is now well-understood that there exists an allowable range of cellular/dendritic spacings during unidirectional solidification. The lower and upper limits of the allowable range are very sharp at the same current growth condition, while average spacing for cellular/dendritic arrays is remarkably history-dependent on solidification parameters, i.e. growth velocity and temperature gradient. In 1990, Warren and Langer [1] put forward a theoretical model to predict the lower limit of the allowable range of primary spacings through a linear stability analysis of the dendritic arrays. In their next paper [2], they modified their model by taking into consideration the effect of no-steady-state solute

* Corresponding author. Fax: + 86 29 5250199

0022-0248/97/$17.00 © 1997 Elsevier Science B.V. All rights reserved
PII S0022-0248(97)00273-X

diffusion field in front of the interface on final selection of a steady-state primary spacing. While Hunt and Lu [3–5] presented a numerical model to predict the lower and upper limits of the allowable range by modelling the cellular/dendritic array growth. Han and Trivedi [6] experimentally investigated the distribution in primary spacing of directionally solidified succinonitrile-1.0% acetone alloy and found the presence of a band of spacings, rather than a unique spacing, under given set of experimental conditions, while Quested and McLean [7] as well as Chopra and Tewari [8] gave the wide distribution of primary spacing in nickel-based superalloys and Pb-10 wt% Sn alloy, respectively. Our previous experimental investigation on the directional solidification of succinonitrile-based alloys [9, 10] has proved that experimentally determined lower limit of the primary dendritic spacing is in excellent agreement with Hunt-Lu model or Warren-Langer model at high growth rate. More recently, Our experimental results of directionally solidified Al–4.5 wt.% Cu alloy on a Vacuum Bridgman apparatus have also shown that the lower limit of dendritic primary spacing agrees well with the prediction of Hunt-Lu numerical model [11]. However, our experimental results obtained in both transparent alloys and Al–4.5 wt% Cu alloy indicated that there exists a large discrepancy in the upper limit between experimental and theoretical values. In general, our experimental results are much larger than theoretical predictions.

Although the recent progresses have greatly improved the knowledge of the cellular/dendritic spacing selection, note that both theoretical and experimental researches have been centered on the constrained growth at low or medium growth rate. Up to now, our understanding on the cellular/dendritic spacing selection under rapid solidification conditions is still very poor. Few experiments are available for technical reason. Fortunately, the newly developed laser rapid resolidification experiment provide us a useful means for rapid solidification researches. During laser surface remelting, there is an extremely high temperature gradient in the laser molten pool, which leads to directional growth of various microstructures. Two main advantages of the experiment are (1) no nucleation is involved, i.e. epitaxial growth (2) the local growth rate and the corresponding microstructure can be determined directly. Since 1989, Laser rapid resolidification experiments have been used to investigate the microstructure evolution as a function of growth rate by several authors [12–18], and the microstructure selection maps of Al–Cu, Al–Fe alloys [13–15], in which various solidified microstructures and phases as functions of composition and growth rate are predicted, have been obtained through their continuous work. However, to the present author's knowledge, only Gremaud et al. [13] investigated the dendritic spacing selection under laser rapid solidification condition. In their experiment, an approximate method was used to determine the average primary spacing, namely, the average spacing value was given by multiplying the maximum value, measured on the longitudinal section, with a factor of 0.66. Moreover, they did not give the distribution range of the dendritic spacing as a function of growth rate.

In the present paper, detailed experiments have been carried out to investigate the celluar/dendritic spacing and its distribution range as a function of growth rate under laser rapid solidification condition.

2. Experimental procedure

Cu–26.6 wt% Mn alloy was prepared by vacuum induction melting the 99.99 wt% Cu and 99.95 wt% Mn in an alumina crucible and pouring into a $20 \times 40 \times 200$ mm rectangular copper mould with alumina coatings. In order to remove inhomogeneities at the surface, the outer 3 mm metal was machined off and specimens of 6 mm square and 30 mm long used for laser resolidification were cut from the remaining ingot. DTA yielded the liquidus temperature and solidus temperature of 1173.63 and 1158.71 K, respectively. In order to minimize the reflection for the laser beam and obtain a similar surface quality for each specimen, all the specimens were ground up to 1000 grit SiC paper and thoroughly cleaned in methanol prior to laser surface resolidification.

Laser resolidification experiments were conducted on a 5 kW CO_2 Laser (Rofin-Sinar RS 850) which can provide a stable multimode output. In

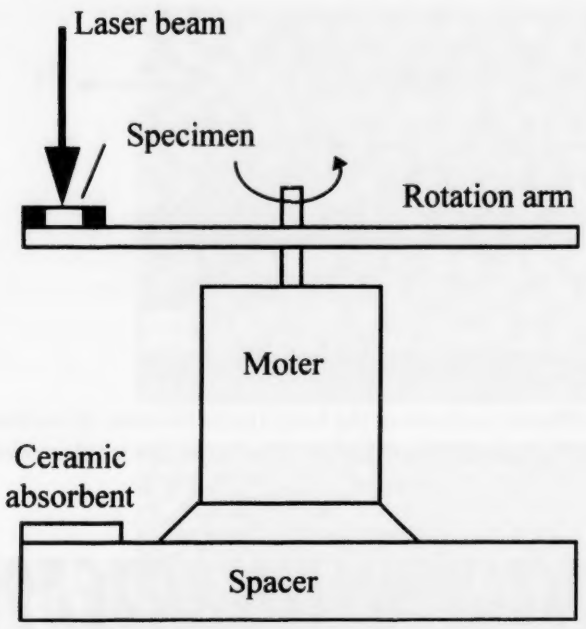

Fig. 1. Schematic diagram of laser rapid scanning apparatus.

order to realize rapid scanning, a horizontal rotating apparatus was used, as shown in Fig. 1. The specimens were fixed on a velocity-controlled rotating arm. The normally incident laser beam was focused to a spot diameter of 0.3 mm by a parabolic copper mirror. During the laser treatment, a continuous flow of 5 1/min of helium was blown to the melted zone through a 6 mm diameter pipe to prevent heavy oxidation. Laser beam scanning velocity (V_b) between 0.001 and 1 m/s were used in this study. At low scanning velocity, the laser power output was decreased to avoid the formation of plasma. Table 1 gives the laser processing conditions.

In order to measure the primary spacing and its distribution as well as to correlate them with the corresponding growth rate, the approach described below was used. Fig. 2 schematically shows the measurement process. Firstly, we serially made the metallographic preparations along XX1 ··· XXn sections of the laser traces [see Fig. 2a] to ensure the selected section to be as perpendicular as possible to the directional growth dendrites/cells within the center part of the section. PIXAR image processing system (VICOM SYSTEMS INC.) was then used to measure the average spacing and its distribution range according to the Neighbour Criterion [19], i.e. looking the structure as a whole, the nearest neighbours of each of the cells are determined. The primary spacing is defined as the average distance between the centre of gravity of neighbouring cells. Secondly, after measurement, we took the longitudinal section (plane A–A) to determine the local growth rate (V_s), which can be simply related to the known scanning velocity, V_b, via the relationship [as shown in Fig. 2b]

$$V_s = V_b \cos\theta, \tag{1}$$

where θ is the angle between V_s and V_b. The details of this method have been described elsewhere [12, 13].

Table 1
Laser processing condition (multimode; spot diameter 0.3 mm; He shielding)

Laser power output (kW)	Power density (W/cm^2)	Scanning velocity (mm/s)	Interaction time (s)
1	1.42×10^6	1	3.00×10^{-1}
1	1.42×10^6	10	3.00×10^{-2}
2	2.83×10^6	20	1.50×10^{-2}
2	2.83×10^6	40	7.50×10^{-3}
2	2.83×10^6	100	3.00×10^{-3}
2.5	3.54×10^6	120	2.50×10^{-3}
2.5	3.54×10^6	240	1.25×10^{-3}
2.5	3.54×10^6	500	6.00×10^{-4}
2.5	3.54×10^6	800	3.75×10^{-4}
2.5	3.54×10^6	1000	3.00×10^{-4}

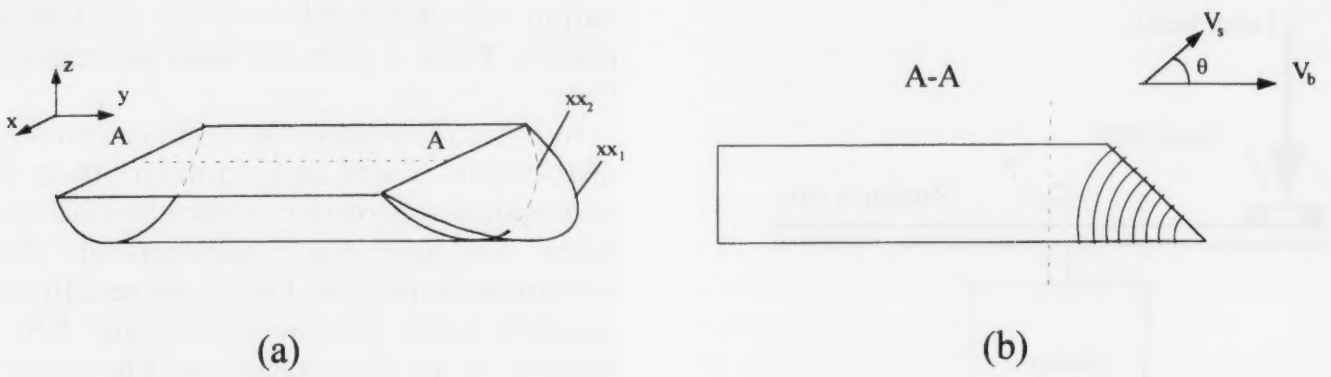

Fig. 2. Schematic diagram for measurement of primary spacing, (a) selecting different sections of the laser traces to esure the selected one exactly perpendicular to the directional growth dendrites/cells, (b) taking the longitudinal section to determine the local growth rate.

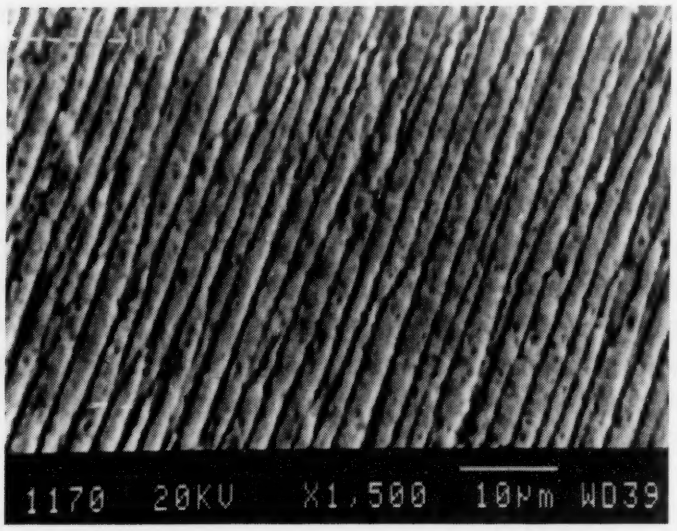

Fig. 3. The directional growth cells (longitudinal section A–A)in the laser molten pool. V_b showing the scanning direction

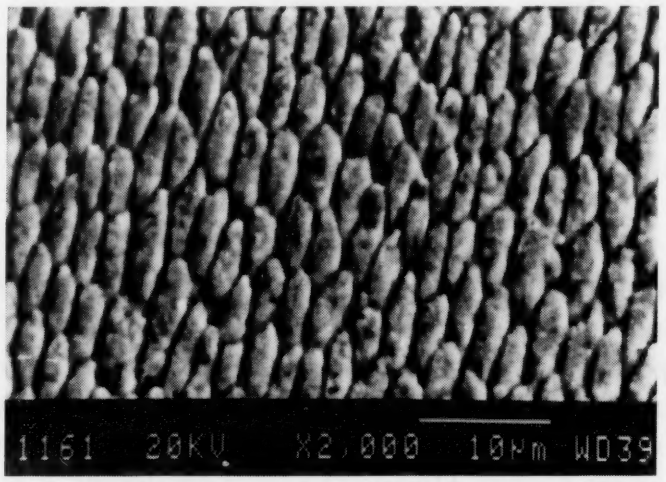

Fig. 4. The typical deformed cells obtained on XXi section, which is due to the selected section not exactly perpendicular to the growth direction of the cells.

3. Results and discussion

Fig. 3 shows the cells in longitudinal section (plane A–A). As there is extremely high temperature gradient in the laser molten pool, the cell directionally grow along heat flow direction. A typical deformed cells will be obtained if the taken transverse section (plane XXi) is not exactly perpendicular to the growth direction of the cells, as shown in Fig. 4.

Fig. 5 shows the variation of microstructures on the transverse section with increasing growth rate. In the growth rate range of 1.1–45.5 mm/s, the dendrites can be observed, as shown in Fig. 5a and Fig. 5b. However, with further increasing growth rate, the fine cells is obtained, as shown in Fig. 5c and Fig. 5g. Experimentally determined critical velocity for dendrite-cell transition is approximately 45.5 mm/s. Table 2 gives the measurement results of primary spacings. From Fig. 5 and Table 2, some experimental laws can be obtained as follows:

(1) There exists a large distribution range in primary spacing under rapid solidification conditions. As the growth rate increases, the distribution range tends to slightly decrease. The ratio of maximum primary spacing to the minimum value, as a function of growth rate, varies between 2.67 and 4. 87.

(2) At relatively low growth rate, both the primary dendritic spacings and the dendrite trunk diameter are large [see Fig. 5a]. With the increase of growth rate, the average spacing decreases and approaches its lower limit. It is interesting to have found that when the growth rate is above a certain

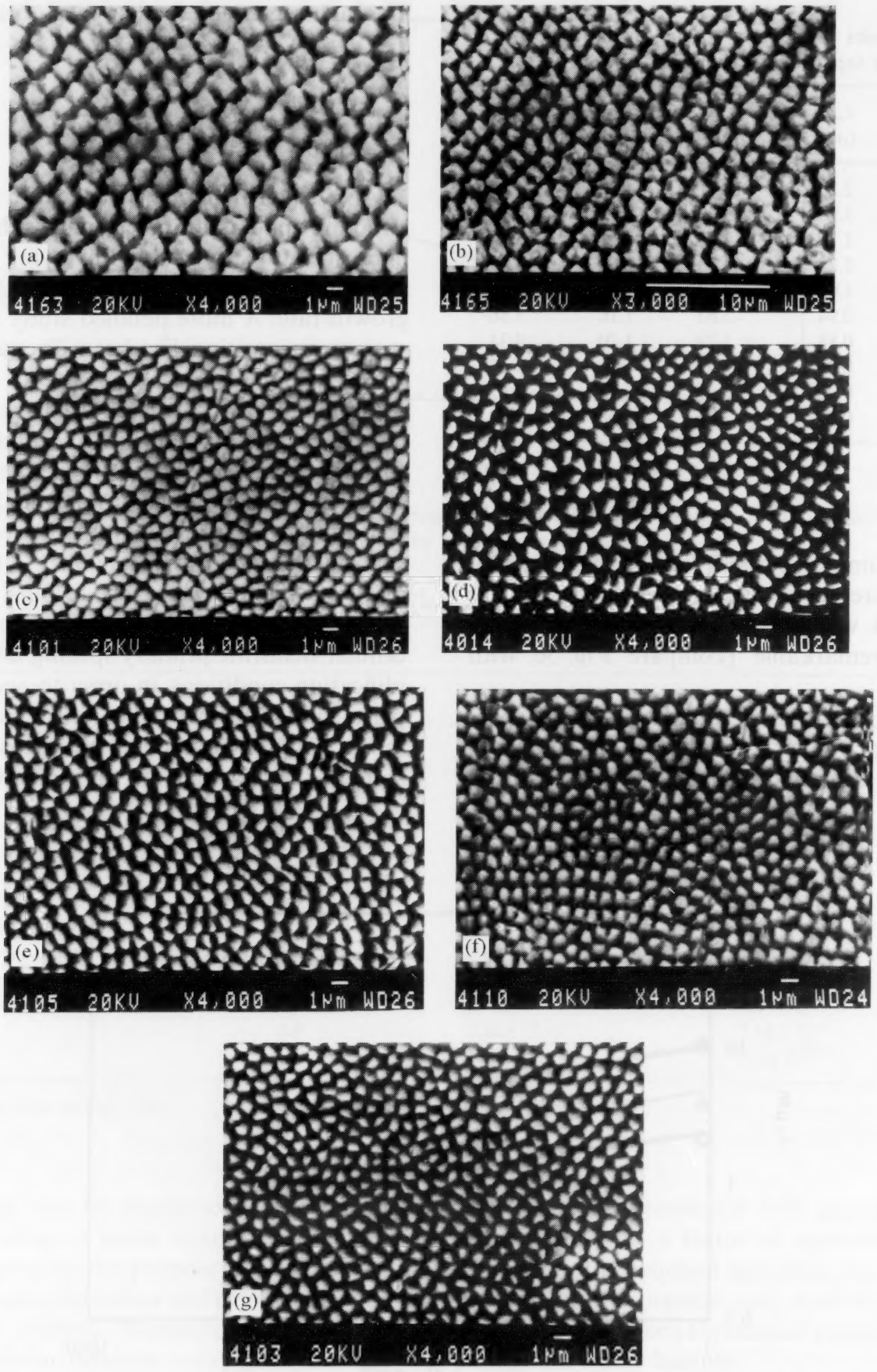

Fig. 5. Variation of the directional growth dendrites/cells on transverse section (XXi) with the increasing growth rate, V_s, (a) $V_s = 9.5$ mm/s, (b) $V_s = 38.4$ mm/s,(c) $V_s = 57.2$ mm/s,(d) $V_s = 78.5$ mm/s, (e) $V_s = 95.6$ mm/s, (f) $V_s = 118.5$ mm/s, (g) $V_s = 140.3$ mm/s.

Table 2
Experimental results of primary spacing as the function of growth rate under rapid solidification condition

Growth rate (mm/s)	λ_{min} (μm)	λ_{min} (μm)	$\bar{\lambda}$ (μm)	$\lambda_{max}/\lambda_{min}$
1.1	2.20	10.71	4.06	4.87
9.5	1.96	5.70	3.95	2.91
14.3	1.25	4.93	2.11	3.94
19.8	1.22	4.33	1.64	3.55
38.4	1.02	3.54	1.64	3.47
57.2	0.94	3.63	1.16	3.86
78.5	0.88	3.79	1.20	4.31
95.6	0.95	3.69	1.13	3.88
118.5	0.90	2.40	1.03	2.67
140.3	0.81	2.45	0.98	3.02

value (approximate 60 mm/s for the experimental alloy), the decreases in average cellular spacing is not significant, whereas the reduction in cell trunk diameter is remarkable [compare Fig. 5c with Fig. 5g].

(3) A clear distribution range of primary spacings, as a function of growth rate, is shown in Fig. 6, which is plotted from the data in Table 2. Through regression analysis, we obtain

$$\lambda_{1max} = 10.68 V_s^{-0.28}, \quad (2)$$

$$\lambda_{1min} = 2.42 V_s^{-0.22}, \quad (3)$$

$$\bar{\lambda}_1 = 5.10 V_s^{-0.33}, \quad (4)$$

(4) When growth rate is above 0.15 m/s, a banded structure appears, and then a fully substructure-free microstructure, probably involving planar front growth, has been observed with further increasing growth rate. A more detailed study of this microstructure transition has been discussed elsewhere [20].

Gremaud et al. [13] reported their experiment results on the primary and secondary dendritic spacings of several Al–Fe alloys under laser rapid solidification conditions. It was found that, for concentrated Al–8 wt% Fe alloy, the average primary spacing and the growth rate obey $\lambda_1 V_s^{0.32} = \text{const.}$ relation, which is very close to ours.

As no analytical model is yet available for the cellular/dendritic primary spacing under rapid solidification conditions, in order to compare our experimental results with theoretical model, the KGT model [21] for rapid dendritic growth was used, in spite of the fact that the tip radius (R), instead of

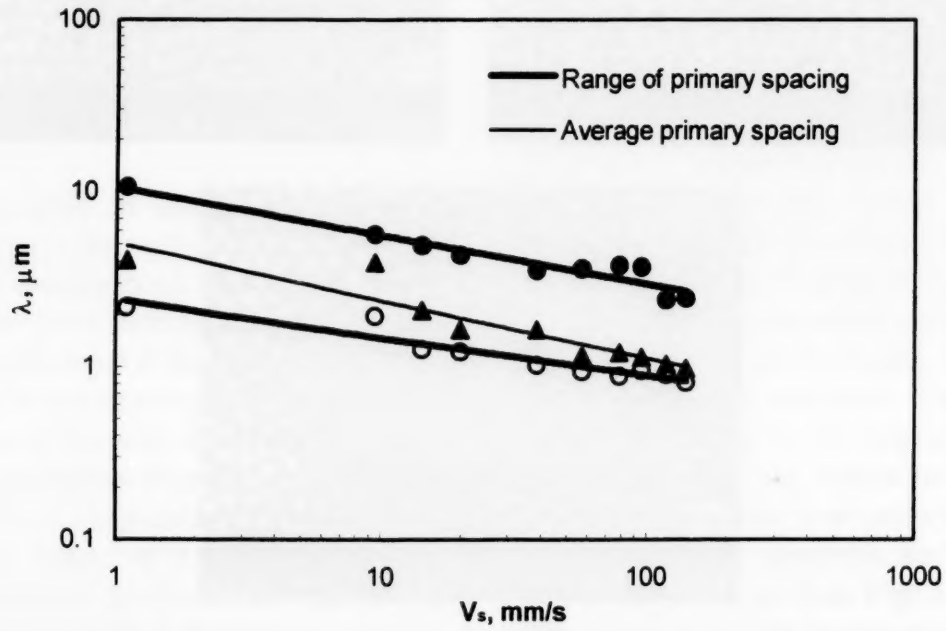

Fig. 6. Selection of primary spacing as a function of growth rate, under laser rapid solidification condition ● – the maximum primary spacing; ○ –the minimum primary spacing; ▲ –the average primary spacing.

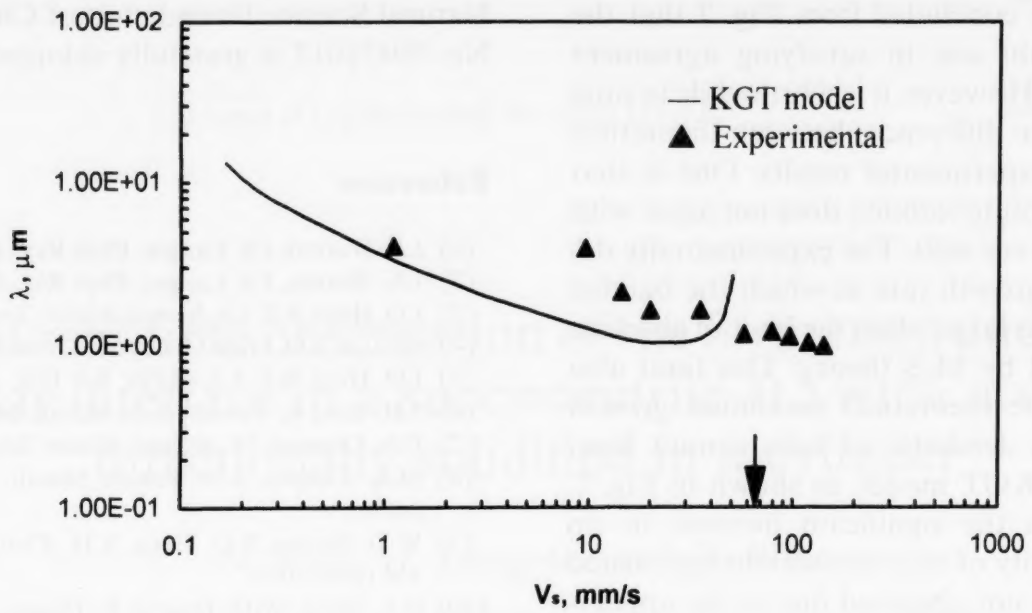

Fig. 7. A comparison between the experimentally measured average primary spacing with two times the tip radius, R, calculated by KGT model. The arrow indicates the limit of absolute stability by M–S theory [27]

Table 3
Thermophysical parameters of Cu–26.6 wt% Mn alloy

Property	Symbol	Unit	Value	Ref.
Melting point of pure Cu	T_m	K	1357.77	[25]
Liquidus temperature	T_L	K	1173.63	
Solidus temperature	T_S	K	1158.71	
Gibbs–Thomson coefficient	Γ	mk	3×10^{-7}	[23]
Distribution coefficient	k		0.75	[24]
Diffusion coefficient (liq.)	D_L	$m^2 S^{-1}$	1.75×10^{-9}	[23]
Slope of liquidus line	m	$K(wt\%)^{-1}$	-1.68	[24]
Thermal conductivity (sol.)	λ_S	$J m^{-1} K^{-1} 1^{-1}$	34	[23]
Thermal conductivity (liq.)	λ_L	$J m^{-1} K^{-1} 1^{-1}$	16	[23]
Thermometric conductivity (sol.)	α_S	$m^2 S^{-1}$	8.8×10^{-6}	[23]
Thermometric conductivity (liq.)	α_L	$m^2 S^{-1}$	4.0×10^{-6}	[23]
Latent heat	ΔH	$J mol^{-1}$	7.14×10^3	[23]
Thermal gradient	G	K m	2.2×10^6	[26][a]

[a]Calculated by heat-flow model [26]

primary spacing, can be predicted by the model. Since the tip radius in metal cannot be obtained from micrographs, for the purpose of comparison, the relation between tip radius and primary spacing must be firstly defined. Recently, the numerical modelling of cellular/dendritic array growth in the high velocity region by Lu et al. [22] has shown that the tip radius predicted by KGT model and primary spacing calculated by numerical model follow a similar tendency with growth rate, both being related by a factor of approximately two. Therefore, it is assumed here that this relationship is valid for the present case, and this makes the comparison between theoretical prediction and experimental result feasible.

The tip radius, as a function of growth rate, are given by KGT model in Fig. 7. The thermophysical parameters used for calculations are listed in

Table 3. It can be concluded from Fig. 7 that the experimental results are in satisfying agreement with KGT model. However, it is worthwhile to note that there exist two differences between theoretical predictions and experimental results. One is that the calculated absolute stability does not agree with the observations very well. The experimentally determined critical growth rate at which the banded structure appears is larger than the limit of absolute stability predicted by M-S theory. This limit also corresponds to the theoretical maximum growth rate above which dendrites or cells cannot form according to the KGT model, as shown in Fig. 7. The other is that the significant increase in tip radius in the vicinity of absolute stability predicted by KGT model is not observed due to the appearance of the banded structure. Whereas, the KGT model predicts the correct dependence of average primary spacing on growth rate both qualitatively and quantitatively in the observed growth rate range.

4. Conclusions

There exists a large distribution range in primary spacing under rapid solidification condition. With the increase of growth rate, both the average spacing and the distribution range tend to decrease. It is interesting to note that when growth rate is beyond a certain value, the average spacing is nearly constant, however, the reduction in the cell trunk diameter is remarkable. The average, maximum and minimum primary spacing of Cu–26.6 wt% Mn, as functions of growth rate, can be given as $\lambda_{max} = 10.68V_s^{-0.28}$, $\lambda_{min} = 2.42V_s^{-0.22}$ and $\bar{\lambda} = 5.10V_s^{-0.33}$, respectively. Our experimental results agree well with the KGT model.

Acknowledgements

The authors thank Professor Y. Miyata for helpful discussions. The financial aid of the National Natural Science Foundation of China under grant No. 59431012 is gratefully acknowledged.

References

[1] J.A. Warren, J.S. Langer, Phys Rev. A 42 (1990) 3518.
[2] J.A. Warren, J.S. Langer, Phys Rev. E 47 (1993) 2702.
[3] J.D. Hunt, S.Z. Lu, Metall. Mater. Trans. A 27 (1996) 611.
[4] S.Z. Lu, J.D. Hunt, J. Crystal Growth 123 (1992) 17.
[5] J.D. Hunt, S.Z. Lu, Mater. Sci. Eng. A 173 (1993) 79.
[6] S.H. Han, R. Trivedi, Acta Metall. Mater. 42 (1994) 25.
[7] P.N. Quested, M. Mclean, Mater. Sci. Eng. 65 (1984) 171.
[8] M.A. Chopra, S.N. Tewari, Metall. Trans. A 22 (1991) 2467.
[9] W.D. Huang, X.G. Geng, Y.H. Zhou, J. Crystal Growth 134 (1993) 105.
[10] G.L. Ding, W.D. Huang, X. Huang, X. Lin, Y.H. Zhou, Acta Metall. Mater. 44 (1996) 3705.
[11] X. Lin, W.D. Huang, G. Ding, Y. Zhou, The 4th Decennial Int. Conf. on Solidification Processing, 1997, to be presented.
[12] M. Zimmermann, M. Carrard, W. Kurz, Acta Metall. 37 (1989) 3305.
[13] M. Gremaud, M. Carrard, W. Kurz, Acta Metall. Mater. 38 (1990) 2587.
[14] M. Gremaud, M. Carrard, W. Kurz, Acta Metall. Mater. 39 (1991) 1431.
[15] S.C. Gill, M. Zimmermann, W. Kurz, Acta Metall. Mater. 40 (1992) 2895.
[16] S.C. Gill, W. Kurz, Acta Metall. Mater. 41 (1993) 3563.
[17] S.C. Gill, W. kurz, Acta Metall. Mater. 43 (1995) 139.
[18] W. Kurz, R. Trivedi, Mater. Sci. Eng. A 179/180 (1994) 46.
[19] A. Schievenbusch, G. Zimmermann, M. Mathes, Mater. Sci. Eng. A 173 (1993) 85.
[20] Q.Y. Pan, X. Lin, W.D. Huang, Y.H. Zhou, Progress in Natural Science, in press.
[21] W. Kurz, B. Gioranola, R. Trivedi, Acta Metell. 34 (1986) 823.
[22] S.-Z. Lu, J.D. Hunt, P. Gilgien, W. Kurz, Acta Metall. Mater. 42 (1994) 1653.
[23] A. Schievenbusch, G. Zimmermann, X.L. Lu, Z. Metallkd 86 (1995) 614.
[24] P.R. Subramanian, D.J. Chakrabarti, D.E. Laughlin, Phase Diagrams of Binary Alloys, ASM, Materials Park, OH, 1990.
[25] C.J. Smithells, Smithells Metals Reference Book, Butterworths, London, 1983.
[26] Q.Y. Pan, PhD Thesis, Northwestern Plytechnical University, China, 1996.
[27] W.W. Mullins, R.F. Sekerka, J. Appl. Phys. 35 (1964) 444.

ELSEVIER

Journal of Crystal Growth 181 (1997) 117–132

JOURNAL OF CRYSTAL GROWTH

In situ and real-time observation of the formation and dynamics of a cellular interface in a succinonitrile–0.5 wt% acetone alloy directionally solidified in a cylinder

N. Noël, H. Jamgotchian*, B. Billia

Laboratoire MATOP (Associé au CNRS), Université d'Aix-Marseille III, Faculté des Sciences et Techniques de St. Jérôme, Case 151, F-13397 Marseille Cedex 20, France

Received 26 July 1996; accepted 11 April 1997

Abstract

In situ and real-time observation of the solid–liquid interface during upward Bridgman growth of succinonitrile–0.5 wt% acetone in a cylinder was carried out. This first article concentrates on the study of the emergence and building of nonplanar patterns. By observation under white light in the solidification direction, bright field images and video records of the interface microstructure were obtained, which allowed dynamical phenomena such as the ripening and arrangement of cellular arrays with time. All results show a significant influence of natural convection in the melt. In particular, a microstructure gradient was observed at the interface. From a phenomenological model based on a boundary layer approach, its origin can be attributed to a ramp in solute concentration along the growth front created by tangential fluid flow. Statistical analyses of the evolution of primary spacing and array disorder show that the stable arrangement can still be described as a honeycomb disturbed by Gaussian noise. Convection was also found to be responsible for primary spacings smaller than that given by theoretical diffusive models and experiments on thin samples.

PACS: 64.70.Dv; 81.30.Fb; 81.10.Fq

Keywords: Directional solidification; Bulk organic alloy; Dynamics of cellular array; Dynamics of grain boundaries

1. Introduction

To improve the understanding of solidification microstructures, experiments have been repeatedly performed on metallic and, for thirty years now, on transparent alloys (see e.g. Refs. [1, 2]). In the present study, we observed directional solidification of a succinonitrile–0.5 wt% acetone alloy in a cylinder. In contradistinction with most of the experiments on transparent alloys, which were conducted on alloys constrained between two glass slides with a narrow separation so that solidification occurred approximately in two dimensions, three-dimensional cylindrical samples were considered in our

* Corresponding author. Fax: + 33 491288775; e-mail: haik@matop.u-3mrs.fr.

0022-0248/97/$17.00 © 1997 Elsevier Science B.V. All rights reserved
PII S0022-0248(97)00274-1

experiments. In directional solidification, three parameters control the process: the thermal gradient G, the growth velocity V and the solute concentration C_∞ of the alloy. Fixing two of these parameters, in practice G and C_∞, we were able to observe consecutively a planar interface, a cellular interface and then a dendritic interface by increasing the velocity.

Among the few previous experimental studies on massive transparent samples, the pioneering work by Schaefer and Glicksman [3] concerning the observation of the initial stages of morphological instability of a planar solid–liquid interface should be mentioned. As the power-off method was used, the control parameters G and V were not separated so that the experimental set-up was close to directional casting but the aspect ratio (20 mm in diameter and 5 mm in height) of the sample was far less than what is usually obtained in directional solidification. Consequently, the experiments were rather representative of morphological instability in the dendritic regime. These authors examined in particular the development of dendrites from an initially smooth, stationary, solid–liquid interface. They showed that imperfections, i.e. grain boundaries or subboundaries and foreign particulate matter, have a critical influence in triggering instability and on the spatial distribution of dendrites. Actually, these experiments complement ours since, in continuity with previous work [4–6], we chose to focus the observation and characterisation on the details of cellular interface development. In order to carry out the in situ and real-time observation we have implemented an optical method for direct imaging of the interface, using bright field illumination. The initial stages of the growth, spreading of perturbations and building of the cellular pattern were observed and analyzed. The influence of fluid flow in the melt on the dynamics of morphological instability was determined.

2. Experimental procedure

2.1. Preparation of succinonitrile–acetone samples

The succinonitrile ($CNCH_2CH_2CN$)–acetone system was retained as, on the one hand, succinonitrile is long known to be one of the transparent organic materials that freeze like typical metals with a non faceted solid/liquid interface [7]. Advantage was taken of transparency to observe the growth forms by optical means which are non-destructive. On the other hand, the physicochemical characteristics of the succinonitrile (SCN)-acetone (AC) system have been precisely determined [8]. Furthermore, over time, the succinonitrile-acetone system has become the standard analogue of binary metallic systems for the study of solidification microstructures. The purification of succinonitrile was achieved in two stages: first, commercial succinonitrile was distilled under vacuum and, second, the resulting material was zone refined. The multistage apparatus is equivalent to that described by Brissaud et al. [9] and the method for succinonitrile has been specified by Rivière et al. [10]. Here, the succinonitrile used in the experiments has undergone 168 passes of the molten zone. In order not to contaminate succinonitrile with air moisture, acetone is added in an airtight chamber containing an inert atmosphere of nitrogen. Just after adding the acetone, the glass observation cell is hermetically closed inside the chamber.

2.2. Experimental set-up and glass observation cell

The solidification device, schematically represented in Fig. 1a, consisted of three parts: a hot chamber (1) and a cold chamber (3), at temperatures, respectively, higher and lower than the melting temperature of the alloy, separated by an adiabatic zone (2). In order to observe the solid–liquid interface, a flat window (4) was mounted at the bottom of the assembly making it possible to send light parallel to the direction of solidification from the bottom to the top. The alloy was contained in a glass cell specifically designed to allow good transmission of light and clear observation. This cell was of 120 mm height and 12 mm inner diameter but only a few tens of millimeters (about 30 mm) could be solidified due to translation limitation. To facilitate observation, it had also a flat window at the bottom (5) which enabled minimal deviation of the light before it reached the interface between the solid and the liquid.

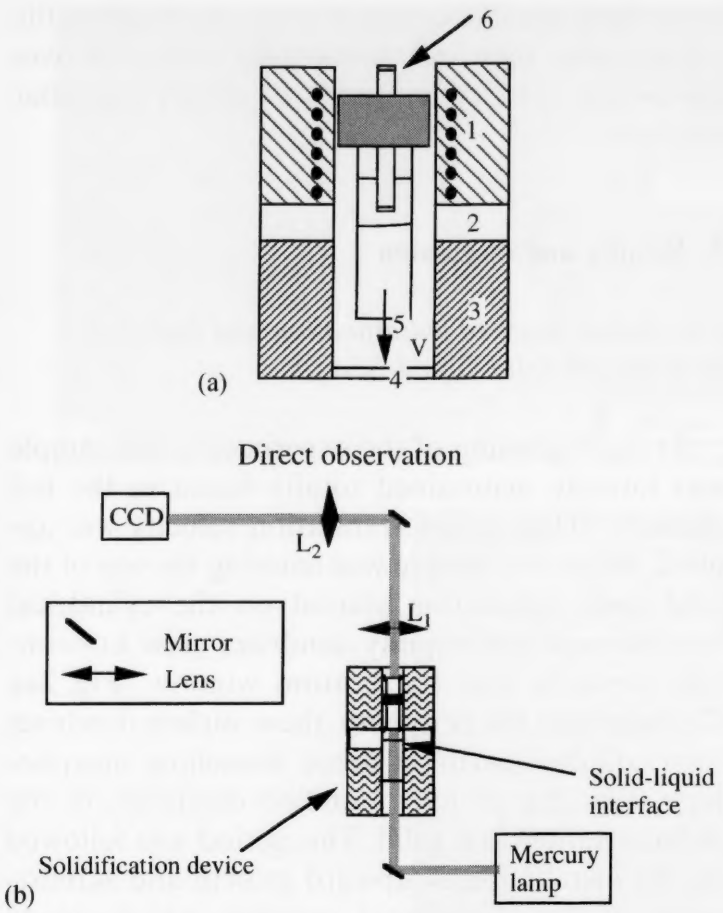

Fig. 1. Schematic representation of (a) the solidification device. (1: Hot chamber, 2: Adiabatic zone, 3: Cold chamber, 4: Flat bottom window, 5: Flat window of the glass observation cell, 6: Endoscopic system of lenses) and (b) the optical set-up: for direct observation, a Hg-vapour lamp was used and light followed path 1.

Furthermore, a group of lenses mounted on a glass tube (6) was immersed in the liquid phase to capture the image of the solid–liquid interface while the alloy was solidifying. The optical system, which acted like an endoscope, can be compared to the system used by McFee [11] except that the thick lens was replaced by a system of two lenses. The sample was translated downwards into the cold zone where solidification occurred. A DC-motor combined with a tachometric feedback ensured a precise control of the velocity of displacement, which ranged from 0.5 to 12 μm/s.

Fig. 1b gives a schematic representation of the whole apparatus. The optical set-up and solidification device were both mounted on a honeycomb-core optical breadboard fixed vertically.

Direct observation was employed to render the shape of the solidification front visible. It consisted in using incoherent light from a mercury-vapour lamp to obtain the image of the solid–liquid interface. In this case, the light rays traversing the sample were collected by the partially immersed system of lenses and the bright field image of the solid–liquid interface was finally projected on the matrix of a CCD camera. A second system of lenses (L_1 and L_2) enabled us to focus on the interface and to choose the magnification of the final image. The CCD camera was connected to a video recorder and also to a computer for image processing. The photographs presented in the following are frozen images of the video records.

2.3. Experimental conditions and procedure

All the experiments presented in this paper were carried out on succinonitrile 0.5 wt% of acetone or thereabouts as the solute content was not controlled after the filling of the observation cell. The hot part of the furnace was set at 120°C and the cold part at 0°C, with a resulting applied temperature gradient G of 24°C/cm in the interface zone. Thermal gradient G and solute concentration C_∞ being fixed, the morphological instability threshold was therefore crossed by increasing the velocity beyond the critical value $V_{c,MS}$. As solid and liquid have almost equal thermal conductivities, the theoretical critical velocity was calculated from the constitutional supercooling criterion:

$$V_{c,MS} = \frac{DGk}{mC_\infty(k-1)}, \tag{1}$$

where D is the diffusion coefficient of solute, k the solute partition coefficient and m the liquidus slope. For dilute SCN-AC alloys, $D = 1.3 \times 10^{-5}$ cm^2/s, $k = 0.1$ and $m = -2.8$ K/wt% so that we found from Eq. (1) a critical velocity $V_{c,MS} = 0.25$ μm/s. This threshold value is far less than its experimental counterpart V_c which was about 2 μm/s. Indeed, in experiments, the solidification front in the observation window, that was kept centered for the requirement of optical alignment, remained smooth and featureless apart from the shallow grooves induced by grain boundaries for translation velocities

less than 2 μm/s. The origin of the difference between the theoretical and experimental values of critical velocity V_c has probably to be sought in the influence of natural convection that existed in our experiments. Fluid flow was evidenced by the motion of foreign particles in suspension in the liquid phase, the convective velocity being of the order of 30 μm/s close to the interface. It is now well established that, when solute is rejected upon solidification ($k < 1$), convection in the bulk of the melt that decreases the solute build-up at the growing front, generally has a stabilizing influence on the break-down of a planar interface [12, 13] which results in a shift of V_c to a higher value. The fact that the observed critical velocity was increased by about an order of magnitude indicates that convective transport was significant under our experimental conditions.

In upward directional solidification of transparent systems the main driving force for convection is the horizontal temperature gradient which induces convection in the whole liquid phase. Therefore, the analysis of morphological instability with fluid flow in the bulk liquid and a stagnant layer ahead of the planar growth front [14] can be used to estimate the degree of convection through the nondimensional width of the diffusive layer adjacent to the solid-liquid interface Δ ($= \delta V/D$ with δ the dimensional width). The width Δ is linked to the effective segregation coefficient k_{eff} ($= k/[k + (1 - k) \times \exp(-\Delta)]$) which, in first approximation, equals the inverse of the shift of the threshold of morphological instability by convection, $V_c/V_{c,MS} = 8$. An order of magnitude of 0.25 follows for Δ.

Two translation velocity profiles were applied during the experiments that differed by the way of settling a smooth solid–liquid interface. At the beginning of each run, we first of all wanted to avoid morphological instability, so that the imposed velocity was chosen below the critical velocity. Yet, a nucleation phase always occurred with the development of dendrites. Stabilization of a flat interface was then achieved in two ways. Either, the velocity was maintained, which allowed the growth of a few millimeters of solid at low velocity until the interface got smooth, or the sample was stopped to create conditions of thermal annealing. In both ways, when the interface looked featureless in the grains and a stable configuration was reached, the velocity was then instantaneously increased over the critical velocity necessary to obtain a cellular interface.

3. Results and discussion

3.1. Initial stage of solidification and building of a smooth solid–liquid interface

At the beginning of the experiments, the sample was initially maintained totally liquid in the hot chamber. Then, a low translation velocity was applied. When the sample was entering the top of the cold zone, nucleation started on the cylindrical crucible wall and rapidly dendrites grew horizontally inwards over the bottom window (Fig. 2a). Coming from the periphery, these surface dendrites then collided leaving a dense branching morphology (Fig. 2b), or fully ramified dendrites, in the polycrystalline first solid. This period was followed by the installation of upward growth and stabilization of the solid-liquid interface which slowly reached the expected state of stability at the applied velocity, i.e. a planar microstructureless interface. At this stage, we observed only a pattern of grain boundaries (Fig. 2c). The stabilization from the first image in Fig. 2 to the last one took a few minutes. These observations bear similarities with those reported by Ludwig and Kurz [15] who studied rapid solidification of very dilute succinonitrile–argon alloys in capillary tubes with square cross-section. Indeed, we also observed that, in the initial stage of solidification, grain boundaries directly originated from the impingement of the surface dendrites.

As grain boundaries have finite interfacial energy, polycrystals were intrinsically metastable and always evolved towards a thermodynamically more stable arrangement. There was thus a competition between grains so as to reduce excess energy stored in the boundaries, very much alike that observed in soap froths. The two basic mechanisms, T1 and T2, causing the changes in the grain network are illustrated in Fig. 3. Grain vanishing (Fig. 3a and Fig. 3b) occurred by mass diffusion under the driving force of curvature-induced pressure and the

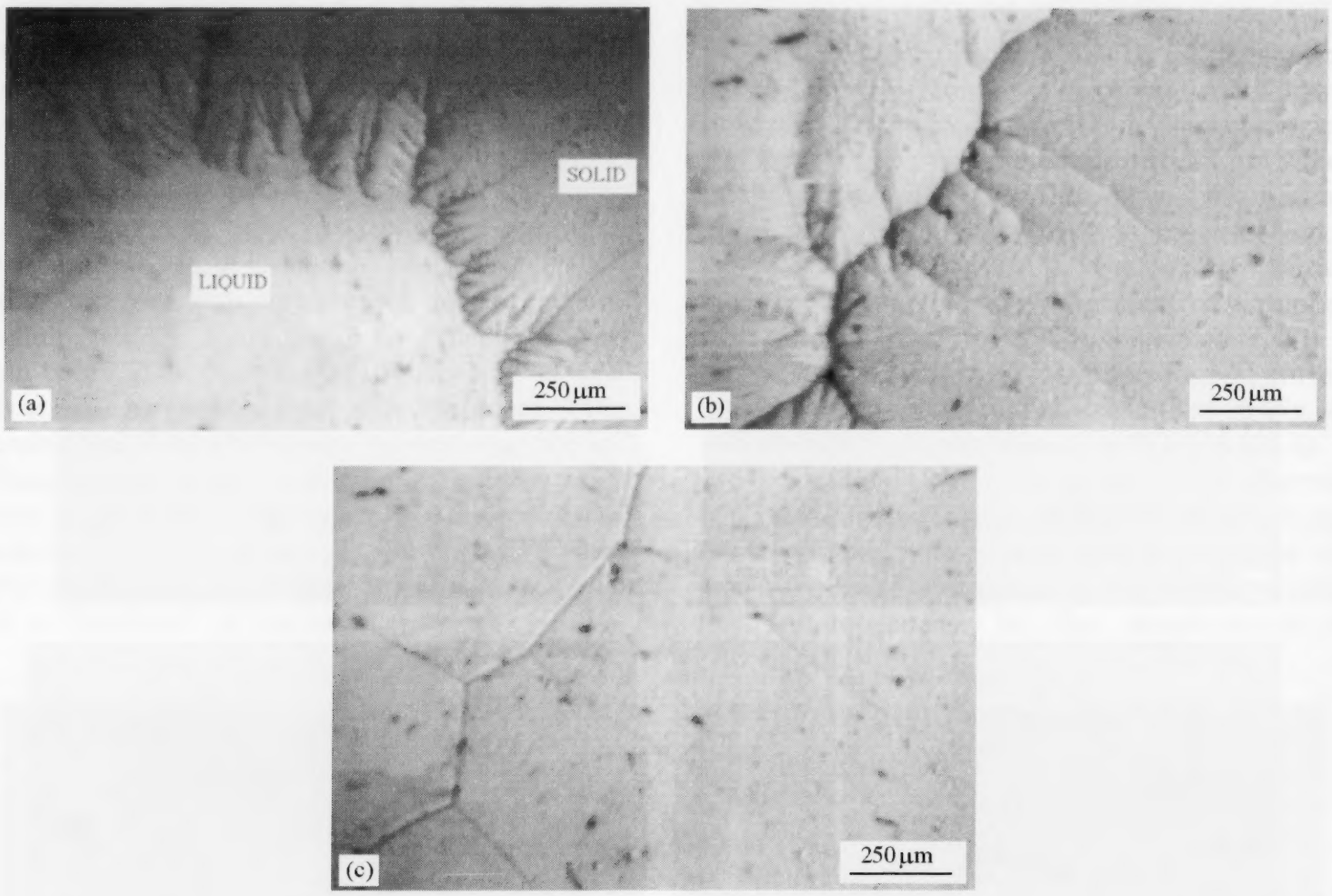

Fig. 2. (a) Solid–liquid interface a few seconds after the sample entered the cold zone. (b) Dendrites colliding 150 s after $2a$. (c) Grain boundaries emerging from the dendrites 325 s after $2a$. Pulling velocity $V = 0.53$ μm/s at the entrance of the cold zone and during the events.

neighbour-switching process (Fig. 3c–Fig. 3e) permitted the rearrangement of the boundary connections. The first configuration (Fig. 3c) evolved because it was unstable with respect to the global ripening of grains at the interface. Incidentally, Fig. 3d, which is only a transient step, confirms that junctions of four grains are not topologically stable.

By undergoing repeated T1 and T2 processes, the numerous grain boundaries migrated and rearranged into a polygonal configuration often close to an irregular honeycomb, of the type observed by Schaefer et al. in an experiment which provided observation of the interface from the liquid side in a reconstructed hologram [16]. It followed that the hexagonal tiling consisted of trijunctions oriented at 120° was the most stable form in mature polycrystals, which is a classical result of topological stability in twodimensionnal space-filling problems [17, 18].

If solidification was stopped by no longer applying a velocity, thermal annealing induced recrystallization with a continuous ripening of the grain distribution. Concomitantly, the number of grain boundaries was decreasing and could even ultimately vanish after overnight treatment. Thus, it was possible for the solid to be converted into a singlecrystal, i.e. to reach the most stable state from the energetic point of view which is a smooth interface without any grain boundary.

As noted by Schaefer et al. [3], the planar interface viewed in the direction of solidification was only visible if grooves issued from the presence of grain boundaries existed at the interface. In the opposite case, which was encountered after annealing,

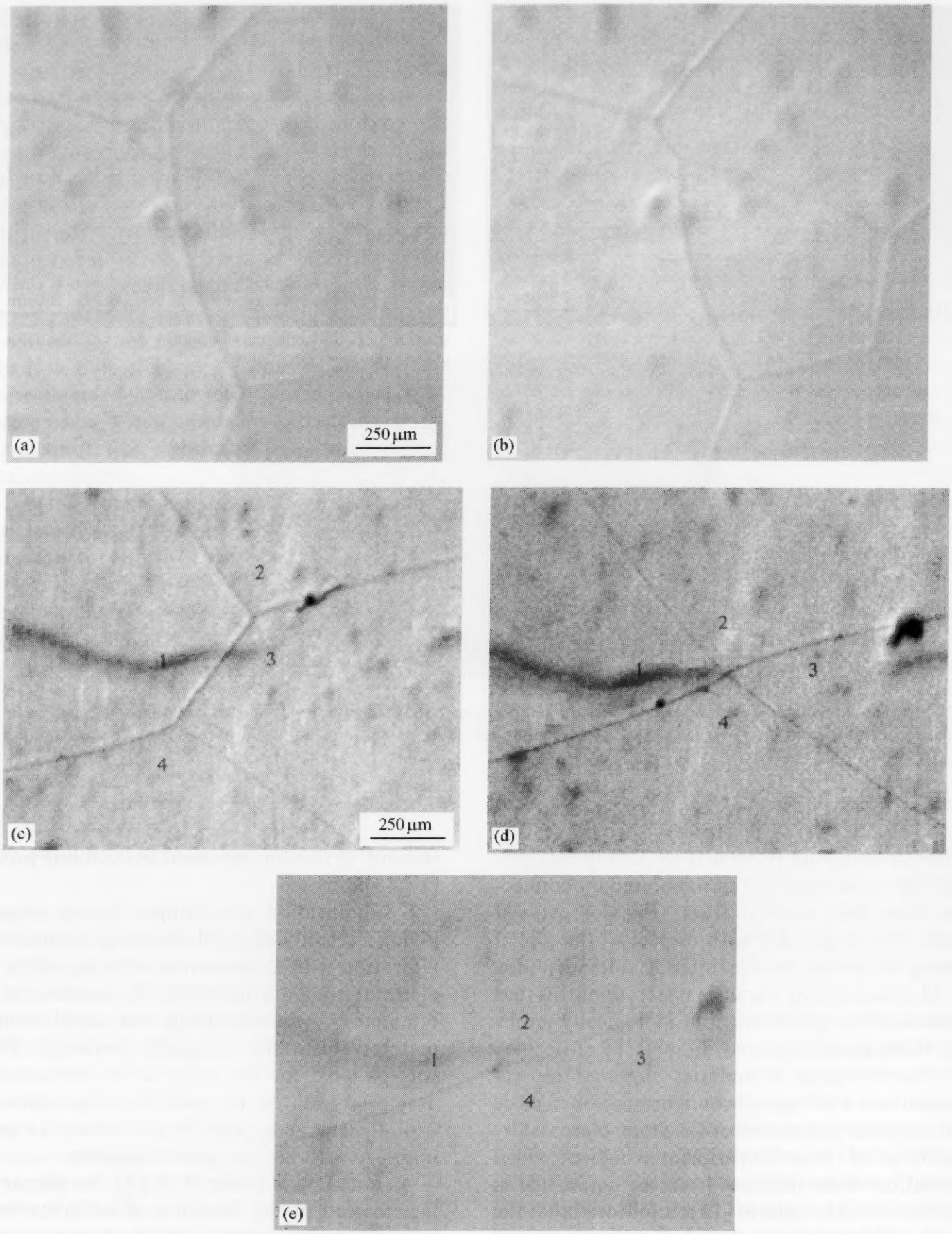

Fig. 3. (a) Several grains, one of which is smaller and has three neighbours ($V = 0$). (b) The smallest grain has disappeared and one trijunction was formed after 120 s. (c) Grain boundaries forming two trijunctions (grains 1 and 3 being neighbours), $t = t_0 - 20$ min. (d) Grain boundaries forming a quadrijunction, $t = t_0$. (e) Grain boundaries again forming two trijunctions (grains 2 and 4 being neighbours), $t = t_0 + 1$ min 20 s. After the growth of surface dendrites, pulling velocity was maintained constant, $V = 0.53$ μm/s, to stabilise the interface.

we could focus on the interface only after the beginning of the development of morphological instabilities which created features on a small scale and thus local modulation of the solid height.

3.2. Morphological instability

3.2.1. Microstructure formation

Fig. 4 presents four stages in the development of a cellular array at a solid-liquid interface free from grain boundaries. Looking at Fig. 4a–Fig. 4d, one sees at a glance that the level of development of the morphological instability was uneven over the interface. Indeed, in the experiment, instability originated roughly from the upper left corner of the image and then propagated towards the lower right corner. The result of this propagation process was that a "gradient" of microstructure was visible, from a developed pattern in the upper left part of the images, even dendritic in Fig. 4d, to shallow cells, or a planar interface (Fig. 4a), in the lower right part. At the propagation front, morphological instability came up as mottled features, from which emerged little hills and ridges. Then, cells became more distinct while the pattern was ripening and, if the translation velocity was kept constant during the experiment, eventually reached a developed state which hardly changed by the end (Fig. 4d). It should be noticed that the state in Fig. 4d corresponds to an amplification of the features in Fig. 4b over only 3.7 diffusion times ($= D/V^2 = 129$ s).

In fact, during the experiment, it was observed that the motion of foreign particles in the liquid just above the interface was in the direction of the microstructure gradient (Fig. 4a). Consequently, the inhomogeneity in the development of

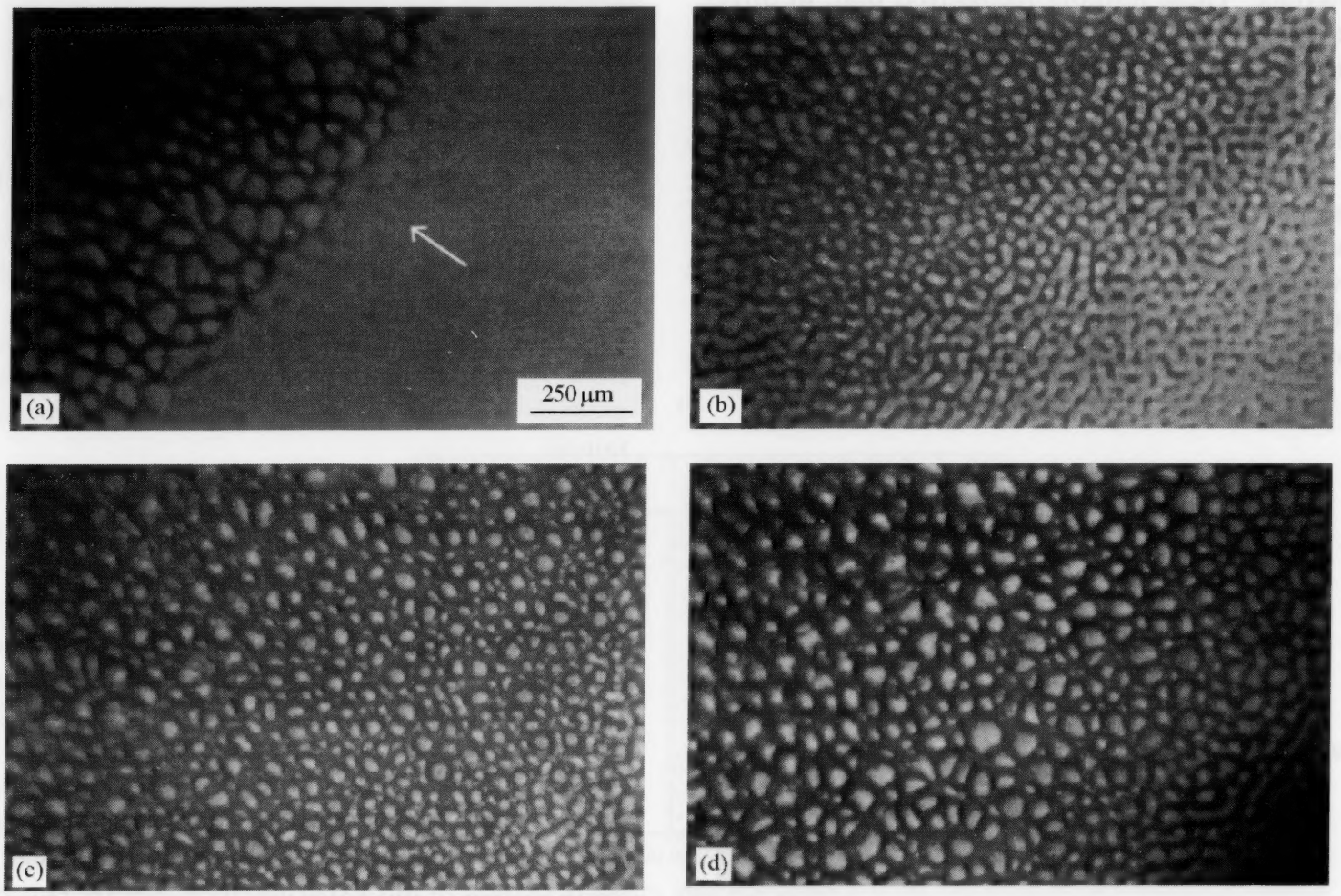

Fig. 4. (a) Developed pattern at $V = 2.12$ μm/s. The arrow gives the convection direction. (b) Propagation of instability upon an increase of the pulling velocity to 3.18 μm/s at $t = t_0$. (c) Intermediate stage ($t = t_0 + 120$ s). (d) Developed microstructure ($t = t_0 + 450$ s).

morphological instabilities at the interface has to be related to the existence of natural convection in the melt. This is not surprising as, on the one hand, organic materials have poor thermal diffusivity κ (i.e. a high Prandtl number $\mathrm{Pr} = \nu/\kappa$ with ν the kinematic viscosity), which renders them prone to important fluid flow driven by radial temperature gradients, and, on the other hand, acetone is lighter than succinonitrile so that in addition there should be some thermosolutal convection [19].

3.2.2. Lateral gradient of instability threshold

Most likely, the solute in the boundary layer adjacent to the solidification front was swept by convection and accumulated upstream. This can be evaluated by using the boundary layer approach proposed by Ostrogorsky and Müller [20] which, in contrast to the stagnant layer model, accounts for convection in the solute layer at the growth interface. These authors recognized that, in directional solidification, the flow typically approaches the solid–liquid interface by making a 90° turn within a short entrance region and then flows along the solidification front as sketched in Fig. 5.

Rather than a slender control volume including the part of the growth interface exposed to the tangential flow, which is worth to model the effective segregation coefficient [20], we consider the small control volume ABCD in Fig. 5 to get an estimate of the lateral solute gradient $\partial C/\partial x$ at the front. When convection is (i) the dominant mode of solute transport in the melt and (ii) (quasi)stationary, solute conservation requires that the outflows, J_{BC} and J_{CD}, through BC and CD should be balanced by the inflows, J_{AB} and J_{AD}, through AB and AD

$$J_{AB} - J_{CD} + J_{AD} - J_{BC} = 0. \tag{2}$$

The outflow of solute incorporated into the solid and the inflow from the bulk, respectively, read

$$J_{BC} = VkC_x\,\mathrm{d}x, \tag{3a}$$

$$J_{AD} = VC_\infty\,\mathrm{d}x. \tag{3b}$$

In a linear approximation, the lateral flows have the form

$$J_{AB} = \int_0^{\delta_{s,x}} V_x(z)\,C_x(z)\,\mathrm{d}z$$

$$= \int_0^{\delta_{s,x}} \frac{U_{s,x}}{\delta_{s,x}}\,z\left[C_\infty + (C_x - C_\infty)\left(1 - \frac{z}{\delta_{s,x}}\right)\right]\mathrm{d}z \tag{4}$$

with $U_{s,x}$ the tangential velocity at the exit of the solute boundary layer. J_{CD} is similar to J_{AB}, with x changed into $x + \mathrm{d}x$. After substitution of Eqs. (3a), (3b) and (4) into the solute balance, Eq. (2), and straightforward algebra, the lateral gradient of solute at the growth front can be obtained

$$\frac{\partial C_x}{\partial x} = 6\,\frac{V}{U_{s,x}}\,\frac{C_\infty - kC_x}{\delta_{s,x}} - \frac{C_x + 2C_\infty}{\delta_{s,x}}\,\frac{\partial \delta_{s,x}}{\partial x}. \tag{5}$$

As $\delta_{s,x} \approx 5\,(D/\nu)^{1/3}\,(x\nu/U_\infty)^{1/2}$ [20], the second term in the RHS of Eq. (5) is always negative and varies as x^{-1} in the downstream direction. The first term, in which phase change is described as a suction effect, is positive when solute is rejected ($k < 1$), which is the case for dilute SCN-AC alloys, and varies as $x^{-1/2}$. Therefore, it follows from Eq. (5) that, at a certain distance from the entrance region, there existed in our experiments a positive concentration gradient along the interface, which created a ramp in the control parameter C_x. When convection is strong, $C_x/C_\infty \approx 1$ so that one gets from

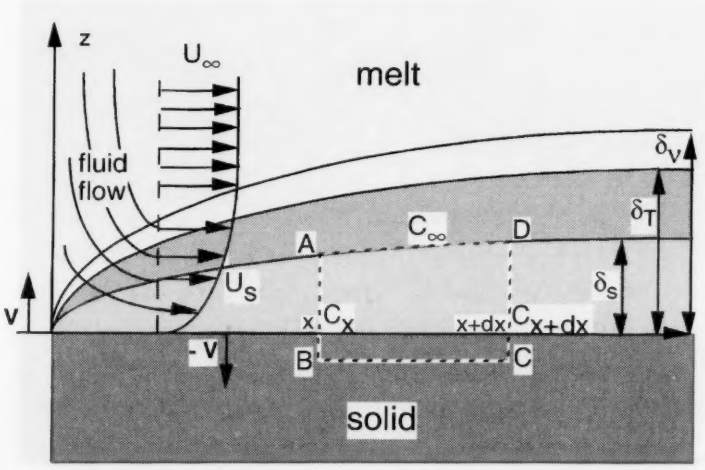

Fig. 5. Sketch of the flow pattern, the solute (width δ_s), thermal (width δ_T) and momentum (width δ_v) boundary layers and the control volume ABCD used in the model.

Eq. (5) and the expression for $\delta_{s,x}$

$$\frac{1}{C_x}\frac{\partial C_x}{\partial x} \approx \frac{6\,V}{5\sqrt{vU_\infty}(D/v)^{2/3}}\frac{1-k}{\sqrt{x}} - \frac{3}{2x}. \quad (6)$$

Other things being unchanged, it follows from the local form of the constitutional supercooling criterion, $V_c C_x(k-1)/Dk = G/m$, that the lateral gradient of instability threshold was equivalent to the solute one, namely $V_c^{-1}\,\partial V_c/\partial x = -C_x^{-1}\,\partial C_x/\partial x$. With $\nu = 2.6\times10^{-2}\,\mathrm{cm^2/s}$ and $U_\infty = 30\,\mu\mathrm{m/s}$, $V_c^{-1}\,\partial V_c/\partial x \approx -27\%/\mathrm{mm}$ at 5 mm from the entrance for the experiment in Fig. 4a. This estimate for the gradient of instability threshold, which is not steep, seems reasonable as an increase of pulling velocity to 3.18 μm/s was sufficient to propagate morphological instability over more than half the observation window, i.e. ≈ 1.5 mm (Fig. 4b).

It should be mentioned that it is because morphological instability occurred in the transient following the increase in pulling velocity V [21, 22] that nonplanar features appeared first in the region of higher solute content and then progressively invaded regions impoverished in acetone as the effective growth velocity approached V.

3.3. Nonplanar patterns

3.3.1. Primary spacing

By using the weighted Wigner–Seitz construction (Fig. 6a), that was previously implemented for

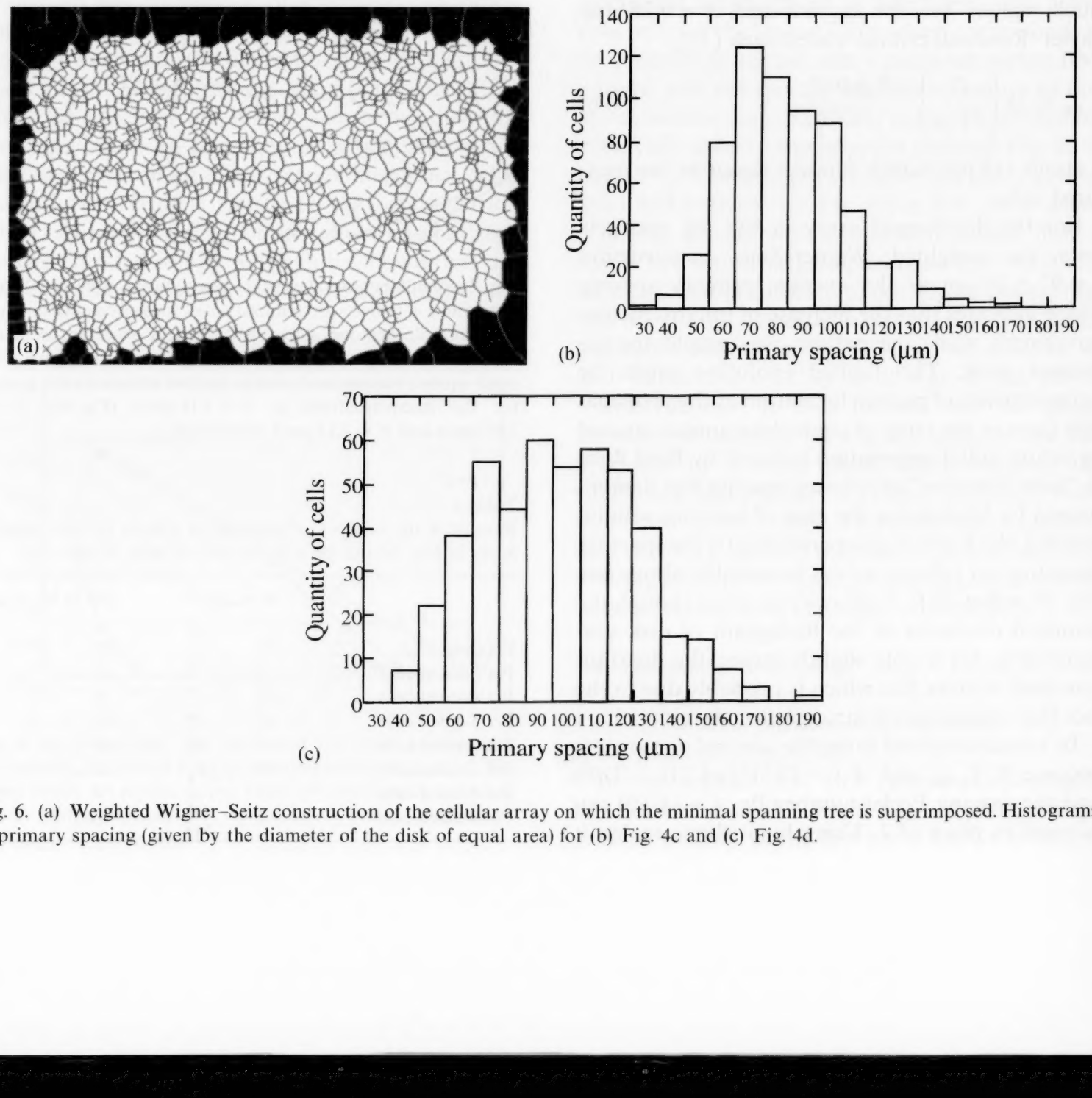

Fig. 6. (a) Weighted Wigner–Seitz construction of the cellular array on which the minimal spanning tree is superimposed. Histograms of primary spacing (given by the diameter of the disk of equal area) for (b) Fig. 4c and (c) Fig. 4d.

Pb–Tl alloys [4], and replacing each cell by a disk of equal area, we could determine from the histogram of the disk diameter (Fig. 6b) an average wavelength of instability, $\lambda_c = 80 \pm 23$ μm (where 23 μm is the standard deviation of the primary spacing distribution), using the results from Fig. 4c in which the spacing does not significantly evolve from the value at onset (visible in the lower right corner of the image). The critical wavelength $\lambda_{c,MS}$ at the threshold of instability under diffusive transport is predicted by the Mullins and Sekerka analysis [23] and, in the low velocity limit, can be calculated from

$$\lambda_{c,MS} = 2\pi \left[\frac{2\Gamma k D^2}{m(k-1)}\right]^{1/3} \frac{1}{C_\infty^{1/3}} \frac{1}{V_{c,MS}^{2/3}}, \tag{7a}$$

where Γ is the capillary constant. With $\Gamma = 6.6 \times 10^{-6}$°C cm, $\lambda_{c,MS}$ equals 460 μm, which is much higher. Yet, for $k_{eff} \approx k$ and $\Delta \approx 0.25$, the Favier–Rouzaud critical wavelength [14],

$$\lambda_{c,FR} \approx 2\pi \left[\frac{G}{\Gamma k_{eff}}\right]^{-1/6} \frac{\Delta D^{2/3}}{V^{2/3}}, \tag{7b}$$

is about 145 μm, which is much closer to the measured value.

For the developped array in Fig. 4d, one gets from the weighted Wigner–Seitz construction $\lambda = 92 \pm 28$ μm as the average primary spacing which indicates that the increase of microstructure wavelength while the pattern was amplifying remained weak. This limited evolution might be a consequence of pattern formation at the propagation front in the ramp of control parameter created by solute radial segregation induced by fluid flow, as "front selection" of primary spacing was demonstrated by Misbah for the case of rotating solidification [24]. From a comparison with the spacings measured on cellular arrays in metallic alloys (see Fig. 19 in Ref. [4]), it follows that, even though the standard deviation of the histogram of disk diameter (Fig. 6c) is only slightly larger, the distribution itself is more flat, which is probably due to the fact that convection is stronger in organic melts.

In nondimensional form, the control parameters become $V/V_{c,MS}$ and A ($= \Gamma k^2 V/(mC_\infty(k-1)D)$) and the spacing Peclet number Pe_λ ($= \lambda V/D$) can be used in place of λ. Using logarithmic scales, it was shown that the data points obtained under diffusive conditions on thin succinonitrile–acetone alloys separate into a cellular sheet and a dendritic sheet [25]. For $V = 3.2$ μm/s, $V/V_{c,MS} = 12.7$, $A = 1.3 \times 10^{-6}$ and $Pe_\lambda = 0.22$. In Fig. 7, the representative point is shifted to the right of the cellular sheet, which reflects the stabilizing effect of fluid flow for systems with $k < 1$, and falls below the dendritic sheet, which reflects the classical decrease of primary spacing under convective transport.

3.3.2. *Microstructure disorder*

The weighted Wigner–Seitz construction was also used to identify topological defects, i.e. cells with a number of sides different from 6, and carry out a statistical analysis of array disorder. It follows from Table 1 that the abundance is about the same

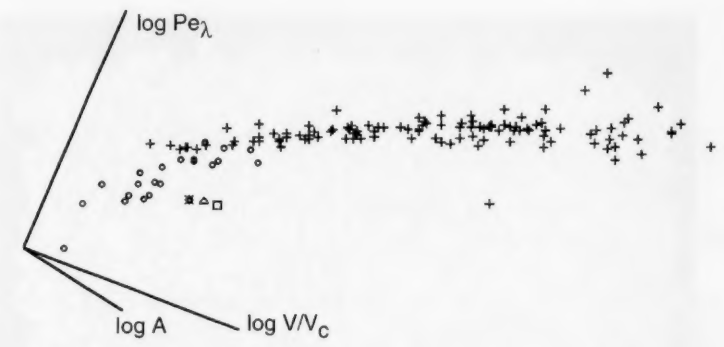

Fig. 7. Simultaneous sideview of the diffusive cellular (◦) and dendritic (+) sheets determined from measurements on thin succinonitrile–acetone alloys. After proper rotations of axes, these sheets are perpendicular to the plane of the figure. The open square, triangle and asterisc are the representative points for the microstructures at $V = 3.18$ μm/s (Fig. 4d), $V = 2.65$ μm/s and $V = 2.12$ μm/s respectively.

Table 1
Results of the analysis of topological defects for the cellular array in Fig. 4d and for a typical Pb–30 wt% Tl alloy [4].

	SCN-AC	Pb-Tl 30 wt%
Pct defects (d)	75	59
Pct 3-sided cells	4	1
Pct 4-sided cells	17	9
Pct 5-sided cells	27	23
Pct 6-sided cells	25	41
Pct 7-sided cells	18	22
Pct 8-sided cells	7	4
Pct 9-sided cells	2	0

for 4–7-sided cells, that conflicts with the results on Pb–Tl alloys which showed a peak of hexagonal cells and pentagons and heptagons as dominant defects.

By using the minimal spanning tree (MST) method, that provides evidence if there is order hidden behind disorder or not, the array arrangement was analysed in the (m, σ)-diagram (m and σ are, respectively, the normalized edgelength and standard deviation of the MST, an example of which is drawn in Fig. 6a). As well as that for the developing array in Fig. 4c (+), the representative point (△) of the cellular array in Fig. 4d falls on the trajectory joining the perfect honeycomb to the random distribution (Fig. 8), which is consistent with observation because in the pictures the gradient of primary spacing that accompanies the visible "gradient" of microstructure is very weak. As this trajectory was obtained by progressively randomizing the regular lattice giving each point a new position such that the distribution of the displacements from ideal positions be a Gaussian of increasing standard deviation [26], array disorder can once more be described as a Gaussian noise superimposed on an ideal array of hexagonal cells. Indeed, this result is similar to that obtained for Pb–Tl alloys [4] which, for the sake of comparison, are also plotted in Fig. 8. It can be shown that the fact that the succinonitrile-acetone data points are closer to the random distribution, as well as the increased flatness of the distribution of n-sided cells, is not due to stronger convection but merely stems from almost but not yet fully complete cell size adjustment.

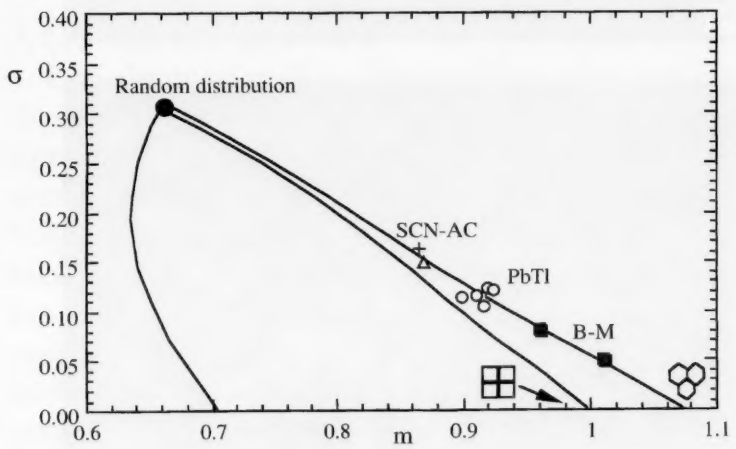

Fig. 8. (m, σ)-diagram. The cross and the open triangle are, respectively, calculated from the analysis of Fig. 4c and Fig. 4d. Open circles are representative points of directionally solidified Pb–Tl alloys. Squares are representative points of Bénard–Marangoni experiments.

Indeed, as they are also based on honeycombs and with less disorder, it is worth to moreover plot data points obtained for Bénard–Marangoni (BM) planforms [27]. Then, the global distortion of the patterns can be measured by the amount of Gaussian disorder introduced in the randomization process (see Fig. 4 in Ref. [26]). The standard deviation of the distribution of the shifts from the ideal positions equals 0.171 for succinonitrile-acetone, 0.132 for Pb–Tl, 0.078 and 0.045 for the BM-experiments and 0.467 for a pattern with σ equal to 90% of its value for the completely random structure. Although all these values are rather small, the basic hexagonal arrangement is detectable with naked eyes only for the lowest value which corresponds to an experiment started with a prepared perfect BM-pattern with the spacing selected by nature so that the dynamics were drastically reduced and the final state very close to the imposed one (see Fig. 6a in Ref. [27]). Visible order is lost for the other asymptotic BM-pattern (see Fig. 6d in Ref. [27]) which was also started with a prepared perfect honeycomb but with a larger spacing so that array dynamics to adopt the natural cell size on the average was important. Topological disorder is even larger and more striking in the SCN-AC arrays (Fig. 4d and Table 1, $d = 75\%$), as it was in the Pb–Tl microstructures. It thus follows that the larger amounts of disorder seen in the pictures are still produced by a small effect, which supports the conclusion that disorder is a highly nonlinear function of the cellular shifts. This observation explains why the MST method remains a sensitive detector to bring forward the underlying honeycomb even at large distances from the onset of instability.

3.4. Dynamical phenomena

3.4.1. Dynamical phenomena in the birth of morphological instability

In our experiments, two typical morphologies were observed in the initial steps of the development of instability. The first one is known as nodes,

or poxes, and is presented in the lower part of Fig. 9a. Nodes are rounded depletions that form over the solid–liquid interface, without any visible arrangement, and appear as dark dots when viewed from above.

On the one hand, Schaefer and Glicksman observed that the initiation of cellular or dendritic growth from such nodes was due to the presence of bits of particulate matter [3]. These particles, probably pushed by the solidification front as growth proceeded, locally retarded the interface and produced pits that acted as inherent finite-size perturbations for the triggering of instability. Also, since the solidification process is a source of acetone, which is a volatile substance, the origin of these nodes could be explained by acetone bubbles, whose formation in the succinonitrile-acetone system has been previously evidenced [28].

On the other hand, McFadden et al. [29] have computed three-dimensional solutions as bands and rectangular and hexagonal planforms. For an aluminum-chromium alloy, only hexagonal nodes are predicted near the onset of morphological instability when the temperature field is linear and surface tension isotropic, which is in agreement with experimental findings [30, 31]. Therefore, the situation is far from being definitely clear, since the possibility of the coexistence of particle-induced nodes with a genuine node microstructure cannot be completely ruled out. Yet, although the linear analysis of morphological instability does not depend on the sign of the perturbations so that projections into the liquid and solid depressions are a priori equivalent phenomena, we believe that the process was actually biased by impurities that were randomly distributed at the interface, in particular

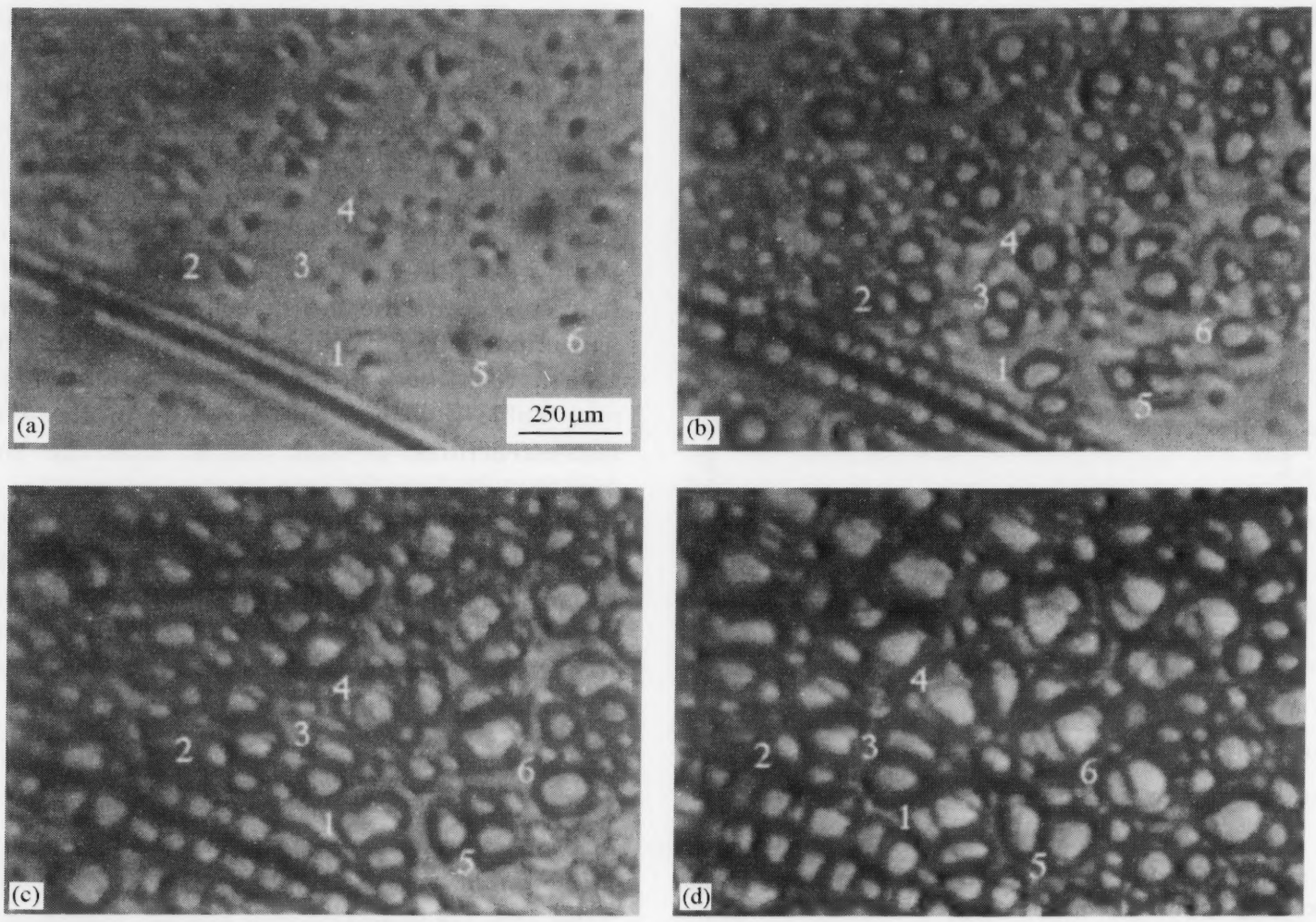

Fig. 9. (a) Nodes as origin of cells (t_0). (b) Annular ridges ($t_0 + 50$ s). (c) Breaking apart of the targets ($t_0 + 110$ s). (d) ($t_0 + 190$ s). $V = 2.12$ μm/s. We observed mainly single cells (4 and 6), cells growing by two (1 and 3) and by three (2 and 5).

because mottled features forming an array of shallow cells were observed at the junction with the smooth stable region in the established patterns, rather than an hexagonal distribution of nodes. Besides, it was shown by McFadden et al. [32] that a nonlinear temperature profile, which is more akin to the experimental situation, can lead to hexagonal cells even near the threshold.

In the second step, the formation of annular ridges around the nodes was observed (Fig. 9a and Fig. 9b). In the very beginning, the annular ridges evolved almost independently but, as soon as their circles of influence began to overlap they tended to behave in a cooperative way and some protrusions appeared in between them in order to fill with cells the remaining smooth interface. Rapidly, each annulus broke down into several pieces (Fig. 9b and Fig. 9c), among which one became dominant and screened the others (Fig. 9c and Fig. 9d). It is of value to note that the dominant projections remained prominent features in the ripened pattern (Fig. 9d), with the major disadvantage of hindering global ordering and the elimination of topological defects. The formation of leading projections might explain why seemingly uncorrelated groupings of dendrites were evidenced on metallic Al–Li alloys [33], all the more because Trivedi and Somboonsuk [34] found that the final spacing of dendrites was identical to that of the long wavelength perturbations which won in the initial transient by screening the short wavelength ones.

3.4.2. Cell size adjustment

Cell elimination (Fig. 10a and Fig. 10b) and cell division (Fig. 10c and Fig. 10d) processes were the operative mechanisms to achieve adjustment of cell size inside the cellular array. For directional solidification under diffusive conditions, it is now experimentally and theoretically established that, both for cells and for dendrites, there exists a band of stable primary spacings rather than perfect selection of a unique value [4, 21, 35]. Consequently, array evolution can be considered locally. The cells in a particular subarea should in principle cease to evolve as soon as they all get installed in the stable band. Yet, further changes with time remain possible as interaction between distant subareas, whose extent is hard to precisely define, can occur, with modifications in a given subarea being able to propagate step by step and eventually affect regions far away. Although convection acted to increase array disorder (see Fig. 8), it can be inferred that the coarsening instability still served to enter small cells from below into the band of allowed sizes. The motivation for the reverse process of cell division was to bring back cells above the stable band, because too large of a size was caught either in the initial transient of earlier competitive growth. In practice, modifications of the size of individual cells went together with some elimination of topological defects (Fig. 10).

As already stated, the average cell size was slightly increasing with time. For a given sampling window in the central part of the solid–liquid interface, this increase can be analysed at long times only because at short times the window was not entirely morphologically unstable (Fig. 11a). A least-squares fit in the form $\lambda^n - \lambda_0{}^n \propto t$ gives n about 10, whereas diffusion controlled coarsening would give 2 or 3 [36, 37]. Actually, a better fit was obtained in the form $\lambda - \lambda_\infty = (\lambda_0 - \lambda_\infty)\exp(-t/\tau)$, (Fig. 11a), from which 130 μm is obtained for the asymptotic average spacing λ_∞ and 660 s for the time constant, which is slightly more than twice the diffusion time ($D/V^2 = 290$ s). In their study of surface patterns in gels, Tanaka et al., who report a power-law variation with $n = 2$ at short times, associate the exponential approach at long times to the emergence of long range order in the building of the honeycomb-based array [38]. Our experiments sustain this conclusion as shown by the evolution of the representative point in the (m, σ)-plane (Fig. 11b), which indicates a convergence towards the line joining the honeycomb to the random distribution. This convergence is followed by a displacement down that line which betrays an improvement of array quality, to a level comparable to that of the Pb–Tl arrays plotted on Fig. 8. This improvement also manifests itself in the shrinkage and steepening of the distribution of n-sided cells (Fig. 11c). Once more, these last remarks stress the fact that slow array dynamics is the limiting process in the potential creation of a preferred pattern with weak spacing selection [39].

The general trends observed in the experiments are qualitatively very comparable to that obtained

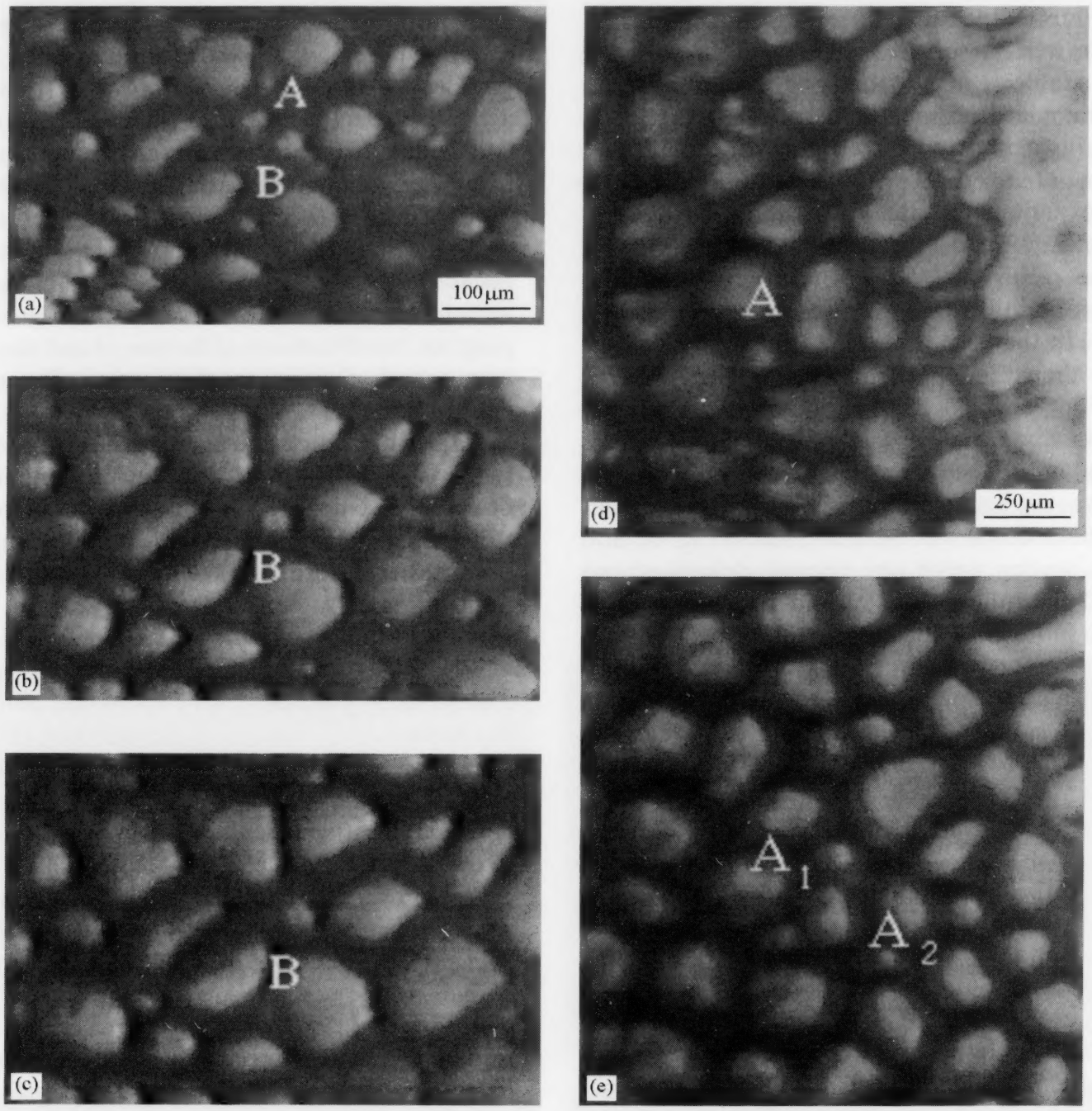

Fig. 10. Competition between cells and size adjustment. Cell elimination: (a) Two small cells surrounded by six larger neighbours, (b) Elimination of cell A, (c) Final image with a six-neighbour cell ($V = 2.12\ \mu m/s$). Cell division: (d), (e).

by numerical simulation in the high velocity limit [40] using an extension to the 3D case of the interface evolution equation derived by Kassner et al. for 2D-directional solidification [41]. Similarly, the array created during the first stages evolves with time from a highly disordered pattern to an array whose representative point in the (m, σ) diagram falls on the curve of the honeycombs disturbed by Gaussian noise.

4. Conclusions

The reported study focussed on the formation and emergence of a cellular interface during directional solidification of a transparent binary alloy in a cylinder, as the first step of a comprehensive programme incorporating deep cells and dendrites. All results show that the influence of convection was significant. In particular, we observed that

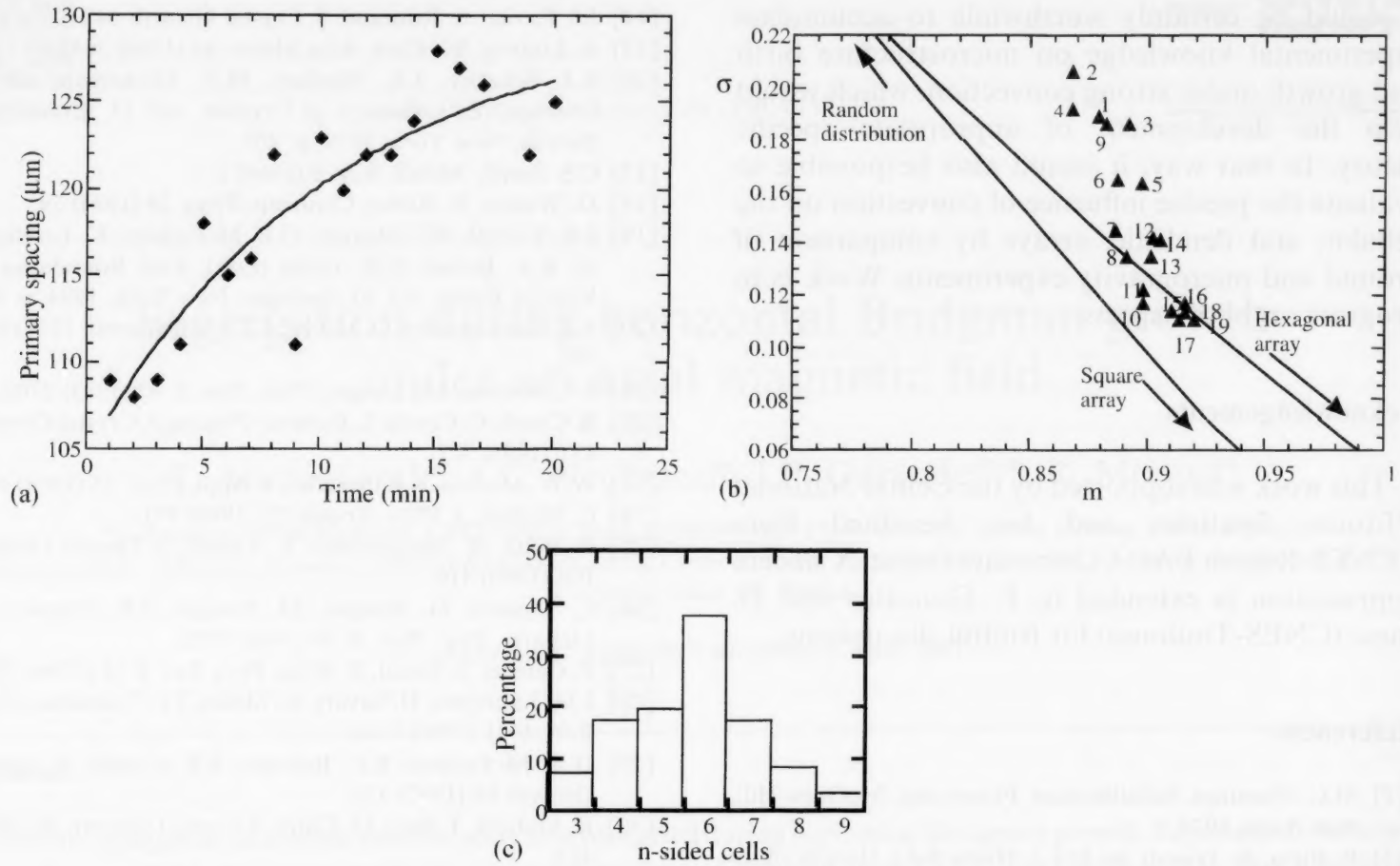

Fig. 11. (a) Cell size variation with time. (b) Evolution in the (m, σ)-plane. (c) Distribution of n-sided cells at the end of the process ($V = 2.12\ \mu m/s$).

the interface was nonhomogeneous from the point of view of its microstructure. By constructing a phenomenological model based on a boundary layer approach, it was possible to attribute the origin of that microstructure gradient to tangential fluid flow which created a ramp in the solute distribution at the growth front. Yet, it follows from both the evolution of primary spacing and the analysis of array disorder in the (m, σ)-diagram that the stable arrangement could still be described as a hexagonal array disturbed by Gaussian noise, whose magnitude is linked to dynamical phenomena in array formation. In the development of morphological instability, the emergence of cells was observed to happen in various groupings, which might provide an efficient way of triggering cellular multiplets in developed patterns [4]. Convection was also responsible for a smaller primary spacing compared to theoretical diffusive models.

Further experiments are obviously needed to get more systematic and more quantitative results and also to achieve longer times of growth. 3D-transparent systems, although they are the most convenient systems to carry out studies on thin samples, are probably a bad choice at 1 g to obtain sound results for comparison with the advanced and sophisticated theories that very generally assume diffusive transport. Nevertheless, 3D-transparent systems have the unique advantage of offering the only practical way for in situ and real-time analysis of the dynamics of formation and selection, if any or on the average, of characteristic shape parameters. On the one hand, dynamics in systems far from equilibrium has long been known to be far more rich in 3D than in 2D. Presently, in particular because there is no way to damp fluid flow in these materials (e.g. magnetic damping is available for metals), microgravity studies seem to be the only feasible way to reach that goal. On the other hand,

it would be certainly worthwhile to accumulate experimental knowledge on microstructure birth and growth under strong convection, which would help the development of appropriate specific theory. In that way, it would also be possible to evaluate the precise influence of convection on the cellular, and dendritic, arrays by comparison of ground and microgravity experiments. Work is in progress on both aspects.

Acknowledgements

This work was supported by the Centre National d'Etudes Spatiales and has benefited from a CNES-Région PACA Doctorate Grant. A sincere appreciation is extended to F. Gonzalez and D. Buso (CNES-Toulouse) for fruitful discussions.

References

[1] M.C. Flemings, Solidification Processing, McGraw-Hill, New York, 1974.
[2] B. Billia, R. Trivedi, in: D.T.J. Hurle (Ed.), Handbook of Crystal Growth. vol. 1B, Elsevier, Amsterdam, 1993, ch. 14.
[3] R.J. Schaefer, M.E. Glicksman, Met. Trans. 1 (1970) 1973.
[4] B. Billia, H. Jamgotchian, H. Nguyen Thi, Met. Trans. A 22 (1991) 3041.
[5] H. Jamgotchian, R. Trivedi, B. Billia, Phys. Rev. E 47 (1993) 4313.
[6] Q. Li, H. Nguyen Thi, H. Jamgotchian, B. Billia, Acta Metall. Mater. 43 (1995) 1271.
[7] K.A. Jackson, J.D. Hunt, Acta Metall. 13 (1965) 1213.
[8] M.A. Chopra, M.E. Glicksman, N.B. Singh, Met. Trans. A 19 (1988) 3087.
[9] M. Brissaud, C. Dolin, J. Le Duigou, B.S. McArdle, J.N. Sherwood, J. Crystal Growth 38 (1977) 134.
[10] A. Rivière, C. Marhic, M. Meyer, M. Lancin, Rev. Phys. Appl. 22 (1987) 221.
[11] R.H. McFee, J. Appl. Phys 40 (1969) 3873.
[12] M. Hennenberg, A. Rouzaud, D. Camel, J.J. Favier, J. Crystal Growth 85 (1987) 49.
[13] S.N. Tewari, M.A. Chopra, J. Crystal Growth 118 (1992) 183.
[14] J.J. Favier, A. Rouzaud, J. Crystal Growth 64 (1983) 367.
[15] A. Ludwig, W. Kurz, Acta Mater. 44 (1996) 3643.
[16] R.J. Schaefer, J.A. Blodgett, M.E. Glicksman, in: A. Chernov (Ed.), Growth of Crystals, vol. 11, Consultant Bureau, New York, 1979, p. 207.
[17] C.S. Smith, Metall. Rev. 9 (1964) 1.
[18] D. Weaire, N. Rivier, Contemp. Phys. 25 (1984) 59.
[19] S.R. Coriell, B.T. Murray, G.B. McFadden, K. Leonartz, in: R.A. Brown, S.H. Davis (Eds.), Free Boundaries in Viscous Flows, vol. 61, Springer, New York, 1994, p. 99.
[20] A.G. Ostrogorsky, G. Müller, J. Crystal Growth 121 (1992) 587.
[21] J.A. Warren, J.S. Langer, Phys. Rev. E 47 (1993) 2702.
[22] B. Caroli, C. Caroli, L. Ramirez-Piscina, J. Crystal Growth 132 (1993) 377.
[23] W.W. Mullins, R.F. Sekerka, J. Appl. Phys. 35 (1964) 444.
[24] C. Misbah, J. Phys. France 50 (1989) 971.
[25] B. Billia, H. Jamgotchian, R. Trivedi, J. Crystal Growth 106 (1990) 410.
[26] C. Dussert, G. Rasigni, M. Rasigni, J.P. Palmari, A. Llebaria, Phys. Rev. B 34 (1986) 3528.
[27] P. Cerisier, S. Rahal, B. Billia, Phys. Rev. E 54 (1996) 3508.
[28] J.M. Laherrere, H. Savary, R. Mellet, J.C. Toledano, Phys. Rev. A 41 (1990) 1142.
[29] G.B. McFadden, R.F. Boisvert, S.R. Coriell, J. Crystal Growth 84 (1987) 371.
[30] K. Shibata, T. Sato, G. Ohira, J. Crystal Growth 44 (1978) 419.
[31] M.A. Audero, H. Biloni, J. Crystal Growth 18 (1973) 257.
[32] G.B. McFadden, S.R. Coriell, R.F. Sekerka, J. Crystal Growth 91 (1988) 180.
[33] H. Nguyen Thi, Q. Li, B. Billia, D. Camel, B. Drevet, J.J. Favier, in: P.R. Sahm, M.H. Keller, B. Schiewe (Eds.), Scientific Results of the German Spacelab Mission D2, DLR, Köln, Germany, 1995, p. 379.
[34] R. Trivedi, K. Somboonsuk, Acta Metall. 33 (1985) 1061.
[35] S. Lu, J.D. Hunt, J. Crystal Growth 123 (1992) 17.
[36] J.W. Martin, R.D. Doherty, Stability of Microstructure in Metallic Systems Cambridge Univ. Press, Cambridge, 1976, ch. 4.
[37] W.J. Boettinger, P.W. Woorhees, R.C. Dobbyn, H.E. Burdette, Met. Trans. A 18 (1987) 487.
[38] H. Tanaka, H. Tomita, A. Takasu, T. Hayashi, T. Nishi, Phys. Rev. Lett. 68 (1992) 2794.
[39] M.C. Cross, P.C. Hohenberg, Rev. Mod. Phys. 65 (1993) 851.
[40] K. Kassner, J.M. Debierre, unpublished.
[41] K. Kassner, C. Misbah, H. Müller-Krumbhaar, A. Valance, Phys. Rev. E 49 (1994) 5477.

ELSEVIER

Journal of Crystal Growth 181 (1997) 133–144

JOURNAL OF CRYSTAL GROWTH

Segregation during horizontal Bridgman growth under an axial magnetic field

T. Alboussière[1,a], A.C. Neubrand[b], J.P. Garandet[b,*], R. Moreau[a]

[a] *Laboratoire EPM-Madylam, CNRS UPR A 9033, ENSHMG, BP 95, F-38402 St. Martin d'Hères Cedex, France*

[b] *Commissariat à l'Énergie Atomique, DTA/CEREM/DEM/LRBS, Centre d'Études Nucléaires de Grenoble, 17 avenue des Martyrs, F-38054 Grenoble Cedex 09, France*

Received 11 April 1997; accepted 11 April 1997

Abstract

Solute segregation in a dilute metallic alloy is investigated during horizontal Bridgman growth. Experiments have been carried out under a permanent uniform axial magnetic field of intensity up to 1.35 T. The field is seen to have a moderate effect on axial segregation. A 2D model for segregation is presented and solved both numerically and in terms of order of magnitude analysis. Accounting for the measurement errors and the 2D nature of the analysis, a good agreement is obtained with the experimental results. The theoretical analyses exhibit a critical value for the magnetic field intensity. Below, the magnetic field has no effect on solute segregation, while above, the effective partition ratio is increasing with increasing magnetic field intensity.

Keywords: Dopant segregation; Bridgman method; Mass transport; Magnetohydrodynamics; Experiments; Order of magnitude analysis

1. Introduction

It is well known that a permanent magnetic field has the effect of reducing the strength of thermogravitational convection in metal melts during solidification. In that respect, magnetic damping and microgravity are two interesting possibilities for reducing fluid velocity in an experiment. In crystal growth, an optimal compositional homogeneity in the resulting solid is observed under diffusive solute transport conditions. Such a result is interesting for doped semi-conductors since they are electrically conducting in the liquid phase and since a high homogeneity is required for electronic or opto-electronic applications. Some studies already report the effectiveness of a steady magnetic field. Hurle et al. [1] use a steady magnetic field to

* Corresponding author. Fax: + 33 476 885117.

[1] Present address: Engineering Department, Cambridge University, Trumpington Street, Cambridge CB2 1PZ, UK.

0022-0248/97/$17.00 © 1997 Elsevier Science B.V. All rights reserved
PII S0022-0248(97)00275-3

stabilize turbulence and hence to eliminate striations, Vives and Perry [2] study the magnetic damping effect on convection during solidification while Matthiesen et al. [3] show experimentally a reduction of the axial segregation, with a strong axial magnetic field during vertical Bridgman growth.

The purpose of this paper is to quantify and model the influence of an axial uniform magnetic field on segregation during alloy solidification in the horizontal Bridgman method. We performed experimental metallic alloy solidifications under different magnetic field intensities and the results are reported here in terms of the effective partition ratio deduced from concentration measurements in the resulting solid. In parallel, we propose a coupled order of magnitude analysis /numerical modelling of the transport phenomena in the melt. To do so, we first study the thermogravitational motion under a magnetic field in the horizontal Bridgman configuration and then focus on the effect of such a flow on segregation. Our model is limited to the dilute alloys to avoid studying the coupling effect of concentration on buoyancy.

Section 2 is devoted to a presentation of our experimental work in terms of growth conditions and results. In Section 3 the MHD liquid flow is analyzed and an order of magnitude analysis is built to estimate segregation. Direct numerical simulations of segregation are also carried out. Finally, the results of these analyses are compared with the experiments.

2. Experimental procedure

2.1. BRAHMS

An experimental device, called BRAHMS (Bridgman related apparatus for hydrodynamic and magnetic studies) was designed for the purpose of horizontal Bridgman growth under an axial magnetic field (see Fig. 1). In our experiments, a metallic alloy Sn–Bi (0.13 or 0.05 at.% Bi) was chosen. This low composition allows us to neglect any solute buoyancy effect, as will be shown in Section 3.1, and also postpones growth interface destabilization. The diameter of the sample was 6 mm – the sample itself being contained in a quartz crucible ($\phi_{int} = 6$ mm, $\phi_{ext} = 10$ mm) – while the directionally solidified length reached 20 cm. Well-controlled experimental conditions were specified: the value of the axial temperature gradient is 24 K cm^{-1} in the melt with uniformity better than 5% from the interface to 12 cm further. The Bitter coil produces a maximum magnetic field

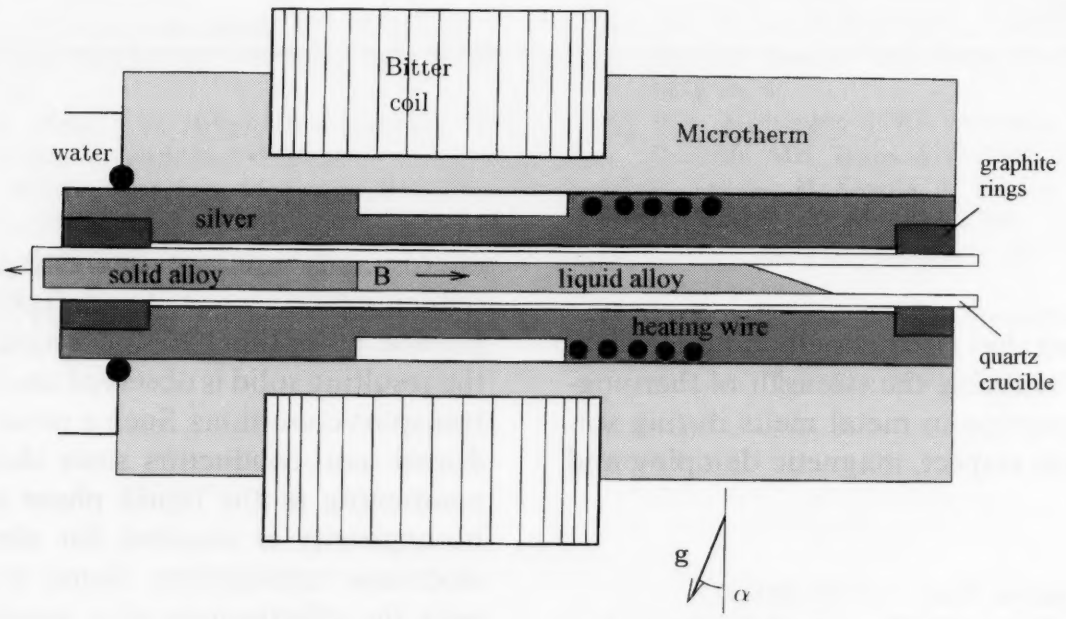

Fig. 1. General view of BRAHMS.

magnitude of 1.35 T; the intensity variation is less than 10% from the interface to 8 cm apart. The crucible and sample were pulled by a step by step motor: each step corresponds to a 0.1 μm axial displacement, and is itself divided in ten, possibly unequal,"micro-steps". The investigated pulling rates range from 2.5 μm s^{-1} to 10 μm s^{-1}.

The thermal principle of BRAHMS is simple and efficient in producing an almost purely axial temperature gradient. The key point is that the sample and crucible are surrounded by a silver tube. Silver has the highest thermal conductivity among metals: 400 W m^{-1} K^{-1} in our working temperature range. Indeed, for a given axial thermal gradient, the axial heat flux is drastically enhanced and makes thus negligible the radial heat losses (which only depend on the insulating material and temperature difference between the external air and the tube). As a result, the temperature gradient is almost axial in the silver. Nevertheless, the question remains of radial heat exchanges between the sample and the silver tube: these exchanges have to be minimized to achieve an axial thermal gradient in the sample. When these exchanges are zero, the axial heat flux in the sample is constant along the axis, since convection heat transport can safely be neglected in liquid tin, that has a Prandtl number of 0.013. Conservation of the heat flux at the interface implies that the axial temperature gradient is twice higher in the liquid than in the solid since the ratio of the thermal conductivity of solid to that of liquid tin is about two. Conversely, if the axial heat conductance of the silver tube mimics that of the sample, no radial heat exchanges will develop. This condition is achieved when the silver cross-section ratio is two between the solid and the liquid sample region (see Fig. 1). The axial temperature gradient (24 K cm^{-1}) is created by heating wires in the hot part, with a 600°C temperature regulation (Eurotherm 818P4) and by a cold water flow in the other side (regulation: $T_{water} = 20°C$). A micro-porous insulating material (Microtherm) has been used outside the silver tube. It has a very low thermal conductivity, from 0.015 W m^{-1} K^{-1} at 20°C to 0.03 W m^{-1} K^{-1} at 500°C.

The thermal core of BRAHMS (the silver tube with its insulating material) has a 50 mm diameter. The smaller this diameter is, the higher can be the magnetic field intensity generated by the coil. In a Bitter coil, instead of winding a wire, the electric circuit is made of a pile of copper annular disks separated by thin electrically insulating Kapton disks. A small sector is cut off in each copper disk while a 20° sector is cut off in each Kapton disk. The electrical current path is controlled by imposing a 20° angular rotation from one copper disk to another, the contact being made through the cut-off sector of the Kapton disk. In order to improve the magnetic field uniformity, the current density can be adjusted by grouping some copper disks in parallel near the ends of the coil. As shown in Fig. 1, this was done in our experimental device. All the disks contain a large number of holes (about 300, $\phi = 1.25$ mm), precisely aligned and forming ducts, where the cooling water can flow. The exchange surface between water and copper is very large, and the pressure loss minimized. From an electrical point of view, a Bitter coil is an optimum solution: first the copper volume fraction is more than 90%, and second the induced 1/r current density distribution renders maximum the ratio of the magnetic field intensity to the electric power needed. We obtain 1.35 T with 90 kW.

Its orientability with respect to gravity is another feature of BRAHMS. As our crucibles were open at the hot side, a 15° angle with the horizontal had to be maintained to prevent molten tin to flow out of the crucible. In fact, as the temperature gradient is almost axial, the buoyant driving force is proportional to the part of gravity orthogonal to the axis (otherwise stated, only the curl of the buoyant force density produces motion).This has been used to simulate a smaller gravity, by varying the inclination of BRAHMS ($\alpha = 15°$, 60° and 75°, see Fig. 1).

2.2. Experimental results

The results of our experiments are related to the axial solute segregation in the solidified sample. This axial segregation is expressed classically as an effective partition ratio k^* (see, Ref. [4]). This effective partition ratio ranges from one for purely diffusive conditions to the equilibrium partition coefficient k for a perfect solute mixing in the liquid phase (in the case of dilute Bi in Sn, $k = 0.26$). The effective partition ratio is assumed constant during

solidification when the solidification parameters are unchanged. After some initial transient, the Scheil law, derived in the perfect mixing case, still applies when replacing k by k^* [5]

$$c_s(f_s) = k^* c_0 (1 - f_s)^{(k^* - 1)}. \quad (1)$$

The symbols c_s, f_s, c_0 denote the mean solute concentration in a solid cross section, the solidified fraction and the initial liquid composition, respectively. Even in an extreme case scenario of purely diffusive mass transfer, the length of the initial transient would not exceed 5 mm for the slowest growth velocity of 2.5 μm s^{-1}. Only a small portion of the 20 cm long samples has to be discarded. In each solidified sample, seven sections are cut out and sent for analysis by the ICP-AES (inductively coupled plasma atomic emission spectroscopy) method: more precisely, at each of the seven positions, two neighbouring 3 mm long samples are analyzed. The mean of both values is recorded, while their difference is characteristic of the measurement uncertainty. The result consists in seven values of c_s for seven different solidified fractions f_s and the measured mean composition of the remaining part of the sample after the directionally solidified part. We adjust k^* and c_i for the Scheil law (1) to best fit these experimental data, using a least square method (see example in Fig. 2). In this example, the directionally solidified length is 193 mm and the total initial liquid sample length is 330 mm. The circles denote the measured concentration values and the full-line curve corresponds to the best fit using a Scheil law (1).

This experimental determination of k^* is performed for several conditions. Our working parameters are the growth rate V_i, the magnetic field intensity B and the tilt angle α of the sample with respect to the horizontal. They act through three non dimensional numbers (see Section 3), namely the solidification Péclet number Pe, the Hartmann number Ha and the product of the Grashof number with the Schmidt Number Gr Sc, defined

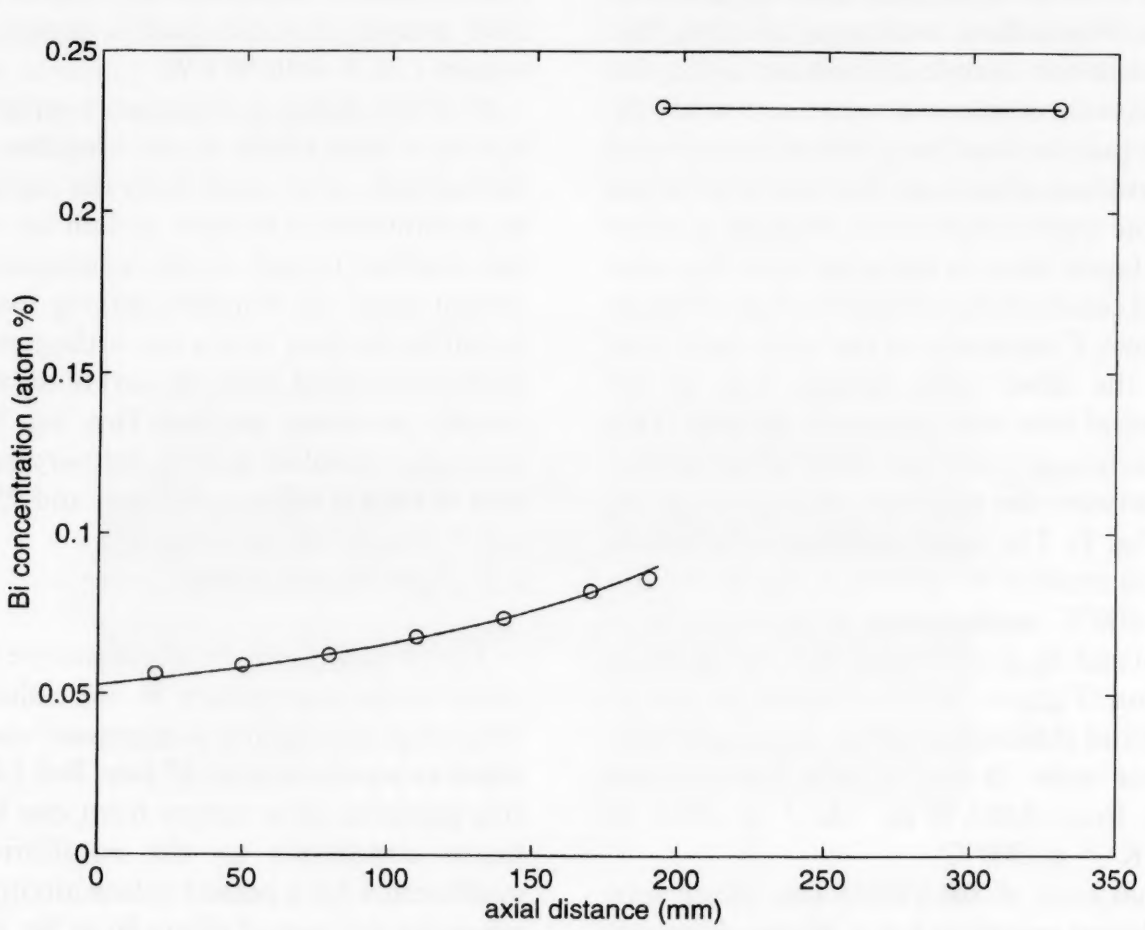

Fig. 2. Example of measured Composition data and fitting procedure for the case Gr Sc = 9.2×10^6, Pe = 23 and Ha = 66.

here as

$$\mathrm{Pe} = \frac{V_i H}{D}, \quad \mathrm{Ha} = \sqrt{\frac{\sigma}{\rho \nu}} BH, \quad \mathrm{Gr} = \frac{\beta g \cos\alpha \, GH^4}{\nu^2},$$

$$\mathrm{Sc} = \frac{\nu}{D}, \tag{2}$$

where H, D, β, g, G, σ, ρ and ν denote the sample diameter (6 mm in our experiments), the solute diffusivity of Bi in liquid Sn, the thermal volume expansion coefficient of liquid tin, earth gravity, the axial thermal gradient (2400 K m^{-1} in our experiments), the electrical conductivity, density and kinematic viscosity of liquid tin (see Table 1 for the physico-chemical properties of dilute SnBi). The Schmidt number Sc only depends on the alloy. Its value, Sc = 200 indicates that solute diffusivity is small compared to kinematic viscosity, a very common feature of metals and semi-conductors. The Hartmann number, scaling the electromagnetic effects on the fluid motion in comparison with viscosity, reaches the maximum value 270 in our experiments when $B = 1.35$ T. In principle, one should also account for solutal buoyancy *via* a solutal Grashof number, but an analysis of the orders of magnitude presented in the next section shows that the thermal buoyancy effect is dominant.

Our results are summarized in Tables 2 and 3. In Table 2, the solidification Péclet number Pe is fixed to 23 (5 μm s^{-1} in our experiments) and three values of the product Gr Sc are investigated (corresponding to the tilt angles $\alpha = 15°$, 60° and 75°).

Table 1
Properties of liquid Sn–Bi dilute alloy. The solute diffusivity and equilibrium partition ratio result from the MEPHISTO space experiments [6]

Symbol	Description	value
T_m	Melting temperature	232°C
ρ	Density	7000 kg m^{-3}
β	Thermal expansion	1.06×10^{-4} K^{-1}
ν	Kinematic viscosity	2.6×10^{-7} m^2 s^{-1}
σ	Electrical conductivity	2.12×10^6 Ω^{-1} m^{-1}
α	Thermal diffusivity	2×10^{-5} m^2 s^{-1}
D	Solute (Bi) diffusivity	1.3×10^{-9} m^2 s^{-1}
κ	Equilibrium partition ratio	0.26

Table 2
Effective partition coefficient for Pe = 23

Gr Sc = 9.2×10^6		Gr Sc = 4.8×10^6		Gr Sc = 2.5×10^6	
Ha	k^*	Ha	k^*	Ha	k^*
		0	0.45	0	0.52
33	0.37	33	0.5		
66	0.39	66	0.44	66	0.69
135	0.41	135	0.5	135	0.79
270	0.44	270	0.56	270	0.82

Table 3
Effective partition coefficient for Gr Sc = 9.2×10^6

Pe = 11.5		Pe = 23		Pe = 46	
Ha	k^*	Ha	k^*	Ha	k^*
0	0.32			0	0.58
33	0.33	33	0.37		
66	0.3	66	0.39	66	0.59
135	0.31	135	0.41	135	0.7
270	0.35	270	0.44	270	0.72

Let us first indicate that, due to composition measurement uncertainty and to the least square method used, the estimated precision for these values of k^* is about ± 5% (see Ref. [7] for more details). As expected, it can be seen that the effective partition ratio increases either for increasing Péclet number or decreasing Gr Sc product (see, e.g., Ref. [8]). Moreover, it is here demonstrated a slight increase of this effective partition ratio with increasing the Hartmann number. If the braking electromagnetic effect is to reduce convection, one should not be surprised with this result. This effect is very small for Hartmann numbers up to 66 and more significant for the highest values (135 and 270). It also appears that the effect of the magnetic field occurs for a smaller Ha value in the case of the smallest Gr Sc product (see Table 2, Gr Sc $= 2.5 \times 10^6$). The values included in a box correspond to experiments for which growth interface destabilization occurred. After solidification, micrographs in a cross-section showed the so-called "poxes". This change in the solidification pattern is accompanied by a kind of "saturation" of the effective partition ratio with respect to the

Hartmann number (see Table 3, Pe = 46). Destabilized growth interfaces are out of the scope of this study, but we can conjecture that axial macrosegregation becomes less sensitive to convection in this regime.

3. Analysis of segregation

If solutal buoyancy can be neglected (the dilute alloy approximation will be discussed in the next paragraph), it is licit to determine first the liquid flow under the influence of thermal buoyancy and an axial magnetic field. The velocity field will then be used as an input in the segregation analysis.

3.1. Analysis of the buoyant MHD flow during solidification

The geometry and conditions for the flow are modeled as shown in Fig. 3. The cavity is a semi-infinite horizontal cylinder with an axial uniform temperature gradient and magnetic field. The magnetic field can safely be assumed undisturbed and we also expect inertial effects to play a negligible role. Indeed, our values for the Grashof number range from 1.24×10^4 to 4.62×10^4. In a cavity with a square cross-section and a length over height aspect ratio of four, Pratte and Hart [9] found experimentally a critical Grashof number of 2×10^5 for the onset of oscillations (they used mercury: Pr = 0.026). In the same configuration, Afrid and Zebib [10] found numerically a critical Grashof number equal to 1.25×10^5 (they assumed a zero Prandtl number). Below this critical value, the flow is steady and the effect of inertia essentially consists in tilting the recirculation loop. Under a magnetic field, the flow is efficiently damped and inertia becomes totally negligible (see Refs. [11, 12]). Using the Boussinesq approximation, two steady governing equations can be written for the divergence-free velocity and electric current density fields, $\boldsymbol{u}$ and $\boldsymbol{j}$ (see Ref. [13]), Ohm's law and the momentum equation:

$$\boldsymbol{j} = \sigma(-\nabla\varphi + \boldsymbol{u} \wedge \boldsymbol{B}), \tag{3}$$

$$\boldsymbol{0} = -\nabla p + \boldsymbol{j} \wedge \boldsymbol{B} - \rho\beta(T - T_0)\boldsymbol{g} - \rho\beta_c(c - c_0)\boldsymbol{g} + \rho\nu\Delta\boldsymbol{u}, \tag{4}$$

where φ and p denote the electric potential and pressure fields respectively, T the temperature field, T_0 a reference temperature (the growth interface temperature for instance), c the composition field, c_0 a reference composition (the initial liquid mean composition for instance) and β_c the solute expansion coefficient. Assuming, as checked in our experiments, a uniform temperature gradient, the relation $T - T_0 = Gz$ holds.

We now estimate the relative strength of thermal and solutal buoyancy forces in the absence of

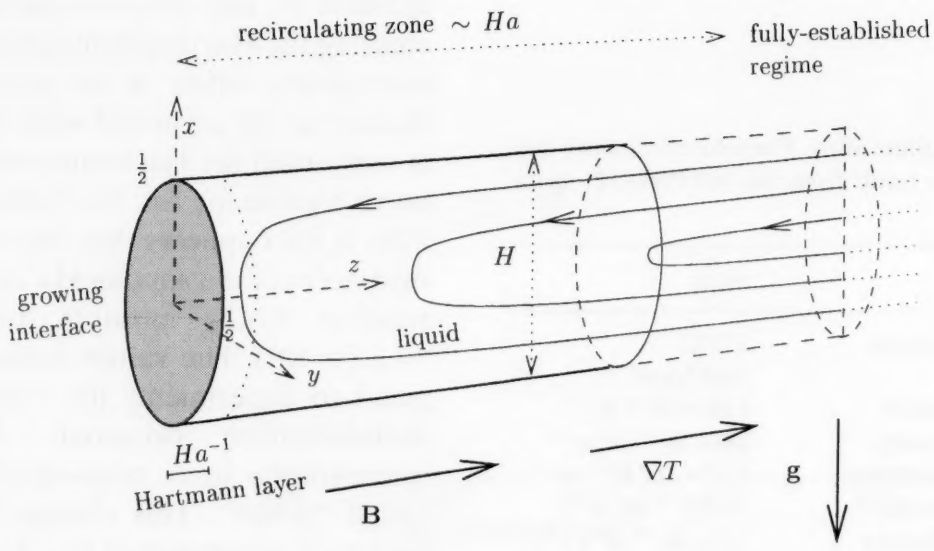

Fig. 3. Flow configuration.

magnetic field. Let us consider the effect of thermal buoyancy alone: the curl of the Navier–Stokes equation can be written,

$$\boldsymbol{0} = -\rho\beta\nabla T \wedge \boldsymbol{g} + \rho\nu\boldsymbol{\Delta}(\mathrm{curl}\,\boldsymbol{u}). \tag{5}$$

The velocity varying over a length scale H, this equation provides us with the following magnitude order,

$$u_T \sim \beta g G \frac{H^3}{\nu}. \tag{6}$$

The same estimate can be found for the velocity induced by solutal buoyancy alone, H being replaced by d, the solute layer typical thickness,

$$u_c \sim \beta_c g \nabla c \frac{d^3}{\nu}. \tag{7}$$

Now, it is important to compare both velocity field at the same location, in the solute boundary layer. The estimate for u_c Eq. (7), satisfies to this condition but not that for u_T, which is estimated at the typical distance H from the growth interface; Eq. (6) must be multiplied by d/H. The ratio of this two contributions is,

$$\frac{u_c(d)}{u_T(d)} \sim \frac{\beta_c \nabla c\, d^2}{\beta G\, H^2}. \tag{8}$$

Anticipating on the analysis in Section 3, the composition gradient at the interface is $V_i/D(1-k)c_i$ from the solute rejection condition, where k, V_i and c_i denote the equilibrium coefficient, growth velocity and composition in the liquid at the interface. An upper bound of the boundary layer thickness d is D/V_i, for the purely diffusive case. Then Eq. (8) takes the form,

$$\frac{u_c(d)}{u_T(d)} \sim \frac{\beta_c(1-k)c_i D}{\beta G H^2 V_i}. \tag{9}$$

The solute expansion coefficient for SnBi is $\beta_c = 0.3$. For our smallest growth velocity $V_i = 5\ \mu\mathrm{m\ s}^{-1}$, and with a maximum 10^{-2}Bi mass composition (c_0/k in the diffusive case), the estimate of Eq. (9) leads to,

$$\frac{u_c(d)}{u_T(d)} \sim 5 \times 10^{-2}.$$

It is licit to drop the solute buoyancy term in Eq. (4). Moreover, as our experiments are found to be far from the purely diffusive case, the contribution of solutal convection is smaller than suggested by the above estimate.

These governing Eqs. (3) and (4) are now written in a non dimensional form, using H, B, D/H, $D\sigma B/H$, DH and $\rho Dv/H^2$ as references for length, magnetic field, velocity, electric current density, electric potential and pressure:

$$\boldsymbol{j} = -\nabla\varphi + \boldsymbol{u} \wedge \boldsymbol{B} \tag{10}$$

$$\boldsymbol{0} = -\nabla p + \mathrm{Ha}^2\, \boldsymbol{j} \wedge \boldsymbol{B} + \mathrm{Gr\,Sc}\, z\boldsymbol{e}_x + \boldsymbol{\Delta u}, \tag{11}$$

where the same symbols have been used for non-dimensional variables. The non-dimensional parameters Gr Sc and Ha appear in these equations, while Pe is still hidden. The Péclet number Pe will intervene, when the growth rate will be considered: in our non-dimensional system, the pulling rate $-\mathrm{Pe}\,\boldsymbol{e}_z$ shall be added to the velocity field $\boldsymbol{u}$ in order to get the velocity field expressed in a coordinate system moving with the interface (see Section 3.2). In the following, only dimensionless quantities will be used.

From Eq. (10) and Eq. (11), a differential operator governing the velocity field can be derived, that helps finding the principal features of the buoyant flow. The curl operator has to be applied twice to Eq. (11) and once to Eq. (10). Direct substitution (see the detailed calculation in Ref. [14] or [15]) then leads to:

$$\mathrm{Ha}^2 \frac{\partial^2 \boldsymbol{u}}{\partial z^2} = \boldsymbol{\Delta}^2 \boldsymbol{u}. \tag{12}$$

Based on Eq. (12), three main regions (see Fig. 3) can be identified in the cavity:

- Hartmann layer: if a boundary layer develops near the solid-liquid interface, its thickness δ_{Ha} leads to the estimates $\partial^2/\partial z^2 \sim 1/\delta_{\mathrm{Ha}}^2$ and $\boldsymbol{\Delta}^2 \sim 1/\delta_{\mathrm{Ha}}^4$. Eq. (12) leads then to the classical Hartmann boundary layer thickness (see Ref. [13]) $\delta_{\mathrm{Ha}} \sim \mathrm{Ha}^{-1}$.
- Recirculating zone: it is well known that Hartmann layers can not admit a significant flow rate [13], while it is obvious that far from the interface, a fully established parallel flow exists without influence of the magnetic field

($\boldsymbol{u} \wedge \boldsymbol{B} = \boldsymbol{0}$). If we look for a recirculating lengthscale L larger than the diameter (1 in our non-dimensional reference), the bi-Laplacian operator scales as 1 while the operator $\partial^2/\partial z^2$ scales as L^{-2}. Eq. (12) leads to $L \sim \mathrm{Ha}$.

- Fully established regime: from the above results, we can deduce that for $z \gg \mathrm{Ha}$, the expected fully established parallel flow exists.

Starting from this organization, the velocity magnitude order can be estimated in the different regions:

- Fully established regime: the flow is purely axial and viscous ($u_x = 0$ and scales as $u_z \sim \mathrm{Gr\,Sc}$, independent of Ha).
- Recirculating zone: by continuity, taking into account the relation $L \sim \mathrm{Ha}$, the vertical component of the velocity field scales as $u_x \sim \mathrm{Gr\,Sc/Ha}$ and the axial component as $u_z \sim (\mathrm{Gr\,Sc/Ha})z^2$.
- Hartmann layer: in this region the vertical component of the velocity reaches zero through the Ha^{-1} thickness, $u_x \sim \mathrm{Gr\,Sc}\, z$. Continuity on the Hartmann layer typical thickness then leads to $u_z \sim (\mathrm{Gr\,Sc/Ha})z^2$.

In order to obtain more precise informations on the velocity field, we now turn to a 2D model, which will also be used for segregation analysis (see Section 3.2). It is assumed that the features of the 3D flow are well described if the analysis is restricted to the vertical axial mid-plane $y = 0$. The cylindrical shape is replaced by the condition $\partial/\partial y = 0$. It can be proved (see Ref. [16]) that the electric potential is zero everywhere, such that Ohm's law takes a simplified form: $\boldsymbol{j}$ is purely directed along y and $j_y = -u_x$. The 2D equations have then been solved using a Fourier expansion analysis. The coefficients were calculated numerically so that boundary conditions are fulfilled ($\boldsymbol{u} = \boldsymbol{0}$). We shall not write here this exact 2D solution, which would require tedious and uninteresting calculations [15]. Suffice it to say that the above-mentioned features described for the 3D cylinder are present (Hartmann layer, recirculating region and fully- established regime). We also derived a simple approximate expression (a few percents departure from the exact solution), for high Hartmann numbers and in the vicinity of the solid-liquid interface, to be used in the order of magnitude analysis of the segregation problem (Section 3.2.2).

If the Hartmann layer is ignored, the velocity field approximates as:

$$u_z = \frac{8\mathrm{Gr\,Sc}}{9\mathrm{Ha}}(-zx + 4zx^3), \tag{13}$$

$$u_x = -\frac{\mathrm{Gr\,Sc}}{18\mathrm{Ha}}(1 - 8x^2 + 16x^4). \tag{14}$$

To take into account the Hartmann layer, the approximate velocity field has to be changed in (see Ref. [14]):

$$u_z = \frac{8\mathrm{Gr\,Sc}}{9\mathrm{Ha}}[-zx + 4zx^3] + \frac{8\mathrm{Gr\,Sc}}{9\mathrm{Ha}^2}[x - 4x^3](1 - \mathrm{e}^{-\mathrm{Ha}\, z}), \tag{15}$$

$$u_x = -\frac{\mathrm{Gr\,Sc}}{18\mathrm{Ha}}[1 - 8x^2 + 16x^4](1 - \mathrm{e}^{-\mathrm{Ha}\, z}). \tag{16}$$

3.2. Analysis of the axial segregation

3.2.1. Numerics

In the quasi-steady approximation, using c_∞ (the composition far from the interface, or mean liquid composition) as a reference for the concentration field, the equation governing concentration in the liquid takes the form:

$$\boldsymbol{u} \,.\, \nabla c - \mathrm{Pe}\frac{\partial c}{\partial z} = \Delta c. \tag{17}$$

Moreover, the boundary conditions consist in a zero normal solute flux at the crucible boundaries ($\partial c/\partial n = 0$), $c = 1$ far from the solidification front and the solute rejection at the interface ($z = 0$):

$$c(1 - k)\mathrm{Pe} = -\frac{\partial c}{\partial z}. \tag{18}$$

It is well known that the solute concentration field forms a boundary layer near the interface and tends towards a uniform composition outside. We will only consider cases for which this solute layer is smaller than the sample diameter. This is the reason why we restricted the numerical calculations to the rectangle of aspect ratio 2 shown in Fig. 4. Nevertheless, the velocity field can not be considered as fully established at the distance 2 from the interface

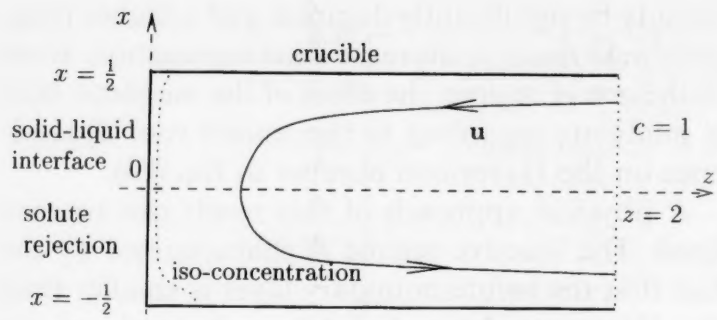

Fig. 4. 2D cavity, for numerical calculations.

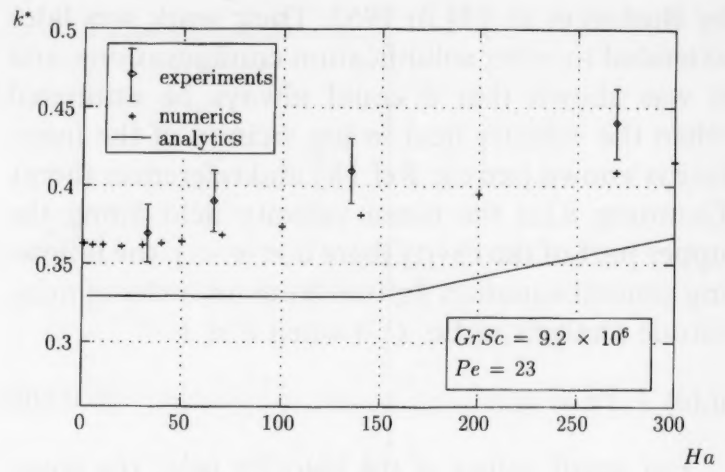

Fig. 5. Comparison between experimental numerical and analytical results.

and is calculated for a semi-infinite cavity. Indeed, the recirculating zone scales as Ha, and one should have such a Ha aspect ratio to get the fully established condition for velocity. For this reason, our exact Fourier series expansion solution proves necessary to determine the correct velocity field, if a reasonable geometry is adopted (it would be numerically difficult to increase the domain length for the velocity field while concentration forms a very thin boundary layer).

The FIDAP software (version 7.06), based on the finite elements method, was used for the calculations, performed on a HP 9000-735 working station. Rectangular, 9 nodes elements have been chosen with quadratic interpolation. The mesh contained 60 nodes in the axial direction and 50 in the transverse direction. The mesh was variable in space and concentrated near the walls. At the growing interface, the first node in the liquid is 1/1000 apart, which determines the smallest solute layer that can be modeled.

Each numerical calculation corresponds to a set of the non-dimensional numbers Gr Sc, Ha, Pe and k. The coefficients of the Fourier series expansion for the velocity field depend on Gr Sc and Ha only. Actually, they essentially depend on Ha, since they are merely proportional to Gr Sc. Then, for a given velocity field, the solute calculation (FIDAP) depends on Pe and k. From the derived concentration field, the effective partition ratio is determined as the product of k and of the mean concentration in the liquid at the growth interface. In Fig. 5, the experimental results are compared to the numerics for $\mathrm{Gr\,Sc} = 9.2 \times 10^6$, $k = 0.26$ and $\mathrm{Pe} = 23$. The calculated values are not identical to the measured ones, but the same tendency of slight increase of k^* with increasing Hartmann numbers is observed. A possible explanation of the discrepancy may be found in the 2D nature of the analysis. We observe from the numerical analysis that the mentioned increase does not start immediately when the Hartmann number becomes larger than one. Indeed, a slight decrease is first observed, and k^* is smaller in the range $0 \leqslant \mathrm{Ha} \leqslant 40$ than without magnetic field.

3.2.2. Order of magnitude analysis

The order of magnitude analysis is based on the estimate of the solute layer thickness attached to the growing interface. Wilson [17] proved that the effective partition ratio is uniquely determined by the knowledge of the solute layer thickness, provided this thickness is defined as follows. Let us denote $\tilde{c}_0$ the mean solute concentration in the liquid near the interface and $\mathrm{d}\tilde{c}/\mathrm{d}z$ the mean axial solute gradient at the interface. The non dimensional solute layer thickness δ is defined as $(\tilde{c}_0 - 1)/ - \mathrm{d}\tilde{c}/\mathrm{d}z$. The relation between k^* and δ is [17]:

$$k^* = \frac{k}{1 - (1 - k)\,\mathrm{Pe}\,\delta}. \tag{19}$$

If δ can be estimated, Eq. (19) then allows us to estimate k*.

The derivation of the solute boundary layer thickness in Czochralski growth was first proposed

by Burton et al. [5] in 1953. Their work was later extended to other solidification configurations, and it was shown that δ could always be estimated when the velocity field in the vicinity of the interface is known (see e.g. Ref. [8] and references there). Denoting $\tilde{u}_z(z)$ the mean velocity field along the upper part of the cavity (here $0 < x < \frac{1}{2}$, the following general equation derived from an order of magnitude analysis of Eq. (17) when $\delta \ll 1$:

$$\tilde{u}_z(\delta) + \mathrm{Pe} = 1/\delta. \tag{20}$$

For small values of the velocity field, the equation leads to $\delta = \mathrm{Pe}^{-1}$, which corresponds exactly to the solution for purely diffusive transport conditions. Conversely, we focus here only on the convective case, when Pe can be neglected in Eq. (20). This approximation allows us to highlight the trends of the influence of the magnetic field. The equation to solve is:

$$\tilde{u}_z(\delta) = 1/\delta. \tag{21}$$

The approximate velocity field given by Eqs. (15) and (16) will be used. Two asymptotic cases can be distinguished: the case when the Hartmann layer is much thinner than δ and the case when it is much larger than δ. In the first case, Eqs. (13) and (14) can be used while, in the second, the $1 - \mathrm{e}^{-\mathrm{Ha}\, z}$ factor is linearized in Eqs. (15) and (16). It is easy to derive $\tilde{u}_z$ and the corresponding solution δ of Eq. (21):

$$\delta < \mathrm{Ha}^{-1} \Rightarrow \tilde{u}_z(z) = -\frac{\mathrm{Gr\,Sc}}{18} z^2$$

$$\Rightarrow \delta = 2.6(\mathrm{Gr\,Sc})^{-1/3}, \tag{22}$$

$$\delta > \mathrm{Ha}^{-1} \Rightarrow \tilde{u}_z(z) = -\frac{\mathrm{Gr\,Sc}}{9\mathrm{Ha}} z$$

$$\Rightarrow \delta = 3(\mathrm{Gr\,Sc})^{-1/2}\mathrm{Ha}^{1/2}. \tag{23}$$

Going back to the conditions $\delta < \mathrm{Ha}^{-1}$ or $\delta > \mathrm{Ha}^{-1}$, the limit between these two asymptotic cases is found, $\mathrm{Ha} \sim (\mathrm{Gr\,Sc})^{1/3}$. For Ha below (resp. above) this value, Eq. (22) holds (resp. Eq. (23)). This relation $\mathrm{Ha} \sim (\mathrm{Gr\,Sc})^{1/3}$ defines a "threshold value" for the magnetic field to become efficient. A smaller magnetic field has no effect on segregation, even though convection may already be significantly damped, and a higher magnetic field tends to decrease axial segregation. Even in the active regime, the effect of the magnetic field is moderate regarding to the square root dependence on the Hartmann number in Eq. (23).

A physical approach of this result can be outlined. The inactive regime is characterized by the fact that the solute boundary layer is smaller than the Hartmann layer. Indeed, at the scale of the solute layer, the velocity field is insensitive to the magnetic field, since the far velocity scales as Ha^{-1} while the Hartmann thickness also scales as Ha^{-1}. Conversely, when the solute layer is larger than the Hartmann layer, mass transport becomes sensitive to the Ha^{-1} decrease of the velocity field.

The above result is drawn in Fig. 5 in full line: the results were derived in terms of k^* using Eq. (19). The discrepancy with numerics and experiments can be explained both by the approximate nature of the order of magnitude analysis and by the neglected Pe number in Eq. (20). Nevertheless, the tendencies compare well. We tried then to check the validity of the order of magnitude analysis, when the convective regime (negligible Pe in Eq. (20)) is well achieved. In Fig. 6, numerical and order of magnitude results (OMA) for δ are compared for a small Péclet number $\mathrm{Pe} = 1$. Two different Gr Sc numbers were investigated, giving opportunity to detect the variation of the threshold $\mathrm{Ha} \sim (\mathrm{Gr\,Sc})^{1/3}$. The Ha number range was enlarged up to $\mathrm{Ha} = 1000$, to improve the comparison. In this Fig. 6, the multiplication factors in Eqs. (22) and (23) have been changed to 4.3 and 4.2, respectively (instead of 2.6 and 3), to best fit the numerical values. In other words, the magnitude order analysis (before modification) and numerical results differ by about 40%: it is a usual feature of an order of magnitude analysis to predict essentially power laws, which are independent of any multiplication by a constant factor. Moreover, the use of the new factors provides an excellent quantitative agreement between OMA and numerical results for the solute boundary thickness. To finish with these multiplication factors, it should be underlined that they are the same for both cases $\mathrm{Gr\,Sc} = 10^6$ and $\mathrm{Gr\,Sc} = 10^8$ and fit equally the two curves. The numerical prediction of the threshold value also seems to obey the relation $\mathrm{Ha} \sim (\mathrm{Gr\,Sc})^{1/3}$.

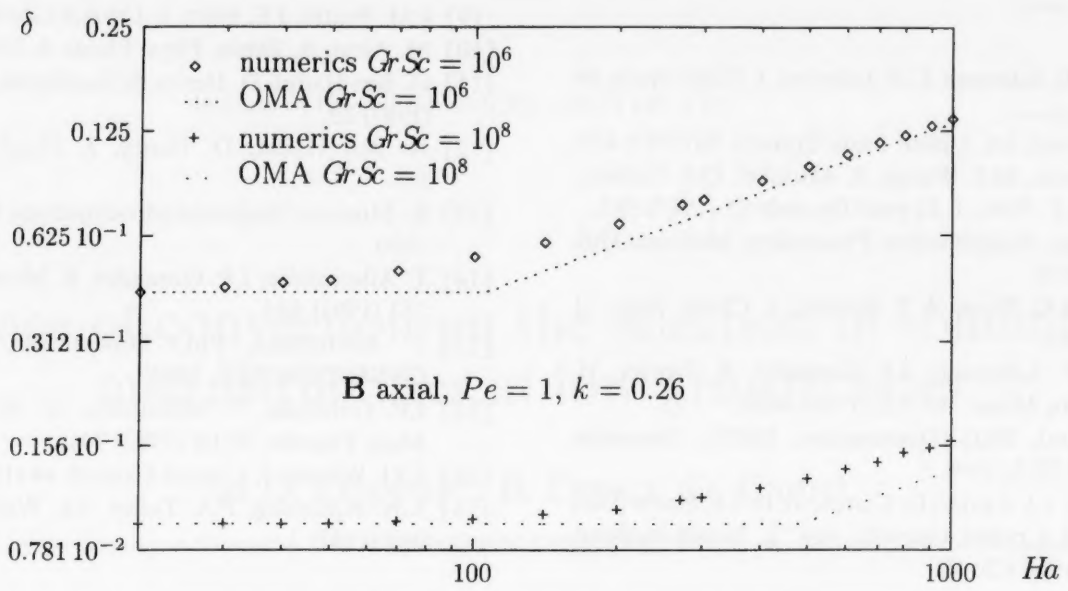

Fig. 6. Comparison between numerical and analytical results.

4. Conclusions

A moderate effect on axial solute segregation has been experimentally demonstrated for tin–bismuth alloys solidified in the presence of an axial magnetic field. The velocity field in the melt has been analyzed in the framework of a 2D model including the braking effect of the magnetic field. This velocity field has been included in a numerical 2D model for concentration and effective partition ratios k*, depending on the applied magnetic field magnitude, have been derived. In parallel, using again this velocity field, an order of magnitude analysis of the solute transport equation has led us to an estimate for the solute boundary layer thickness. This thickness and the effective partition ratio k* being in unique correspondence, order of magnitude analysis and numerical results have been compared, with fair agreement with experimental values. Moreover, the order of magnitude analysis has revealed two distinct regimes for the magnetic field influence. The thickness δ is found to scale as $(\mathrm{Gr\,Sc})^{-1/3}$ when $\mathrm{Ha} \ll (\mathrm{Gr\,Sc})^{1/3}$ and as $(\mathrm{Gr\,Sc})^{-1/2}\mathrm{Ha}^{1/2}$ when $\mathrm{Ha} \gg (\mathrm{Gr\,Sc})^{1/3}$. An axial magnetic field thus has to be strong enough before it can have an impact on axial segregation.

The method of segregation analysis under magnetic field developed in this paper can be extended to other aspects. Radial segregation, the case of a transverse vertical magnetic field and also the vertical Bridgman configuration with axial magnetic field [15, 7] have already been investigated. More generally, as soon as an expression for the velocity field is available, these analyses (numerical and in terms of magnitude orders) can be followed. For instance, analytical expressions for the flow in Czochralski growth configurations have been obtained (see, e.g., Ref. [18] and references there).

To conclude, some ideas deserve to be highlighted. As already reported [8], only the velocity field within the solute boundary layer controls its thickness: in the regime $1 \ll \mathrm{Ha} \ll (\mathrm{Gr\,Sc})^{1/3}$, the average velocity field intensity decreases with increasing values of Ha, while its value at the solute layer scale remains unchanged, meaning that there will be no effect of the magnetic field. It is also important to insist again on the benefits gained with the order of magnitude analysis. Estimates of the effective partition coefficient and of its dependence with respect to the magnetic field intensity are derived in terms of concise equations that can be easily used by a practician to account for his own growth conditions.

Acknowledgements

The present work was conducted within the framework of the GRAMME agreement between the CNES and the CEA.

References

[1] D.T.J. Hurle, E. Jakeman, C.P. Johnson, J. Fluid Mech. 64 (1974) 565.
[2] C. Vives, C. Perry, Int. J. Heat Mass Transfer 30 (1987) 479.
[3] D.H. Matthiesen, M.J. Wargo, S. Motakef, D.J. Carlson, J.S. Nakos, A.F. Witt, J. Crystal Growth 85 (1987) 557.
[4] M.C. Flemings, Solidification Processing, McGraw-Hill, New York, 1974.
[5] J.A. Burton, R.C. Prim, W.P. Slichter, J. Chem. Phys. 21 (11) (1953) 1987.
[6] J.J. Favier, P. Lehmann, J.J. Garandet, B. Drevet, H. Herbillon, Acta Mater. 44 (12) (1996) 4899.
[7] A.C. Neubrand, PhD Dissertation, INPG, Grenoble, CENG/DEM/SES, 1995.
[8] J.P. Garandet, J.J. Favier, D. Camel, in: D.T.J. Hurle (Ed.), Handbook of Crystal Growth, vol. 2, North-Holland, Amsterdam, 1994 Ch. 12.
[9] J.M. Pratte, J.E. Hart, J. Crystal Growth 102 (1990) 54.
[10] M. Afrid, A. Zebib, Phys. Fluids A 2 (8) (1990) 1318.
[11] H. Ben Hadid, D. Henry, S. Kaddeche, J. Fluid Mech. 333 (1997) 23.
[12] H. Ben Hadid, D. Henry, J. Fluid Mech. 333 (1997) 57.
[13] R. Moreau, Magnetohydrodynamics, Kluwer, Dordrecht, 1990.
[14] T. Alboussière, J.P. Garandet, R. Moreau, J. Fluid Mech. 253 (1993) 545.
[15] T. Alboussière, PhD Dissertation, INPG, Grenoble, CENG/DEM/SES, 1994.
[16] J.P. Garandet, T. Alboussière, R. Moreau, Int. J. Heat Mass Transfer 35 (4) (1992) 741.
[17] L.O. Wilson, J. Crystal Growth 44 (1978) 247.
[18] L.N. Hjellming, P.A. Tolley, J.S. Walker, J. Fluid Mech. 249 (1993) 1.

ELSEVIER

Journal of Crystal Growth 181 (1997) 145–159

JOURNAL OF CRYSTAL GROWTH

Influence of convection on the selection of solidification microstructures at low growth rates

M.D. Dupouy*, B. Drevet, D. Camel

Commissariat à l'Energie Atomique-Grenoble, DTA/CEREM/DEM/SPCM/LRBS 17 rue des Martyrs, 38054 Grenoble Cedex 9, France

Received 11 March 1996; accepted 28 February 1997

Abstract

The influence of thermal convection on the selection of microstructures is studied in directional solidification at low growth rates. Using the concept of solute boundary layer, the composition of the alloy at the different transitions between planar, eutectic and cellular fronts is predicted under a stationary regime and also in the presence of longitudinal macrosegregation. Furthermore, the appearance of mixed microstructures owing to radial segregation is discussed. Predictions concerning the planar/eutectic and cellular/eutectic transitions are checked against experimental results obtained with hypo-eutectic Sn–Cu alloys.

Keywords: Solidification microstructures; Natural convection; Selection

1. Introduction

Much effort is being devoted to prediction of the solidification microstructures as a function of the control parameters, namely initial alloy composition, thermal gradient and solidification rate. As these parameters can vary in a very wide range depending on the solidification process involved (which can be crystal growth from the melt as well as rapid solidification by melt spinning for instance), it has proved very useful to use scaling analysis and to propose characteristic lengths to predict microstructural transitions and scales [1]. Previous work, however, mainly concentrated on cases where solute transport in the liquid near the front is controlled by diffusion (i.e. convection can be neglected). This condition is not necessarily satisfied when forced convection is applied, or when natural convection is present and solidification rate is low. For instance, it is now well known that the threshold for transition from a planar to a cellular front [2] (i.e. morphological destabilization), or from an eutectic to a dendritic front [3] (i.e. coupled zone limit) can be strongly displaced, simply due to buoyancy flows which are present even when solidification is performed in a vertical stabilizing configuration.

* Corresponding author.

0022-0248/97/$17.00 © 1997 Published by Elsevier Science B.V. All rights reserved
PII S0022-0248(97)00191-7

These effects have been first qualitatively described using a stagnant-film hypothesis [4] (see, for instance, the analysis of the influence of convection on the morphological instability threshold of the planar front [5]). More recent work has shown that a more physical concept of solute boundary layer could be defined and that scaling laws could be determined for this quantity as a function of convective conditions [6]. This concept proved to be very successfull in describing the segregations appearing during directional solidification with a planar front, at least in the situation, mainly considered up to now, where only thermal buoyancy is present (i.e. density differences due to concentration variations are sufficiently low for solutal buoyancy to be neglected) [6].

In the present work, we propose to use this concept to make a general description of the transitions between planar, eutectic and cellular or dendritic fronts in directional solidification, in the presence of convection, as was briefly proposed in Ref. [7]. The analysis is restricted here to the study of the influence of thermal buoyancy. Consistently, we only consider low solidification rates, where this type of convection is relevant. This enables us to predict the microstructures occurring for stationary solidification conditions, as well as the possible nonuniformities of these microstructures along the solid/liquid front. Also, the microstructural transitions associated with longitudinal macrosegregation are discussed. Particular attention is paid to the planar–eutectic boundary and to the planar–eutectic–cellular triple junction which, to our knowledge, have not been considered up to now. Predictions concerning these last boundaries are checked against experiments performed on hypo-eutectic Sn–Cu alloys.

2. Theory of microstructure selection

Let us consider one side of a classical eutectic phase diagram between solids A and B (eutectic temperature T_E and eutectic composition C_E). For the sake of simplicity, the solidus and liquidus are supposed to be linear (liquidus slope m_l, defined positive, and partition ratio k). The solidification parameters are the initial composition of the alloy C_0 (expressed in B species) ranging from pure A to C_E, the temperature gradient G and the solidification rate R. Three types of solidification patterns can be formed: the planar front of phase A, the A–B eutectic front, and cells (or dendrites) of A advancing ahead of the A–B eutectic front.

We will first recall the specific boundary conditions which apply in each case. Then, the microstructure selection diagram will be straightforwardly obtained for the case of pure diffusive transport by using the classical minimum undercooling criterion. Finally the approach will be extended to the case where convection is present.

2.1. Boundary conditions at the different fronts

2.1.1. Planar front

Let C_{Li} and C_{Si} be the concentrations, respectively, on the liquid and solid side of the interface and T_i the temperature at the front. The following boundary conditions apply:

- thermodynamic equilibrium at the interface :

$$C_{Si} = kC_{Li}, \tag{1}$$

$$T_i = T_M - m_l C_{Li}, \tag{2}$$

where T_M is the melting temperature of pure A,

- and solute balance across the interface:

$$D\left.\frac{dC}{dz}\right|_i = R(C_{Si} - C_{Li}), \tag{3}$$

with z normal coordinate (positive towards the liquid) and D liquid diffusion coefficient.

2.1.2. Eutectic front

The eutectic front is here considered on a mesoscopic scale, which is larger than the eutectic spacing but smaller than the scale where transverse segregation effects might occur. Let $\bar{C}_{Li}$ and $\bar{C}_{Si}$ be the concentrations on the liquid and solid side of the interface, averaged at this scale. The classical microscopic model of Jackson and Hunt [8] determines $\bar{C}_{Li}$ and T_i as a function of solidification rate and the fraction f_{AE} of phase A in the eutectic, which is linked to $\bar{C}_{Si}$ and the solubility limits

C_A and C_B by

$$C_{Si} = C_B - f_{AE}(C_B - C_A). \quad (4)$$

It is found that $(T_E - T_i)$ can be assumed independent of C_0 and is an increasing function of R, as well as $|\bar{C}_{Li} - C_E|$ if the eutectic system presents nonsymetrical properties. For the present case where we restrict to low solidification rates, we can admit that

$$\bar{C}_{Li} = C_E, \quad (5)$$

$$T_i = T_E. \quad (6)$$

Besides, a solute balance similar to (3) applies provided the local quantities are replaced by the averaged ones.

2.1.3. Cellular (dendritic) front

As the eutectic one, the cellular front is here described on a mesoscopic scale. But in addition, this front has a finite thickness, the liquid fraction f_L varying from 1 at T_i to a minimum value f_E at T_E where it transforms into eutectic. By convention, we will take $z = 0$ at T_E and $z = z_t$ at T_i. We will adopt here the simple description of Flemings [9], with no constitutional undercooling in the intercellular liquid, i.e. we suppose that local radial solutal gradients can be neglected. This approximation remains satisfactory in the vicinity of the stability threshold of the planar front, as long as the cellular spacing λ remains smaller than the diffusion length (i.e. Peclet number $R\lambda/D$ is smaller than one). Besides, one has to consider that the temperature gradient to be introduced in the Flemings model should be defined as

$$G_{eff} = \frac{dT_i(z)}{dz}, \quad (7)$$

where $T_i(z)$ is the temperature taken along the solid/liquid interface. When the thermal conductivities of the liquid and solid phases are different, G_{eff} has some intermediate value between liquid and solid temperature gradients. This value depends, in principle, on the location along the cell for a given cell shape. For less and less deep cells, it should tend towards the value obtained in the linear stability analysis of Mullins and Sekerka, for planar growth. We will adopt this last value given by

$$G_{eff} = \frac{K_S G_S + K_L G_L}{K_S + K_L}, \quad (8)$$

where K_S and G_S (respectively, K_L and G_L) stand for the thermal conductivity and temperature gradient on the solid (respectively, liquid) side. Applying the local thermodynamic equilibrium (Eq. (2)) to the intercellular liquid of composition $C_{Li}(z)$, one then gets

$$T_i(z) = T_M - m_\ell C_{Li}(z)$$

and

$$\frac{dC_{Li}(z)}{dz} = -\frac{G_{eff}}{m_\ell}. \quad (9)$$

A classical local solute balance can be done in a representative element at position z inside the front, as initially proposed by Flemings [9]. It allows to determine the variation of the liquid fraction f_L between T_i and T_E. Simple analytical solutions can be derived for the two extreme cases, where

- solute diffusion in the solid is negligible

$$f_L(z) = \left[\frac{C_{Li}(z) - DG_{eff}/(m_\ell(1-k)R)}{C_{Li}(z_t) - DG_{eff}/(m_\ell(1-k)R)}\right]^{-1/(1-k)}, \quad (10a)$$

- solute diffusion in the solid is complete

$$f_L(z) = -\frac{k}{1-k} + \frac{1}{1-k}\left[\frac{C_{Li}(z) - DG_{eff}/(m_\ell(1-k)R)}{C_{Li}(z_t) - DG_{eff}/(m_\ell(1-k)R)}\right]^{-1}. \quad (10b)$$

Here, in contrast with Fleming's formulation, the tip concentration $C_{Li}(z_t)$ is not specified and depends on transport conditions in the bulk. The same holds for z_t, the distance between the dendrite tips and the eutectic front, which is directly linked to $C_{Li}(z_t)$ by

$$z_t = \frac{m_\ell}{G_{eff}}(C_E - C_{Li}(z_t)). \quad (11)$$

At T_E, the remaining liquid transforms into eutectic so that the eutectic fraction is given by

$$f_E = f_L(T_E). \tag{12}$$

The average concentration $\bar{C}_{SE}$ of this eutectic is given by a solute balance across the eutectic front similar to Eq. (3):

$$D\frac{G_{eff}}{m_\ell} = R(C_E - \bar{C}_{SE}) \tag{13}$$

and phase fractions inside the eutectic are again given by Eq. (4).

A global solute balance between T_i and T_E can also be used alternatively if one is primarily interested in the macrosegregation. This is simply a form of Eq. (3) where C_{Si} is replaced by an average concentration $\bar{C}_S$ including both the primary phase and the eutectic.

In the dendritic regime, the previous model is no longer strictly valid near the tips. More specifically, it can still be used to evaluate liquid fractions far from the tips, but it underestimates the tip undercooling. As a consequence, the boundary of the coupled zone is no longer correctly predicted. This situation is, however, not worthy of consideration in the present study, as boundary layer solute transport is not relevant in this case and external flows are not expected to have an influence, except if they would be strong enough to affect the solute field right at the dendrite tips, which is not very likely to occur as far as thermal buoyancy is concerned.

2.2. Microstructure selection in diffusive transport conditions

Here we consider only the stationary regime which is obtained after an initial transient where solute builds up ahead of the solidification front. Then, the average concentration $\bar{C}_S$ of the solid formed is equal to the initial alloy concentration C_0:

$$\bar{C}_S = C_0. \tag{14}$$

If we define the size δ of the solute boundary layer ahead of the front by

$$-\left.\frac{dC}{dz}\right|_i = \frac{C_{Li} - C_0}{\delta}, \tag{15}$$

application of Eqs. (3) and (15) gives the classical result

$$\delta = \frac{D}{R}. \tag{16}$$

We apply a minimum undercooling criterion for microstructure selection (i.e. the prevailing microstructure is that for which T_i is maximum):

$$T_i = \max(T_i^{planar}, T_i^{cellular}, T_i^{eutectic}). \tag{17}$$

Then, using the boundary conditions for the different fronts (1)–(3), (5), (6) and (9), the condition of stationary diffusive transport (14) and the microstructure selection criterion (17), one finds the following conditions for microstructure transitions:

- planar–cellular transition

$$C_0^{PC} = \frac{G_{eff}Dk}{Rm_\ell(1-k)}; \tag{18}$$

- cellular–eutectic transition at

$$C_0^{CE} = C_E - \frac{G_{eff}D}{Rm_\ell}; \tag{19}$$

- planar–eutectic transition at the solubility limit

$$C_0^{PE} = kC_E. \tag{20}$$

One can notice that the planar–cellular transition predicted by Eq. (18) is consistent with the Mullins and Sekerka's instability threshold, at small Peclet number, provided that we adopt for G_{eff} the mean value proposed by Mullins and Sekerka and given by Eq. (8). One has also to notice that, rigorously speaking, the value of G_{eff} at the cellular–eutectic transition is not necessarily the same as at the planar–cellular transition. We will, however, make this assumption for the sake of simplicity. Then, a triple junction between the three microstructure domains is predicted and defined by

$$C_0 = kC_E, \tag{21a}$$

$$R = R_C = \frac{DG_{eff}}{m_\ell(1-k)C_E}. \tag{21b}$$

Above the critical rate R_C, the planar and eutectic domains are separated by the cellular domain. Below R_C, the cellular microstructure can no longer be obtained and there is a direct transition from planar to eutectic growth.

The value of R_C primarily depends on the freezing temperature range $m_l(1-k)C_E$ of the alloy whose composition is at the solubility limit kC_E. For $k \ll 1$, this quantity is equivalent to the depth $T_M - T_E$ of the eutectic phase diagram. Characteristic values of R_C are given in Table 1 for different alloys, assuming a typical gradient of 10 K/mm. In practice, rates below R_C can be reached in systems with an eutectic depth in the range of 10 K or less.

Eqs. (18)–(20) allow us to build a microstructure map at low growth rates. Fig. 1 gives the microstructure map as a function of R and C_0 for the Sn–Cu alloy with $G_{eff} = 5.5$ K/mm and physico-chemical parameters of Table 1 (taken from Refs. [10–14]).

Table 1
Physico-chemical parameters and calculated values of critical rate R_C with $G_{eff} = 10$ K/mm for different binary systems

System A–B	C_E (wt% B)	$T_M - T_E$ (K)	D (m^2/s)	$\lvert m_l \rvert$(K/wt% B)	k	R_C (μm/s)
Sn–Cu	0.94 Ref. [10]	5	2.7×10^{-9} Ref. [12]	5.3 Ref. [10]	6.4×10^{-3} calc. from Refs. [10, 14]	5.4
Al–Ni	5.69 Ref. [11]	20.5	5×10^{-9} Ref. [13]	3.6 Ref. [11]	3.7×10^{-3} calc. from Ref. [11]	2.4
Al–Fe	1.84 Ref. [11]	5.4	3×10^{-9} Ref. [13]	3 Ref. [11]	3.4×10^{-2} calc. from Ref. [11]	5.6

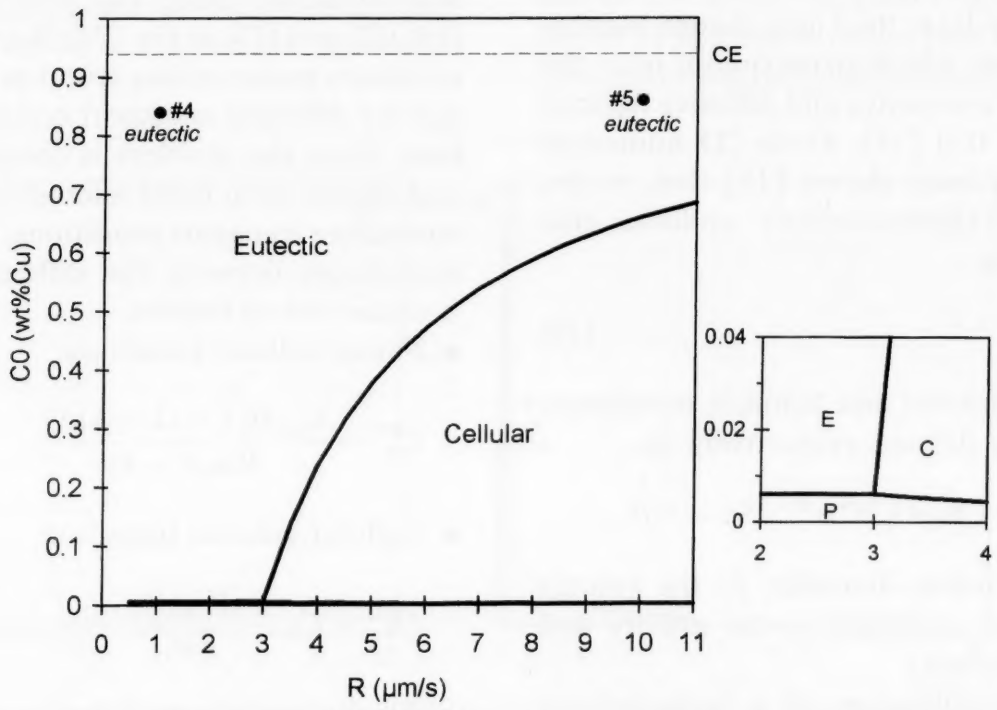

Fig. 1. Calculated microstructure map for the Sn–Cu alloy in purely diffusive conditions ($G_{eff} = 5.5$ K/mm) and experimental results (full circles) of vertical upwards solidifications (P = planar, E = eutectic, C = cellular).

2.3. The boundary layer models of solute convective transport

Since the classical work of Burton et al. [15], it is well known that forced convection reduces the extent of the solute boundary layer δ ahead of a planar front, according to well-defined scaling laws. Here, we will define δ by Eq. (15) as initially suggested by Wilson [16]. Then, the nondimensional convecto-diffusive parameter, defined as the ratio of δ to its reference value D/R in diffusive conditions (Eq. (16))

$$\Delta = \delta R/D \tag{22}$$

is lower than unity. More recent detailed work on directional solidification with thermal buoyancy [6] has shown that the concept of a solute boundary layer can still be applied, provided that allowance is made for a possible dependence of δ on the position along the front. Thus, for planar front solidification in a horizontal configuration, δ is found to be nearly uniform along most of the interface, specially in the upper region where the flow is directed towards the interface. On the other hand, an increase of δ due to solute accumulation is observed in a small part of the region of outward flow near the lower boundary. As it will be detailed later, this boundary-layer thickness change induces a radial segregation, which is maximum near the transition between convective and diffusive regimes (Δ of the order of 0.7) [17]. From 2D numerical calculations, it has been shown [18] that, in the region where δ is approximately uniform, this quantity is given by

$$\Delta = 4.5\mathrm{Pe}\,(\mathrm{Gr}\,\mathrm{Sc})^{-1/3}. \tag{23}$$

Here the Peclet, Grashof and Schmidt nondimensional numbers are defined, respectively, as

$$\mathrm{Pe} = HR/D, \quad \mathrm{Gr} = \beta_T g G_L H^4/\nu^2, \quad \mathrm{Sc} = \nu/D,$$

where H is the crucible diameter, β_T the volume thermal expansion coefficient, g the gravity and ν the kinematic viscosity.

For eutectic solidification of a hypo-eutectic alloy in a horizontal configuration, the same scaling law is obtained for Δ, with only a slightly different constant factor [19]:

$$\Delta = 4.1\mathrm{Pe}\,(\mathrm{Gr}\,\mathrm{Sc})^{-1/3}. \tag{24}$$

As already observed in planar front solidification, the radial segregation profile exhibits an off-centered minimum in the upper part of the section. The concentration is maximum in the bottom region where it is close to the eutectic composition [19].

We will admit here that the scaling law (23) or (24) can be extended to the case of the solute transport ahead of a cellular front. Such an approximation should be valid so far as the solutal boundary layer is large compared to the cellular spacing.

2.4. Microstructure selection under stationary convective transport

In this section, we will suppose that the length of the solidifying sample is infinite, i.e. that segregation phenomena do not modify the concentration of the bulk liquid which remains equal to C_0.

2.4.1. Region of interface where δ is minimum

C_{Si} (or $\bar{C}_{Si}$, $\bar{C}_S$) C_{Li} (or $\bar{C}_{Li}$) and thus the front (or cell tip) temperature T_i can be determined for each microstructure using Eqs. (1)–(3), (5), (6), (8), (9), (15), (22) and (23) or Eq. (24). We will admit that the minimum undercooling criterion (17), which is verified for diffusion transport conditions, still applies here. Then the problem is completely determined and allows us to build microstructure maps under convective transport conditions. The expressions of boundaries between the different microstructure domains are as follows:

- Planar/cellular transition:

$$C_0^{PC} = \frac{G_{eff} D[1-(1-k)\Delta]}{R m_\ell (1-k)}; \tag{25}$$

- Cellular/eutectic transition:

$$C_0^{CE} = C_E - \frac{\Delta G_{eff} D}{R m_\ell}; \tag{26}$$

- Planar/eutectic transition:

$$C_0^{PE} = C_E[1-(1-k)\Delta]. \tag{27}$$

Thus, the solidification front will be:

- planar, for $C_0 < \min(C_0^{PC}, C_0^{PE})$;
- eutectic, for $C_0 > \max(C_0^{PE}, C_0^{CE})$;
- cellular (or dendritic), for $C_0^{PC} < C_0 < C_0^{CE}$.

An example of a resulting microstructure map as a function of C_0 and R is shown in Fig. 2 for the Sn–Cu system with physico-chemical parameters of Table 1, values of v and β_T relative to pure tin ($v = 2.6 \times 10^{-7}$ m^2/s [20], $\beta_T = 10^{-4}$ K^{-1} [21]) and $\delta = 110$ μm, which is representative of horizontal solidification in a cylinder of diameter $H = 6.5$ mm with a thermal gradient $G_{eff} = 5.5$ K/mm.

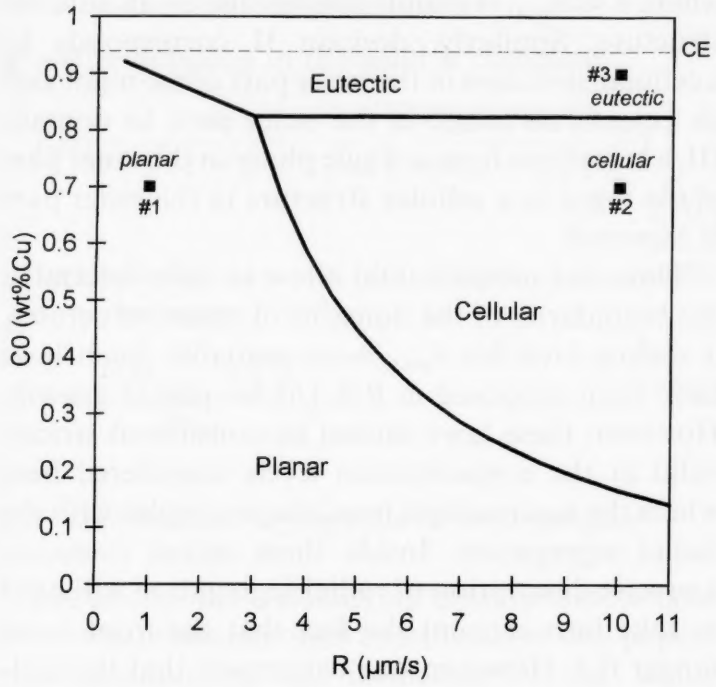

Fig. 2. Calculated microstructure map for the Sn–Cu alloy with $\delta = 110$ μm, representative of horizontal solidification in a cylinder of diameter 6.5 mm with $G_{eff} = 5.5$ K/mm, and experimental results (full squares).

By comparison with the case of pure diffusive transport, the following main remarks can be made: (i) the critical rate R_C remains unchanged, (ii) the planar domain is more extended while the eutectic one is reduced and (iii) the cellular domain is more or less conserved but shifted towards higher C_0 values.

One can also notice that, if expressed as a function of $\bar{C}_{Si}$ instead of C_0 (i.e. using only Eqs. (1)–(3), (5), (6), (8), (9) and (17)), the problem is formally identical to that under diffusive transport, which means that the solid concentrations C_S^{ij} at the transition between microstructures i and j are simply given by Eqs. (18)–(20). In other words, convection modifies the microstructure maps only through the macrosegregation it generates.

2.4.2. Radial segregation

As briefly mentioned in Section 2.3, in a horizontal configuration, the vertical motion of the fluid near the interface can lead to non-uniformity of the size of the solute boundary layer. This is clearly shown by isoconcentration lines of Fig. 3 for planar front and eutectic solidifications. Solute accumula-

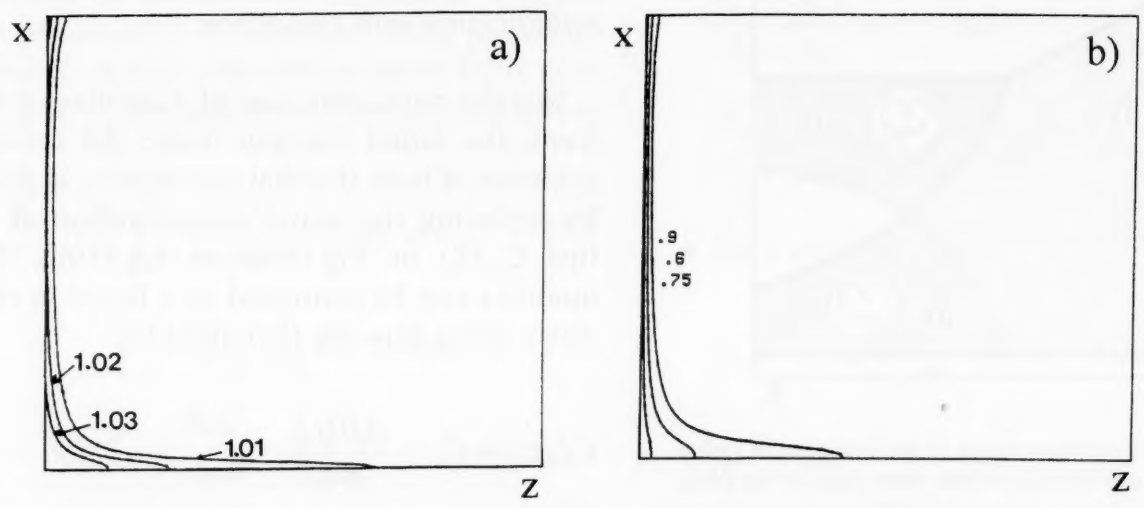

Fig. 3. 2D numerical simulations of isoconcentration lines near the solid/liquid interface in (a) planar front solidification for the case $C_0 = 1$, Gr Sc $= 10^7$, Pe $= 2$ (from Ref. [17]) and in (b) eutectic solidification for the case $C_{Li} = 1$, $C_0 = 0.5$, Gr Sc $= 10^6$, Pe $= 2$ (from Ref. [19]) in a horizontal configuration.

tion occurs principally in the bottom corner, where we can define a maximum value δ_{max} for δ, and slightly in the top corner. It also appears in Fig. 3 that δ has a minimum value δ_{min} along the main part of the interface. Variations of the solute boundary-layer thickness give rise to radial segregation phenomena. Indeed, using Eqs. (1), (3), (5), (9), (15) and (22), the solid concentration can be expressed as a function of C_0 and Δ:

$$\text{planar:} \quad C_{Si} = \frac{kC_0}{1-\Delta(1-k)}, \tag{28}$$

$$\text{eutectic:} \quad \bar{C}_{Si} = C_E - \frac{C_E - C_0}{\Delta}, \tag{29}$$

$$\text{cellular:} \quad \bar{C}_S = C_0 + \frac{G_{eff}D(\Delta - 1)}{Rm_\ell}. \tag{30}$$

As shown by Eqs. (25)–(27), the boundaries C_0^{ij} between microstructures i and j depend on Δ. A schematic microstructure map is represented on Fig. 4 with two series of boundaries corresponding, respectively, to δ_{min} and δ_{max}. In this figure, the three domains I–III correspond to regions where microstructural transitions can occur inside the cross section of the solidifying ingot, owing to the presence of radial segregation. In domain I, the alloy composition C_0 is such that $C_0^{PE}(\delta_{max}) < C_0 < C_0^{PE}(\delta_{min})$ if $R < R_C$ and $C_0^{CE}(\delta_{max}) < C_0 < C_0^{PC}(\delta_{min})$ if $R > R_C$. Thus, a single phase with planar front solidification is formed in the center of the ingot where $\delta \approx \delta_{min}$, whereas the periphery, where $\delta \approx \delta_{max}$, is mainly constituted by an eutectic structure. Similarly, domain II corresponds to a cellular structure in the inner part of the ingot and an eutectic structure in the outer part. In domain III, a transition from a single phase in the inner part of the ingot to a cellular structure in the outer part is expected.

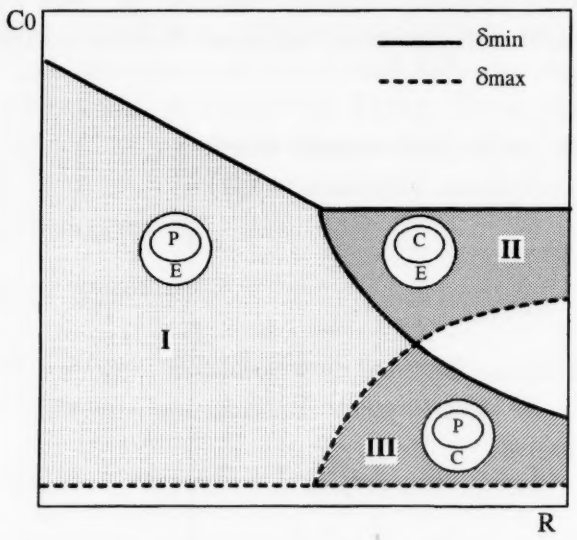

Fig. 4. Schematic microstructure maps in the presence of radial segregation. Full lines are relative to the inner part of the cross section of the ingot (minimum value of δ) whereas dashed lines are relative to the outer part (maximum value of δ). In domains I–III, different microstructure transitions occur inside the cross section of the ingot (P = planar, E = eutectic, C = cellular).

Thus, our model would allow to fully determine the boundaries of the domains of mixed structures, if scaling laws for δ_{max} were available. Such laws have been proposed in Ref. [6] for planar growth. However, these laws cannot be considered strictly valid at the concentration levels considered here where the macroscopic front shape couples with the radial segregation. Inside these mixed domains, a precise description of radial segregation will need to take into account the fact that the front is no longer flat. However, one can expect that the scaling of δ, in the region where it is minimum (i.e. where the flow is going towards the front) remains valid.

2.5. Microsegregation in cellular or dendritic solidification with convection

For the particular case of a cellular or dendritic front, the liquid fraction inside the mush, in the presence of bulk thermal convection, is determined by replacing the liquid concentration at dendrite tips $C_{Li}(z_t)$ in Eq. (10a) or Eq. (10b). This last quantity can be expressed as a function of C_0 and Δ, by using Eqs. (9), (15) and (22):

$$C_{Li}(z_t) = C_0 + \frac{\Delta D G_{eff}}{Rm_\ell}, \tag{31}$$

$$C_{Li}(z) = C_E - \frac{G_{eff}z}{m_\ell} \quad (0 \leqslant z < z_t). \tag{32}$$

More conveniently, f_L can be expressed as a function of C_0^{PC} given by Eq. (25) in the two extreme cases, where

- solute diffusion in the solid is negligible:

$$f_L(z) = \left[\frac{G_{eff}(z_t - z)}{m_\ell(C_0 - C_0^{PC})} + 1\right]^{-1/(1-k)}. \quad (0 < z < z_t) \tag{33a}$$

- solute diffusion in the solid is complete:

$$f_L(z) = -\frac{k}{1-k} + \frac{1}{1-k}\left[\frac{G_{eff}(z_t - z)}{m_\ell(C_0 - C_0^{PC})} + 1\right]^{-1}. \tag{33b}$$

In the same way, the total length of the mushy zone becomes

$$z_t = \frac{m_\ell(C_0 - C_0^{CE})}{G_{eff}}. \tag{34}$$

2.6. Longitudinal segregation in finite samples

Let us consider a solidifying ingot of finite length. The initial transient (not considered in this paper), corresponding to the formation of the solute boundary layer of extent δ, is followed by a quasi-steady state. During this stage, segregation phenomena induce a solute enrichment of the bulk liquid and thus an increase of its composition C_∞. In the presence of radial segregation, the mean concentration $\tilde{C}_S$ of the solid formed at a given instant is obtained by integration, along the interface of area S, of Eqs. (28)–(30) in which C_0 is now replaced by C_∞, depending on the microstructure involved:

$$\text{planar:} \quad \frac{\tilde{C}_S}{C_\infty} = \frac{k}{S}\int_S \frac{1}{1 - \Delta(1-k)}\,dS = k_{eff}, \tag{35}$$

$$\text{eutectic:} \quad \frac{\tilde{C}_S - C_E}{C_\infty - C_E} = \frac{1}{S}\int_S \frac{1}{(\Delta)}\,dS = k'_{eff}, \tag{36}$$

$$\text{cellular:} \quad (\tilde{C}_S - C_\infty)\frac{Rm_\ell}{G_{eff}D} = \frac{1}{S}\int_S (\Delta - 1)\,dS = K. \tag{37}$$

Here we suppose a quasi-steady state for δ, i.e. that Δ is independent of C_∞. Thus, the left-hand sides of Eqs. (35)–(37) can be assumed constant when solidification proceeds. One can notice that, for eutectic solidification, the constant is a concentration ratio analogous to the effective partition ratio k_{eff} obtained in planar solidification. This is no longer the case for cellular solidification, where the constant is proportional to a concentration difference.

Let us consider now that the microstructure remains the same along the whole length of the ingot. Assuming that the densities of solid and liquid are equal, the longitudinal segregation profile can be obtained by integrating the following equation:

$$(C_\infty - \tilde{C}_S)\,df_S = (1 - f_S)\,dC_\infty \tag{38}$$

from $C_\infty = C_0$ for $f_S = 0$, where f_S is the solidified fraction. Note that the term of solute accumulation in the mushy zone of the cellular (or dendritic) front is neglected in this formulation. Using Eqs. (35)–(37), one gets

- for a planar front

$$\frac{C_\infty}{C_0} = (1 - f_S)^{k_{eff}-1}, \tag{39a}$$

$$\frac{\tilde{C}_S}{C_0} = k_{eff}(1 - f_S)^{k_{eff}-1}; \tag{39b}$$

- for an eutectic front:

$$\frac{C_\infty - C_E}{C_0 - C_E} = (1 - f_S)^{k'_{eff}-1}, \tag{40a}$$

$$\frac{\tilde{C}_S - C_E}{C_0 - C_E} = k'_{eff}(1 - f_S)^{k'_{eff}-1}, \tag{40b}$$

- for a cellular front

$$(C_\infty - C_0)\frac{Rm_\ell}{G_{eff}D} = K\ln(1 - f_S), \tag{41a}$$

$$(\tilde{C}_S - C_0)\frac{Rm_\ell}{G_{eff}D} = K[1 + \ln(1 - f_S)]. \tag{41b}$$

In Eqs. (39a), (39b), (40a), (40b), (41a) and (41b), k_{eff}, k'_{eff} and K are given, respectively, by Eqs. (35)–(37).

Eq. (39b) is known as the Scheil's law established with complete mixing in the liquid, in which k has been simply replaced by k_{eff}.

According to Eqs. (39a) and (40a) and Eq. (41a), variations of the bulk liquid concentration C_∞ can give rise to a transition from microstructure i to microstructure j at a given value of f_S, as soon as C_∞ reaches the boundary composition C_0^{ij} (Eqs. (25)–(27)). However, between the fully i microstructure and the fully j microstructure, a mixed $i+j$ microstructure is expected owing to radial segregation, as described in Section 2.4 (see also Fig. 4). As longitudinal segregation in a mixed structure cannot be simply modelled, the solidified fraction at which the transition between the mixed structure and the structure j occurs cannot be predicted.

Such transitions have been observed experimentally in hypo-eutectic alloys and will be discussed in the next section.

3. Experiment

Sn–Cu alloys of composition either close to the eutectic ($C_E = 0.94$ wt% Cu [9]) or hypo-eutectic have been solidified in a classical Bridgman furnace already described in a previous paper [19], both in horizontal and vertical upward configuration. The temperature gradient in the liquid phase is 6 ± 0.5 K/mm. The length and diameter of the grown samples are approximately 100 and 6.5 mm, respectively. The growth conditions of the five samples considered in this work are summarized in Table 2.

Copper was dosed by means of atomic absorption on slices roughly 5 mm thick to obtain the longitudinal segregation profiles (Fig. 5a and Fig. 5b). In order to determine radial segregation (Fig. 5c), local surface fractions of Sn cells and Cu_6Sn_5 fibres of the eutectic structure were measured on slices normal to the growth axis, using scanning electron microscopy and image analysis [19]. Surface fraction measurements were then converted into copper concentration, assuming that all the copper is concentrated in the Cu_6Sn_5 fibres. Indeed, as the solubility of copper in tin is very small (6×10^{-3} wt% Cu at T_E [14]), it may be safely neglected.

Concerning the hypo-eutectic alloys elaborated horizontally (samples Nos. 1 and 2 in Table 2), large radial and longitudinal segregations are observed for both investigated growth rates (Fig. 5 and Ref. [19]). Owing to these segregations, solidification outside the coupled zone can be observed. Indeed, in the first part of the ingots, monophased tin at $R = 1$ μm/s and cellular tin at $R = 10$ μm/s are found in the center of the ingots, whereas the eutectic is confined to the periphery of the cross section (Fig. 6). As exposed in Section 2.4, these mixed structures can be explained with the variations of Δ along the interface and if one refers to Fig. 4, experimental conditions correspond to domain I at $R = 1$ μm/s and domain II at $R = 10$ μm/s. A transition from a mixed structure to a purely eutectic structure on the cross section occurs at a solidified fraction $f_{S,tr} = 0.30$ at $R = 1$ μm/s and $f_{S,tr} = 0.54$ at $R = 10$ μm/s (Fig. 6).

The particular shape of the cellular and monophased domains of the longitudinal sections of

Table 2
Experimental and calculated parameters for Sn–Cu growth

Experimental						Adjusted		Numerical
Reference experiment	Furnace orientation	C_0 (wt% Cu)	R (μm/s)	G_L (K/mm)	$f_{S,tr}$	$C_{\infty,tr}$ (wt% Cu)	$\bar{\Delta}$	Δ_{min} from Ref. [19]
No. 1	Horizontal	0.70	1	5.6	0.30	0.92 ± 0.01	0.06 ± 0.02	0.043
No. 2	Horizontal	0.70	10	5.3	0.54	0.83	0.37	0.36
No. 3	Horizontal	0.90	10	5.7	–	–	0.45	–
No. 4	Vertical	0.84	1	6.3	–	–	0.8	–
No. 5	Vertical	0.86	10	6.4	–	–	1	–

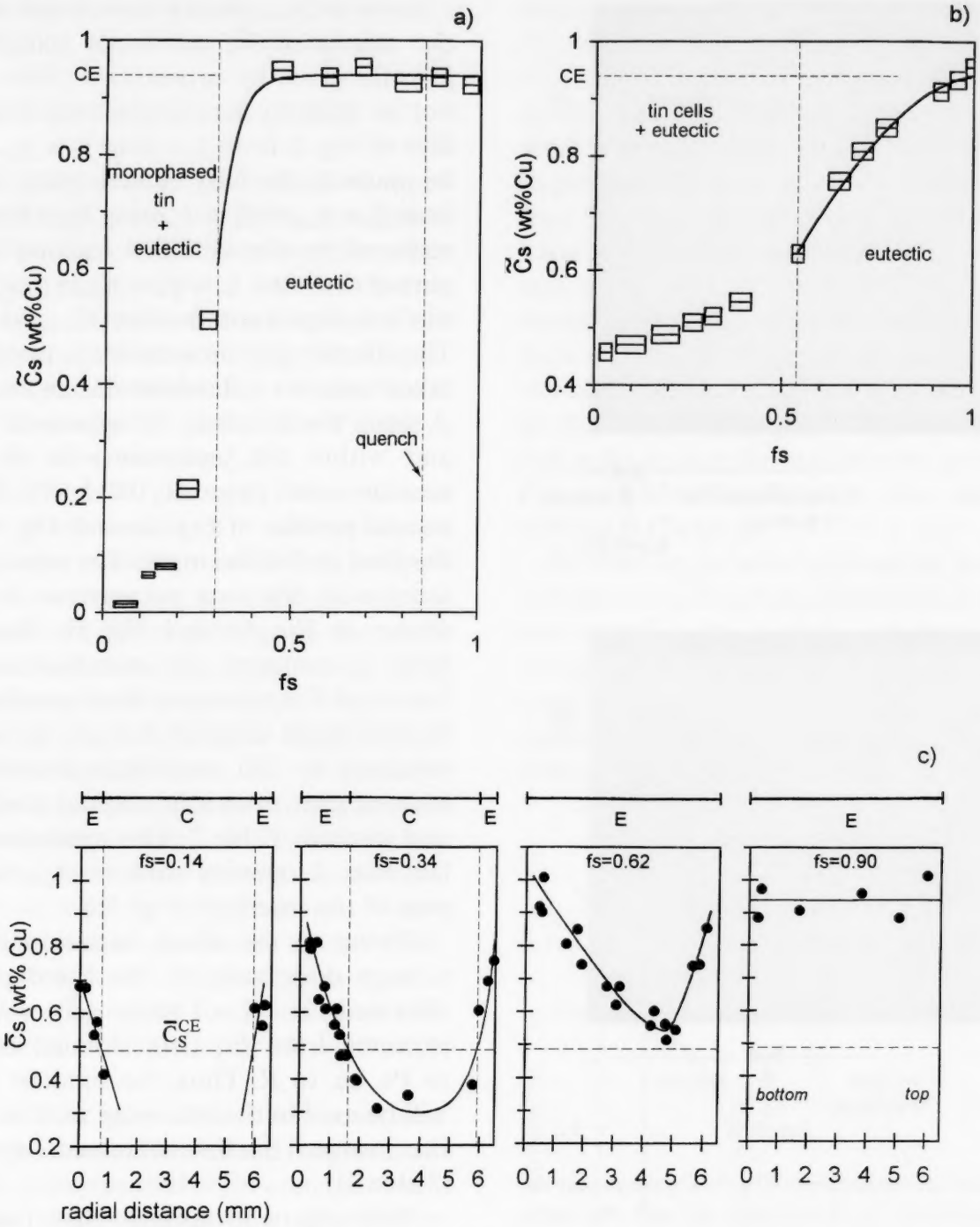

Fig. 5. (a) and (b): Longitudinal segregation profiles for Sn–0.70 wt% Cu alloys elaborated horizontally at $R = 1$ μm/s (a) and $R = 10$ μm/s (b); experimental points (rectangles) and calculated curves in the purely eutectic part of the samples (full lines) using Eq.(40b). (c); Experimental radial segregation profiles in the same sample than (b) for increasing solidified fractions f_S (E = eutectic, C = cellular).

Fig. 6 can be qualitatively explained taking into account both longitudinal and radial segregations. Experimental radial composition profiles for increasing solidified fractions are shown in Fig. 5c in the case of the cellular/eutectic transition. They exhibit an off-centered minimum, in agreement with the results of numerical simulation of eutectic growth given in Ref. [19]. For $f_S < f_{S,tr}$, a cellular structure is observed in the center part of the ingot, corresponding to $\bar{C}_S < \bar{C}_S^{CE}$, where $\bar{C}_S^{CE}$ is the local solid concentration relative to the cellular/eutectic transition. As f_S increases, the radial concentration

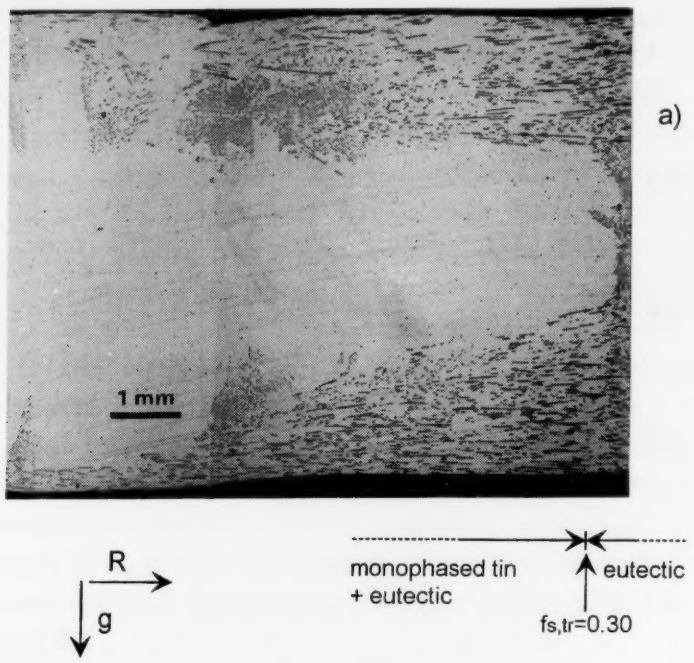

Fig. 6. Longitudinal sections of Sn–0.70 wt% Cu alloys near the planar/eutectic transition at $R = 1$ μm/s (a) and the cellular/eutectic transition at $R = 10$ μm/s (b).

profile moves toward higher concentrations owing to the existence of longitudinal segregation. As a consequence, the size of the cellular domain is reduced, explaining why the extent of the cellular or monophased regions of Fig. 6 decreases when f_S increases. According to Eq. (34), we can expect that the cellular front is very shallow near the observed transition, and consequently, convection inside the mushy zone should be negligible.

As before $f_{S,tr}$, there is not a single microstructure, the calculated $\tilde{C}_S$ curves for planar and cellular growths given by expressions (39b) and (41b) cannot be fitted to the experimental longitudinal profiles of Fig. 5 from $f_S = 0$ to $f_S = f_{S,tr}$. Such fits can be made in the fully eutectic parts of the samples from $f_S = f_{S,tr}$ to $f_S = 1$, using Eq. (40b) in which f_S is replaced by the solidified fraction in the eutectic part of the ingot $f_e = (f_S - f_{S,tr})/(1 - f_{S,tr})$ and C_0 by the bulk liquid composition $C_{\infty,tr}$ at the transition. The effective partition ratio k'_{eff} given by Eq. (36) is taken equal to $1/\bar{\Delta}$, where $\bar{\Delta}$ is an averaged value of Δ along the interface. In agreement with Eq. (40b) and within the uncertainty in the composition measurements (typically 0.015 wt% Cu), the experimental profiles of Fig. 5a and Fig. 5b reach C_E at the final end of the ingot. The calculated $\tilde{C}_S$ curves fitted with the two parameters $\bar{\Delta}$ and $C_{\infty,tr}$ are shown in Fig. 5a and Fig. 5b. Best-fit values of these parameters are summarized in Table 2. Values of $\bar{\Delta}$ are found to be in good agreement with the minimum value of Δ along the interface (Δ_{min}), obtained by 2D numerical simulation of hypoeutectic growth in a horizontal configuration [19] and given in Table 2. This agreement is due to the fact that Δ remains close to Δ_{min} along the main part of the interface (Fig. 3b).

Owing to the sharp variation of $\tilde{C}_S$ (Fig. 5a), a large dispersion on the fitted parameter $\bar{\Delta}$ is obtained at $R = 1$ μm/s ($\bar{\Delta} = 0.06 \pm 0.02$). As expected from Eq. (24), Δ must be proportional to Pe, i.e. to R. Thus, the smallest value $\bar{\Delta} = 0.04$ will be used in the following, as it is consistent with the value $\bar{\Delta} \cong 0.4$ obtained at $R = 10$ μm/s (Table 2).

With regard to samples Nos. 1 and 2 described above, segregation phenomena decrease strongly and even disappear when the initial concentration is close to C_E (sample No. 3) or for the samples grown vertically (samples Nos. 4 and 5). For these experiments, only fitted parameters $\bar{\Delta}$ are given (Table 2) and the reader is referred to Ref. [21] for the longitudinal segregation profiles. If compared to sample No. 2 elaborated in the same configuration, sample No. 3 exhibits a less important segregation and, consequently, solidification takes place inside the coupled zone in the whole length of the ingot. Also evidenced from large values of $\bar{\Delta}$ of

Table 2, convection has no effect on mass transfer for the samples Nos. 4 and 5 grown vertically.

3.1. Comparison with theoretical predictions

As explained in Section 2, microstructure maps for Sn–Cu alloys were built in diffusive conditions (Fig. 1) and for horizontal solidifications in a cavity of 6.5 mm height representative of experiments (Fig. 2). The value of the effective temperature gradient used in these calculations was taken equal to the average experimental gradient in the liquid phase $G_L = 5.5$ K/mm, as for eutectic Sn–Cu alloys the ratio G_L/G_S is close to unity [22].

Large values of $\bar{\Delta}$ for samples Nos. 4 and 5 (Table 2) are characteristic of a diffusive mass transfer. Thus, experimental points (R, C_0) representative of these two samples, as well as the microstructure observed at the beginning of the ingot where the bulk liquid composition C_∞ is close to C_0, are put on the microstructure map of Fig. 1. In the same way, experimental points of samples Nos. 1–3 elaborated horizontally are set in Fig. 2. An excellent agreement is found between experimental results and theoretical predictions, as the microstructures observed in the five samples considered here are consistent with the expected ones. Particularly, the critical rate $R_C = 3$ μm/s of the triple junction lies between the investigated growth rates giving rise to monophased tin for $R = 1$ μm/s and cellular or eutectic structures for $R = 10$ μm/s (Fig. 2).

Let us now consider microstructural transitions occurring in the presence of radial and longitudinal segregation. The experimental solid concentration $\bar{C}_S^{CE}$ at the cellular/eutectic transition, observed in the presence of radial segregation, is obtained from the concentration profiles of Fig. 5c: $\bar{C}_S^{CE} = 0.48$ wt% Cu. This value is in semi-quantitative agreement (30%) with the theoretical value $\bar{C}_S^{CE} = C_0^{CE} = 0.67$ wt% Cu given by Eq. (19).

One may also compare experimental and calculated values of the bulk liquid concentration at the transition between the mixed and eutectic structures, occurring at the solidified fraction $f_{S,tr}$ on the longitudinal profile (Fig. 5a and Fig. 5b). Variations of C_∞ from the initial concentration C_0 (0.70 wt% Cu) to C_E have been drawn on the microstructure map of Fig. 7 (thick dashed lines) for samples Nos. 1 and 2 with $G_{eff} = 5.5$ K/mm. Thus, a planar/eutectic transition may be observed at the lower growth rate when C_∞ reaches C_0^{PE}, while a cellular/eutectic transition may occur at the higher growth rate when C_∞ reaches C_0^{CE}. Using Eqs. (26) and (27) with $\Delta = \bar{\Delta}$ and $G_{eff} = G_L$ (see values in Table 2), one obtains $C_0^{PE} = 0.90$ wt% Cu and $C_0^{CE} = 0.84$ wt% Cu. These calculated values are in quantitative agreement with the values of the bulk liquid concentration at the transition $C_{\infty,tr}$, obtained by the fit of the longitudinal segregation profiles of Fig. 5a and Fig. 5b: $C_{\infty,tr} = 0.92 \pm 0.01$ wt% Cu for the planar/eutectic transition and $C_{\infty,tr} = 0.83$ wt% Cu for the cellular/eutectic transition (Table 2).

To sum up, a better agreement between experimental and calculated compositions is found when one considers the bulk liquid composition at the mixed structure/eutectic structure transition, instead of the local solid concentration at the transition occurring radially on a slice of the ingot. This result is mainly due to the accuracy of the

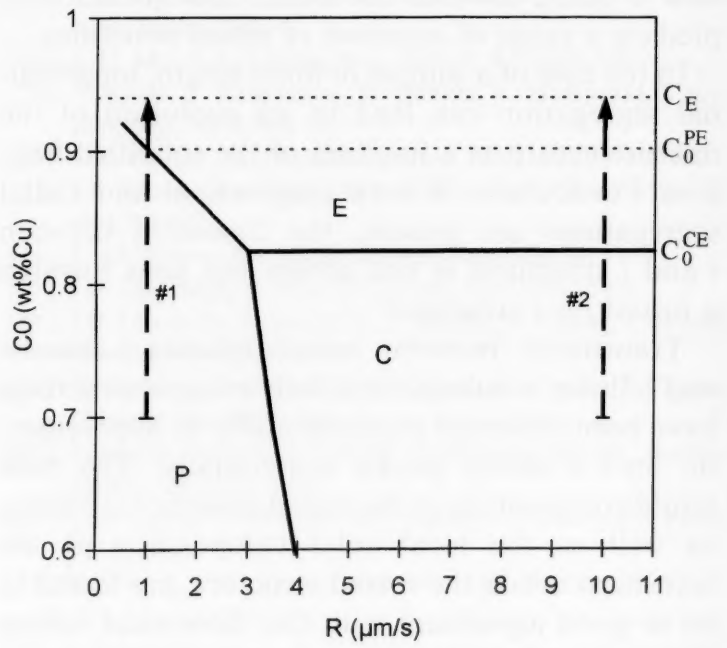

Fig. 7. Calculated microstructure map for the Sn–Cu alloy with $\delta = 110$ μm, representative of horizontal solidification in a cylinder of diameter 6.5 mm with $G_{eff} = 5.5$ K/mm, and variations of the bulk liquid concentration C_∞ from the initial concentration C_0 to C_E during solidification of samples Nos. 1 and 2 (thick dashed lines) (P = planar, E = eutectic, C = cellular).

experimental measurements. Indeed, local solid concentrations cannot be precisely determined in the presence of radial segregation, as the employed method based on image analysis leads to an average value on a given image field.

4. Conclusion

The purpose of this paper was to study the influence of thermal convection on the transitions between planar, eutectic and cellular fronts in directional solidification.

The microstructure selection under a stationary regime, i.e. for a sample of infinite length, was first treated, using scaling laws for the extent δ of the solute boundary layer ahead of the growing front. With regard to purely diffusive conditions, the microstructural transitions can be strongly displaced owing to segregation phenomena. Due to the variation of δ along the front (effect of radial segregation), microstructural transitions do not occur simultaneously at any point on the front. Our model allows a quantitative determination of the transition conditions in the region where δ is minimum (i.e. flow is going towards the front), and qualitatively predicts a range of existence of mixed structures.

In the case of a sample of finite length, longitudinal segregation can lead to an evolution of the microstructure as a function of the solidified fraction. Particularly, if both longitudinal and radial segregations are present, the transition between i and j structures is not abrupt but goes through a mixed $i + j$ structure.

Transitions between mixed (planar + eutectic and cellular + eutectic) and fully eutectic structures have been observed experimentally in hypo-eutectic Sn–Cu alloys grown horizontally. The bulk liquid composition at the mixed/eutectic transition, as well as the local solid composition at the transition inside the mixed structure, are found to be in good agreement with the theoretical values. However, only a posteriori composition measurements can be compared with calculated data. Further work is needed to model both longitudinal and radial segregation in mixed structures, in order to predict where microstructural transitions will be located in the sample. This would need to take into account the fact that the front is no longer isothermal, and thus nonplanar at the macroscopic scale.

5. Nomenclature

C_A	solubility limit in phase A
C_B	solubility limit in phase B
C_E	eutectic composition
C_{Li}	interfacial liquid composition
$\bar{C}_{Li}$	average local liquid composition at the interface
C_{Si}	interfacial solid composition
$\bar{C}_{Si}$	average local solid composition at the interface
$\bar{C}_S$	average local solid composition
$\tilde{C}_S$	solid composition averaged at the scale of the sample diameter
$\bar{C}_{SE}$	average eutectic composition in the intercellular zone
$\bar{C}_S^{CE}$	average local solid composition at the cellular/eutectic transition
C_0	initial composition
C_0^{PC}	bulk liquid composition at the planar/cellular transition
C_0^{PE}	bulk liquid composition at the planar/eutectic transition
C_0^{CE}	bulk liquid composition at the cellular/eutectic transition
C_∞	bulk liquid composition
$C_{\infty,tr}$	experimental bulk liquid composition at a microstructural transition
D	diffusion coefficient
f_e	solidified fraction in the eutectic part of the ingot
f_E	eutectic fraction in cellular structure
f_L	liquid fraction in the mushy zone
f_S	solidified fraction
$f_{S,tr}$	solidified fraction at a microstructural transition
g	gravity
G_{eff}	effective temperature gradient
G_L, G_S	liquid and solid temperature gradients
H	crucible diameter
k	partition coefficient

k_{eff}	effective partition ratio for a planar front
k'_{eff}	effective partition ratio for an eutectic front
K	segregation constant for a cellular front
K_L, K_S	liquid and solid thermal conductivities
m_ℓ	liquidus slope
R	solidification rate
R_C	critical rate at the planar/cellular/eutectic triple junction
S	interface area
T_E	eutectic temperature
T_i	interfacial temperature
T_M	melting temperature of pure A
z	coordinate normal to the interface
z_t	coordinate of the tips of a cellular (dendritic) front
β_T	volume thermal expansion coefficient
δ	extent of the solute boundary layer
λ	cellular spacing
ν	kinematic viscosity

5.1. Dimensionless parameters

$\Delta = \delta R/D$	convecto-diffusive parameter
$\bar{\Delta}$	average value of Δ along the interface
$\mathrm{Pe} = HR/D$	Peclet number
$\mathrm{Gr} = \beta_T g G_L H^4/\nu^2$	Grashof number
$\mathrm{Sc} = \nu/D$	Schmidt number

Acknowledgements

Dr. J.P. Garandet is gratefully acknowledged for fruitful discussions on the topic. This study has been conducted in the framework of the GRAMME agreement between the CNES and the CEA.

References

[1] R. Trivedi, W. Kurz, Acta Metall. Mater. 42 (1994) 15.
[2] K. Shibata, T. Sato, G. Ohira, J. Crystal Growth 44 (1978) 419.
[3] W.J. Boettinger, F.S. Biancaniello, S.R. Coriell, Metall. Trans. A 12A (1981) 321.
[4] J.J. Favier, A. Rouzaud, J. Crystal Growth 64 (1983) 367.
[5] M. Hennenberg, A. Rouzaud, D. Camel, J.J. Favier, J. Crystal Growth 85 (1987) 49.
[6] J.P. Garandet, J.J. Favier, D. Camel, in: D.T.J. Hurle (Ed.), Handbook of Crystal Growth 2, North-Holland, Amsterdam, 1994.
[7] M.D. Dupouy, D. Camel, J.J. Favier, Acta Metall. 37 (1989) 1143.
[8] K.A. Jackson, J.D. Hunt, Trans. Met. Soc. AIME 236 (1966) 1129.
[9] M.C. Flemings, Solidification Processing, McGraw-Hill, New York, 1974.
[10] T.R.A. Davey, J.V. Happ, Trans. Inst. Mining Met. Ser. C 78 (1969) 108.
[11] T.B. Massalski (Ed.), Binary Alloy Phase Diagram, ASM, New York, 1990.
[12] C.H. Ma, R.A. Swalin, Acta Metall. 8 (1960) 388.
[13] T. Ejima, T. Yamamura, N. Uchida, Y. Matsuzaki, J. Jpn. Inst. Met. 44 (1980) 316.
[14] C.E. Homer, H. Plummer, J. Inst. Metals 64 (1939) 169.
[15] J.A. Burton, R.C. Prim, W.P. Schlichter, J. Chem. Phys. 21 (1953) 1987.
[16] L. O Wilson, J. Crystal Growth 44 (1978) 247.
[17] J.P. Garandet, J. Crystal Growth 114 (1991) 593.
[18] J.P. Garandet, A. Rouzaud, T. Duffar, D. Camel, J. Crystal Growth 113 (1991) 587.
[19] B. Drevet, J.P. Garandet, D. Camel, J.J. Favier, J. Crystal Growth 129 (1993) 549.
[20] Smithells, Metals Reference Handbook, 5th ed., Butterworths, London, 1976.
[21] L.D. Lucas, Techniques de l'Ingénieur/Métallurgie, Form M65, Paris, 1984.
[22] B. Drevet, PhD Thesis, INP Grenoble, France, 1991.

ELSEVIER

Journal of Crystal Growth 181 (1997) 160–164

JOURNAL OF CRYSTAL GROWTH

Letter to the Editors

Study of periodically poled Czochralski-grown Nd : Mg : $LiNbO_3$ by chemical etching and X-ray microanalysis

I.I. Naumova[a,*], N.F. Evlanova[a], O.A. Gilko[a], S.V. Lavrishchev[b]

[a] *Physical Department, Moscow State University, Moscow 119899, Russian Federation*
[b] *General Physics Institute, Russian Academy of Science, Moscow 117924, Russian Federation*

Received 14 August 1996; accepted 20 March 1997

Abstract

Nd : Mg : $LiNbO_3$ bulk single crystals with periodically poled ferroelectric domain structure were grown by Czochralski technique along [2 $\bar{1}$ $\bar{1}$ 0] (X-axis) and along the normal to the face (0 1 $\bar{1}$ 2). The domain structure with period 4–30 μm was studied by selective chemical etching and metallographic microscope. The distribution of the impurities along the growth directions was measured by wave dispersive X-ray (WDX) microanalysis. The domain structure of crystals and the distribution of impurities are strongly dependent on the seed orientation.

1. Introduction

Bulk periodically poled $LiNbO_3$ single crystal is a promising material for nonlinear optical devices, such as second-harmonic generation [1–3] and optical parametric oscillation [4] using quasi-phase-matching (QPM) [5]. Periodic reversals of spontaneous polarization (P_s) in the doped $LiNbO_3$ crystal correlate with the periodic reversals in the sign of the nonlinear coefficient. To compensate the phase-velocity dispersion, the nonlinear coefficient should be modulated with the period $\Lambda = 2\,ml_c$, where $m = 1, 2, 3\ldots$ is the order of the phase-matched harmonic and l_c is the coherence length of the interaction. Uniform micron-scale periodic structures with flat domain boundaries are needed for QPM-devices.

In the Czochralski-grown doped $LiNbO_3$ single crystals, a periodic domain structure is connected with rotation-induced growth striations. Some observations of growth striations and associated ferroelectric domains in $LiNbO_3$ doped with Cr [6, 7] and Y [8, 9] were made. Tasson et al. [6] suggested that the gradient of impurity concentration in $LiNbO_3$ crystal influences the orientation of P_s. The correlation between the growth striations, temperature fluctuations at the crystal–melt interface and yttrium distribution in the rotation-induced growth striations in $LiNbO_3$ crystals grown along the X-axis was studied by Ming et al. [8]. By X-ray microanalysis they measured the yttrium

* Corresponding author.

0022-0248/97/$17.00 © 1997 Published by Elsevier Science B.V. All rights reserved
PII S0022-0248(97)00246-7

distribution along the normal to domain boundaries. A steep change in the concentration (at its minimum) corresponds to a smooth domain boundary, and a slow change (at its maximum) corresponds to a rough boundary.

Owing to the presence of the close-packed (0 1 $\bar{1}$ 2) face at the growth front, flat and thin ferroelectric domain boundaries were formed in crystals with Y–Mg, Dy–Mg and Nd–Mg binary doping [10]. The index of refraction is changed near to domain walls and a linear diffraction grating is formed. In previous studies of Y : Mg : $LiNbO_3$ crystal it was shown that face-type diffraction gratings had a nonsine shape [11]. This was evident from the Bragg diffraction of light in high orders. The dependence of diffraction efficiency on 15 orders was used to determine the amplitudes of Fourier harmonics and to restore the profile of grating through a reverse Fourier transform. The grating has a profile of two sharp peaks of different width (0.2 and 0.5 μm) and height per one period. The shapes of these peaks were attributed to different domain wall shapes, "head-to-head" and "tail-to tail" configurations.

2. Experiments and results

2.1. Crystal growth

Periodically poled Nd :Mg : $LiNbO_3$ single crystals were grown from a close to congruently melting composition (Li/Nb = 0.942) along the X-axis and along the normal to the (0 1 $\bar{1}$ 2) face (Fig. 1). In the latter case, the seed was cut from a slice of YZ-cut at an angle of 57° with respect to the Z-axis. Crystals were pulled at a rate 5–12 mm/h and a rotation rate of 6–20 rpm. The (0 1 $\bar{1}$ 2) face on the growth front was about 10 mm for boules 20 mm in diameter and, therefore, in the central part of boule, domain walls coincided with the face (Fig. 1a). The period of the regular domain structure (Λ) was determined by the rate ratio of pulling to rotation (Λ = 4–30 μm). The (0 1 $\bar{1}$ 2) face on the growth front of the double-doped $LiNbO_3$ crystals favored the formation of narrow, flat, sharp, regularly spaced boundaries of ferroelectric domains. Flat domain walls (Λ = 5.5 μm) in

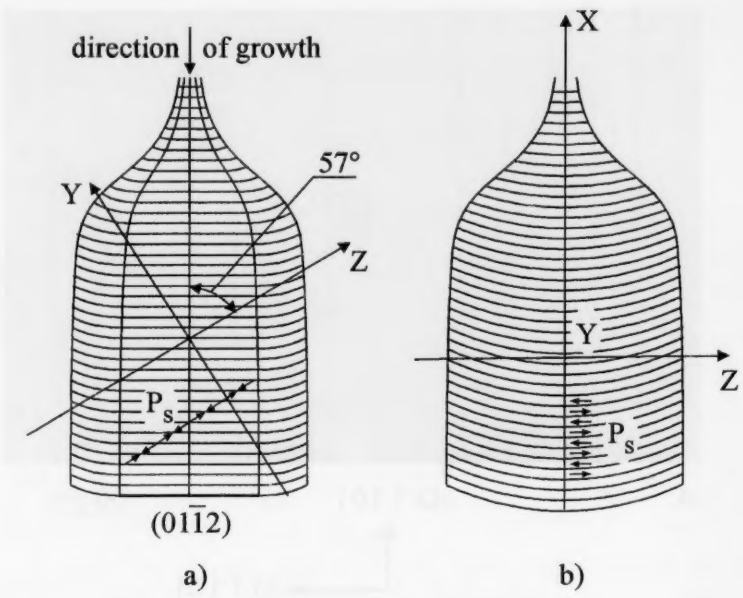

Fig. 1. The schematic image of the periodically poled $LiNbO_3$ crystals grown by Czochralski method along the normal to the (0 1 $\bar{1}$ 2) face (a) and along X-axis (b).

the $LiNbO_3$ crystals doped with (Y, Mg) were observed by SEM in secondary electron emission mode [12].

Rare-earth ions have been introduced in the $LiNbO_3$ matrix and are very well known as laser ions. Analysis of the Rutherford bakscattering for different rare-earth ions in Czochralski-grown $LiNbO_3$ crystals has shown that trivalent lanthanides are located inside the Li^+ octahedra, but shifted from the Li^+ position towards the nearest oxygen plane [13]. This shift increases linearly with the ionic radius of the impurity; for Nd^{3+} with ionic radius of 1.08 Å, the shift is 0.4 Å.

2.2. Chemical etching studies

The ferroelectric domain structure in the Nd : Mg : $LiNbO_3$ crystals was studied by selective chemical etching. We etched the cross-sectional surface of the crystals with 1 : 2 v/v mixture of HF and HNO_3 acids in a Pt-crucible at boiling temperature. As a preliminary, the crystal surface was ground and polished. After etching we observed the samples using a metallographic microscope. Nd : Mg : $LiNbO_3$ crystals grown along the normal to the (0 1 $\bar{1}$ 2) face have the domain boundaries parallel to this face and the most flat (Fig. 2A). Fig. 2B shows that the domain walls in the

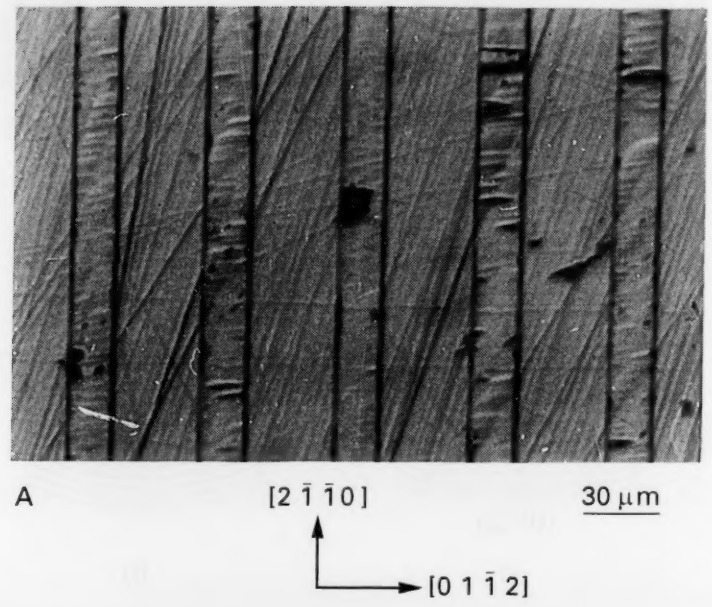

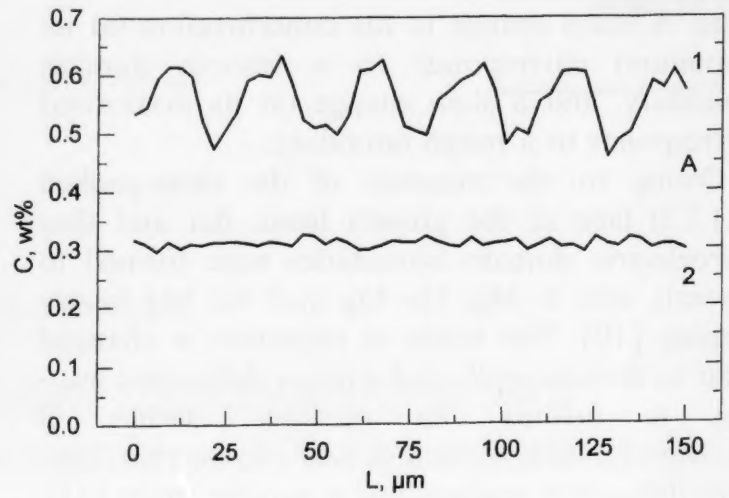

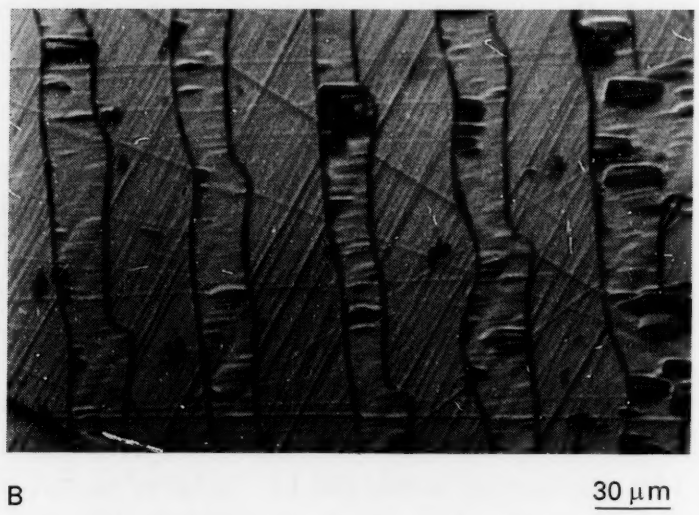

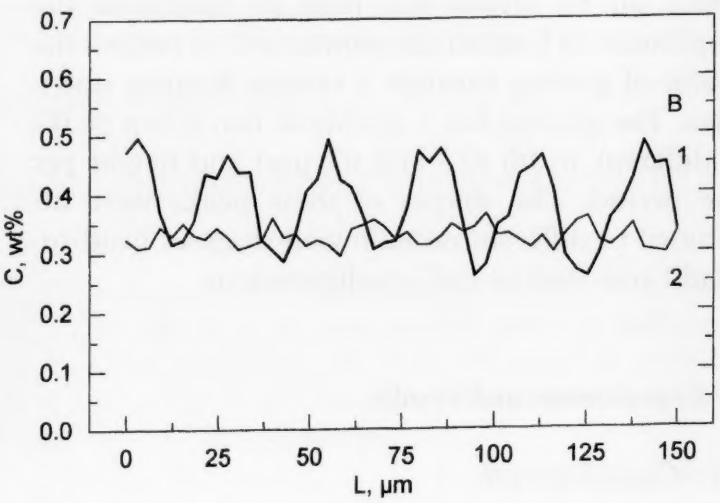

Fig. 2. The domain structure of Nd : Mg : $LiNbO_3$ crystal grown along the normal to the (0 1 $\bar{1}$ 2) face and the corresponding WDX measurements of the Nd (curve 1) and Mg (curve 2) distributions: (A) the central region of crystal with flat domain walls formed by the face; (B) the adjacent region. Marker represents 30 μm.

nonfacet region of crystal have a rough shape. Nd : Mg : $LiNbO_3$ crystals grown along the X-axis have heterogeneous domain structure which consists of periodically poled 10–15 mm squared (Fig. 3A) and single domain regions, about 10 mm squared (Fig. 3B). Periodically poled and single domain regions are situated next to the axis of the crystal.

2.3. X-ray microanalysis

The distribution of Nd and Mg concentration of as-grown crystals along the normal to the growth striations was measured by means of wave dispersive X-ray microanalysis in the scanning electron microscope JSM-840. Camebax SX-50 was used for impurity concentration measurements. Oxides of dopants were used as standards. Coating of the surface with an Au-film (100 Å) screens the charge pattern. The diameter of the probe did not exceed 0.1 μm, the energy of electrons amounted to 20 KeV, the scanning interval was 1–3 μm. The relative experimental error of the measurements of the Nd concentration amounts to about 2%, and for Mg about 1%.

In the Nd : Mg : $LiNbO_3$ crystals grown along the normal to the (0 1 $\bar{1}$ 2) face the distribution of

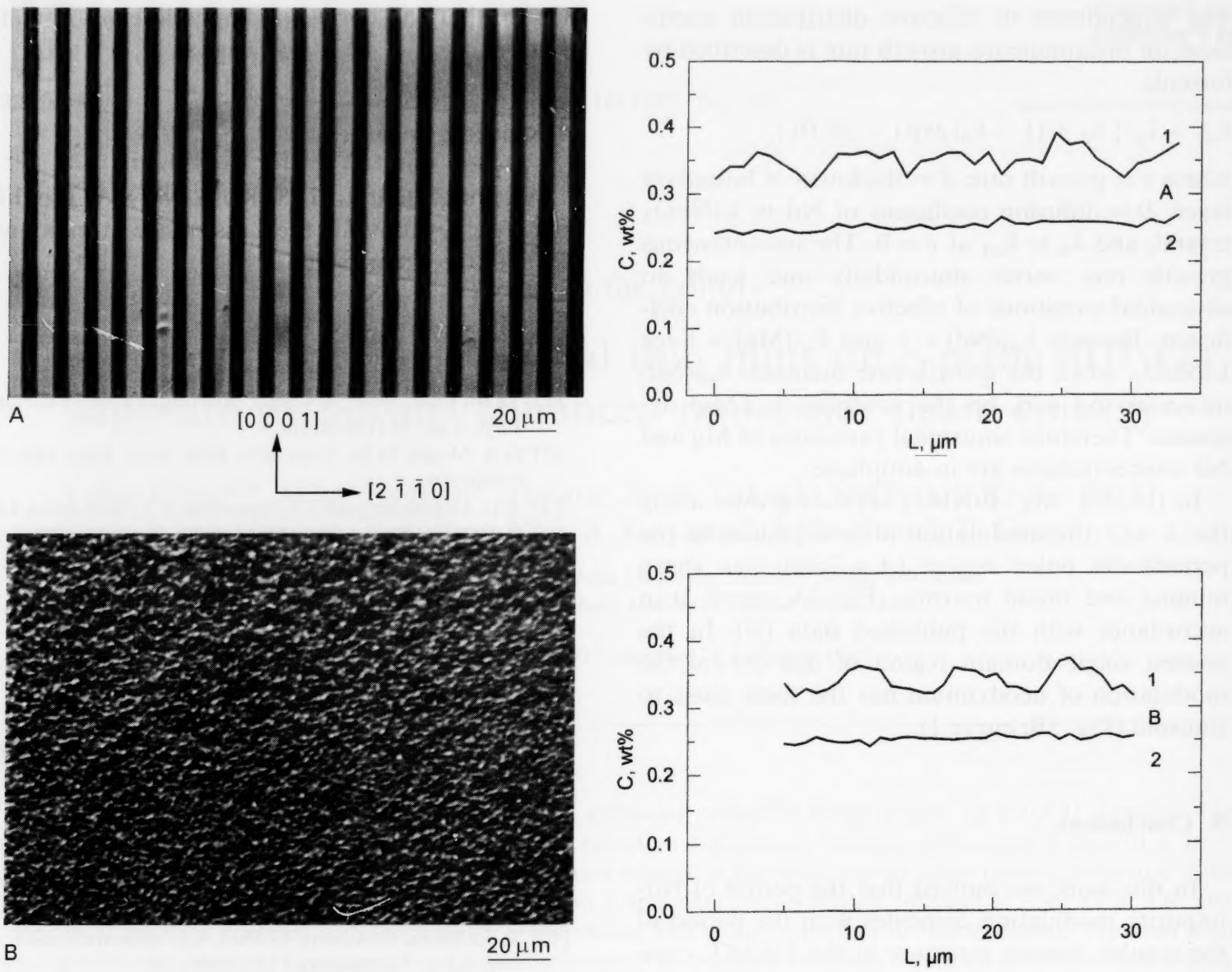

Fig. 3. The domain structure of Nd : Mg : $LiNbO_3$ crystal grown along X-axis and the corresponding WDX measurements of the Nd (curve 1) and Mg (curve 2) distributions: (A) periodically poled rigion; (B) single domain region. Marker represents 20 μm.

the neodymium concentration (c, wt%) has the form close to a sinusoid with period corresponding to the period of the regular domain structure, $\Lambda = 27$ μm (Fig. 2A, curve 1). The effective distribution coefficient (k_{eff}) of trivalent rare-earth ions in $LiNbO_3$ crystal is about 0.1. It has been known, that this value for Nd can be enhanced by several times by co-doping with Mg [14, 15]. The distribution of magnesium is more uniform (Fig. 2A, curve 2), $k_{eff} = 1.2$ [14, 16]. It is found that magnesium as a second dopant improves the quality of the regular domain structure, stimulates fixing of domain walls on growth striations [10]. According to our calculation k_{eff} for magnesium is close to one. The concentration of Nd is larger in the crystal region formed by the facet ($k_{eff} = 0.64$); outside the "face region", $k_{eff} = 0.42$ (Fig. 2A, Fig. 2B, curve 1). The difference in the values of k_{eff} arises since different growth mechanisms operating in the faceted and peripheral areas of the $LiNbO_3$ crystal.

Fig. 2B (curves 1, 2) shows that the dependences of Nd and Mg distributions have the tendency to be in antiphase. This result can be explained in the framework of the Burton–Prim–Slichter theory [17].

The dependence of effective distribution coefficient on instantaneous growth rate is described by formula

$$k_{\text{eff}} = k_0/\{\, k_0 + (1 - k_0) \exp(-v\delta/D) \,\},$$

where v = growth rate, δ = thickness of boundary layer, D = diffusion coefficient of Nd in $LiNbO_3$ crystal, and k_0 is k_{eff} at $v = 0$. The instantaneous growth rate varies sinusoidally and leads to sinusoidal variations of effective distribution coefficient. Because $k_{\text{eff}}(\text{Nd}) < 1$ and $k_{\text{eff}}(\text{Mg}) > 1$ for $LiNbO_3$, when the growth rate increases $k_{\text{eff}}(\text{Nd})$ increases too and, on the contrary, $k_{\text{eff}}(\text{Mg})$ decreases. Therefore, sinusoidal variations of Mg and Nd concentrations are in antiphase.

In the Nd : Mg : $LiNbO_3$ crystals grown along the X-axis the modulation of neodymium in the periodically poled region ($\Lambda = 7\ \mu\text{m}$) has sharp minima and broad maxima (Fig. 3A, curve 1) in accordance with the published data [8]. In the nearest single domain region of this crystal the modulation of neodymium has the form close to sinusoid (Fig. 3B, curve 1).

3. Conclusions

In this work we showed that the period of Nd-impurity modulation coincides with the period of the regular domain structure in the $LiNbO_3$ crystals. The domain structure in the region of crystal formed by the (0 1 $\bar{1}$ 2) face has flat boundaries and the concentration of Nd-impurity is larger in this region. In the double-doped $LiNbO_3$ crystals the concentrations of Nd and Mg impurities have a tendency to be in antiphase. It is found that the different growth directions of the $LiNbO_3$ crystals gave rise to different types of the Nd-impurity distribution and correspondingly different domain patterns.

Acknowledgements

We are grateful to D.S. Kulikova, S.A. Blokhin and V.A. Dyakov for their assistance in many aspects of the experiment.

References

[1] Ya-lin Lu, L. Mao, S. Cheng, N. Ming, Yu-tian Lu, Appl. Phys. Lett. 59 (1991) 516.
[2] G.A. Magel, M.M. Fejer, R.L. Byer, Appl. Phys. Lett. 56 (1990) 108.
[3] A.L. Aleksandrovskii, I.I. Naumova, V.V. Tarasenko, G.I. Yakovleva, Kvantovaya Elektronika 16 (1989) 2086.
[4] L.E. Myers, G.D. Miller, R.C. Eckardt, M.M. Fejer, R.L. Byer, W.R. Bosenberg, Opt. Lett. 20 (1995) 52.
[5] J.A. Armstrong, N. Bloembergen, J. Ducuing, P.S. Pershan, Phys. Rev. 127 (1962) 1918.
[6] M. Tasson, H. Legal, H. Gay, J.C. Peuzin, F.C. Lissalde, Ferroelectrics 13 (1976) 479.
[7] A. Feisst, A. Räuber, J. Crystal Growth 63 (1983) 337.
[8] N. Ming, J. Hong, D. Feng, J. Mater. Sci. 17 (1982) 1663.
[9] I.I. Naumova, V.V. Tarasenko, G.I. Yakovleva, A.L. Aleksandrovskii, 7th All-Union Conf. on Crystal Growth, Proc. 3, Moscow, 1988, p. 265.
[10] I.I. Naumova, Crystallogr. Rep. 39 (1994) 1029.
[11] A.L. Aleksandrovskii, I.I. Naumova, O.A. Gliko, V.I. Pryalkin, Kvantovaya Elektronika 23 (1996) 657.
[12] R. Le Bihan, D. Alberty, D. Pain, A.L. Aleksandrovskii, I.I. Naumova, Ferroelectrics 172 (1995) 181.
[13] A. Lorenzo, H. Jaffrezic, B. Roux, G. Boulon, J. Garcia-Solé, Appl. Phys. Lett. 67 (1995) 3735.
[14] K. Nassau, H.J. Levinstein, G.M. Loiacono, J. Chem. Solids 27 (1986) 551.
[15] B.C. Grabmaier, F. Otto, J. Crystal Growth 79 (1986) 682.
[16] K.G. Belabaev, A.A. Kaminskii, S.E. Sarkisov, Phys. Status Solidi (a) 28 (1975) k17.
[17] J.A. Burton, R.C. Prim, W.P. Slichter, J. Chem. Phys. 21 (1953) 1987.

ELSEVIER

Journal of Crystal Growth 181 (1997) 165–169

JOURNAL OF CRYSTAL GROWTH

Letter to the Editors

Growth of ZnO single crystal thin films on *c*-plane (0 0 0 1) sapphire by plasma enhanced molecular beam epitaxy

Yefan Chen[a,*], D.M. Bagnall[a], Ziqiang Zhu[a], Takashi Sekiuchi[a], Ki-tae Park[a], Kenji Hiraga[a], Takafumi Yao, S. Koyama[b], M.Y. Shen[b], T. Goto[b]

[a] *Institute for Materials Research, Tohoku University, Aoba-ku, Sendai 980, Japan*
[b] *Department of Physics, Tohoku University, Sendai 980, Japan*

Received 20 January 1997; accepted 28 February 1997

Abstract

ZnO single crystal thin films were grown by plasma enhanced molecular beam epitaxy on (0 0 0 1) sapphire. The growth modes of ZnO epilayers were investigated by reflection high-energy electron diffraction. A transition from two-dimensional nucleation to three-dimensional nucleation is found at the initial growth stage. Optical properties of the films, studied by photoluminescence spectroscopy, exhibit a dominant bound exciton emission at 3.361 eV at 4 K, and a deep level emission centered at 2.42 eV which is associated with either impurities or native defects. The deep level emission which is successfully suppressed to 1/500 of intensity of the excitonic emission. Fabrication of these high-quality ZnO epilayers had lead to observation of stimulated emission at room temperature.

PACS: 78.66.Hf; 81.05.Dz; 81.15.Hi

Keywords: Growth; ZnO; Plasma; MBE; Sapphire; Optoelectronic

Wide and direct band-gap semiconductor materials are of considerable interest for use within blue and ultra-violet (UV) optical devices such as light emitting diodes and laser diodes. In recent years SiC, III–V nitrides and ZnSe based II–VI semiconductors have all been extensively studied for their optical properties [1]. Zinc oxide (ZnO) is a wide and direct band-gap II–VI semiconductor, it has an energy gap of 3.37 eV at room temperature [2], and is another material which may yet find uses in commercial blue and UV light emitting devices.

Previous reports on thin film ZnO have described a variety of deposition techniques, including magnetron sputtering [3], chemical vapor deposition (CVD) [4] and pulsed laser deposition

* Corresponding author. E-mail: yfchen@imr.tohoku.ac.jp.

0022-0248/97/$17.00 © 1997 Elsevier Science B.V. All rights reserved
PII S0022-0248(97)00286-8

[5]. ZnO films are commonly used for surface acoustic wave devices or as transparent electrodes. For ZnO to be of use in optoelectronic devices, however high-quality single crystal thin films with structures of monolayer dimensions need to be grown. This requires high quality and accurately controllable growth techniques, however, techniques such as molecular beam epitaxy (MBE) and metalorganic chemical vapor deposition, are not yet well developed for ZnO. There has been only one report on the MBE growth of ZnO [6], where ZnO was grown as a buffer layer for GaN. In the present paper, we report the growth of ZnO films on (0 0 0 1) sapphire substrates by microwave plasma enhanced MBE.

The ZnO films were grown in a home-made MBE system. The growth chamber is evacuated by an oil-free turbo molecular pump, which produces a base vacuum of around 5×10^{-10} Torr. A conventional Knudsen cell is used to evaporate elemental zinc of 6N purity. Active oxygen, produced by a microwave plasma source, is injected into the MBE chamber via a quartz pipe with the flow rate controlled by a leak valve.

Before growth, the sapphire substrates were degreased by successive supersonic cleaning in acetone, methanol and deionized water, then chemically etched in hot (160°C) solution of 3 : 1 $H_2SO_4 : H_3PO_4$ for 10 min and blown dry in dry nitrogen. After chemical cleaning and etching, specimens were bonded to a molybdenum substrate block with indium solder and then inserted into the MBE system. After thermal cleaning at 800°C for 5 min, the substrates were exposed to a gentle O_2 plasma at 600°C for 30 min. This treatment resulted in a sharp streaky RHEED pattern with Kikuchi lines (see Fig. 1a) indicative of a smooth and clean surface suitable for epitaxial growth. During growth the O_2 overpressure was set at 1×10^{-4} Torr whilst the microwave plasma source was operated at 120 W. Under these conditions, optical emission spectroscopy of the plasma shows a predominance of the atomic transition at 777 nm [7], indicating the efficient production of the oxygen atom by the plasma source. The ZnO films were grown at 500–550°C with a growth rate of about 0.1 μm/h. As grown ZnO films are transparent with mirror-like appearance.

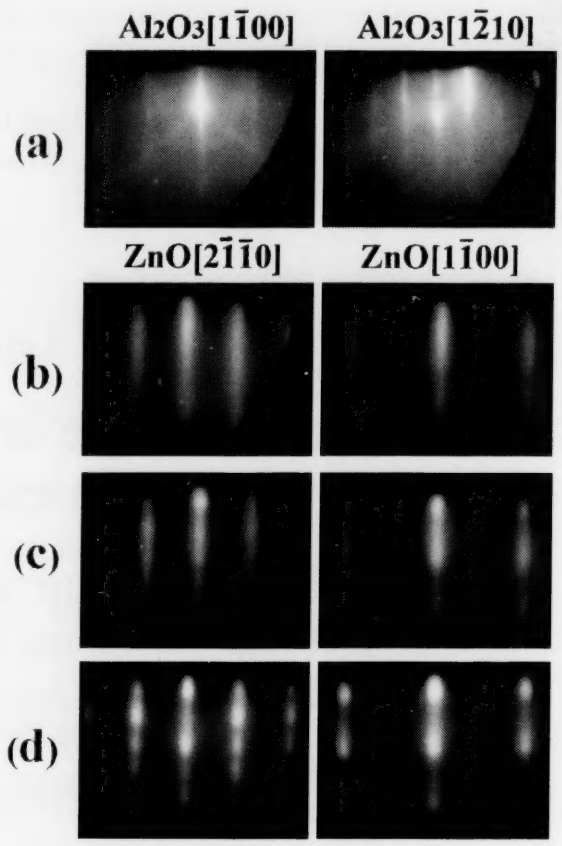

Fig. 1. RHEED patterns of: (a) (0 0 0 1)Al_2O_3 substrate after thermal and O_2 plasma cleaning; and ZnO epilayer (b) after 10 min growth; (c) after 20 min growth; (d) after 1 h growth.

The epitaxial relationship between the ZnO overlayer and the sapphire substrate and the growth modes of ZnO were studied by reflection high-energy electron diffraction (RHEED) during growth. X-ray diffraction (XRD) and scanning electron microscopy (SEM) were used to investigate crystal quality and surface morphology. XRD θ-rocking curves were obtained by a Philips X Pert-MRD high-resolution diffractometer with Cu $K\alpha_1$ radiation diffracted by four-crystal Ge(2 2 0) monochromator. Photoluminescence (PL) measurements were performed with excitation by He-Cd laser (325 nm). For high excitation the frequency-tripled output (355 nm) of a Nd : YAG laser, operating at repetition rate of 10 Hz, was used.

Fig. 1 shows the RHEED patterns during different stages of ZnO growth. At the initial growth stage (Fig. 1b), a streaky pattern was observed, this suggests two-dimensional epitaxial growth and is similar to observations made during the growth of GaN on sapphire (0 0 0 1) [8]. The [2 $\bar{1}$ $\bar{1}$ 0] direc-

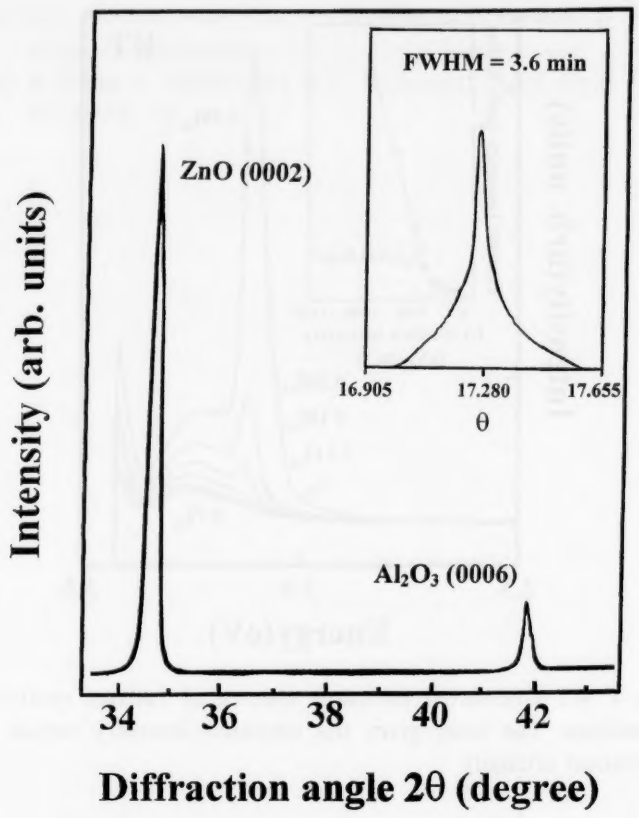

Fig. 2. X-ray diffraction of a ZnO epilayer on (0 0 0 1)Al_2O_3 with inset of corresponding θ-rocking curve.

tion of the ZnO is found to align with the [1 $\bar{1}$ 0 0] direction of the Al_2O_3, and [1 $\bar{1}$ 0 0] direction of the ZnO aligns with the [1 $\bar{2}$ 1 0] direction of the Al_2O_3. After 20 min growth (equivalent to about 30 nm of ZnO), a spotty pattern appears to superimpose on the streaky pattern, indicating the formation of islands on the growth surface (Fig. 1c). Subsequently, the intensity of spotty pattern increases, while the streaky pattern gradually disappears (Fig. 1d). It is noted that this phenomena of an initial two-dimensional nucleation followed by three-dimensional nucleation contrasts with the observations during the epitaxy of InAs or InGaAs on GaAs [9], which are well known as a typical Stranski-Kranstanov growth mode. In the case of epitaxy of InGaAs on GaAs, growth of the first epitaxial overlayer on a mismatched substrate is pseudomorphic whilst strain is accommodated within the epitaxial layer. Above a certain critical thickness, the epitaxial layer releases strain to yield dislocations, and a change to an island growth mode results. In the case of ZnO growth on Al_2O_3, the very large mismatch between ZnO and sapphire substrate ($\sim$16%) does not allow a coherent layer-by-layer growth to exceed the scale of about one monolayer [10]. This is confirmed by the RHEED observations as the lattice constant determined from the separation of diffracted streaky patterns is approximately equal to the bulk value of ZnO, indicating a relaxed ZnO epilayer.

The post-growth SEM studies of the morphology of the ZnO show a predominantly smooth surface with some scattered crystallites. It is suggested that these crystallites begin formation at the growth mode transition to yield the superimposed spotty and streaky RHEED patterns.

The crystallinity of the films was examined by XRD. A typical θ–2θ scan is shown in Fig. 2, with the inset showing the corresponding θ-rocking curve scan. The θ–2θ scan gives the ZnO(0 0 0 2) peak at 34.6°, while the full-width at half- maximum (FWHM) obtained from the θ rocking curve is 3.6 min. It is noted that the peak in θ-rocking curve displays a Lorentzian line shape which can be fitted with two peaks, a broad one with long tails surrounding a sharp one. This feature is possibly related to structural defects, such as strain and dislocations, originating from the interface.

Fig. 3 shows PL spectra of a ZnO film grown at 550°C measured at 4 K and room temperature, respectively. The low-temperature PL spectrum (Fig. 3b) exhibits a strong near band edge emission at 3.361 eV, with a FWHM of 5.5 meV. This peak has been previously attributed to an exciton bound to a neutral impurity [2]. The peaks located at 3.289 and 3.217 eV are the longitudinal optical phonon replicas of the 3.361 eV peak with 1LO and 2LO. A very weak and broad deep level emission (about 1/500 of intensity of excitonic emission) centered at 2.42 eV can also be seen. It is reported that either impurities or native defects are responsible for the deep level emission [11]. At room temperature, the near band edge emission shifts to 3.292 eV and is broadened to 117 meV (see Fig. 3a). Even at room temperature, the deep level emission is relatively weak. We believe that the ultra-high vacuum environment of MBE and use of the microwave plasma oxygen source significantly assists the fabrication of low impurity, low defect density, epitaxial ZnO thin films, this is evidenced by a

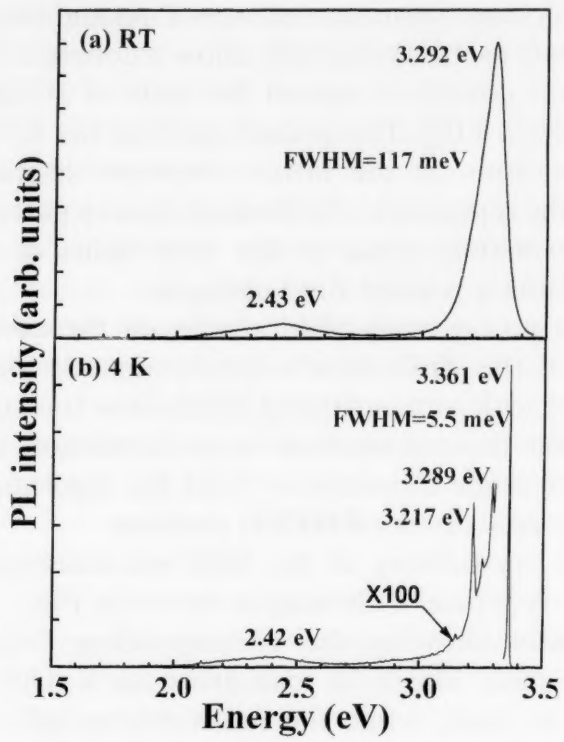

Fig. 3. Photoluminescence spectra obtained from ZnO epilayer on (0 0 0 1)Al_2O_3 at (a) room temperature and (b) 4 K, respectively.

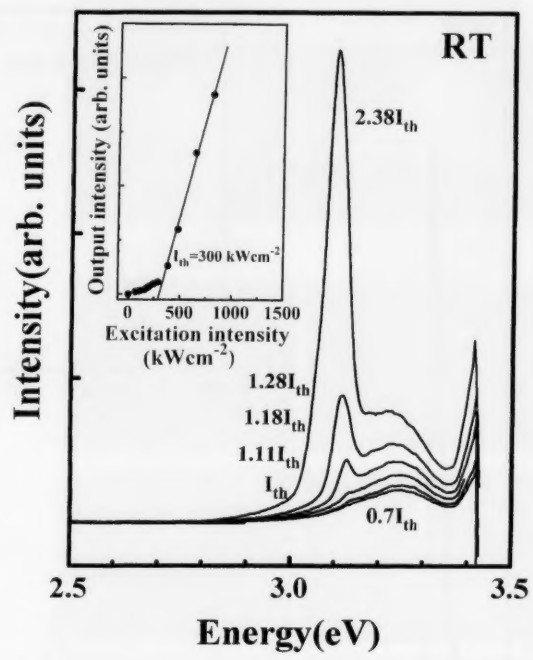

Fig. 4. RT stimulated emission spectra at various excitation intensities. The inset gives the emission intensity versus the excitation intensity.

reduction in the magnitude of the deep level emission, when compared to bulk material and CVD epilayers [11].

The considerably reduced level of impurities and defects in these ZnO films has enabled the observation of room temperature stimulated emission. Photoluminescence spectra taken in a high excitation regime and detected perpendicular to the growth plane are shown in Fig. 4. At relatively low excitation powers a single emission peak is observed at 3.25 eV. This is the near band edge emission shifted from its expected energy of 3.37 eV as a result of significant heating caused by the excitation laser. This peak increases linearly with the increasing excitation, (see inset of Fig. 4), as is expected for spontaneous emission. As the excitation is increased above the threshold intensity of about 300 kW/cm^2 a narrow emission feature appears on the low-energy side of the spontaneous emission peak at around 3.08 eV. At this point emission intensity begins to increase superlinearly with excitation power, providing clear evidence of stimulated emission.

In summary, we have succeeded in the MBE growth of ZnO single crystal films by using a microwave plasma oxygen source. The RHEED observations reveal a three-dimensional growth mode after a transition from an initial two-dimensional growth. PL studies demonstrate the very high quality of ZnO films. Room temperature stimulated emission from these ZnO films has been observed.

References

[1] H. Morkoç, S. Strite, G.B. Gao, M.E. Lin, B. Sverdlov, J. Appl. Phys. 76 (1994) 1363.
[2] C. Klingshirn, Phys. Status Solidi (b) 71 (1975) 547.
[3] Akihiro Hachigo, Hideaki Nakahata, Kenjiro Higaki, Satoshi Fujii, Shin-ichi Shikata, Appl. Phys. Lett. 65 (1996) 2556.
[4] T. Minami, H. Nanto, S. Takata, Jpn. J. Appl. Phys. 23 (1984) L280.
[5] Shunichi Hayamizu, Hitoshi Tabata, Hidekazu Tanaka, Tomoji Kawai, J. Appl. Phys. 80 (1996) 787.
[6] M.A.L. Johnson, Shizuo Fujita, W.H. Rowland Jr., W.C. Hughes, J.W. Cook Jr., J.F. Schetzina, J. Electron. Mater. 25 (1996) 855.
[7] P. O'Keeffe, S. Komuro, S. Den, T. Morikawa, Y. Aoyogi, Jpn. J. Appl. Phys. 30 (1991) L834.

[8] R.C. Powell, N.-E. Lee, Y.-W. Kim, J.E. Greene, J. Appl. Phys. 73 (1993) 189.
[9] S. Guha, A. Madhukar, K.C. Rajkumar, Appl. Phys. Lett. 57 (1990) 110.
[10] R.J. Hauenstein, D.A. Collins, X.P. Cai, M.L. O'Steen, T.C. McGill, Appl. Phy. Lett. 66 (1995) 2861.
[11] S. Bethke, H. Pan, B.W. Wessels, Appl. Phys. Lett. 52 (1998) 138.

Classification codes and Keywords

Elsevier Science B.V. invites the submission of classification codes and keywords for this journal.

Classification codes and keywords will enhance the disclosure of the articles published in this journal.

Authors are requested to submit at least one and at the most four classification code numbers, and up to six keywords of their own choice.
Both the classification codes and the keywords should be included on the abstract page when the manuscript is submitted.
The codes and keywords will appear below the abstract in the printed article.

The classifications codes in use for this journal are the Physics and Astronomy Classification Scheme (PACS '96) and the Mathematics Subject Classification Scheme (MSC '91). Both schemes are accessible on the Elsevier Home Page (http://www.elsevier.nl).

PACS is also available online on the American Institute of Physics Web server (http://www.aip.org/pacs). MSC is available on both the American Mathematical Society e-math information service (http://e-math.ams.org/msc) and on the server of Zentralblatt für Mathematik in Germany (http://www.zblmath.fiz-karlsruhe.de/class).

Elsevier Science acknowledges the American Institute of Physics, the American Mathematical Society and Zentralblatt für Mathematik for their kind permission to reprint the PACS and MSC classification schemes and to load these on to the Elsevier Web server.

For further information, please contact the publisher:

Elsevier Science B.V.
Physics and Materials Science
Box 2759, 1000 CT Amsterdam
The Netherlands

◆ ◆ ◆ ◆ ◆ ◆ ◆

ultramicroscopy

Editor: Pieter Kruit

.....Also for SPM techniques!

Associate Editor for Scanning Probe Microscopy:

Stuart M. Lindsay

✓ ***a high quality presentation of your article***

✓ ***in the top journal in the field of Microscopy***

✓ ***with the highest citation ranking***

1997 Subscription information:
Volumes 67-71 (20 issues) NLG 2620.00/USD 1617.00
ISSN 0304-3991

ORDER FORM

☐ Please send me a FREE SAMPLE COPY of Ultramicroscopy

☐ Please send me INSTRUCTIONS TO AUTHORS of Ultramicroscopy

Name:.....
Institute/Company: .....
Address: .....
Post/Zip code:.....
City:.....
Country: .....

ELSEVIER SCIENCE

New York
Elsevier Science
P.O. Box 945
New York, NY 10159-0945
USA
Tel: (+1) 212-633-3730
(Toll Free number for North American customers:
1-888-4ES-INFO (437-4636))
Fax: (+1) 212-633-3680
E-mail: usinfo-f@elsevier.com

Amsterdam
Elsevier Science
P.O. Box 211
1000 AE Amsterdam
The Netherlands
Tel: (+31) 20-485-3757
Fax: (+31) 20-485-3432
E-mail: nlinfo-f@elsevier.nl

Tokyo
Elsevier Science
9-15, Higashi-Azabu 1-chome
Minato-ku, Tokyo 106
Japan
Tel: (+81) 3-5561-5033
Fax: (+81) 3-5561-5047
E-mail: info@elsevier.co.jp

Singapore
Elsevier Science
No. 1 Temasek Avenue
#17-01 Millenia Tower
Singapore 039192
Tel: (+65) 434-3727
Fax: (+65) 337-2230
E-mail: asiainfo@elsevier.com.sg

Please quote the following code with all orders/requests: NAS

Journal of Crystal Growth

Instructions to Authors (short version)

Submission of papers
Manuscripts (one original + two copies), should be sent to a member of the Editorial Board or preferably to an appropriate subject Associate Editor. News or announcements should be submitted through the Principal Editor; a duplicate should be sent directly to Elsevier Science B.V., address given below.
Original material. Submission of a manuscript implies it is not being simultaneously considered for publication elsewhere and that the authors have obtained the necessary authority for publication.

Types of contributions
Original research papers, Letters to the Editors and Priority communications are welcome. They should contain an Abstract (of up to 200 words) and a Conclusion section, which particularly in the case of theoretical papers translates the results into terms readily accessible to most readers.
As a guideline: *experimental papers* should not be longer than 16 double-spaced typed pages, and 8 figures + tables; for *theoretical papers* a maximum of 20 pages and 10 figures + tables is suggested.
Letters and Priority communications should not be longer than 5 double-spaced typed pages, and 3 figures + tables. They will be given priority in both the refereeing and production processes. The faster production schedule may preclude sending proofs of Letters and Priority communications to authors.

Manuscript preparation
Contributions may be written in English, French or German. They should have an abstract in English. The paper copies of the text should be prepared with double line spacing and wide margins, on numbered sheets.
Structure. Please adhere to the following order of presentation: Article title, Author(s), Affiliation(s), Abstract, PACS codes and keywords, Main text, Acknowledgements, Appendices, References, Figure captions, Tables.
Corresponding author. The name, complete postal address, telephone and fax numbers and the e-mail address of the corresponding author should be given on the first page of the manuscript.
Classification codes/keywords. Please supply one to four classification codes (PACS and/or MSC) and up to six keywords of your own choice that describe the content of your article in more detail.
References. References to other work should be consecutively numbered in the text using square brackets and listed by number in the Reference list. Please refer to the more detailed instructions for examples.

Illustrations
Illustrations should also be submitted in triplicate: one master set and two sets of copies. The *line drawings* in the master set should be original laser printer or plotter output or drawn in black india ink, with careful lettering, large enough (3–5 mm) to remain legible after reduction for printing. The *photographs* should be originals, with somewhat more contrast than is required in the printed version. They should be unmounted unless part of a composite figure. Any scale markers should be inserted on the photograph itself, not drawn below it.
Colour plates. Figures may be published in colour, if this is judged essential by the Editor. The Publisher and the author will each bear part of the extra costs involved. Further information is available from the Publisher.

After acceptance
Important. When page proofs of the accepted manuscripts are made and sent out to authors, this is in order to check that no undetected errors have arisen in the typesetting (or file conversion) process. At the proof stage only printer's errors may be corrected. No changes in, or additions to, the edited manuscript will be accepted.
Notification. The authors will receive the final answer of acceptance or rejection from the Office of the Principal Editor and will be invited to supply an electronic version of the accepted text, if this is not already available.
Copyright transfer. In the course of the production process you will be asked to transfer the copyright of the article to the Publisher. This transfer will ensure the widest possible dissemination of information.

Electronic manuscripts
The Publisher welcomes the receipt of an electronic version of your accepted manuscript. If there is not already a copy of this (on diskette) with the journal editor at the time the manuscript is being refereed, you will be asked to send a file with the text of the accepted manuscript directly to the Publisher by e-mail or on diskette (allowed formats 3.5″ or 5.25″ MS-DOS, or 3.5″ Macintosh) to the address given below. (When e-mailing a non-ASCII word-processor file, you should encode it, e.g. with UUENCODE or BinHex, so as to retain all formatting codes.) The name and version of the word-processing program and the type of operating system should always be indicated. Please note that no deviations from the version accepted by the Editor of the journal are permissible without the prior and explicit approval by the Editor. Such changes should be clearly indicated on an accompanying printout of the file.

Author benefits
No page charges. Publishing in Journal of Crystal Growth is free.
Free offprints. The corresponding author will receive 50 offprints free of charge. An offprint order form will be supplied by the Publisher for ordering any additional paid offprints.
Discount. Contributors to Elsevier Science journals are entitled to a 30% discount on all Elsevier Science books.

Further information (after acceptance)

Elsevier Science B.V., J. Crystal Growth
Issue Management Physics
and Materials Science
P.O. Box 2759, 1000 CT Amsterdam
The Netherlands
Fax: +31 20 485 2319/ +31 20 485 2704
E-mail: matsci-de-f@elsevier.nl

North-Holland, an imprint of Elsevier Science

JOURNAL OF
CRYSTAL GROWTH

Volume 181 (1997) Nos. 1/2

Abstracted/Indexed in: Aluminium Industry Abstracts; Chemical Abstracts; Current Contents: Physical, Chemical and Earth Sciences; EI Compendex Plus; Engineered Materials Abstracts; Engineering Index: INSPEC; Metals Abstracts

CONTENTS

Classical semiconductors

Influence of substrate misorientation on quality of active region and performance of GaAs/AlGaAs triple-quantum-well lasers grown by molecular beam epitaxy
D.H. Zhang, C.Y. Li and S.F. Yoon 1

Study of Zn diffusion into GaSb from the vapour and liquid phase
A.W. Bett, S. Keser and O.V. Sulima 9

Characterization of defect structures in magnetic liquid encapsulated Kyropoulos grown InP single crystals
H. Chung, W. Si, M. Dudley, D.F. Bliss, R. Kalan, A. Maniatty, H. Zhang and V. Prasad 17

Silicon doping of InGaAs grown by MOVPE using tertiarybutylarsine
X.G. Xu, Ch. Giesen, J. Xu, M. Heuken and K. Heime 26

Carbon and silicon doping in GaAs and AlAs grown on (3 1 1)-oriented GaAs substrates by metalorganic chemical vapor deposition
K. Tateno and C. Amano 33

Oxygen solubility in Si melts: influence of boron addition
K. Abe, T. Matsumoto, S. Maeda, H. Nakanishi, K. Hoshikawa and K. Terashima 41

Electronic materials

Crystal growth and optical properties of $Ti^{3+}:YAl_3(BO_3)_4$ and $Ti^{3+}:GdAl_3(BO_3)_4$
G. Wang, T.P.J. Han, H.G. Gallagher and B. Henderson 48

Oxygen nonstoichiometry in copper iron oxide [$CuFeO_{2+\delta}$] single crystals
T.-R. Zhao, M. Hasegawa and H. Takei 55

Solution growth; industrial, biological and molecular crystallization

Diffusion and cluster formation in aqueous solutions of potassium aluminum sulfate
S. Kim, A.S. Myerson and M. Kohl 61

Transition of octacalcium phosphate to hydroxyapatite in solution at pH 7.4 and 37°C
M. Iijima, H. Kamemizu, N. Wakamatsu, T. Goto, Y. Doi and Y. Moriwaki 70

Crystallogenesis studies in microgravity with the Advanced Protein Crystallization Facility on Space-Hab-01
M. Riès-Kautt, I. Broutin, A. Ducruix, William Shepard, R. Kahn, N. Chayen, D. Blow, K. Paal, W. Littke, B. Lorber, A. Théobald-Dietrich and R. Giegé 79

Crystallographic analyses of lysozyme and collagenase microgravity grown crystals versus ground controls
I. Broutin, M. Riès-Kautt and A. Ducruix 97

General subjects

Primary spacing selection of Cu–Mn alloy under laser rapid solidification condition
Q.Y. Pan, W.D. Huang, X. Lin and Y.H. Zhou 109

In situ and real-time observation of the formation and dynamics of a cellular interface in a succinonitrile–0.5 wt% acetone alloy directionally solidified in a cylinder
N. Noël, H. Jamgotchian and B. Billia 117

Segregation during horizontal Bridgman growth under an axial magnetic field
T. Alboussière, A.C. Neubrand, J.P. Garandet and R. Moreau 133

Influence of convection on the selection of solidification microstructures at low growth rates
M.D. Dupouy, B. Drevet and D. Camel 145

Letters to the Editors

Study of periodically poled Czochralski-grown $Nd:Mg:LiNbO_3$ by chemical etching and X-ray microanalysis
I.I. Naumova, N.F. Evlanova, O.A. Gilko and S.V. Lavrishchev 160

Growth of ZnO single crystal thin films on *c*-plane (0 0 0 1) sapphire by plasma enhanced molecular beam epitaxy
Y. Chen, D.M. Bagnall, Z. Zhu, T. Sekiuchi, Ki-tae Park, K. Hiraga, T. Yao, S. Koyama, M.Y. Shen and T. Goto 165

0022-0248(199710)181:1/2;1-9